NUREG/CR-6469
SAND96-2289

Experiments to Investigate Direct Containment Heating Phenomena with Scaled Models of the Calvert Cliffs Nuclear Power Plant

Manuscript Completed: August 1996
Date Published: February 1997

Prepared by
T. K. Blanchat, M. M. Pilch, M. D. Allen

Sandia National Laboratories
Albuquerque, NM 87185

R. Lee, NRC Project Manager

Prepared for
Division of Systems Technology
Office of Nuclear Regulatory Research
U.S. Nuclear Regulatory Commission
Washington, DC 20555-0001
NRC Job Code W6162

DISCLAIMER

ABSTRACT

The Surtsey Test Facility at Sandia National Laboratories (SNL) is used to perform scaled experiments for the Nuclear Regulatory Commission (NRC) that simulate High Pressure Melt Ejection (HPME) accidents in a nuclear power plant (NPP). These experiments are designed to investigate the effects of direct containment heating (DCH) phenomena on the containment load. In previous experiments, high-temperature, chemically reactive (thermitic) melt was ejected by high-pressure steam into a scale model of either the Zion or Surry NPP. The results from the Zion and Surry experiments can be extrapolated to other Westinghouse plants; however predicted containment loads cannot be generalized to certain types of Combustion Engineering (CE) plants. In most Westinghouse plants, there is (1) an intermediate compartment that is large compared to the reactor cavity but small compared to the main containment volume, and (2) there is no significant line-of-sight pathway for debris transport from the cavity to the main containment volume. Containment compartmentalization is the dominant mitigating feature. These two conditions are not satisfied for five CE plants: Calvert Cliffs 1 and 2, Millstone 2, Arkansas Nuclear One Unit 2, and Palisades. In particular, although these plants have an intermediate subcompartment, that is, the steam generator compartment, there is no flow path from the cavity to that compartment. The dispersal of melt from the cavity is predominately to the dome through the annular gap around the RPV. This circumvents the main mitigation associated with containment compartmentalization that exists in Zion and most other Westinghouse PWRs.

In all of the DCH integral effects testing conducted to-date, single phase superheated steam was used to drive the molten core simulant. This is based on the assumption that no water remains in the lower plenum at vessel breach because all the water has been vaporized by the time the vessel fails. However, if saturated water is present, then the driving fluid for molten core materials will be a two-phase water mixture at the time of vessel breach. The discharge of the water as film and droplets with the entrained debris will provide a potential heat sink since some of the thermal and chemical energy in the debris would be used to vaporize the water and may quench part of the melt. The increased amount of steam may also increase the hydrogen production from debris/steam oxidation. However, the potential for enhancing the DCH load due to hydrogen burning may be reduced due to an increased steam fraction that may inert the atmosphere and suppress a hydrogen burn.

Calvert Cliff-like plant geometries and the impact of codispersed water were addressed as part of the overall DCH issue resolution. Integral effects tests were performed with a $1/10^{th}$ scale model of the Calvert Cliffs NPP inside the Surtsey test vessel. The experiments investigated the effects of codispersal of water, steam, and molten core simulant materials on DCH loads under prototypic accident conditions and plant configurations. The results indicated that large amounts of coejected water reduced the DCH load by a small amount. Large amounts of debris were dispersed from the cavity to the upper dome (via the annular gap).

CONTENTS

CONTENTS (concluded)

LIST OF FIGURES

LIST OF FIGURES (continued)

LIST OF FIGURES (continued)

LIST OF FIGURES (continued)

LIST OF FIGURES (concluded)

LIST OF TABLES

LIST OF TABLES (concluded)

EXECUTIVE SUMMARY

A series of seven experiments were performed to investigate DCH phenomena in a 1/10th scale model of the Calvert Cliffs nuclear power plant. The Calvert Cliffs plant is typical of Combustion Engineering (CE) plants with a Bechtel annular cavity, a design that represents 5 out of the 15 CE plants in the United States. These types of cavities do not have instrument tunnels like Westinghouse plants, as do the Zion and Surry plants studied previously; in plants with Bechtel annular cavity designs the only debris dispersal pathway to the dome region is through the annular gap between the RPV wall and the biological shield wall. In these types of plants, mitigation of containment loads due to trapping in the subcompartments that was important in resolving the DCH issue for Westinghouse designs is absent, i.e., debris can be transported directly to the dome. Understanding the impact on DCH loads of debris transport to the dome was a primary goal of these experiments.

Plant analyses of Zion, Surry, and Calvert Cliffs with SCDAP/RELAP5 showed that if the RPV dries out, the surge line or hot leg will fail and the RCS will rapidly depressurize. Hence the most likely scenario that can lead to a HPME is an accident in which the operator intervenes and refloods the RPV but is unable to prevent vessel failure. Previous DCH experiments were performed with steam as the driving fluid. However, since water overlying the molten corium is likely, the CE experiments were designed to investigate the impact of coejected water on DCH loads. The results indicated that large amounts of coejected saturated water reduce the DCH load by 15 to 20% in the experiments.

The methodology chosen to simulate a coejected water accident scenario involved reacting the thermite directly in the cavity and, after waiting for the reaction to proceed to completion, introducing high-pressure water or steam into the cavity through a hole in the bottom head of the RPV. Results of all seven Calvert Cliffs experiments indicated that 58% of the total debris recovered posttest was transported to the upper dome. In the Zion and Surry tests without the annular gap modeled, only 7% to 10% of the total debris recovered was found in the upper dome. In addition, these tests indicated that a Calvert Cliffs cavity has a substantially smaller coherence ratio than in the Zion and Surry configurations. Measurements indicated that debris was dispersed from the cavity in less than 0.1 second, whereas the blowdown of the scaled RCS volume was several seconds.

Significant amounts of hydrogen, preexisting in the Surtsey atmosphere and also produced by the thermite reaction with condensate water, burned in the reactive atmosphere tests prior to the HPME event and moderately pressurized the vessel (~0.1 MPa). Hydrogen combustion prior to the HPME event is an artifact of the experimental method and, therefore, is not prototypic of a NPP accident. Experiment data suggest that potential hydrogen combustion during the HPME event did not contribute to loads, which may simply mean there was not enough hydrogen remaining to make a significant impact on the loads. These uncertainties in hydrogen combustion and timing in the experiments preclude taking credit for potential mitigation of hydrogen combustion resulting from coejected water in NPP analyses.

ACKNOWLEDGMENTS

The authors express their gratitude to Michael Oliver and Tom Thornhill, who were the electronics and instrumentation engineers for these experiments, and to Tim Covert, Frank Wilkins, and Gilbert Jefferson, who were the mechanical technicians. Three summer students participated in the performance of the test: Eric Antrim, Reginald Tillman, and Jose Walters. All operations at the Surtsey test site were performed under the capable management of the site resident mechanical engineer, Robert Nichols. T.Y. Chu and Richard Griffith reviewed the report, providing numerous helpful comments. Mary Lou Garcia typed, compiled, and edited the manuscript.

Additional guidance for the experiment programs was provided by a six-member DCH Experiment Technical Review Group (TRG). They included R.E. Henry (FAI), M. Ishii (Purdue), F.J. Moody (GE), S. Levy (Levy and Associates), M. Corradini (U. of Wisconsin), and R. Schneider (ABB Combustion Engineering). The DCH working group for the experimental program consisted of representatives of the sponsor (NRC), universities and industry (TRG), and the national laboratories (SNL), and met periodically to discuss new results and decide future directions.

This work was sponsored by the Accident Evaluation Branch of the Office of Research of the U.S. Nuclear Regulatory Commission. Input and valuable guidance were supplied by C.G. Tinkler and R.Y. Lee.

NOMENCLATURE

A_{annul}	=	area of annulus
A_f	=	cavity floor area
A_{floor}	=	floor area
A_g	=	flow area in gap
A_h	=	hole area
A_{mw}	=	manway area
ANL	=	Argonne National Laboratory
A_{nz}	=	flow area of nozzle cutouts
$A_{nz,bottom}$	=	projected area of nozzles on gap
A_w	=	cavity wall area
c_d	=	drag coefficient
$c_{p,d}$	=	specific heat of debris
$c_{v,a}$	=	specific heat of atmosphere
C_d	=	discharge coefficient
$C_{d,h}$	=	hole discharge coefficient
CC	=	Calvert Cliffs
CE	=	Combustion Engineering
CES	=	combustion engineering scoping
cm	=	centimeter
C_p	=	specific heat
$C_{R\tau}$	=	constant in coherence correlation
d	=	drop diameter
dt	=	time derivative
dV_w	=	change in accumulator water volume
D	=	drop diameter
DCH	=	direct containment heating
D_h	=	hole diameter
D^o_h	=	initial hole diameter
e_{bias}	=	statistical bias
E_{total}	=	total energy of corium or thermite melt
FAI	=	Fauske & Associates, Inc.
FEA	=	finite element analysis
f^0_{NC}	=	initial mole fraction of noncondensibles
f_{coh}	=	fraction of blowdown steam coherent with dispersal
f_{disp}	=	dispersed from cavity
f_{dome}	=	transported outside subcompartment
f_{eject}	=	ejected into cavity
f_g	=	fraction of dispersed flow
f_i	=	subcompartment volume fraction (0.43) or dome volume fraction (0.57)
f_{mw}	=	fraction of dispersed melt going out manway
f_{Nc}	=	noncondensible gas fraction
f_{nz}	=	fraction of melt flow going out nozzle cutouts

$f_{nz,flow}$	=	fraction of melt flow carried by gas out the nozzle cutouts
$f_{nz,splash}$	=	fraction of melt flow going out nozzle cutouts due to splashing
$f_{recovery}$	=	recovery fraction
FSAR	=	Final Safety Analysis Report
f_{trans}	=	transported to dome
f_w	=	fraction of liquid water vaporized
F	=	force
g	=	acceleration due to gravity
G	=	mass flux
$G_{bernouli}$	=	Bernouli mass flux
G_{exp}	=	experiment mass flux
GGS	=	gas grab sample
G_{HEM}	=	homogeneous equilibrium mass flux
h	=	distance between orifice and liquid surface
h_{Al2O3}	=	heat transfer coefficient through alumina
h_c	=	concrete heat transfer coefficient
h_c	=	depth of depression
$h_{d,g}$	=	debris/gas heat transfer coefficient
h_{dwn}	=	downward heat transfer coefficient
h_{fg}	=	heat of fusion
$h_{f,Al2O3}$	=	heat of fusion for alumina
h_{Fe}	=	iron phase heat transfer coefficient
h_g	=	enthalpy of saturated steam at containment pressure
$h^o_{l,s}$	=	initial enthalpy of saturated water
h_r	=	radiation heat transfer coefficient
h_{up}	=	upward heat transfer coefficient
H	=	dome or containment height
HPME	=	high pressure melt ejection
IDCOR	=	Industry Degraded Core Rulemaking Program
IETs	=	Integral Effects Tests
kg	=	kilogram
kN	=	force, kilonewtons
K_{Al2O3}	=	thermal conductivity of alumina
K_c	=	thermal conductivity of concrete
K_{Fe}	=	thermal conductivity of iron
Ku	=	Kutateladze number
L	=	characteristic turning length
LHS	=	left hand side
LOCA	=	loss of coolant accident
m	=	meter
m_a	=	mass of atmosphere
m_d	=	mass of debris
m_g	=	gas mass

NOMENCLATURE (continued)

m^o_g	=	initial gas mass
m^o_w	=	initial water mass
MPa	=	megapascal
mw_g	=	molecular weight of gas
$\dot{m}_g$	=	mass flow rate
$\dot{m}^o_g$	=	initial gas flow rate
$\dot{m}^o_w$	=	initial water flow rate
M	=	mass
M_d	=	thermite mass
M_{disp}	=	mass dispersed from cavity
M_g	=	gas mass
$M_{g,e}$	=	RCS gas mass at end of entrainment interval
MJ	=	megajoule
M^o_d	=	initial thermite charge
M^o_g	=	initial gas mass
M_{roof}	=	mass frozen on roof
mtonnes	=	metric tons
$M_{w/cold}{}^o$	=	mass of cold water
Mw_{eff}	=	effective molecular weight
MW_g	=	gas molecular weight
MW_{H2O}	=	molecular weight of water
$\dot{M}$	=	jet momentum flow
$\dot{M}^o_g$	=	initial gas mass flow rate
$\dot{M}_w$	=	water flow rate
N	=	gas moles
N^0_{H2}	=	initial number of gas moles of hydrogen
N^0_i	=	initial number of gas moles of species i
N^0_{N2}	=	initial number of gas moles of nitrogen
N^0_{O2}	=	initial number of gas moles of oxygen
N^0_{total}	=	the total pretest moles of gas
N_{coh}	=	coherent moles
N_{H2}	=	moles of hydrogen
$N_{H2,e}$	=	hydrogen entrained into jet
N_i	=	subcompartment or dome gas moles
N^o_{acc}	=	initial moles in accumulator
$N^o_{H2,dm}$	=	total moles initial in dome
NPP	=	nuclear power plant
NRC	=	Nuclear Regulatory Commission
N^t_{H2}	=	moles of hydrogen in the Surtsey vessel at time t
$N^t_{H2,burned}$	=	moles of hydrogen burned in the Surtsey vessel at time t

NOMENCLATURE (continued)

$N^t_{H2,produced}$	=	moles of hydrogen produced in the Surtsey vessel at time t
N^t_i	=	moles of gas species i in the Surtsey vessel at time t
N^t_{O2}	=	moles of oxygen in the Surtsey vessel at time t
P	=	vessel pressure
P^*	=	normalized pressure
P^+	=	normalized pressure transient term
P_a	=	ambient pressure
P_{crit}	=	critical pressure
P_e	=	pressure at end of entrainment interval
$P_{e,RCS}$	=	RCS pressure at end of entrainment interval
P_m	=	minimum pressure
P_{min}	=	minimum pressure
P^o	=	initial pressure
P^o_{RCS}	=	initial RCS pressure
psi	=	pounds per square inch
psia	=	pounds per square inch, absolute
$\dot{P}_{exp}$	=	experimental depressurization rate
PWR	=	pressurized water reactor
R	=	universal gas constant
RCB	=	reactor containment building
RCP	=	reactor coolant pump
RCS	=	reactor coolant system
RHS	=	right hand side
R_r	=	coherence ratio
R_u	=	universal gas constant
$\dot{R}_{HT}$	=	heat transfer rate
RPV	=	reactor pressure vessel
s	=	second
SASM	=	Severe Accident Scaling Methodology
SG	=	steam generator
Sh	=	Schmidt number, ratio of the pneumatic viscosity to the mass diffusivity
SMMD	=	sieve mass median diameter
SNL	=	Sandia National Laboratories
t	=	time
t^*	=	normalized time
t_e	=	entrainment interval
t_{ref}	=	reference time
T	=	temperature
TCE	=	two-cell equilibrium
T_f	=	final temperature
T_g	=	gas temperature
T_i	=	subcompartment or dome average gas temperature

T_{melt}	=	debris temperature
TMI-2	=	Three Mile Island - 2
$T_{mp,oxide}$	=	melting temperature of oxide
TOF	=	time of flight
T^o	=	initial temperature
T^o_a	=	initial atmosphere temperature
T^o_d	=	initial debris temperature
T^o_g	=	initial gas temperature
T^o_{RCS}	=	initial RCS temperature
TRG	=	Technical Review Group
$T_{w,o}$	=	initial wall temperature
v_d	=	debris velocity
V	=	volume
V^*_g	=	orifice gas velocity
V_c	=	cavity volume
V_{cav}	=	cavity volume
V_g	=	volume of gas
$V_{g,f}$	=	final gas volume
V_i	=	subcompartment or dome gas volume
V^o	=	initial volume
V^o_g	=	initial volume of gas
V^o_{gn}	=	initial volume of gas in the nozzle
V^o_w	=	initial water volume
V_{RCS}	=	RCS volume
V_{tot}	=	freeboard gas volume
V_w	=	water volume
$V_{w,f}$	=	final water volume
X^0_i	=	initial (background) mole fraction of species i at time t=0 in the containment vessel
X_g	=	fraction of blowdown water that flashes to vapor
X_{H2}	=	hydrogen concentration
$X_{H2}(dwn)$	=	downward flammability limit
$X_{H2}(up)$	=	upward flammability limit
X_{O2}	=	oxygen concentration
X^t_i	=	mole fraction of species i at time t
X^t_{N2}	=	mole fraction of nitrogen at time t

Greek

α_c	=	thermal diffusivity of concrete
Δe_d	=	specific energy of debris
Δe_{H2}	=	hydrogen combustion energy

$\Delta e_{reaction}$	=	specific heat of reaction
$\Delta e_{thermal}$	=	specific thermal energy
$\Delta e_{combined}$	=	specific combined energy
ΔE_i	=	energy contributor to DCH
ΔM_g	=	change in gas mass
ΔP	=	change in pressure
$\Delta P_{meas,i}$	=	measured pressure rise
$\Delta P_{pred,i}$	=	predicted pressure rise
$\mathcal{D}$	=	steam/hydrogen binary diffusion coefficient
ε	=	emissivity
ρ	=	melt density
ρ_w	=	water density
$\rho_{g,cav}$	=	gas density in cavity
$\rho_{g,s}$	=	(gas) steam density
$\rho_{l,s}$	=	liquid (water) density
ρ^o	=	initial density
ρ_g	=	gas density
ρ_d	=	drop density
ρ_L	=	liquid density
ρ^*_g	=	orifice density
τ_b	=	blowdown time constant
τ_e	=	entrainment time
σ^2_{rms}	=	variance
τ_{burp}	=	"burp" time constant
τ_{motion}	=	time constant to move liquid away from impingement region
τ_{disp}	=	dispersal time constant
η_{meas}	=	measured efficiency
η_{mass}	=	mass fraction frozen on roof
η_{KE}	=	kinetic efficiency
τ_{trap}	=	trapping time constant
τ_{HT}	=	heat transfer time constant
ψ	=	debris/atmosphere heat capacity ratio
ν	=	stoichiometric coefficient
μ	=	melt viscosity
γ	=	isentropic exponent
π_1	=	scaling group
π_2	=	scaling group
σ	=	Stefan Boltzman constant, surface tension
δ	=	melt layer thickness

1.0 INTRODUCTION

In a core melt accident, if the reactor pressure vessel (RPV) fails while the reactor coolant system is at high pressure, the expulsion of molten core debris may pressurize the reactor containment building (RCB) beyond its failure pressure. A failure in the bottom head of the RPV, followed by melt expulsion and blowdown of the reactor coolant system (RCS), will entrain molten core debris in the high-velocity steam/water mixture. This chain of events is called a high-pressure melt ejection (HPME). Three mechanisms may cause a rapid increase in pressure and temperature in the reactor containment: (1) efficient debris-to-gas heat transfer, (2) exothermic metal/oxygen reactions, and (3) hydrogen combustion. These processes that lead to increased loads on the containment building are collectively referred to as direct containment heating (DCH).

DCH experiments have been previously conducted at Sandia National Laboratories (SNL), Argonne National Laboratory (ANL), and Fauske and Associates (FAI). These early DCH experiments were reviewed as part of an NRC-sponsored effort known as the Severe Accident Scaling Methodology (SASM) Program (Zuber et al. 1991). As a result of SASM recommendations, the NRC-sponsored experiment programs were redirected towards performing counterpart experiments at two different physical scales: $1/10^{th}$ linear scale at SNL and $1/40^{th}$ linear scale at ANL. These counterpart experiments included geometrically scaled simulations of the Zion or Surry nuclear power plant (NPP) structures and had the initial conditions closely tied to postulated accident scenarios. These experiments, called the Integral Effects Tests (IETs), were designed to provide integral effects data on HPME/DCH phenomena from large-scale, prototypic experiments. The primary measurements include pressures, temperatures, and gas concentrations.

The initial integral effects tests were conducted by SNL at the Surtsey Facility using $1/10^{th}$ linear scale models of the Zion NPP structures; these tests are designated as IET-1, IET-1R, IET-3, IET-4, IET-5, IET-6, IET-7, IET-8A, and IET-8B (Allen et al. 1994). These experiments used models of the Zion structures, including the bottom head of the RPV, biological shield wall, reactor cavity, instrument tunnel, containment basement floor, seal table room, refueling canal, steam generators, reactor coolant pumps (RCPs), and operating deck.

Four additional integral effects tests were performed by SNL under even more prototypic conditions with scale models of the Surry NPP (Blanchat et al. 1994). The experiments were conducted at $1/6^{th}$ linear scale (IET-9, IET-10, and IET-11) at the Containment Technology Test Facility (CTTF) and at $1/10^{th}$ linear scale (IET-12) at the Surtsey Facility. Hydrogen combustion was examined under more prototypic atmospheric conditions, i.e. air/steam/hydrogen atmospheres likely to occur in an accident scenario.

While it appears possible to extrapolate the results obtained thus far to other Westinghouse plants, predicted containment loads cannot be generalized to certain Combustion Engineering (CE) plants. In most Westinghouse plants, there is (1) an intermediate compartment that is large compared to the reactor cavity but small compared to the main containment volume, and (2) there is no significant line-of-sight pathway for debris transport from the cavity to the main containment

volume. Containment compartmentalization is the dominant mitigating feature. These two conditions are not satisfied for some CE plants, specifically, Calvert Cliffs 1 and 2, Millstone 2, Arkansas Nuclear One Unit 2, and Palisades. In particular, although the Calvert Cliffs-like plants have an intermediate subcompartment, that is, the steam generator compartment, there is no flow path from the cavity to that compartment. The dispersal of melt from the cavity is predominately to the dome through the annular gap around the RPV. This circumvents the main mitigation associated with containment compartmentalization that exists in Zion and most other PWRs.

In all of the DCH integral effects testing (e.g., SNL/ANL IETs for Zion, SNL IETs for Surry) conducted to-date, single-phase superheated steam was used to drive the molten core simulant. This was based on the assumption that no water remained in the lower plenum at vessel breach because all of the water had been vaporized by the time the vessel failed. However, analyses of core melt progression indicated that saturated water will still be present in the lower head at the time of lower head failure. In addition, operator intervention accidents (e.g., TMI-2) are likely to have large quantities of subcooled water in the vessel at the time of vessel failure. The coherent water/steam and debris entrained from the cavity would provide a potential heat sink since some of the thermal and chemical energy in the debris would be used to vaporize the liquid water and quench part of the melt. The increased amount of steam may also increase the hydrogen production from debris/steam interactions. However, the potential for enhancing the DCH load due to hydrogen burning may be reduced due to the increased steam fraction which could inert the atmosphere and suppress a hydrogen burn.

The potential effects upon DCH loads caused by the coejection of liquid water with molten core materials could be significant. Therefore, the NRC requested that SNL design and test an apparatus that can be used to conduct high pressure melt ejection experiments with coejection of water and molten core simulants. The technical guidance for the initial conditions of the coejected water experiments was provided by the Accident Evaluation Branch of the NRC and a six member Technical Review Group (TRG). The TRG included R.E. Henry (FAI), M. Ishii (Purdue), F.J. Moody (GE), S. Levy (Levy and Associates), M. Corradini (U. of Wisconsin), and R. Schneider (ABB Combustion Engineering).

Many scoping experiments were performed to demonstrate the feasibility of driving a corium simulant out of a RPV lower head model into a scaled cavity using high-pressure water. Most of the scoping tests yielded unsatisfactory results, either due to early water interaction with unreacted thermite that caused an incomplete thermite reaction or due to large steam vaporization pressures inside the melt generator when the high-pressure saturated water contacted the molten thermite. As a result, the methodology chosen to conduct the coejected water tests involved reacting the thermite directly in the cavity and, after waiting for the reaction to proceed to completeness, introducing high-pressure water or steam into the cavity through a 4-cm hole in the bottom head of the RPV. The following sections describe the design basis for the tests and give the test description and results of seven DCH experiments conducted in the Surtsey test vessel that used a $1/10^{th}$ scale model of the Calvert Cliffs NPP.

2.0 EXPERIMENT DESCRIPTION

The Calvert Cliffs-like design was based on three principles: 1) geometrically scale the key parameters as close as possible, 2) maintain design flexibility, and 3) perform cost effective and efficient modifications to existing $1/10^{th}$ scale Surry NPP structures. Certain key design parameters were identified, mostly flow areas, obstruction areas, and flight paths.

Figure 1 shows the $1/10^{th}$ scale Calvert Cliffs structures installed in the Surtsey vessel. The main structure modifications included building a refueling canal, missile shield, and operating deck. The existing Surry operating deck was removed. The new operating deck was located at the top of the existing Surry crane wall. Appropriate scaled openings were placed in the operating deck to simulate the reactor coolant pump (RCP) and the steam generator (SG) vent paths. Most of the basement crane wall openings were sealed to obtain the scaled flow area. A $1/10^{th}$ scale missile shield was designed to sit above the top of the refueling canal wall.

Figure 2 shows an isometric view of the Calvert Cliffs subcompartment structures and the RPV model. Since the dimensions for the Calvert Cliffs RPV were very similar to the Surry RPV, the existing RPV model design was used. A robust cavity design was necessary because large cavity pressures could not be ruled out during the HPME. It was necessary to build a new cavity to meet the design requirements. The cavity modifications include sealing the pathway to the in-core instrument tunnel, raising the floor, decreasing the cavity diameter below the nozzles, and cutting holes for the access hatch and primary loop piping pathways.

Figure 3 shows the RPV model and cavity that was used in these experiments, which are referred to as the Combustion Engineering Scoping (CES) tests and the Combustion Engineering (CE) tests. Although these experiments are referred to as the CES and CE tests, only 5 of the 15 CE NPPs in the United States are Calvert Cliffs-like with a Bechtel annular cavity design in which the only flow path out of the cavity is through the annular gap between the RPV and the biological shield wall. The crucible (or melt generator) was not used to react the thermite as it was in the earlier IET tests; the thermite was reacted on the cavity floor in all of the CE experiments.

Figures 4, 5, and 6 show plan views of the subcompartment structures in the Surtsey vessel near the Surtsey port levels 4, 5, and 6, respectively. Level 4 shows a view at the basement level, level 5 shows the view at the refueling canal, and level 6 gives the view from above the operating deck.

The melt/water delivery setup for the coejected water tests is shown in Figure 7. A 12.7-cm diameter tube filled with iron oxide/aluminum thermite (33.2 kilogram (kg)) with a small amount of alumina diluent was placed on the floor of the cavity. The tube was about 142 cm long. In the three CES experiments, which utilized a cold, nitrogen-inerted Surtsey atmosphere, the bag was formed from polyethylene material that was heat sealed at the seams. In the four CE experiments, which utilized a prototypic air/steam/hydrogen atmosphere, the bag was formed using Teflon material that was sealed at the seams using a chemical etching process along with a polysulfide adhesive. A prototype bag was tested at 373 K and was determined to

be water-tight. It was estimated that a 2.5-cm deep pool of melt formed in the cavity after the thermite reaction was complete. A 2.5-cm high concrete plug was attached to the cavity floor below the exit hole to prevent jetting of water directly into the melt pool. A thin (2-cm thick) concrete plug was formed in the cavity access hatch to prevent melt from flowing out of the cavity during the reaction process. A flow nozzle attached to the lower head of the RPV model was used as a transition piece from the 10 cm pipe to the 5 cm schedule 40 pipe. The flow nozzle had either a 5.25-cm diameter exit hole or a 4-cm diameter exit hole. The nozzle ensured that as the water rushed down the pipe that the compression of the gas in the pipe would sweep melt away from the exit hole prior to water ejection. The nozzle also reduced the gas volume in the crucible and minimized the amount of melt that would be entrained into the annular gap and out of the cavity by the gas jet. A 0.6 cm steel tube penetrated the cavity access hatch plug and was used to drain condensate water out of the cavity during the vessel and structure heatup.

2.1 Geometry and Initial Conditions: The Design Basis

The goal was to perform integral effects tests in geometrically scaled Calvert Cliffs-like structures with initial conditions generally selected to be well within the expected range of full-scale plant behavior. The geometry and initial conditions selected for the CE DCH experiments were guided by the pump seal LOCA sequence initiated by a station blackout. The Calvert Cliffs NPP was chosen as a representative CE plant with a Bechtel annular cavity design to study the effect of key structures on DCH loads (Pilch 1994a). The decision was based on (1) the expected similarity of loads for all CE plants with Bechtel annular cavity designs, and (2) the Calvert Cliffs IDCOR Type F narrow gap cavity design would maximize debris transport to the dome, which in turn should maximize potential DCH loads.

2.1.1 Facility Geometry

The cavity and RPV holddown were redesigned to meet the following requirements: 1) cavity design pressure of 6.9 megapascals (MPa) with a safety factor of 2 to yield and 2) RPV holddown tabs designed to 6.9 MPa with a safety factor of 4 to yield. The existing Surry cavity steel cylinder (1 cm thick) could not withstand the required design pressure. Various means of strengthening the cavity were reviewed (internal and external steel bands and inserts, steel rope or braid, etc.); however, it was decided to construct a new cavity and insert it into the existing cavity. The decision was based on cost, schedule, and confidence of the design analysis.

The new cavity was constructed from rolled 2.5-cm thick ASTM-A36 steel plate. The steel cylinder was welded to a 7.6-cm thick base plate that was then welded to the existing cavity floor. All welds in the cavity and RPV holddown assembly (Figure 3) were NDE tested by dye penetrant to ensure weld integrity in accordance with the methods suggested by the ASME Boiler and Pressure Vessel Code. The upper part of the steel shell (at and above the nozzle penetrations) was constructed using rolled 3.8-cm thick A36 steel plate. Six RPV holddown tabs (5 cm thick by 15 cm wide) were welded to the top of the cylinder. Finite element analysis (FEA) was performed on the cavity using a boundary condition of 6.9 MPa on all internal surfaces with the exception of a 27.6 MPa pressure load on the underside of the tabs. The FEA showed a Von Mises stress of 117 MPa in the center of the cylinder (a small part of the nozzle

cutout reached a stress of 152 MPa; however, the analysis did not take into account the stress reduction that would occur after the piping representing the flow area through the biological shield was welded to the cutouts). The maximum stress on the tabs was about 58.6 MPa. This class of steel has a yield strength of 248 MPa and an ultimate tensile strength of 476 MPa. Therefore, based on the FEA, the steel shell had a safety factor of 2.1 to yield and the tabs had a safety factor of 4.2 to yield. Hand calculations were performed that gave good agreement with the FEA.

Finite element analysis was also performed on the existing RPV shell and holddown using a boundary condition of 6.9 MPa on all external surfaces. The FEA determined a Von Mises stress of 110 MPa in the center of the RPV cylinder (with small hotspots below and between the nozzles reaching a stress of 145 MPa). The maximum stress on the holddown blocks was small, only about 34.5 MPa. Therefore, based on the FEA, the existing RPV steel shell had a safety factor of 1.7 to yield. This was deemed sufficiently close to the design requirement to not incur additional cost redesigning the RPV model. Hand calculations were also performed on the RPV model that gave good agreement with the FEA. The only modification to the RPV assembly was the addition of twelve 1.9 cm bolts (two bolts per tab and associated holddown block) that were used to snug the RPV holddown blocks against the bottom of the cavity tabs and remove any clearance that could contribute to dynamic loading.

The length and width of the Calvert Cliffs missile shield are 5.4 m and 7.6 m, respectively. The shield sits about 1.5 m above the top of the refueling canal wall, with a 0.9 m gap between the edge of the missile shield and the steam generator room wall. Therefore, the gap is a flowpath along all four sides of the shield (though probably small along the SG room sides). The 1/10th scale missile shield design incorporated these features.

The 1/10th scale missile shield and tie-down was designed to be very robust. The missile shield was constructed using a 10 cm steel channel framework with #5 bar welded to the channel on 15 cm centers. The minimum concrete compressive strength within the frame was 20.7 MPa. For the tie-down, four threaded steel rods (1.9-cm thick) were welded to the cavity steel. The threaded 1.9 cm rods anchored the four corners of the missile shield to the cavity. It was estimated that there would be about 2.2 kN applied to the missile shield by debris flowing out of the cavity. The safety factor to yield was over 100 (assuming only one rod in pure tension).

The RPV lower head hole diameter plays a key role in determining the rate of RCS blowdown, which in turn controls the rate and magnitude of melt dispersal from the cavity. A scaled hole of ~4 cm was chosen for the CE DCH experiments to allow comparison with the 1/10th scale Zion and Surry DCH experiments. The scenario considered for the Zion and Surry experiments was a penetration-type failure of the lower head. Such a failure could occur by the ejection of an in-core instrument guide from the lower head or by melt flow into the guide tube causing the tube to rupture outside the lower head. The initial size of such a failure is ~0.025 meter (m), but melt flow through the hole will cause it to ablate to a much larger size. A final hole size of ~0.4 m was computed with an ablation model (Pilch 1994c). The calculation was carried out using the melt mass (scaled to Surry, i.e., 43 metric tons (mtonnes)) and

composition specified in the SASM document (Zuber et al. 1991). Note that the Calvert Cliffs lower head contains no penetrations.

Table 1 lists geometric comparisons for the CE DCH experiments. The table is based on the Calvert Cliffs (CC) subcompartment structures that were shown in FSAR drawings. The key design parameters (flow areas, obstruction areas, and flight paths) are shaded in the appropriate table row. The key parameters have been closely scaled; this is shown by comparing the Scaled column with the Surtsey column.

2.1.2 Melt Mass and Composition

The experiments employ iron oxide/aluminum thermite as a high temperature, chemically reactive simulant for corium. Geometric scaling of the melt mass for the experiment is not strictly applicable because of material property differences between corium and thermite. The amount of thermite used in the experiments was selected so that the experiments would have the same potential for pressurization as the reactor application.

The mass of thermite chosen for the CE DCH experiments was based on the Calvert Cliffs upper bound melt mass distributions for the splinter scenario V, where the total melt mass was
63.7 mtonnes (Pilch et al. 1995). Scenario V represents a core melt accident where operator actions are assumed to repressurize the RCS to 16 megapascal (MPa). The RPV is refilled with water to the hot leg nozzles (80-100 mtonnes) and the steam remaining in the RCS is at saturation.

In the Zion and Surry DCH experiments, small amounts of chromium were added to the iron oxide/aluminum thermite to cool the molten thermite to temperatures more prototypic of corium and to make the oxidation potential more prototypic of corium. The melt composition for Scenario V is expected to be largely oxidic; hence, the chromium was replaced with an appropriate amount of alumina in the CE experiments to reduce the metallic component The amount of alumina that was added was based on maintaining the same ratio of aluminum to iron oxide and the same heat capacity of the chromium-doped melts. Table 2 presents constituent mass, mole, and volume fractions of the melt products for an upper bound Calvert Cliffs corium from Scenario V and an alumina doped thermite. Thermophysical properties of the Calvert Cliffs NPP melt and a $1/10^{th}$ scale Surtsey CE test melt using an alumina doped thermite were determined using the TCE model (Pilch 1991) and are given in Table 3. The 63.7 mtonnes of corium has a total combined thermal and chemical energy of 95×10^3 megajoule (MJ). This yields a required melt energy of 95 MJ for the $1/10^{th}$ scale CE DCH tests. Therefore, based on the combined thermal and chemical specific energy of the thermitic melt, the required melt mass for the CE experiments was 33.2 kg.

Three scoping tests were performed with the oxidic thermite melt simulant (Blanchat 1995). The purpose of the scoping tests was to: 1) ensure ignition of the new thermite mixture in which the chromium was replaced with alumina, 2) measure the time from ignition to melt plug failure (using a $1/10^{th}$ scale crucible and 30 kg of oxidic thermite), and 3) measure the melt

temperature. The thermite was ignited using a pyrofuse. Melt temperatures of 2200 K to 2500 K were measured. The average burn time was 6.0 seconds (s).

Two scoping test were performed using a 33 kg tube of oxidic thermite laying on the concrete floor of a test cavity (dimensions similar to the scaled Calvert Cliffs cavity). The purpose of the tests was to determine the minimum delay time after ignition of the thermite prior to commencing the HPME (to ensure reaction completeness). The concrete floor was dry in the first experiment. The thermite appeared to be fully reacted after 12 s. A dark slag appeared to form on the surface of the melt pool by 30 s. A 0.6 cm deep pool of water was placed on the floor in the second test. Again, the thermite appeared to be fully reacted by 12 seconds. However, the burn seemed more intense (due to the production of hydrogen from the iron oxidation reaction with water) and slag was not seen until about 50 s after ignition.

2.1.3 Driving Pressure and Fluid

One of the main objectives for the CE DCH experiments was to investigate the effects of codispersal of water, steam, and molten core materials on DCH load. Tests that use only small amounts of lower plenum water may not significantly capture the potential DCH load reduction mechanism. Therefore, the amount of water and melt that was used was scaled according to the Scenario V amounts of saturated water (80-100 mtonnes) and the corresponding core melt mass (63.7 mtonnes). A driving pressure of 8 MPa was chosen (versus 16 MPa) because of: 1) recommendations of the Technical Review Group, 2) to allow comparison with the $1/10^{th}$ scale Zion DCH experiments which were performed at 7 MPa, and 3) the cost to modify the system to operate at higher pressures. Note that there is a related scenario (splinter scenario VI) in which water exists only in the lower plenum (<20-30 mtonnes); the RCS gas is superheated to ~1000 K which yields a driving pressure of about 8 MPa. One test used a driving pressure of about 4 MPa to determine the effectiveness of depressurization procedures that may be used in accident mitigation strategies.

2.1.4 Test Setup and Initial Conditions

In CES-1, CES-2, and CES-3, following leak checks of the Surtsey vessel (the vessel leakage rate was typically on the order of 690 Pa/hr, based 12-hour leak checks at 0.2 MPa), the vessel was inerted with nitrogen gas using a feed and bleed procedure and was then pressurized with nitrogen to about 0.2 MPa. The oxygen concentration in the vessel at the beginning of the tests was about 0.2 mole percent (mole %).

In CE-1, CE-2, CE-3, and CE-4, following leak checks of the Surtsey vessel using bottled air, the vessel was vented to about 0.09 MPa at a temperature of about 285 K. At test conditions, this amount of air in Surtsey would provide the same amount of air as in the Calvert Cliffs NPP at operating conditions (0.1 MPa, 311 K). The vessel was then heated and filled with steam until the vessel pressure reached about 0.22 MPa. The average gas temperature inside the Surtsey vessel was about 377 K at the end of the heatup. Water condensed on the vessel walls and the

Calvert Cliffs structures during the 5-7 hour heatup and the condensate water was manually drained from the cavity (~17 kg) and vessel floor (1700 kg) during the steaming process.

In CE-1, the air and steam concentrations in the vessel at the beginning of the test were approximately 58 mole % and 42 mole %, respectively, based on partial pressures. A small amount of preexisting hydrogen gas was placed inside the vessel in the CE-2, CE-3, and CE-4 experiments, yielding air, steam, and hydrogen concentrations of about 55 mole %, 41 mole %, and 4 mole %, respectively, based on partial pressures and the measured addition of hydrogen.

The accumulator driving fluid varied. In CES-1, cold water (100 kg) was placed in the $1/10^{th}$ scale accumulator (empty volume = 0.2544 m^3) and was driven using nitrogen gas. In CES-2 and CE-3, saturated steam was used as the driving fluid. In CES-3, CE-1, CE-2, and CE-4, 100 kg of water was placed inside the accumulator. Heaters on the accumulator and 10 cm piping to the burst diaphragms were energized. After about seven hours, the accumulator wall, water, and steam temperatures had equilibrated at 571 K (532 K for CE-4). This produced saturated water and a saturation steam pressure of about 8.4 MPa (4.3 MPa for CE-4) inside the accumulator. Note that the RPV exit hole diameter changed from 5.25 cm to 4.0 cm after the CES-2 experiment.

A pyrofuse embedded in the tube was used to ignite the thermite. In CES-1, CES-2, and CES-3, thirteen seconds after the thermite ignition, the burst diaphragms that contained the water and/or steam in the accumulator were failed to initiate the high pressure melt ejection process. In CE-1 and CE-2, controller problems delayed burst diaphragm failure until 29 s and 45 s had elapsed, respectively. A delay time of 29 s was chosen for the CE-3 and CE-4 experiments to allow replicate experiments using prototypic atmospheres. The time of burst diaphragm failure was used to set the zero time for the HPME. The initial conditions for the CE DCH experiments are summarized in Table 4.

2.2 Measurements and Instrumentation

The most significant variables to be measured in the CE DCH experiments were: (1) the increase in pressure and temperature in the Surtsey vessel, (2) the cavity pressure, (3) the accumulator pressure, (4) the number of gram-moles (g·moles) of driving water/steam, (5) the number of g·moles of hydrogen generated by the reaction of metallic debris with steam and water, (6) the number of g·moles of hydrogen burned, (7) the mass and location of debris recovered from the Surtsey vessel, and (8) the debris particle size. In addition, strain measurements on key components in or near the ejection path, flow velocity of the ejected accumulator water, accumulator water level, and visual recordings of the event were made. The instrumentation and techniques used to make these measurements are summarized in Table 5 and described in the sections below.

2.2.1 Pressure Measurements

Pressure transducers with ranges of 0-0.69 MPa were used to measure the pressure in the upper dome of the Surtsey vessel. Pressure transducers with ranges of 0-20.7 MPa were used to

measure the gas pressure in the steam accumulator. Two strain gauge-type pressure transducers with ranges of 0-3.5 MPa and 0-34.5 MPa were used to measure the gas pressure in the scaled reactor cavity. These gages were located in tapped holes at two locations in the cavity wall, near the cavity floor, and in the annular gap just before the cavity exit (Figure 3). Two quartz pressure transducers with ranges of 0-34.5 MPa and 0-104.4 MPa (2 ms response time) were used to measure dynamic gas pressures in the cavity. Air and hydrogen manifold pressures (and temperatures) were recorded. The number of gas moles added to the Surtsey vessel was calculated using the number of standard 44 liter compressed gas cylinders installed on a manifold, the cylinder volume (0.044 m^3), the manifold initial pressure and temperature, and the manifold final pressure and temperature. The noncondensible gas and steam fractions at the start of each experiment were then calculated using the initial moles of air and hydrogen and the measured pressure and average gas temperature data at time t = 0 minutes, along with P, V, T ideal-gas law relationships.

The specified accuracy from the manufacturer for the pressure transducers is less than ± 0.50 percent at full-scale output. These instruments are routinely recalibrated at SNL against instruments traceable to the National Institute of Standards and Technology, and accuracies are always within the manufacturer's specifications. The data acquisition system recorded data from the strain-gage pressure transducers at a rate of 1400 data points per second per channel from thermite ignition to about 120 seconds following the HPME. Data from the quartz gages was recorded at a rate of 20,000 data points per second per channel (50 microsecond resolution) from thermite ignition to about 5 seconds following the HPME.

2.2.2 Temperature Measurements

The bulk gas temperature above the operating deck in the Surtsey vessel will be measured with thermocouple rakes. Figures 1 and 2 show the 20 thermocouple locations for the bulk gas measurements. There were three vertical thermocouple rakes installed in the vessel; the rakes were located ~0.76 m from the vessel wall with equally-spaced thermocouples (0.61 m spacing). Arrays A, B, and C were installed on the operating deck. Two thermocouple rakes (array SCA and array SCB) were installed in the basement below the operating deck. Figures 2 and 3 show the locations of these arrays. The three type-K thermocouples on these arrays are also equally-spaced (0.91 m). All type-K thermocouples used to measure vessel gas temperature were made of 0.127-millimeter (mm) wire with a thin Teflon sheathing. The time constant for these thermocouples is ~0.1 s. The temperature range is 273 K to 1523 K. The maximum error using the manufacturer's calibration is ± 9.4 K at 1523 K.

Type-K thermocouples were installed in the Surtsey vessel steel walls and also in the concrete subcompartment structures. In some tests, four high-temperature tungsten-rhenium type-C thermocouples, comprised of 0.38-mm diameter wire with a 1.6-mm diameter stainless steel sheath, were installed in the cavity and annular gap. These thermocouples measured the temperature of the debris/gas as it exited the cavity and entered the subcompartment structures. The temperature range for the thermocouples are 273 K to 2593 K. The maximum error using the manufacturer's calibration is ±25.9 K with a 0.9-s time constant.

The temperature of the driving steam/water in the steam accumulator tank and connecting 10 cm piping was measured using nine type-K thermocouples. Measurements from these thermocouples were important because the measured temperature and pressure in the accumulator tank was used to calculate the number of g·moles of steam or nitrogen driving gas. The temperature of the steam accumulator shell was measured using three type-K thermocouples that were placed in the top and bottom hemispheres and in the vertical cylindrical wall. These thermocouples monitored and controlled the electric heaters on the accumulator shell, which heated the accumulator steel and water to the desired temperature. The 10 cm piping, from the bottom of the accumulator to the rupture disk holder, had similar heaters, controllers, and instrumentation.

An optical pyrometer was used to measure the temperature of the debris as it exits the cavity and also the timing of the debris entrainment out of the cavity. The pyrometer (type 11x30, Ircon Inc., Niles, IL) was located in the basement and was focused (through a window in the refueling canal) just above the cavity exit. The optical pyrometer had a response time of 1.5 ms to 95 percent of its full range. A mid-to-high range controller was installed on the 11x30 pyrometer. The controller can measure temperatures between 1873 K and 2773 K with a specified accuracy of 1 percent of the full-scale temperature. In a transient event such as a HPME experiment, the accuracy of the pyrometer measurement is expected to be no better than ±25 K.

2.2.3 Gas Composition

Twenty pre-evacuated 500-cm^3 gas grab sample (GGS) bottles were used to collect samples from the vessel at several locations and times. Five GGS stations were mounted on Surtsey. One station was located on the Surtsey top head and sampled gas high in the dome (5.5 m above the floor). Two stations were located circumferentially about Surtsey and sampled gas at a height of 3.05 m above the floor (through the level 6 ports). One station was located at the level 4 port and sampled basement gas at 0.61 m above the floor. One station sampled gas in the refueling canal (only at 15 s and 30 s into the transient). Each station contained four GGS bottles and the sample times were : 1) background, 2) 15 s, 3) 30 s, and 4) 2 min. after the HPME. In addition, two samples were taken at thirty minutes after the HPME after the vessel was mixed using internal mixing fans (in some experiments mixing fans were turned on earlier; in two experiments the mixing fans were not turned on). With the exception of the 15 s GGS, each sample line was purged for at least 30 seconds immediately prior to sampling. All of the gas samples were analyzed using gas mass spectroscopy by the Gas Chromatography and Mass Spectrometry Laboratory at Sandia.

2.2.4 Posttest Debris Recovery

The total debris mass dispersed into the Surtsey vessel and the debris mass in specific locations was determined by a very careful posttest debris recovery procedure. The following measurements were made: (1) all cavity surfaces (including the annular gap between the cavity wall and the RPV model), (2) all surfaces on the refueling canal, (3) on the operating deck, (4) on the vessel wall, dome surface, and structures above the operating deck, (5) all surfaces inside the

basement, and (6) in the vertical annulus between the vessel wall and the crane wall and on the Surtsey floor. A posttest sieve analysis of the debris that was recovered outside of the subcompartment structures was performed for each test. A standard set of 35 sieves was used (U. S. series 9.5 mm to 38 micrometer).

2.2.5 Cameras

Two high resolution 1.3 cm CCD color cameras were used in the CE DCH experiments. One camera was mounted outside the dome penetration, viewing the DCH event from above through a 2.5 cm thick tempered glass window. One camera viewed the DCH event through a tempered glass window mounted on a level 6 port, with a view that looked across the operating deck at the missile shield and cavity exit.

2.2.6 Additional Measurements

Breakwires were placed across the annular gap exit and at the refueling canal openings. The breakwires were intended to give timing information on entry of debris out of the cavity and into the Surtsey dome region. The breakwire failure time, in conjunction with measured distances, should yield debris velocity information.

In two tests, four photodiodes were used to measure the timing of the debris entrainment in the annular gap and out of the cavity. The photodiodes (equally spaced ~0.4 m apart) were mounted in the cavity wall along a vertical axis.

Two 0.6-cm square strain gages with ranges of -2 to 2% strain were attached to the cavity steel liner during construction. Identical strain gages were attached to the missile shield holddown bolts.

Accumulator water level and water velocity measurements through the 10 cm blowdown piping were attempted. Calculations indicate that 70 kg of water would be expelled from the accumulator in about 0.4 to 0.7 s, followed by a `typical' accumulator blowdown of the remaining steam in about 3-4 s. The water expulsion is very quick, with a transient peak water velocity on the order of 25 to 40 meter/second (m/s) in the 10 cm pipe; therefore, these instruments must have a fast response time (<50 ms).

A differential pressure transducer with a range from 0-26 m (0-0.1 MPa differential) of water (that can operate in a 13.8 MPa saturated steam system) was used to measure accumulator water level. The response time for this instrument was 2 ms. The transducer was mounted outside the Surtsey vessel. Fluid filled instrument lines were used to connect the instrument to the accumulator to minimize line effects on the response time of the measurement.

A pitot-static tube for the 10 cm pipe was designed by SNL and was used with a 0-6.9 MPa differential pressure transducer that can operate in 13.8 MPa saturated steam conditions. The response time for this instrument is 88 ms. The transducer was mounted outside

the Surtsey vessel. Fluid filled instrument lines were used to connect the instrument to the accumulator to minimize line effects.

Table 1. Geometric comparisons for the CE DCH experiments

Geometric Parameters	Calvert Cliffs	Scaled	Surtsey
Scale	Plant	1/10th	1/10th
Reactor Coolant System			
RCS Volume (m^3)	3.1434	0.3143	0.2544
Melt Mass (kg)	59.3×10^3	n/a	30.0
Melt Volume (m^3)	7.27	n/a	7.73×10^{-3}
Reactor Pressure Vessel			
RPV Lower Head I.D. (m)	4.368	0.4368	0.3969
RPV Shell Mid-Vessel O.D. (m)	4.822	0.4822	0.5461
RPV Seal Ledge O.D. (m)	5.588	0.5588	0.6223
RPV Lower Head Volume (m^3)	21.830	0.0218	0.0276
Melt/Lower Head Volume Ratio	0.3330	0.3330	0.2801
Length from Melt Plug to Cavity Floor (m)	0.500	0.0500	0.0500
Length from Melt Plug to Nozzle Centerline (m)	8.300	0.8300	0.7833
Length of RPV Shell and Bottom Head (m)	10.377	1.0377	1.2186
RPV Nozzle Average O.D. (m)	1.434	0.1434	0.1524
Hole Diameter (m)	0.400	0.0400	0.0400
Annular Gap/Cavity			
Effective Annular Gap below Nozzles (m)	0.493	0.0493	0.0443
Effective Annular Gap at Nozzles (m)	1.119	0.1119	0.0995
Effective Annular Gap at Cavity Exit (m)	0.787	0.0787	0.0847
Flow Area below Nozzles (m^2)	8.230	0.0823	0.0825
Area Blocked by Nozzles (nozzle centerline) (m^2)	5.798	0.0580	0.0910
Flow Area at Nozzles (m^2)	15.24	0.1524	0.2017
Flow Area at Cavity Exit (m^2)	15.77	0.1577	0.1679
Cavity Diameter below Nozzles (m)	5.808	0.5808	0.6349
Cavity Diameter at Exit (m)	7.163	0.7163	0.8191
Cavity Empty Volume (m^3)	326.0	0.3260	0.4694
Cavity Free Volume (m^3)	145.4	0.1454	0.2169
Cavity Floor Area (m^2)	26.49	0.2649	0.3167
Cavity Height (m)	10.833	1.0833	1.1826
Cavity Access Hatch Width (square) (m)	0.762	0.0762	0.0762
Cavity Access Hatch Flow Area (m^2)	0.581	.0058	0.0058
Loop Piping and Cavity Cutouts (Hot 2X, Cold 4X)			
Hot Leg O.D. (m)	1.276	0.1276	n/a
Cold Leg O.D. (m)	0.908	0.0908	n/a
Hot Leg Cutout Diameter (m)	1.727	0.1727	0.1365
Cold Leg Cutout Diameter (m)	1.372	0.1372	0.1365
Hot Leg Area (m^2)	1.279	0.0128	n/a

Table 1. Geometric comparisons for the CE DCH experiments

Geometric Parameters	Calvert Cliffs	Scaled	Surtsey
Cold Leg Area (m^2)	0.648	0.0065	n/a
Total Leg Area (m^2)	5.149	0.0515	n/a
Hot Leg Cutout Area (m^2)	2.343	0.0234	0.0146
Cold Leg Cutout Area (m^2)	2.272	0.0227	0.0146
Total Cutout Area (m^2)	13.775	0.1377	0.0878
Total Bypass Flow Area (Cutout - Leg) (m^2)	8.626	0.0863	0.0878
Refueling Canal			
Length (m)	21.361	2.1361	2.1336
Major Height (m)	11.418	1.1418	1.0160
Minor Height (m) (above biological shield)	7.620	0.7620	0.7012
Width (m)	7.632	0.7632	0.8179
Volume (m^3)	1554.9	1.5549	1.8521
Missile Shield			
Length (m)	5.398	0.5398	0.5398
Width (m)	7.632	0.7632	0.8726
Area (m^2)	41.195	0.4119	0.4761
Height Above Cavity Exit (m)	7.925	0.7925	0.8382
Refueling Canal Openings (2X)			
Effective Length (m)	7.982	0.7982	0.7965
Width (m)	7.632	0.7632	0.8179
Flow Area (m^2)	60.918	0.6092	0.6515
Total Flow Area (m^2)	121.84	1.2184	1.3032
RCP Vent Openings (4X)			
Length (m)	3.759	0.3759	n/a
Width (m)	2.553	0.2554	n/a
Flow Area (m^2)	9.599	0.0960	n/a
Total Flow Area (m^2)	38.34	0.3840	0.4032
Steam Generator Openings (2X)			
Length (m)	7.693	0.7693	n/a
Width (m)	5.855	0.5855	n/a
Occluded Area (m^2)	29.13	0.2913	n/a
Flow Area (m^2)	15.92	0.1592	n/a
Total Flow Area (m^2)	31.84	0.3184	0.3084
Basement/Operating Deck Openings			
Containment Cross-sectional Area (m^2)	1233.1	12.3312	10.5071
Operating Deck Area (without openings) (m^2)	676.8	6.7680	6.3150
Total Operating Deck Opening Area (m^2) (S/G and RCP Removal Hatch Openings)	70.23	0.7023	0.7116
Basement/Cranewall Flow Area (m^2)	209.0	2.0901	2.2664

Table 1. Geometric comparisons for the CE DCH experiments

Geometric Parameters	Calvert Cliffs	Scaled	Surtsey
Containment Building			
Length (m)	55.37	5.5372	5.4864
Diameter (m)	39.62	3.962	3.6576
Aspect Ratio (L/D)	1.397	1.3974	1.5
Length from Basement Floor to Operating Deck (m)	17.98	1.7983	2.2352
Length from Cavity Exit to Dome (m)	44.65	4.4653	3.4925
Empty Volume (m^3)	62241.5	62.2415	56.710
Structure Volume (m^3)	5607.8	5.608	7.260
Total Freeboard Volume (m^3)	56633.7	56.634	49.450
Freeboard Volume above Operating Deck (m^3)	34458.2	34.458	27.927
Freeboard Volume below Operating Deck (m^3)	22175.5	22.175	21.523
Freeboard Volume Ratio (Above OPS Deck/Total)	0.6084	0.6084	0.565
Freeboard Volume Ratio (Above OPS Deck/Below OPS Deck)	1.5539	1.5539	1.298

Table 2. Melt composition

Constituent	Mass Fraction		Mole Fraction		Volume Fraction	
	Corium §	Thermite ¶	Corium	Thermite	Corium	Thermite
UO_2	0.8477	0.0000	0.7056	0.0000	0.7503	0.0000
ZrO_2	0.1272	0.0000	0.2323	0.0000	0.2149	0.0000
Zr	0.0251	0.0000	0.0620	0.0000	0.0348	0.0000
Fe *	0.0000	0.5315	0.0000	0.6559	0.0000	0.3172
Cr	0.0000	0.0000	0.0000	0.0000	0.0000	0.0000
Ni	0.0000	0.0000	0.0000	0.0000	0.0000	0.0000
Al_2O_3	0.0000	0.4543	0.0000	0.3078	0.0000	0.6527
Al	0.0000	0.0142	0.0000	0.0363	0.0000	0.0300

§ Corium mass fractions are based on the Calvert Cliffs scenario V upper bound limits, shown in NUREG/CR-6338.

¶ Alumina-based oxidic thermite.

* Steel specie mass fractions of 0.72 for Fe, 0.18 for Cr, and 0.09 for Ni were used if steel was present.

Table 3. Material properties of the melt

Property/Parameter	Corium Scenario V	Thermite w/ alumina
Mass (kg)	63700	33.15
Volume (m^3)	7.9177	0.0085
Moles (g·moles)	283436	479.7
Mw_{eff} (kg/mole)	0.2247	0.0691
$\Delta e_{reaction}$ (MJ/mole)	0.0371	0.0157
$\Delta e_{thermal}$ (MJ/mole)	0.2980	0.1820
$\Delta e_{combined}$ (MJ/mole)	0.3350	0.1980
E_{total} (MJ)	95.0×10^3	95.0
ν (moles H_2/moles melt)	0.1241	0.7104
C_p (J/mole/K)	119.1	82.8
C_p (J/kg/K)	525.7	1198.5
K (W/m/K)	5.0	19.6
ρ (kg/m^3)	8045	3879
ρ ($mole/m^3$)	3.58×10^4	5.64×10^4
μ (Pa s)	0.0151	0.0074
$T_{mp,oxide}$ (K)	2450	2200
T_{melt} (K)	2800	2500

Table 4. Initial conditions for the CES and CE experiments

		CES-1	CES-2	CES-3	CE-1		CE-2		CE-3		CE-4	
Thermite composition (kg) iron oxide aluminum alumina Mass of the thermite charge (kg)					24.09 7.49 1.64 33.22							
Accumulator pressure (MPa)		8.274	8.523	8.329	8.634		8.340		8.030		4.330	
Accumulator gas or steam temperature (K)		311	607	571	573		571		622		532	
Accumulator volume (m^3)		0.2544										
Moles of accumulator gas or steam (g·moles) at t = 0 s		494 (N_2)	538	301	310		301		477		156	
Moles of accumulator water (g·moles) at t = 0 s		5556	0	5255	5245		5255		0		5400	
Time between thermite ignition and HPME (s)		13	13	13	29		45		29		29	
Exit hole diameter (m)		0.0525		0.0400								
Exit hole area (m^2)		0.0022		0.0013								
Annular gap area (m^2)		0.0825										
Vessel pressure prior to ignition (MPa)		0.2024	0.2027	0.2021	0.2103		0.2195		0.2360		0.2355	
Vessel temperature (K)		298	316	305	378		376		384		380	
Vessel gas moles (g·moles)		4091	3851	3986	3346		3506		3700		3730	
Gas composition					Dry	Wet	Dry	Wet	Dry	Wet	Dry	Wet
in the Surtsey vessel (mole %)	Steam	0.0	0.0	0.0	0.0	41.9	0.0	41.0	0.0	43.6	0.0	44.2
	N_2	99.3	99.6	99.1	78.1	45.4	73.2	43.2	72.9	41.1	72.5	40.4
	O_2	0.2	0.4	0.2	20.9	12.2	19.6	11.6	19.6	11.0	19.4	10.9
	H_2	0.0	0.1	0.4	0.0	0.0	6.2	3.7	6.7	3.8	7.2	4.0
	Other	0.50	0.0	0.3	1.1	0.6	0.9	0.5	0.9	0.5	0.9	0.5
Freeboard volume inside subcompartment structures (m^3)[1]					21.5							
Freeboard volume in upper dome (m^3)					27.9							
Total freeboard volume (m^3)					49.4							

[1] The Surtsey empty volume is 56.71 m^3.

Table 5. CES and CE experiments instrumentation summary

Description	Range	Manufacturer and Model #	Response Time	Comments
Vessel Press	0-100 psia	Kulite/Strain Gage BM-1100	122 μsec	
Vessel Press	0-100 psia	Kulite/Strain Gage BM-1100	122 μsec	
Vessel Press	0-300 psia	Precise Sensor/Strain Gage 555	182 μsec	
Vessel Press	0-300 psia	Precise Sensor/Strain Gage 555	182 μsec	
Accumulator Press	0-3000 psig	Trans Metrics/Strain Gage P53HT	57.2 μsec	
Accumulator Press	0-5000 psig	Trans Metrics/Strain Gage P53HT	57.2 μsec	
Burst Diaphragm Press	0-5000 psig	Trans Metrics/Strain Gage P53HT	57.2 μsec	
Burst Diaphragm Press	0-5000 psig	Trans Metrics/Strain Gage P53HT	57.2 μsec	
Cavity Press	0-500 psia	Trans Metrics/Strain Gage P52HT	112 μsec	Below RPV
Cavity Press	0-500 psia	Trans Metrics/Strain Gage P53HT	112 μsec	Near Exit
Cavity Press	0-10000 psig	Trans Metrics/Strain Gage P53HT	18 μsec	Below RPV
Cavity Press	0-30000 psig	Kistler/Quartz 6230	1 μsec	Below RPV
Cavity Press	0-30000 psig	Kistler/Quartz 6230	1 μsec	Below RPV
Cavity Pyrometer	1873-2773 K			
Ignitor Trigger				
Ignitor Battery				
Accumulator TC	Type K TC	Watlow Gordon	4 sec	Gas High
Accumulator TC	Type K TC	Watlow Gordon	4 sec	Gas/Water Mid
Accumulator TC	Type K TC	Watlow Gordon	4 sec	Water Low
TC Array A1	Type K TC	On Site	150 msec	Top
TC Array A2	Type K TC	On Site	150 msec	
TC Array A3	Type K TC	On Site	150 msec	
TC Array A4	Type K TC	On Site	150 msec	Bottom
TC Array SA1 (Below OP Deck)	Type K TC	On Site	150 msec	Top
TC Array SA2	Type K TC	On Site	150 msec	
TC Array SA3	Type K TC	On Site	150 msec	Bottom
TC Array B1	Type K TC	On Site	150 msec	Top
TC Array B2	Type K TC	On Site	150 msec	
TC Array B3	Type K TC	On Site	150 msec	
TC Array B4	Type K TC	On Site	150 msec	Bottom
TC Array SB1 (Below OP Deck)	Type K TC	On Site	150 msec	Top
TC Array SB2	Type K TC	On Site	150 msec	
TC Array SB3	Type K TC	On Site	150 msec	Bottom
TC Array C1	Type K TC	On Site	150 msec	Top
TC Array C2	Type K TC	On Site	150 msec	
TC Array C3	Type K TC	On Site	150 msec	
TC Array C4	Type K TC	On Site	150 msec	
TC Array C5	Type K TC	On Site	150 msec	
TC Array C6	Type K TC	On Site	150 msec	Bottom
Gas Grab	Various Levels	20 Samples		Various Times
Cavity TC Array	Type C TC	Watlow Gordon	500 msec	2 top, 2 bot
Cavity Photodiode Array	4 diodes	Motorola		top, mid, bot
Missile Shield Strain	± 2% strain	Micromeasurements		Holddown Bolts
Break wires	Annular Gap and Refueling Canal exit	On Site		
4-inch Pipe DP	0-1000 psid	Sensotec TJE/7564-01	89 μsec	Flow Rate
Accumulator DP	± 15 psid	Sensotec A-5/5466-01	2 ms	Water Level

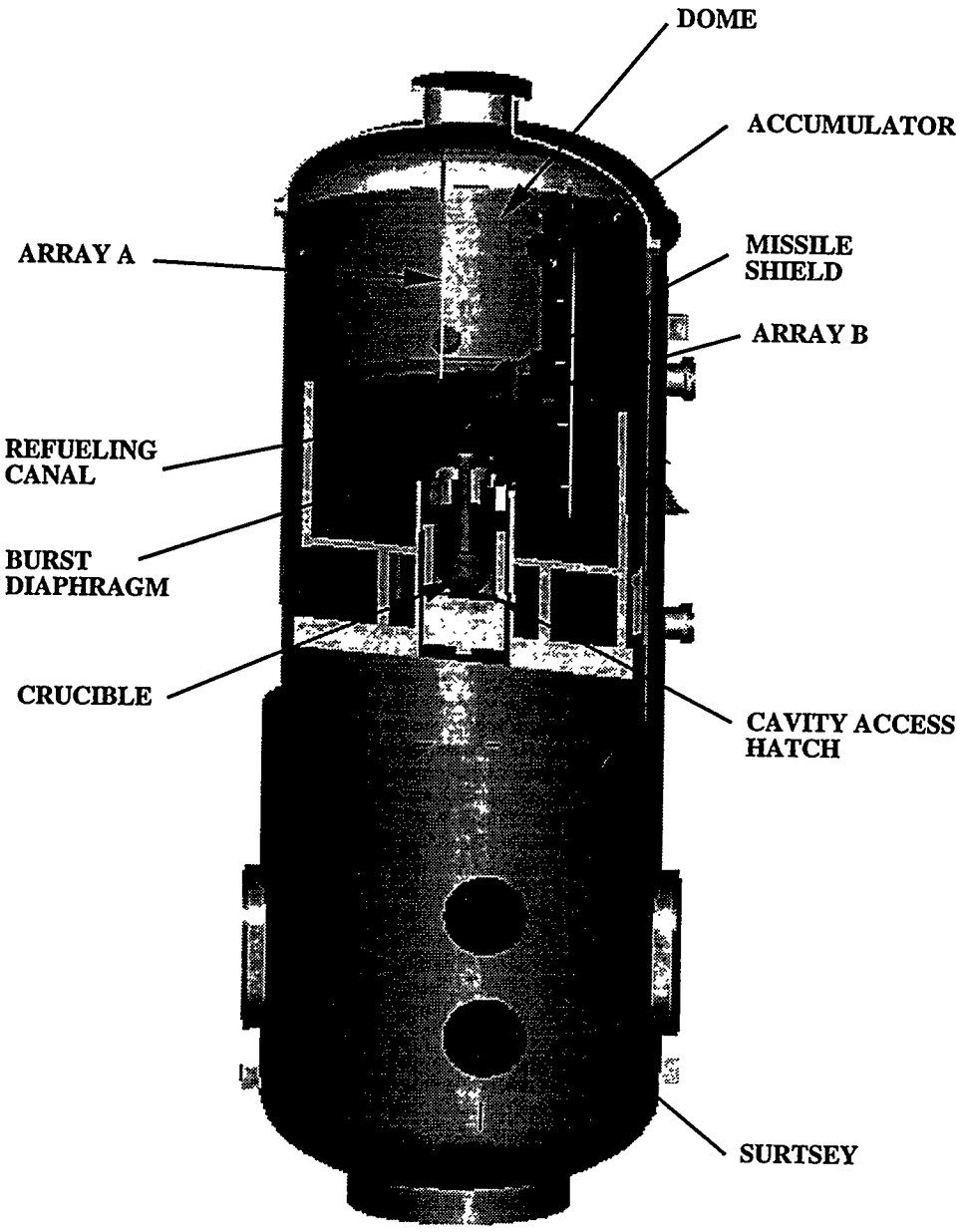

Figure 1. The Surtsey vessel, high-pressure melt ejection system, subcompartment structures, and thermocouple arrays used in the 1/10th scale CE DCH experiments.

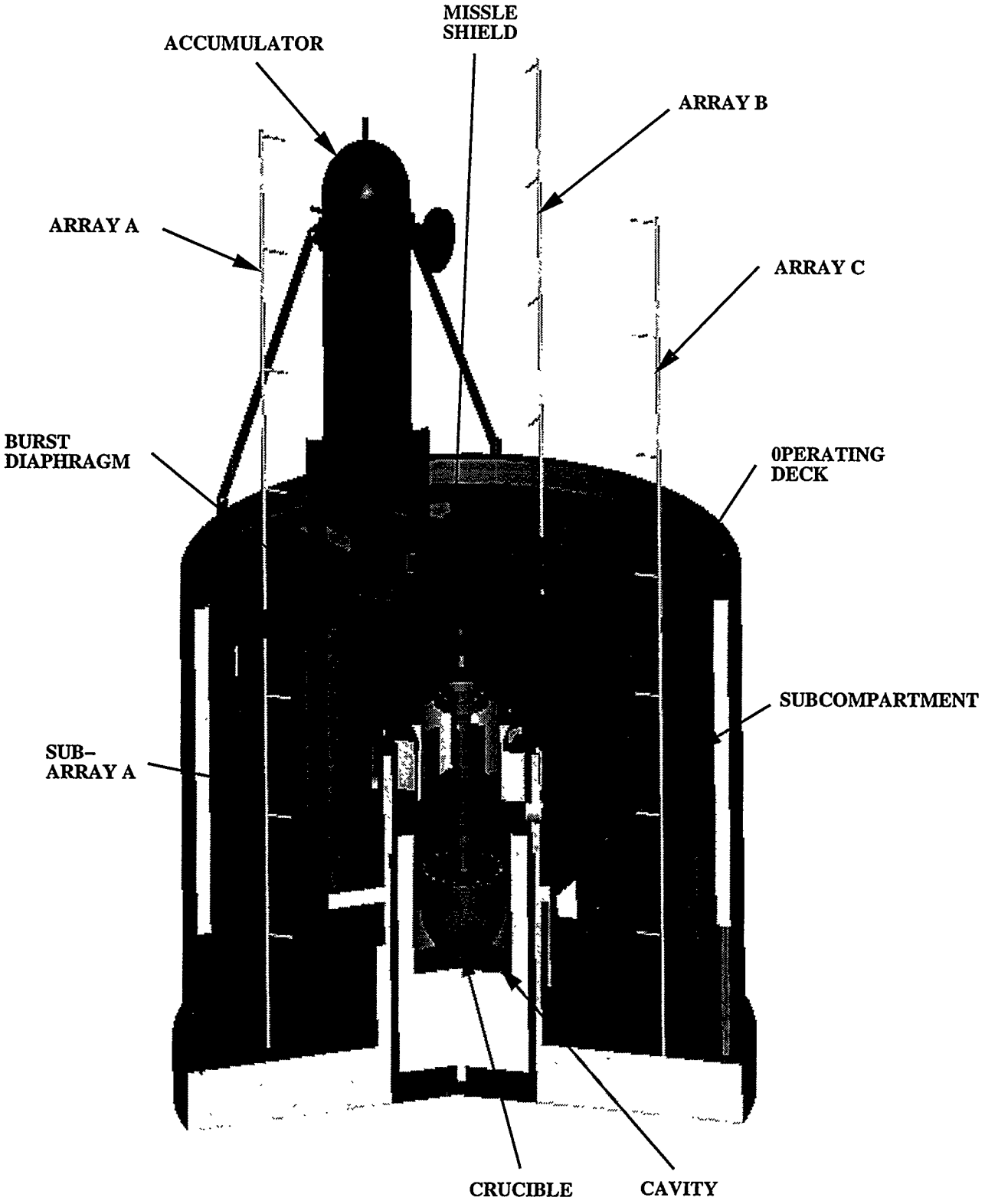

Figure 2. An isometric view of the Calvert Cliffs subcompartment structures and RPV model.

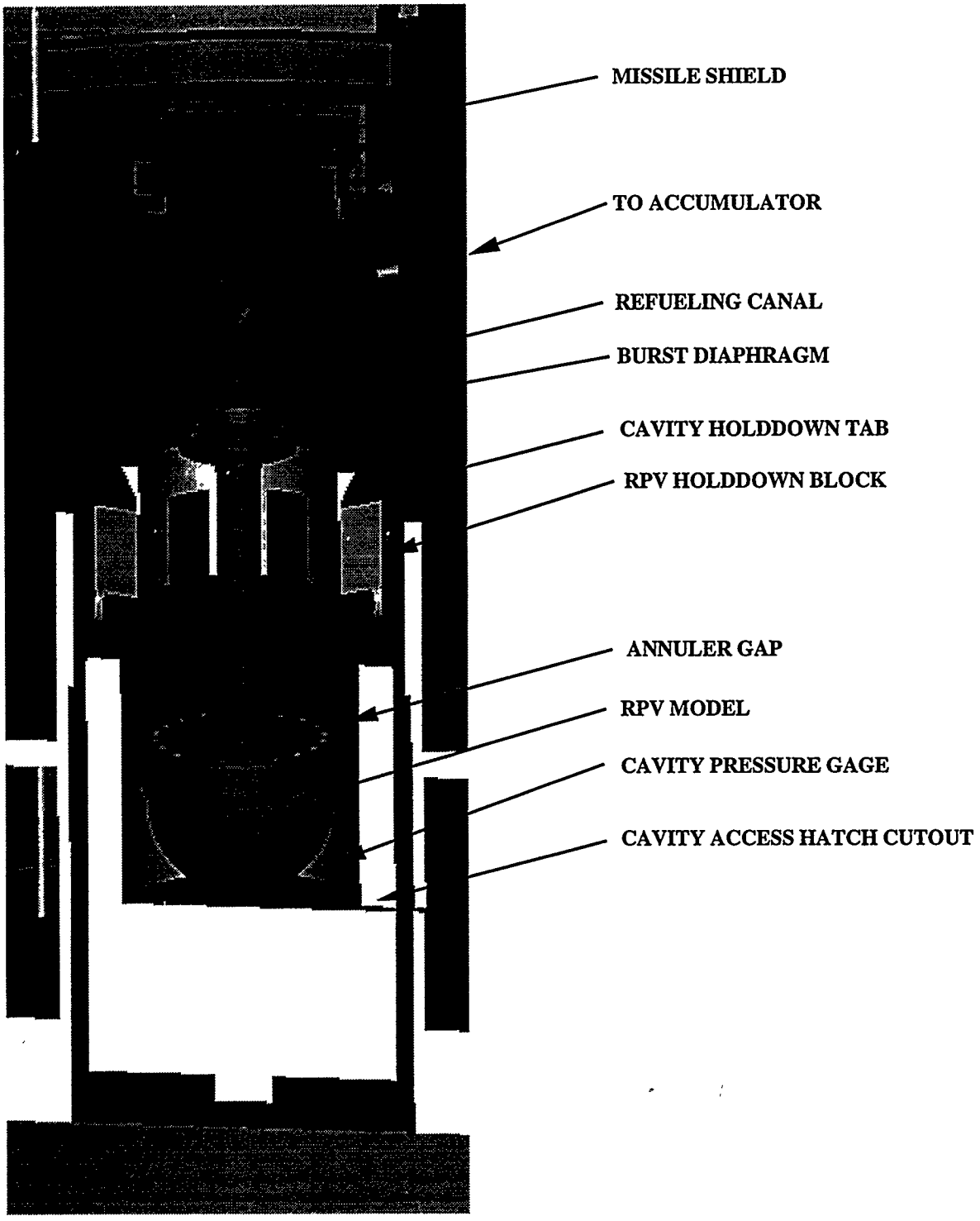

Figure 3. The RPV model (with melt generator) and cavity used in the 1/10th scale CE DCH experiments.

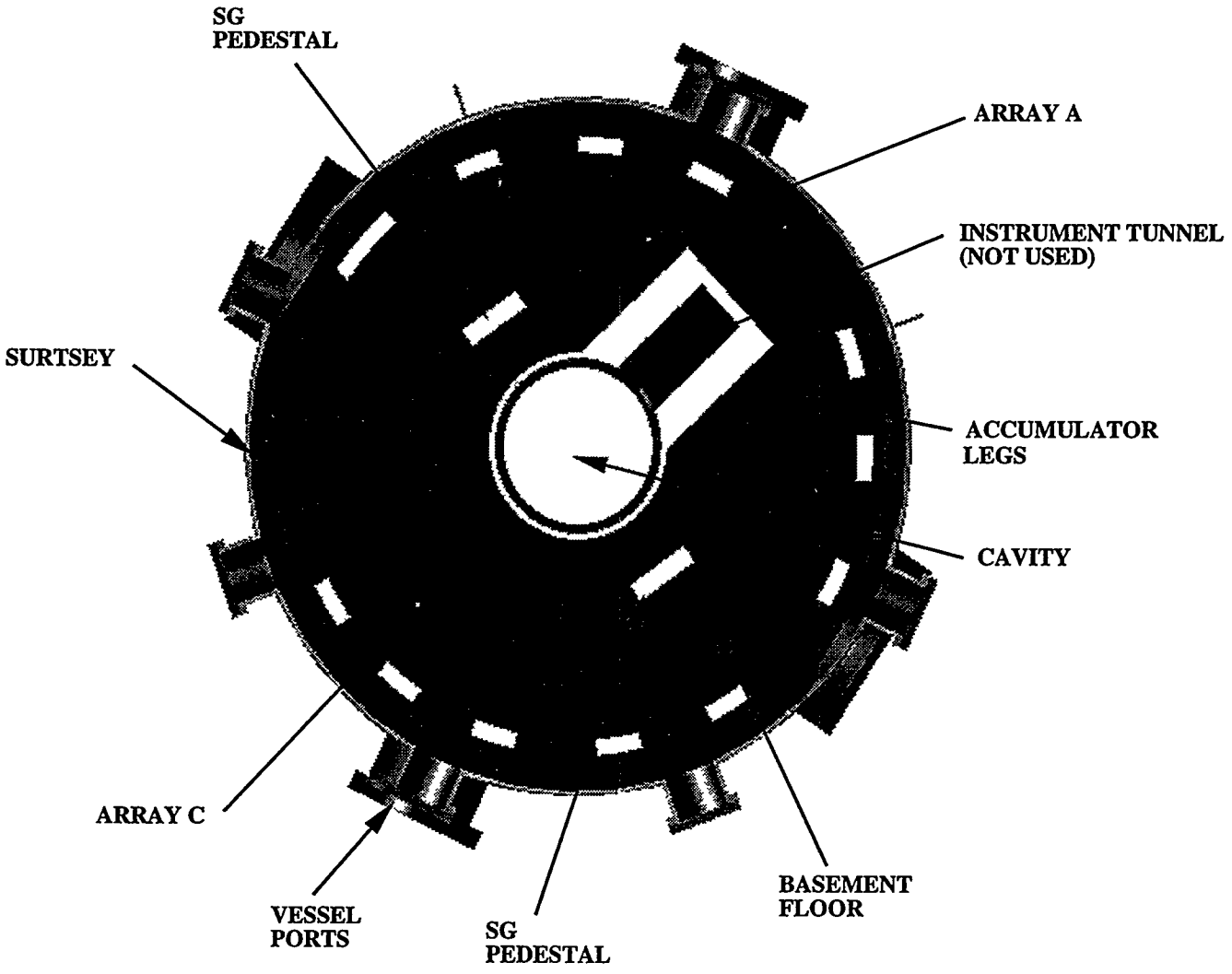

Figure 4. Plan view of structures at Level 4.

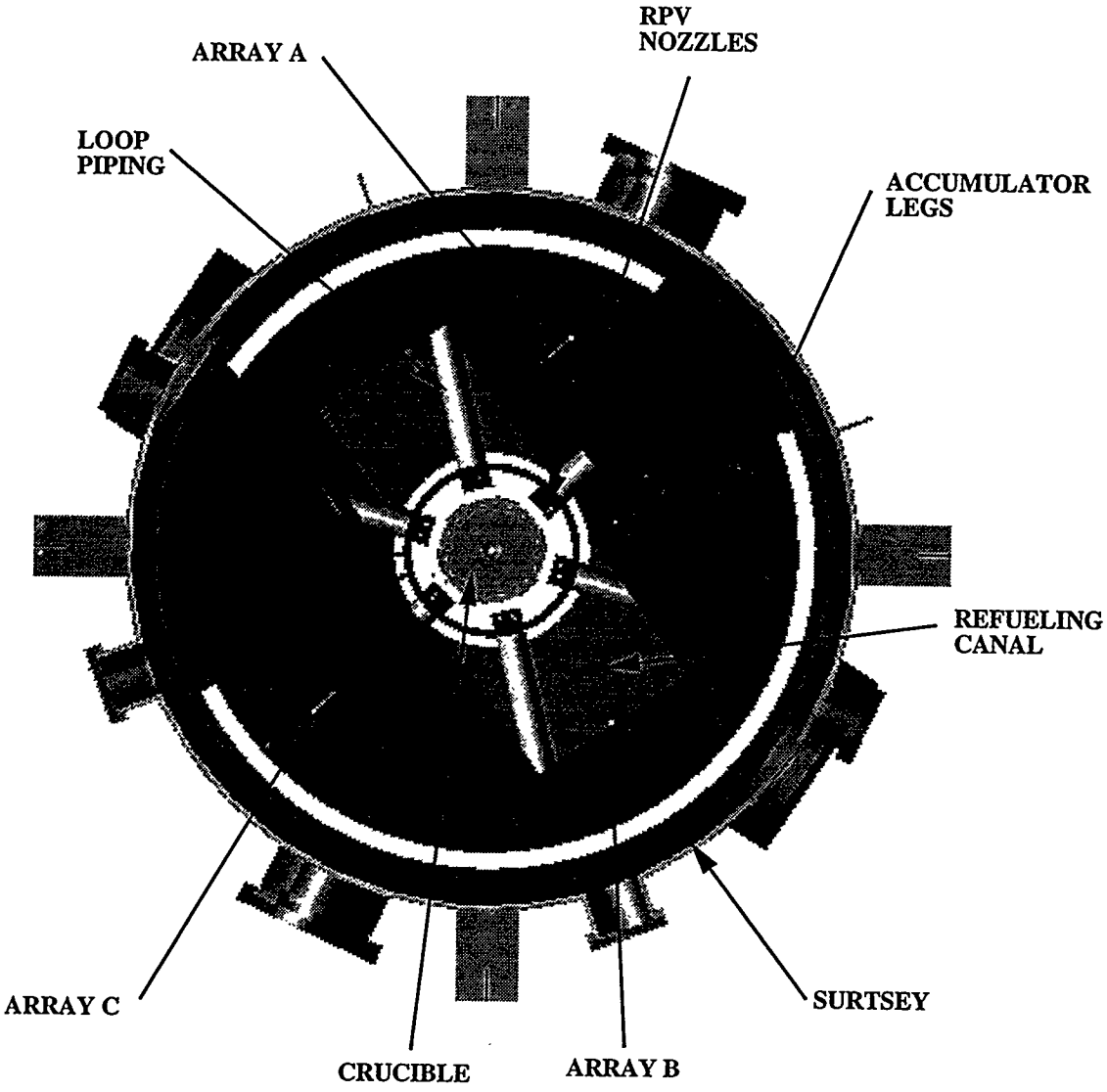

Figure 5. Plan view of structures at Level 5.

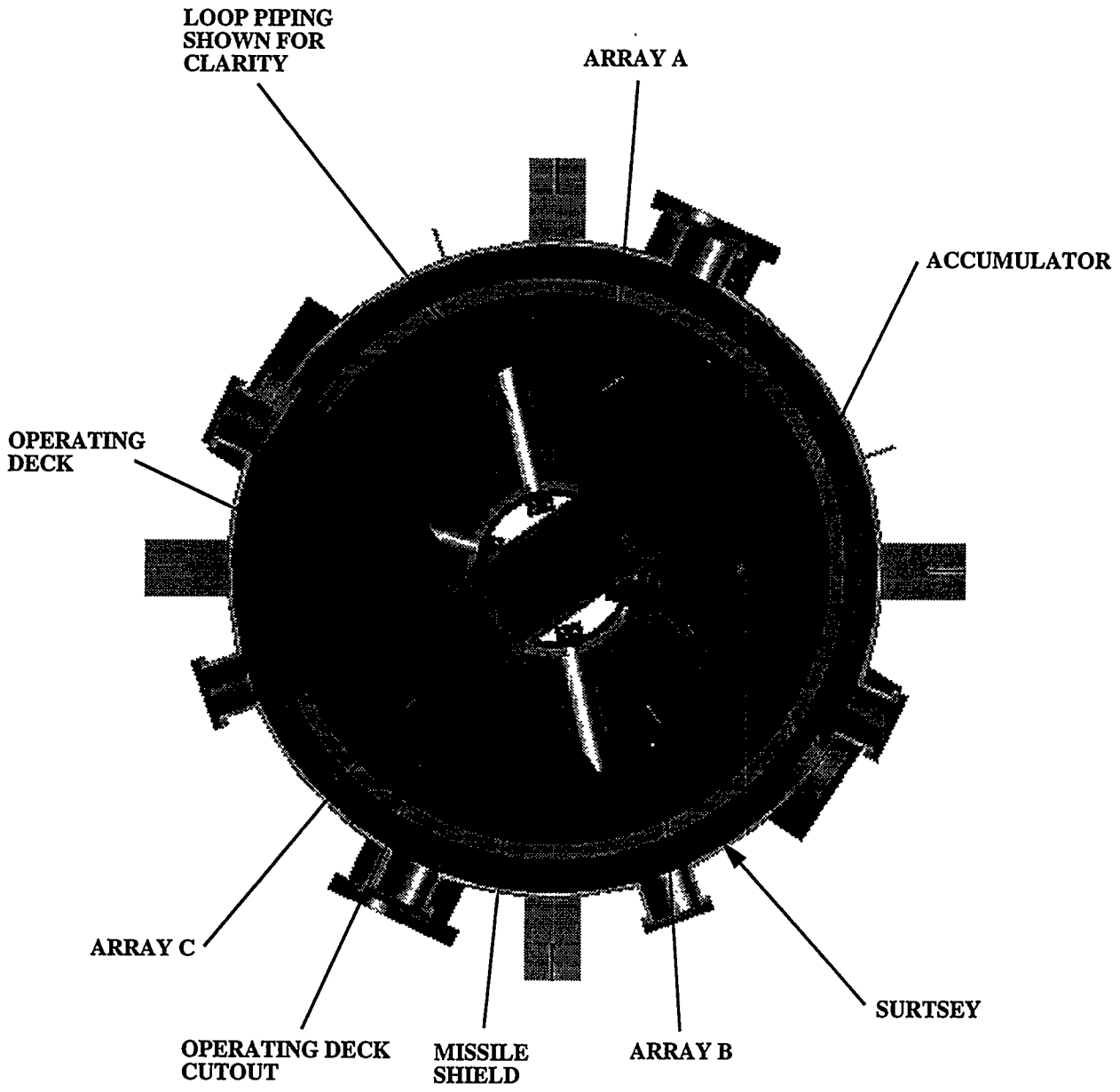

Figure 6. Plan view of structures at Level 6.

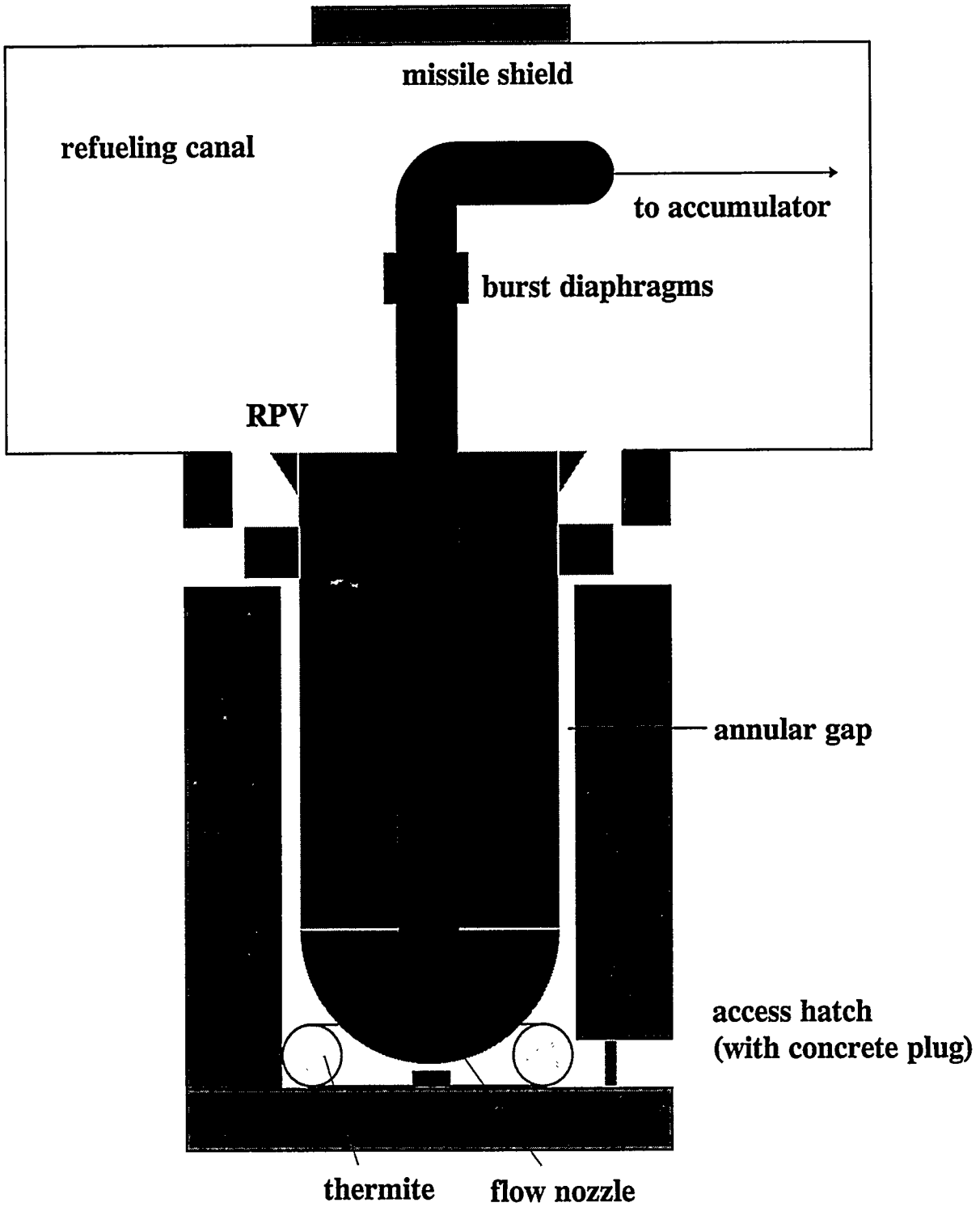

Figure 7. Cavity configuration for delivery of melt in the CE experiments.

3.0 EXPERIMENTAL RESULTS

3.1 Blowdown History

Figures 8 through 14 give the blowdown history for the seven CE experiments. These figures show the relationship between burst diaphragm pressure and accumulator pressure, and the resultant cavity pressure as the melt is entrained out of the cavity during the HPME. Note that the ratio of the cavity pressurization time to the accumulator blowdown time is very small. At t = -0.2 s, the signal to fail the burst diaphragms was sent. At t = 0 s, the burst diaphragms failed. Note that the longer blowdown times in CES-3, CE-1, CE-2, CE-3, and CE-4 were caused by the change in the flow nozzle diameter (from 5.25 cm to 4.0 cm). Also note the increased rate of pressure decay in the accumulator pressure data in the CES-1 test (at 0.8 s), in the CES-3, CE-1, and CE-2 tests (at 2.4 s), and in the CE-4 test (at 3.2 s). This was due to the transition between water ejection and gas ejection.

Figure 9 shows that the accumulator pressure did not track the blowdown very well in the CES-2 experiment. Typically, accumulator pressure tracks burst diaphragm pressure after equilibration. The gages were affected by heat after melt landed on them. Figure 15 compares the accumulator pressure during the blowdown for the seven experiments. For the CES-2 experiment, the burst diaphragm pressure was assumed to give accumulator pressure after equilibration. Pinhole leaks (due to melt impacts) were found posttest in the lines connecting the pressure transducers to the burst diaphragms in the CES-3 experiment. These leaks caused the lower than expected measured burst diaphragm pressure after the HPME (see Figure 10).

Accumulator gas temperature is shown in Figure 16. The gas temperature was used in conjunction with the accumulator pressure to determine the amount of moles of driving gas at the start of the blowdown. The steam temperature closely tracked saturation temperature during the blowdowns that involved saturated water or saturated steam.

3.2 Vessel Pressure

Three figures plot vessel pressure at different time scales for each experiment (Figures 17 through 37). The first pressure plot shows the big picture, giving vessel pressure 60 seconds prior to melt ejection (t = 0 s) to 600 seconds after the HPME. The thermite ignition time is also shown. The next figure examines the two pressure increases that occurred in each test: the first increase was due to heating of the gas in the vessel during the thermite reaction interval and the second increase was due to the HPME. The third figure of each set examines in detail the vessel pressure increase during the HPME.

The vessel pressurized immediately after thermite ignition. In the tests with the nonreactive atmospheres, the vessel pressurized slightly (0.02 MPa). In CE-1, a reactive atmosphere *without* preexisting hydrogen, the vessel pressurize increase was about 0.06 MPa. In the CE-2, CE-3, and CE-4 tests, which contained a reactive (air and steam) atmosphere *with* preexisting hydrogen, the vessel pressurize increase was about 0.12 MPa. The cause for the initial pressure rise was apparent from the camera views inside the Surtsey vessel. When the

vessel was inerted with nitrogen, a thick black aerosol cloud rose out of the cavity annular gap, engulfed the refueling canal and missile shield, and filled the Surtsey vessel in about six seconds. When the vessel atmosphere was reactive, a gray/white (possibly steam) cloud and flames rose out of the cavity annular gap. The fire was very intense; the flames erupted from the refueling canal and rose at least one meter above the operating deck. Some molten particles were ejected out of the cavity and onto the operating deck. The cloud was much lighter in color than in the nonreactive atmosphere tests. Note that interactions of the melt with residual condensate water in the cavity could form steam and hydrogen, which could have burned as it was pushed out of the cavity.

Figures 38 and 39 compare vessel pressure at different time scales for all of the CE experiments. Direct comparisons of vessel pressures between the CES experiments, performed in nitrogen atmospheres, and the CE experiments, performed in air/steam atmospheres (sometimes with hydrogen), are misleading due to differences in the specific heats of nitrogen compared to air/steam. These differences will be accounted for in the Analysis section. Figure 39 shows that during the HPME, the vessel peak pressure increase ranged from 0.2 MPa to 0.3 MPa and was reached at about t = 3 s; however, between 75% and 90% of the vessel pressure increase occurred by about t = 0.1 s (closely tracking the cavity pressure transient). The side camera usually captured the HPME in only one frame; this yields a debris entrainment interval out of the cavity in the range of 33 ms. In that one frame, the molten debris rose upward in the refueling canal; some of the debris impacted the bottom of the missile shield and was deflected to the side and out of the refueling canal. A few tenths of a second later, molten debris would fall downward in front of the side camera window (over a one second interval).

3.3 Cavity Pressure

Figures 40 through 46 compare cavity pressure with vessel pressure for the CE experiments. The cavity peak pressure usually occurred at about t = 0.06 s, followed by an equilibration with the vessel pressure by t = 0.1-0.2 s. The debris entrainment interval is defined as that period of time when the cavity pressure exceeds the vessel pressure. The cavity pressurization was due to the acceleration of debris out of the cavity and corresponded closely to the ejection measured by the pyrometer, which was mounted on the outside of the refueling canal, looking through a quartz window directly across the cavity exit. In a few tests, the pyrometer trace and the cavity pressure trace both showed an entrainment interval of about 0.1 to 0.2 s (confirming the video interpretation). However, the pyrometer time was normally unusable due to the intense aerosol generation during the thermite reaction interval. Again, note that the cavity pressure equilibrated with the vessel pressure immediately after the debris entrainment interval, even though the accumulator blowdown has just started (with high pressure and large amounts of water remaining in the accumulator). The cavity does not pressurize during the remaining blowdown because of the large area ratio (>38) between the annular gap and the flow nozzle exit.

Figure 47 compares the cavity pressure in the seven CE DCH experiments. Peak pressure in the inerted tests (with thermite reaction intervals of about 12 s) ranged from 2.8 MPa to 3.3

MPa. Peak pressures in the reactive atmosphere tests (with thermite reaction intervals of 29 s to 44 s) ranged from 0.4 MPa to 1.7 MPa.

3.4 Vessel Gas Temperatures

Figures 48 through 54 show the vessel average gas temperatures determined from the thermocouple arrays located above and below the operating deck in the CE experiments. Standard linear averaging was used for the dome and subcompartment gas temperatures. A mole-average bulk gas temperature is derived below.

$$< T >_{average} = \frac{\Sigma\ N_i\ T_i}{\Sigma\ N_i} = \frac{\Sigma\ \frac{P\ V_i}{R\ T_i}\ T_i}{\Sigma\ \frac{P\ V_i}{R\ T_i}} = \frac{V_{Tot}}{\Sigma\ \frac{V_i}{T_i}} = \frac{1}{\Sigma\ \frac{f_i}{T_i}} \qquad (3.1)$$

where

f_i = subcompartment volume fraction (0.43) or dome volume fraction (0.57)
N_i = subcompartment or dome gas moles
P = vessel pressure
R = universal gas constant
T_i = subcompartment or dome average gas temperature
V_{Tot} = freeboard gas volume
V_i = subcompartment or dome gas volume.

Note that the region below the operating deck (43% of the total freeboard volume) stays relatively cool both during the thermite reaction period and also during the HPME. This was typical behavior for all of the experiments. Figures 55 and 56 compare the calculated dome average gas temperatures in the Surtsey vessel in the CE experiments during the thermite reaction interval and during the HPME, respectively. Figures 57 and 58 compare the calculated mole-average gas temperatures in the Surtsey vessel in the CE experiments during the thermite reaction interval and during the HPME, respectively. Figures 59 through 65 show the calculated number of moles of gas in the Surtsey vessel (using the ideal gas law with pressure data and mole-average gas temperatures) for each experiment.

3.5 Video Results and Interpretation

Two CCD cameras were used to view the inside of the Surtsey vessel. One camera looked down from the window port in the Surtsey upper head and one camera looked across the operating deck directly at the missile shield through a level 6 window port.

In CES-1, the thermite was ignited at t = -13 s. Almost immediately, a thick black aerosol cloud rose out of the cavity annular gap, engulfed the refueling canal and missile shield, and filled the Surtsey vessel (by t = -6 s). The camera view was obscured for the next six

seconds. At t = 0 s, the burst diaphragms failed, and a flash of orange light was seen in both views. The upper head video showed molten particles impacting the top window. Debris ejection out of the cavity was captured by the level 6 port camera in only one frame; this yields a cavity entrainment interval on the order of 33 ms. In that one frame, the molten debris was seen rising upward in the refueling canal; some of the debris impacted the bottom of the missile shield and was deflected to the side and out of the refueling canal. A few tenths of a second later, molten debris was seen falling downward in front of the level 6 camera window (over a one second interval).

In CES-2, the thermite was ignited at t = -13 s. The top view showed that a thick black aerosol cloud rose out of the cavity annular gap (t = -8 s), engulfed the refueling canal and missile shield, and filled the Surtsey vessel (by t = -3 s). The top camera view was obscured for the next three seconds. The side view showed that the aerosol cloud filled the refueling canal by t = -7 s. At t = 0 s, the burst diaphragms were failed, and a flash of orange light was seen in the top (upper head) view. The upper head video showed molten particles impacting the top window over an interval of about 0.15 s to 0.30 s. The side camera failed due to a circuit trip during the HPME (caused by melt impacting and breaking the internal lights), and no entrainment of debris from the cavity was seen in that view.

In CES-3, the thermite was ignited at t = -13 s. The top view showed that a thick black aerosol cloud rose out of the cavity annular gap (t = -8 s), engulfed the refueling canal and missile shield, and filled the Surtsey vessel (by t = -4 s). The top camera view was obscured for the next four seconds. The side view showed that the aerosol cloud filled the refueling canal by t = -8 s. At t = 0 s, the burst diaphragms were failed, and a flash of orange light was seen in the top (upper head) view. The upper head video showed molten particles violently impacting the top window over an interval of about 0.17 s. Slower moving molten particles were seen either slowly rising or dripping from the upper head for an additional 0.5 s. The side camera captured the HPME in only one frame (0.033 s). The side view was dark for the next four frames, then falling molten drops were seen for about 0.25 s, followed by 0.75 s of drifting molten drops.

In CE-1, the top view showed light reflecting off of the wet concrete surfaces. Water was seen dripping from the dome onto the missile shield. Note that in the CES tests, the surfaces were dry. The thermite was ignited at t = -29 s. The top view showed that smoke and flames started to rise out of the cavity annular gap at t = -25 s. An aerosol or steam cloud obscured the flame at t = -24 s. The cloud was much lighter in color than in the other tests, gray/white versus dark black, which may be indicative of steam formation. At t = -22 s, the cloud reached the top window and obscured the top view. At t = 0 s, glowing orange molten particles impacted the top window. The molten particles violently impacted the top window over an interval of about 0.25 s. Slower moving molten particles were seen either slowly rising or dripping from the upper head for an additional 0.25 s. A combustion flame could not be seen through the aerosol cloud. The side view showed that a smoke or steam cloud and fire impacted the bottom of the missile shield at t = -25 s. At t = -24 s, the whitish-colored cloud filled the refueling canal and obscured the flames that exited the cavity. The view was still mostly obscured by the cloud at t = -22 s; however, flames were seen licking the missile shield. At t = -21 s, an intense fire ball erupted from the refueling canal. Molten particles were ejected out of the cavity and fell onto the

operating deck. At t = -19 s, either the flames had stopped or the aerosol or steam cloud completely obscured the view. At t = 0 s, when the burst diaphragms were failed, the side camera did not capture the HPME (note that in the previous three tests, the HPME was seen in only one frame). The side view showed molten drops falling for about 0.25 s, followed by 0.75 s of drifting molten drops.

In CE-2, the thermite was ignited at t = -45 s. The top view showed an aerosol or steam cloud, flames, and molten debris violently rising out of the cavity annular gap at t = -44 s. The glowing-orange cloud reached the top of the vessel about three seconds later and obscured the camera view. However, unlike the previous tests where the view immediately turned black, the cloud glowed orange for an additional three seconds, as if it was backlit by a flame source. At t = 0 s, glowing orange molten particles impacted the top window. The amount of molten particles seen in the top view seemed substantially less than that seen in previous tests. The side view showed that an intense fire and a small burst of molten debris erupted from the refueling canal at t = -43 s. The flames were seen for about three seconds, until an aerosol or steam cloud obscured the view. At t = 0 s, when the burst diaphragms were failed, the side camera did not capture the HPME (as in CE-1) The side view showed molten drops falling for about 0.5 s. Again, the amount of falling molten particles seen in the side view seemed substantially less than that seen in previous tests.

In CE-3, the thermite was ignited at t = -29 s. The top view showed an aerosol or steam cloud, flames, and molten debris violently rising out of the cavity annular gap at t = -26 s. The glowing-orange cloud reached the top of the vessel about two seconds later and obscured the camera view. The cloud then pulsed and glowed orange for an additional six seconds, as if it was backlit by a flame source (similar to the CE-2 test, except much stronger and about three seconds longer). At t = 0 s, glowing orange molten particles impacted the top window. The particle stream lasted about 0.5 s, but again, as seen during the thermite reaction interval, the view pulsed orange (as if from a flame plume) for an additional two seconds. This glowing view immediately after the HPME was not seen in the CE-2 water-driven, melt ejection test. The side view showed that an intense fire and a small burst of molten debris erupted from the refueling canal at t = -26 s. The flames were seen for about three seconds, until an aerosol or steam cloud obscured the view. The view remained black until t = 0 s. At t = 0 s, when the burst diaphragms were failed, the side camera did not capture the HPME (as in CE-1 and CE-2). The side view showed molten drops falling for about 1 s; no orange glows were seen.

In CE-4, the thermite was ignited at t = -29 s. The top view showed an aerosol or steam cloud, flames, and molten debris violently rising out of the cavity annular gap at t = -26 s. The glowing-orange cloud reached the top of the vessel about two seconds later and obscured the camera view. The cloud then pulsed and glowed orange for an additional four to five seconds, as if it was backlit by a flame source (similar to the CE-2 and CE-3 tests). At t = 0 s, glowing orange molten particles impacted the top window. Particles could be seen in the top view for about 1 s. The top view did not pulse orange after the HPME (as was seen only in the CE-3 test). The side view showed that an intense fire and a small burst of molten debris erupted from the refueling canal at t = -26 s. The flames were seen for about three seconds, until an aerosol or steam cloud obscured the view. The view remained black until t = 0 s. At t = 0 s, when the burst

diaphragms were failed, the side camera did not capture the HPME (as in CE-1, CE-2, and CE-3). The side view showed molten drops falling for about 1 s; no orange glows were seen.

3.6 Debris Recovery Summary

Debris in the Surtsey vessel was recovered from six locations: (1) all cavity surfaces (including the annular gap between the cavity wall and the RPV model), (2) all surfaces on the refueling canal, (3) on the operating deck, (4) on the vessel wall, dome surface, and structures above the operating deck, (5) all surfaces inside the basement, and (6) in the vertical annulus between the Surtsey vessel wall and the crane wall and on the Surtsey floor. A posttest sieve analysis of the debris that was recovered from the operating deck floor was performed for each test. A standard set of 35 sieves was used (U. S. series 9.5 mm to 38 mm). Table 6 gives the debris recovery summary which lists the locations of all debris recovered in the CE DCH experiments. Table 6 and Figure 66 also show the posttest sieve analysis results. The particle size analysis discounted all debris with sizes >9.4 mm and <0.038 mm. The particle size sieve mass median diameter (SMMD) for all of the tests was on the order of 0.3 mm with a near lognormal distribution. Note that the SMMD was ~0.6 mm in the CE-4 experiment; the slightly larger SMMD was probably due to the lower driving pressure.

Table 7 gives the mass balance for the CE experiments. A recovery fraction greater than one indicates that the total mass available for dispersal into the Surtsey vessel was greater than the initial thermite charge due to ablation of concrete in the cavity, contaminants (breakwires, thermocouples, etc.), and oxidation of metallic debris. Table 7 also gives transport fractions based on the mass balance. The definitions for computing the transport fractions from the mass balance are also shown. The transport fractions depend on the mass recovered from the locations specified. Debris from the floor area could not be collected following the CE-2, CE-3, and CE-4 experiments because the CE structures were not removed between tests. The amount of debris in the Surtsey vessel (dome, walls, and floor) for those experiments was estimated using an average total recovered mass of 38.55 ± 0.16 kg, based on the four previous experiments. This was done to allow calculation of the mass balance and the transport fractions.

Some of the debris that is transported to the dome area falls back into the refueling canal. All of the debris found in the refueling canal was included in the debris found outside subcompartment structures because: (1) the missile shield does not appear to be very effective in trapping debris, and (2) the debris in the refueling canal directly heats the gas in the region above the operating deck.

3.7 Gas Composition Measurements

Gas grab samples used to measure the vessel atmospheric composition were taken at a dome penetration, at two level 6 port (operating deck) penetrations, and also in the basement and in the refueling canal (using extension lines) in all experiments with the exception of CES-1 (operating deck samples only). All samples were taken following a 30 s line purge (with the exception of a 15 s purge for the 15 s gas samples). The times of the samples were set for

background, 15 s, 30 s, 2 min., and 30 min. Mixing fans attached to the underside of the Surtsey vessel upper head were operated prior to taking the background samples. The 30 min. samples were also well-mixed with the exception of CES-1 and CE-1. The mixing fans were energized earlier in a few experiments. The gas concentrations measured in the CES and CE experiments are given in Tables 8 through 14.

The gas grab samples were taken from an atmosphere containing a mixture of steam and noncondensible gases. If the sample bottles were cold, it was determined experimentally that they would pressurize to vessel pressure with only noncondensible gas. Gas mass spectroscopy was performed on gases from sample bottles at room temperature. Since the steam in the bottles condensed prior to analysis, the measurements are only of noncondensible gases; thus, the mole percent of the individual gas species determined for each bottle must be adjusted by a noncondensible gas fraction (f_{NC}). The pretest or background noncondensible gas fraction could be calculated based on the gas and steam additions to the Surtsey vessel during the charging process. For example, in CE-4, venting air from the vessel after the leak check (to 0.092 MPa at 288 K) prior to the steam addition placed 1931 g·moles of air inside the Surtsey vessel. After steam was added to Surtsey to adjust the atmosphere conditions to 0.234 MPa and 378 K, then about 149 g·moles of hydrogen gas was added. Immediately before the thermite ignition, the total moles of noncondensible gas (air and hydrogen) and steam was 3730 g·moles. Therefore (assuming no leakage), the background noncondensible gas fraction was 0.558. This method yields background wet-basis gas concentrations inside the Surtsey vessel of 44.2 mole % steam, 51.8 mole % air (40.4 mole % nitrogen, 10.9 mole % oxygen), and 4.0 mole % hydrogen. On a dry basis, the concentrations were 92.8 mole % air and 7.2 mole % hydrogen.

There were usually small differences between the concentrations calculated with the method described above and the values determined from mass spectroscopy analyses. For example, Table 14 shows the results of dry-basis gas mass spectroscopy analyses performed by SNL after the CE-4 experiment. Multiplying the concentrations of the background gas grab sample measurement (listed in Table 14) by the background noncondensible gas fraction yields wet-basis gas concentrations. The background wet-basis gas concentrations inside the Surtsey vessel determined from mass spectroscopy were 44.8 mole % steam, 40.6 mole % nitrogen, 10.3 mole % oxygen, and 3.7 mole % hydrogen.

The need to estimate the posttest noncondensible gas fraction introduces uncertainty in the calculated amounts of posttest hydrogen. The nitrogen-ratio method described below does not require an estimate of the posttest noncondensible fraction (Blanchat et al., 1994). It does, however, require the pretest noncondensible fraction. The data and assumptions required for the nitrogen-ratio method are listed below:

1. The initial noncondensible fraction, f^0_{NC}, must be known.
2. The total pretest moles of gas, N^0_{total}, including steam and noncondensible gases, must be known.
3. The measured ratios of the pretest and posttest noncondensible gases must be known.

4. It must be assumed that nitrogen is neither produced nor consumed by chemical reactions.
5. It must be assumed that leakage between the time for which the pretest numbers apply and the time of the posttest samples does not change the ratios of the noncondensible fractions.

Let X^0_i be the initial (background) mole fraction of species i at time t = 0 in the containment vessel and let N^0_{total} be the initial number of steam and noncondensible gas moles in the vessel. The initial number of gas moles for all species is

$$N_i^0 = X_i^0 \; N_{total}^0 \; . \tag{3.2}$$

Let X^t_i be the mole fraction of species i at time t. For the various posttest times, the number of moles of nitrogen is assumed to be unchanged, and the numbers of moles of the other gases are therefore given by

$$N_i^t = N_{N_2}^0 \frac{X_i^t}{X_{N_2}^t} \; . \tag{3.3}$$

It is not necessary to know the posttest noncondensible fraction; only the ratio of the posttest gas species mole fraction is needed. Furthermore, provided all noncondensible gases leak in the same proportion, a correction for posttest leakage is not needed.

Given the pretest moles of O_2 and H_2 from the noncondensible fraction method and posttest moles of O_2 and H_2 from the nitrogen-ratio method, the moles of H_2 burned and the moles of H_2 produced can be computed from

$$N_{H_2,\,burned}^t = 2\,(N_{O_2}^0 - N_{O_2}^t) \tag{3.4}$$

$$N_{H_2,\,produced}^t = N_{H_2}^t - N_{H_2}^0 + N_{H_2,\,burned}^t \; . \tag{3.5}$$

Table 15 gives the results for the amounts of hydrogen produced and burned for all of the experiments based on the nitrogen-ratio method and using the 30 min. gas grab sample data. The nitrogen-ratio hydrogen combustion results assume metal/steam reactions only; i.e. it assumes that none of the oxygen decrease was due to direct metal/oxygen reaction. The gas sampling procedures and results for each experiment are described below.

CES-1

Gas grab samples to measure the vessel atmospheric composition were taken at a level 6 port connection following a 30-s purge; the times of the samples were background, 2 minutes, and 30 minutes. Table 8 shows that the average background oxygen concentration was 0.2 mole %. The 2-min. and 30-min. samples measured 0.1 mole %. This small change was either due to

hydrogen combustion or debris oxidation and will be considered negligible. The 2-min. hydrogen concentration was 2.9 mole %. The hydrogen concentration measured at 30-min. was 2.3 mole %. The gases in the vessel were probably not completely well-mixed at 2-min.; therefore, the hydrogen production amounts will be based on the 30-min. data. The initial vessel gas moles was 4091. An additional 494 g·moles of nitrogen gas was added to the vessel during the accumulator blowdown. The total amount of gas moles in the vessel at 30-min. was 4585 g·moles. Therefore, a maximum of 105 g·moles of hydrogen were produced (4585 g·moles x 0.023).

The 105 g·moles of produced hydrogen is probably over estimated. Note that mixing fans were not turned on prior to obtaining the 30 min. gas samples. Later experiments showed that gross stratification across the operating deck can exist. For example, in CES-3, hydrogen concentrations at the operating deck were 5.2 mole % and 3.3 mole % in the basement. The hydrogen concentration above the operating deck reduced to 3.7 mole % after the fans were turned on. Simple mole-averaging of the above and below deck concentrations yields a value of 4.2 mole %, close to the well-mixed measured value. The above deck hydrogen concentration in CES-3 decreased by a factor of 0.71 after the mixing fans were turned on. Assuming that the same reduction would have occurred in CES-1 if the mixing fans were turned on, yields a well-mixed hydrogen concentration of 1.6 mole % and a hydrogen production of 75 g·moles.

CES-2

Gas grab samples to measure the vessel atmospheric composition were taken at a dome penetration, at two level 6 port (operating deck) penetrations, and also in the basement and in the refueling canal (using extension lines). All samples were taken following a 30-s line purge (with the exception of a 15-s purge for the 15-s gas samples). The times of the samples were background, 15 s, 30 s, 2 min., and 30 min. There are five gas grab sample stations with four sample bottles at each station. During the HPME, melt impacted a dome light and caused a GFCI to trip; the electrical fault tripped all breakers attached to that circuit. Unfortunately, gas grab stations 1 and 4 lost electrical power. The result was that the 15 s, 30 s, and 2 min. refueling canal samples and also the 2 min. operating deck samples were not taken.

Table 9 shows the results of gas mass spectroscopy analyses performed by SNL. The average background oxygen concentration was 0.4 mole %. The 15 s, 30 s, and 2 min. average hydrogen concentrations were 5.6 mole %, 5.7 mole %, and 5.1 mole %, respectively. All of these concentrations represent volumes above the operating deck. Thirty minutes after the HPME, the mixing fans were turned on for two minutes, the samples lines were purged for 30 s, and then two samples were taken at the level 6 port. The average hydrogen concentration in the Surtsey vessel was 3.65 mole %. The decrease was probably due to the forced mixing of the basement volume (with suspected lower hydrogen concentrations) with the dome volume. This conclusion is supported by the temperature data which indicates that a strong stratification immediately occurred and remained in place through the 30-minute sample time.

The hydrogen production amounts are based on the 30-min. gas grab sample data. The initial vessel gas moles was 3851. The steam moles from the accumulator blowdown had condensed by thirty minutes. It is assumed that the number of moles in the vessel at thirty minutes is equal to the initial amount (note that at t = 30 min., the ideal gas law yields 3711 g·moles, based on a pressure of 0.20 MPa and a volume-average gas temperature of 324 K). Therefore, 141 g·moles of hydrogen were produced in CES-2 (3851 g·moles x 0.0365).

CES-3

Gas grab samples to measure the vessel atmospheric composition were taken at a dome penetration, at two level 6 port (operating deck) penetrations, and also in the basement and in the refueling canal (using extension lines). All samples were taken following a 30 s line purge (with the exception of a 15 s purge for the 15 s gas samples). The times of the samples were background, 15 s, 30 s, 2 min., and 30 min. Mixing fans attached to the underside of the Surtsey vessel upper head are operated prior to taking the background and the 30 minute samples.

Table 10 shows the results of gas mass spectroscopy analyses performed by SNL. The average background oxygen concentration was 0.2 mole %. The 15 s, 30 s, and 2 min. average hydrogen concentrations in the dome and operating deck regions were 5.8 mole %, 5.3 mole %, and 5.2 mole %, respectively. All of these concentrations represent volumes above the operating deck. Twenty five minutes after the HPME, the mixing fans were turned on for about four minutes, the samples lines were purged for 30 s, and then two samples were taken at the level 6 port. The average hydrogen concentration in the Surtsey vessel was 3.65 mole %. The decrease was due to the forced mixing of the basement volume (with measured lower hydrogen concentrations at 15 s, 30 s, and 2 min. of 2.9 mole %, 2.8 mole %, and 3.3 mole %, respectively) with the dome volume.

The hydrogen production amounts are based on the 30-min. gas grab sample data. The initial vessel gas moles was 3986. The steam moles from the accumulator blowdown had condensed by thirty minutes. It is assumed that the number of moles in the vessel at thirty minutes is equal to the initial amount (note that at t = 30 min., the ideal gas law yields 4120 g·moles, based on a pressure of 0.22 MPa and a volume-average gas temperature of 318 K). Therefore, 145 g·moles of hydrogen were produced in CES-3 (3986 g·moles x 0.0365).

CE-1

Gas grab samples used to measure the vessel atmospheric composition were taken at a dome penetration, at two level 6 port (operating deck) penetrations, and also in the basement and in the refueling canal (using extension lines). All samples were taken following a 30-s line purge (with the exception of a 15-s purge for the 15-s gas samples). The times of the samples were set for background, 15 s, 30 s, 2 min., and 30 min. However, there was a 104-s delay in the start of the gas grab sample sequence; consequently the sample times were 119 s, 134 s, 3.7 min., and 30 min. Mixing fans attached to the underside of the Surtsey vessel upper head were only operated prior to taking the background samples.

The pretest or background noncondensible gas fraction could be calculated based on the gas and steam additions to the Surtsey vessel during the charging process. Venting the vessel (to 0.0938 MPa at 290 K) prior to the steam insertion placed 1945 g·moles of noncondensible gas inside the Surtsey vessel. Immediately before the thermite ignition, the total moles of noncondensible gas and steam was 3346 g·moles. Therefore (assuming no leakage), the background noncondensible gas fraction was 0.5813.

Table 11 shows the results of gas mass spectroscopy analyses performed by SNL. Multiplying the concentrations of the background gas grab sample measurement by the background noncondensible gas fraction yields the wet-basis gas concentrations. The background wet-basis gas concentrations inside the Surtsey vessel were 41.9 mole % steam, 45.5 mole % nitrogen, 12.0 mole % oxygen, and 0.0 mole % hydrogen.

Thirty minutes after the HPME, the samples lines were purged for 30 s, and then two samples were taken at the level 6 port. The mixing fans were not turned on (inadvertently) prior to the taking of the 30-min. gas grab samples. However, it appears that some mixing did occur between the 3.7 min. sample time and the 30 min. sample time, evident by the decrease in hydrogen and the increase in oxygen concentrations measured above the operating deck. Mole-averaging of the oxygen and hydrogen concentrations at 3.7 minutes gives results very close to the measured values at 30 minutes. The mixing may have been enhanced by the hot structures (at 373 K) as opposed to the cold structures in the CES experiments which promoted thermal stratification. The average gas concentrations (dry-basis) in the Surtsey vessel were 0.0 mole % steam, 77.9 mole % nitrogen, 17.2 mole % oxygen, and 3.1 mole % hydrogen. The posttest wet-basis gas concentrations were 49.2 mole % steam, 39.6 mole % nitrogen, 8.7 mole % oxygen, and 1.6 mole % hydrogen. The posttest moles of O_2 and H_2 (and other noncondensibles) along with the posttest steam fraction were computed using the nitrogen-ratio method. The hydrogen production amounts are based on the 30-min. gas grab sample data. Hydrogen moles increased by 60 and oxygen moles decreased by 65. Therefore, 191 g·moles of hydrogen were produced and 130 g·moles of hydrogen were burned in CE-1.

CE-2

Gas grab samples used to measure the vessel atmospheric composition were taken at a dome penetration, at two level 6 port (operating deck) penetrations, and also in the basement and in the refueling canal (using extension lines). All samples were taken following a 30-s line purge. The times of the samples were set for background, 15 s, 30 s, 2 min., and 30 min. However, a problem concerning the burst diaphragm failure time also affected the posttest gas grab sample times. The operator had to manually obtain the gas grab samples; consequently the sample times were 120 s, 211 s, 5.7 min., and 30 min. Mixing fans attached to the underside of the Surtsey vessel upper head were operated prior to taking the background samples and all of the posttest samples.

The pretest or background noncondensible gas fraction could be calculated based on the gas and steam additions to the Surtsey vessel during the charging process. Venting the vessel (to 0.0896 MPa at 278 K) prior to the steam insertion placed 1939 g·moles of air inside the Surtsey vessel. About 129 g·moles of hydrogen gas was added. Immediately before the thermite ignition, the total moles of noncondensible gas (air and hydrogen) and steam was 3506 g·moles. Therefore (assuming no leakage), the background noncondensible gas fraction was 0.59.

Table 12 shows the results of gas mass spectroscopy analyses performed by SNL. Multiplying the concentrations of the background gas grab sample measurement by the background noncondensible gas fraction yields the wet-basis gas concentrations. The background wet-basis gas concentrations inside the Surtsey vessel were 41.0 mole % steam, 43.2 mole % nitrogen, 11.6 mole % oxygen, and 3.7 mole % hydrogen.

The posttest moles of O_2 and H_2 (and other noncondensibles) along with the posttest steam fraction was computed using the nitrogen-ratio method. Thirty minutes after the HPME, the samples lines were purged for 1 min., and then two samples were taken at the level 6 port. The mixing fans were turned on prior to the taking of the 30-min. gas grab samples. The average gas concentrations (dry-basis) in the Surtsey vessel were 0.0 mole % steam, 76.3 mole % nitrogen, 15.4 mole % oxygen, and 5.9 mole % hydrogen. The posttest wet-basis gas concentrations were 47.3 mole % steam, 40.3 mole % nitrogen, 8.1 mole % oxygen, and 3.1 mole % hydrogen.

Table 15 gives the results for the amounts of hydrogen produced and burned. The hydrogen production amounts are based on the 30-min. gas grab sample data. Hydrogen moles decreased by 12 and oxygen moles decreased by 102. Therefore, 191 g·moles of hydrogen were produced and 202 g·moles of hydrogen were burned in CE-2.

CE-3

Gas grab samples used to measure the vessel atmospheric composition were taken at a dome penetration, at two level 6 port (operating deck) penetrations, and also in the basement and in the refueling canal (using extension lines). The times of the samples were background, 15 s, 30 s, 2 min., and 30 min. All samples (except the 15 s) were taken following a 30 s line purge. Mixing fans attached to the underside of the Surtsey vessel upper head were operated prior to taking the background samples and the 2-min. and the 30-min. posttest samples.

The pretest or background noncondensible gas fraction could be calculated based on the gas and steam additions to the Surtsey vessel during the charging process. Venting the vessel (to 0.091 MPa at 284 K) prior to the steam addition placed 1934 g·moles of air inside the Surtsey vessel. About 139 g·moles of hydrogen gas was added. Immediately before the thermite ignition, the total moles of noncondensible gas (air and hydrogen) and steam was 3700 g·moles. Therefore (assuming no leakage), the background noncondensible gas fraction was 0.56.

Table 13 shows the results of gas mass spectroscopy analyses performed by SNL. Multiplying the concentrations of the background gas grab sample measurement by the background noncondensible gas fraction yields the wet-basis gas concentrations. The background wet-basis gas concentrations inside the Surtsey vessel were 43.6 mole % steam, 41.1 mole % nitrogen, 11.0 mole % oxygen, and 3.8 mole % hydrogen.

The posttest moles of O_2 and H_2 (and other noncondensibles) along with the posttest steam fraction were computed using the nitrogen-ratio method. Thirty minutes after the HPME, the samples lines were purged for 1 min., and then two samples were taken at the level 6 port. The mixing fans were turned on prior to the taking of the 30-min. gas grab samples. The average gas concentrations (dry-basis) in the Surtsey vessel were 0.0 mole % steam, 80.2 mole % nitrogen, 13.0 mole % oxygen, and 4.5 mole % hydrogen. The posttest wet-basis gas concentrations were 48.9 mole % steam, 41.0 mole % nitrogen, 6.6 mole % oxygen, and 2.3 mole % hydrogen. Hydrogen moles decreased by 54 and oxygen moles decreased by 161. Therefore, 269 g·moles of hydrogen were produced and 323 g·moles of hydrogen were burned in CE-3.

CE-4

Gas grab samples used to measure the vessel atmospheric composition were taken at a dome penetration, at two level 6 port (operating deck) penetrations, and also in the basement and in the refueling canal (using extension lines). The times of the samples were background, 15 s, 30 s, 2 min., and 30 min. All samples (except the 15 s) were taken following a 30-s line purge. Mixing fans attached to the underside of the Surtsey vessel upper head were operated prior to taking the background samples and the 30-min. posttest samples.

The pretest or background noncondensible gas fraction could be calculated based on the gas and steam additions to the Surtsey vessel during the charging process. Venting the vessel (to 0.092 MPa at 288 K) prior to the steam addition placed 1931 g·moles of air inside the Surtsey vessel. About 149 g·moles of hydrogen gas was added. Immediately before the thermite ignition, the total moles of noncondensible gas (air and hydrogen) and steam was 3730 g·moles. Therefore (assuming no leakage), the background noncondensible gas fraction was 0.558. This method yields background wet-basis gas concentrations inside the Surtsey vessel of 44.2 mole % steam, 51.8 mole % air (40.4 mole % nitrogen, 10.9 mole % oxygen), and 4.0 mole % hydrogen. On a dry basis, the concentrations were 92.8 mole % air and 7.2 mole % hydrogen.

Table 14 shows the results of dry-basis gas mass spectroscopy analyses performed by SNL. Multiplying the concentrations of the background gas grab sample measurement by the background noncondensible gas fraction yields wet-basis gas concentrations. The background wet-basis gas concentrations inside the Surtsey vessel determined from mass spectroscopy were 44.8 mole % steam, 40.6 mole % nitrogen, 10.3 mole % oxygen, and 3.7 mole % hydrogen.

The posttest moles of O_2 and H_2 along with the posttest steam fraction were computed using the nitrogen ratio method. Thirty minutes after the HPME, the samples lines were purged

for one minute, and then two samples were taken at the level 6 port. The mixing fans were turned on prior to taking the 30-min. gas grab samples. The average gas concentrations (dry-basis) in the Surtsey vessel were 0.0 mole % steam, 77.8 mole % nitrogen, 14.3 mole % oxygen, and 5.6 mole % hydrogen. The posttest wet-basis gas concentrations were 51.8 mole % steam, 37.5 mole % nitrogen, 6.9 mole % oxygen, and 2.7 mole % hydrogen.

Table 15 gives the results for the amounts of hydrogen produced and burned based on the nitrogen-ratio method. The hydrogen production amounts are based on the differences between the background concentration data (from gas addition measurements) and the 30-min. gas grab sample data. Hydrogen moles decreased by 41 and oxygen moles decreased by 128. Therefore, 215 g·moles of hydrogen were produced and 256 g·moles of hydrogen were burned in CE-4.

Table 6. Debris mass balance in kg for the CES and CE experiments

Location	CES-1	CES-2	CES-3	CE-1	CE-2	CE-3	CE-4
Basement	6.990	7.100	7.005	6.870	6.215	5.215	4.020
Missile shield (lower surface)	combined with refueling canal	2.070	1.050	0.840	1.760	1.910	1.640
Refueling canal [1]	7.515	3.195	3.000	1.860	2.900	4.575	1.840
Operating deck (including top of missile shield) [1]	6.925	4.050	3.610	4.210	4.135	4.885	3.370
Surtsey vessel (dome, walls, and floor) [1]	12.025	16.285	18.320	18.585	not recovered (15.71)[2]	not recovered (8.230)[2]	not recovered (11.105)[2]
Cavity (walls, floor, annular gap, and RPV walls)	5.070	5.670	5.380	6.070	7.830	13.735	16.575
Crucible	N/A						
Accumulator (top) [1]	0.220	combined with refueling canal	0.140	0.145	combined with operating deck	combined with operating deck	combined with operating deck
Total Recovered	38.745	38.370	38.505	38.580	38.550 (22.840)[2]	38.550 (30.320)[2]	38.550 (27.445)[2]
Particle size SMMD (mm)	0.286	0.289	0.335	0.274	0.306	0.272	0.568

[1] Debris considered as outside structures for the mass balance.

[2] The amount of debris recovered from the Surtsey vessel was calculated by subtracting the actual amount of debris that was recovered in CE-2, CE-3, and CE-4 from the total recovered debris average (38.550 ± 0.156 kg, based on CES-1, CES-2, CES-3, and CE-1).

Table 7. Mass balance for the CES and CE experiments

MASS BALANCE (kg)	CES-1	CES-2	CES-3	CE-1	CE-2	CE-3	CE-4
Initial thermite charge, M_d° (a)	33.22	33.22	33.22	33.22	33.22	33.22	33.22
Crucible (b)	N/A						
Cavity (c)	5.070	5.670	5.380	6.070	7.830	13.735	16.575
Inside structures (d) (d = f - e - c)	6.990	9.170	7.920	7.710	7.975	7.125	5.660
Outside structures (e) [1]	26.685	23.530	25.070	24.800	22.745 [1]	17.690 [1]	16.315 [1]
Total Recovered (f)	38.745	38.370	38.505	38.580	38.550 [1]	38.550 [1]	38.550 [1]
Recovery fraction, $f_{recovery} = f/a$	1.17	1.16	1.16	1.16	1.16	1.16	1.16
THERMITE TRANSPORT FRACTIONS							
Ejected into cavity, $f_{eject} = 1 - b/a$ (only if < 1)	1.0	1.0	1.0	1.0	1.0	1.0	1.0
Dispersed from cavity, $f_{disp} = (d+e)/(c+d+e)$	0.869	0.852	0.860	0.843	0.797	0.644	0.570
Transported outside subcompartment, $f_{dome} = e/(d+e)$	0.792	0.720	0.760	0.763	0.740	0.713	0.742
Transported to dome, $f_{trans} = f_{eject} * f_{disp} * f_{dome}$	0.688	0.613	0.654	0.653	0.590	0.459	0.423
Thermite transported to dome, $M_d = M_d^\circ * f_{trans}$	22.86	20.38	21.73	21.37	19.60	15.25	14.05

[1] The amount of debris found outside structures assumes that the average total recovered debris mass is 38.550 kg. See Table 6 for details.

Table 8. Gas concentration measured in the CES-1 experiment

Location	Label	Start Time → Duration	Species (mole %)				
			N_2	O_2	H_2	CO [1]	CO_2
1 (Level 6)	G1-B	-2 m → 10 s	99.1	0.2	0.0	-	0.0
	G2-B	-2 m → 10 s	99.4	0.2	0.0	-	0.1
	G3-2m	2 m → 10 s	96.4	0.1	2.9	-	0.1
	G4-2m	2 m → 10 s	96.2	0.1	2.9	-	0.1
	G5-30m[2]	30 m → 10 s	97.2	0.1	2.2	-	0.1
	G6-30m	30 m → 10 s	97.0	0.1	2.4	-	0.1
Background Mean			99.3	0.20	0.00	-	0.05
Background Standard Deviation			±0.2	±0.00	±0.0		±0.07
Posttest Mean (2 m)			97.1	0.10	2.9	-	0.10
Posttest Standard Deviation			±0.1	±0.00	±0.0		±0.00
Posttest Mean (30 m)			96.3	0.10	2.3	-	0.10
Posttest Standard Deviation			±0.14	±0.00	±0.1		±0.00

[1] CO analyses were not performed due to equipment failure.

[2] Mixing fans were not turned on prior to taking the 30-min. samples.

Table 9. Gas concentrations measured in the CES-2 experiment

Time	Label	Location	Species (mole %)					
			N_2	O_2	H_2	CO_2	CO	Argon
background	1-box5 [2]	dome	-	-	-	-	-	-
	2-box1	ops deck	99.5	0.5	0.1	0.0	0.0	0.0
	3-box1	ops deck	99.6	0.5	0.1	0.0	0.0	0.0
	4-box4	basement	99.8	0.2	0.1	0.0	0.0	0.0
15 s	5-box5	dome	94.0	0.1	5.9	0.1	0.5	0.0
	6-box2	ops deck	93.7	0.4	5.9	0.1	0.4	0.0
	7-box2	ops deck	93.6	0.2	6.0	0.1	0.5	0.1
	8-box4 [1]	basement	-	-	-	-	-	-
	9-box2	refuel canal	95.0	0.4	4.5	0.1	0.1	0.0
30 s	10-box5	dome	94.2	0.1	5.7	0.1	0.5	0.0
	11-box3	ops deck	-	-	-	-	-	-
	2	ops deck	93.8	0.5	5.7	0.1	0.5	0.0
	12-box3	basement	-	-	-	-	-	-
	13-box4 1	refuel canal	95.8	0.2	4.0	0.1	0.3	0.0
	14-box2							
2 min	15-box5	dome	94.7	0.1	5.1	0.1	0.4	0.0
	16-box1	ops deck	-	-	-	-	-	-
	1	ops deck	-	-	-	-	-	-
	17-box1 1	basement	-	-	-	-	-	-
	18-box4 1							
30 min[3]	19-box3	ops deck	96.0	0.3	4.0	0.1	0.3	0.0
	20-box3	ops deck	96.7	0.2	3.3	0.1	0.2	0.0
background mean ± std. dev.			99.6±0.2	0.4±0.2	0.1±0.0	0.0±0.0	0.0±0.0	0.0±0.0
15 s mean ± std. dev.			94.1±0.6	0.3±0.2	5.6±0.7	0.1±0.0	0.4±0.2	0.0±0.1
30 s mean ± std. dev.			94.6±1.1	0.3±0.0	5.7±0.0	0.1±0.0	0.4±0.1	0.0±0.0
2 min mean ± std. dev.			94.7±n/a	0.1±n/a	5.1±n/a	0.1±n/a	0.4±n/a	0.0±n/a
30 min mean ± std. dev.			96.4±0.5	0.3±0.1	3.7±0.5	0.1±0.0	0.3±0.1	0.0±0.0

[1] Sample stations lost electrical power.

[2] Bottles leaked.

[3] Mixing fans were turned on prior to taking the 30-min. samples.

Table 10. Gas concentrations measured in the CES-3 experiment

Time	Label	Location	Species (mole %)					
			N_2	O_2	H_2	CO_2	CO	Argon
background	1-box5	dome	99.4	0.0	0.2	0.1	0.2	0.0
	2-box1	ops deck	99.5	0.2	0.1	0.2	0.4	0.0
	3-box1	ops deck	98.6	0.6	0.4	0.1	0.2	0.0
	4-box4	basement	98.8	0.1	0.7	0.1	0.0	0.0
15 s	5-box5	dome	93.5	0.1	6.0	0.1	0.4	0.0
	6-box2	ops deck	93.8	0.1	5.6	0.1	0.4	0.1
	7-box2	ops deck	93.7	0.0	5.7	0.1	0.3	0.1
	8-box4	basement	96.5	0.2	2.9	0.1	0.0	0.0
	9-box2	refuel canal	96.5	0.0	4.4	0.0	0.3	0.1
30 s	10-box5	dome	94.2	0.0	5.7	0.1	0.4	0.0
	11-box3	ops deck	94.0	0.7	5.0	0.1	0.2	0.1
	12-box3	ops deck	94.7	0.0	5.2	0.1	0.2	0.0
	13-box4	basement	96.6	0.5	2.8	0.2	0.1	0.0
	14-box2	refuel canal	95.5	0.1	4.0	0.1	0.3	0.0
2 min	15-box5	dome	94.1	0.0	5.4	0.2	0.3	0.0
	16-box1	ops deck	94.3	0.1	5.1	0.1	0.4	0.1
	17-box1	ops deck	94.0	0.0	5.0	0.3	0.3	0.0
	18-box4	basement	96.6	0.1	3.3	0.0	0.2	0.0
30 min[3]	19-box3	ops deck	95.9	0.0	3.6	0.1	0.2	0.1
	20-box3	ops deck	95.9	0.0	3.7	0.0	0.1	0.0
background mean ± std. dev. [1]			99.1±0.4	0.2±0.3	0.4±0.3	0.1±0.1	0.2±0.2	0.0±0.0
15 s mean ± std. dev. [2]			93.7±0.2	0.1±0.1	5.8±0.2	0.1±0.0	0.4±0.1	0.1±0.1
30 s mean ± std. dev. [2]			94.3±0.4	0.2±0.4	5.3±0.4	0.1±0.0	0.3±0.1	0.0±0.1
2 min mean ± std. dev. [2]			94.1±0.2	0.0±0.1	5.2±0.2	0.2±0.1	0.3±0.1	0.0±0.1
30 min mean ± std. dev. [1]			95.9±0.0	0.0±0.0	3.7±0.1	0.1±0.1	0.2±0.1	0.1±0.1

1 Averaged over all samples.

2 Average of dome and operating deck samples.

3 The mixing fans were turned on prior to taking the 30-min. samples.

Table 11. Gas concentrations measured in the CE-1 experiment

Time	Label	Location	Species (mole %)					
			N_2	O_2	H_2	CO_2	CO	Argon
background	1-box5	dome	78.3	20.6	0.0	0.0	0.0	0.9
	2-box1	ops deck	78.3	20.7	0.0	0.0	0.0	0.9
	3-box1	ops deck	78.0	20.6	0.2	0.0	0.0	0.9
	4-box4	basement	78.2	20.7	0.0	0.0	0.0	1.0
119 s	5-box5	dome	78.1	16.9	3.3	0.7	0.4	0.9
	6-box2	ops deck	77.7	16.8	3.5	0.8	0.2	0.9
	7-box2	ops deck	77.8	16.7	3.6	0.9	0.3	1.0
	8-box4	basement	78.1	18.6	2.0	0.4	0.1	0.9
	9-box2	refuel canal	77.9	17.8	2.6	0.6	0.0	1.0
134 s	10-box5	dome	78.9	17.1	2.1	0.9	0.2	1.0
	11-box3	ops deck	77.6	17.3	3.0	0.8	0.2	1.0
	12-box3	ops deck	78.2	17.0	3.0	0.8	0.3	1.0
	13-box4	basement	77.8	19.0	1.8	0.4	0.1	1.0
	14-box2	refuel canal	77.9	17.9	2.5	0.6	0.1	1.0
3.7 min.	15-box5	dome	77.8	16.9	3.2	0.8	0.3	1.0
	16-box1	ops deck	77.9	16.7	3.5	0.8	0.4	1.0
	17-box1	ops deck	77.6	16.8	3.7	0.8	0.3	1.0
	18-box4	basement	78.1	18.0	2.3	0.5	0.2	1.0
30 min.[3]	19-box3	ops deck	77.9	17.2	3.0	0.7	0.2	1.0
	20-box3	ops deck	77.8	17.2	3.1	0.7	0.2	0.9
Dry-Basis								
background mean ± std. dev. [1]			78.2±0.1	20.7±0.1	0.0±0.1	0.0±0.0	0.0±0.0	0.9±0.1
119 s mean ± std. dev. [2]			77.9±0.2	16.8±0.1	3.5±0.2	0.8±0.1	0.3±0.1	0.9±0.1
134 s mean ± std. dev. [2]			78.2±0.7	17.1±0.2	2.7±0.5	0.8±0.1	0.2±0.1	1.0±0.1
3.7 min. mean ± std. dev. [2]			77.8±0.2	16.8±0.1	3.5±0.3	0.8±0.0	0.3±0.1	1.0±0.0
30 min. mean ± std. dev. [1]			77.9±0.1	17.2±0.0	3.1±0.1	0.7±0.0	0.2±0.0	1.0±0.1
Wet-Basis								
background mean [1]			45.5	12.0	0.0	0.7		
30 min. mean [1]			39.6	8.7	1.6	1.0		

1 Averaged over all samples.

2 Average of dome and operating deck samples.

3 The mixing fans were inadvertently not turned on prior to taking the 30-min. samples.

Table 12. Gas concentrations measured in the CE-2 experiment

Time	Label	Location	Species (mole %)					
			N_2	O_2	H_2	CO_2	CO	Argon
background	1-box5	dome	73.5	18.8	6.3	0.2	0.0	1.0
	2-box1	ops deck	73.5	18.9	6.2	0.1	0.0	1.0
	3-box1	ops deck	73.7	19.0	6.2	0.1	0.0	1.0
	4-box4	basement	73.4	18.8	6.2	0.0	0.0	1.0
120 s[4]	5-box5	dome	76.4	14.2	5.8	1.6	0.0	1.0
	6-box2	ops deck	77.4	14.3	5.9	1.5	0.1	0.9
	7-box2	ops deck	77.0	14.3	5.9	1.4	0.0	0.9
	8-box4	basement	76.1	16.1	5.7	1.0	0.0	1.0
	9-box2	refuel canal	77.0	14.8	5.5	1.3	0.0	0.9
211 s[4]	10-box5	dome	76.1	15.4	5.6	1.2	0.0	1.0
	11-box3	ops deck	77.4	15.3	5.2	1.1	0.0	0.9
	12-box3	ops deck	76.4	15.3	6.1	1.1	0.0	0.8
	13-box4	basement	76.1	16.2	4.8	1.0	0.0	1.0
	14-box2	refuel canal	75.8	15.3	6.4	1.0	0.0	0.9
5.7 min.[4]	15-box5	dome	75.5	15.3	5.8	1.3	0.1	1.0
	16-box1	ops deck	-	-	-	-	-	-
	17-box1	ops deck	76.3	15.6	5.8	1.2	0.0	1.0
	18-box4	basement	75.9	15.6	5.8	1.2	0.0	1.0
30 min.[4]	19-box3	ops deck	76.2	15.3	5.8	1.0	0.0	0.9
	20-box3	ops deck	76.2	15.4	6.0	1.0	0.0	1.0
Dry-Basis								
background mean ± std. dev. [1]			73.6±0.1	18.9±0.1	6.2±0.1	0.1±0.1	0.0±0.0	1.0±0.0
120 s mean ± std. dev. [2]			77.1±0.3	14.3±0.1	5.9±0.1	1.5±0.1	0.0±0.1	0.9±0.1
211 s mean ± std. dev. [2]			76.6±0.7	15.3±0.1	5.6±0.5	1.1±0.1	0.0±0.0	0.9±0.1
5.7 min. mean ± std. dev. [2,3]			75.9±0.6	15.5±0.2	5.8±0.0	1.3±0.1	0.1±0.1	1.0±0.0
30 min. mean ± std. dev. [1]			76.2±0.0	15.4±0.1	5.9±0.1	1.0±0.0	0.0±0.0	1.0±0.1
Wet-Basis								
background mean [1]			43.2	11.6	3.7	0.5		
30 min. mean [1]			40.3	8.1	3.1	1.4		

[1] Averaged over all samples.

[2] Average of dome and operating deck samples.

[3] Sample 16-box1 leaked.

[4] Mixing fans were operated prior to taking all posttest samples.

Table 14. Gas concentrations measured in the CE-4 experiment

Time	Label	Location	Species (mole %)					
			N_2	O_2	H_2	CO_2	CO	Argon
background	1-box5	dome	72.7	18.6	6.9	0.0	0.0	0.8
	2-box1	ops deck	72.9	18.5	6.8	0.7	0.0	0.8
	3-box1	ops deck	72.0	18.3	6.8	0.3	0.0	0.8
	4-box4	basement	73.1	18.6	6.9	0.1	0.0	0.8
15 s	5-box5	dome	82.7	9.7	3.4	2.2	0.2	0.9
	6-box2	ops deck	82.8	10.0	4.0	2.2	0.1	1.0
	7-box2	ops deck	81.0	10.2	3.9	2.0	0.1	1.3
	8-box4	basement	75.0	16.4	5.9	0.6	0.0	0.8
	9-box2	refuel canal	81.0	11.0	4.8	2.0	0.2	1.0
30 s	10-box5	dome	83.1	9.8	3.9	2.0	0.2	0.9
	11-box3	ops deck	82.3	10.8	3.8	1.9	0.1	1.1
	12-box3	ops deck	81.2	10.9	4.4	1.9	0.1	1.0
	13-box4	basement	75.9	16.8	4.4	0.5	0.0	0.9
	14-box2	refuel canal	80.0	12.3	5.0	1.7	0.1	1.0
2 min.	15-box5	dome	81.1	11.2	4.2	1.8	0.1	0.9
	16-box1[4]	ops deck	-	-	-	-	-	-
	17-box1[4]	ops deck	-	-	-	-	-	-
	18-box4	basement	75.7	15.8	6.2	0.8	0.0	0.9
30 min.	19-box3	ops deck	77.7	14.2	5.5	1.1	0.1	1.1
	20-box3	ops deck	77.8	14.3	5.6	1.2	0.0	1.0
Dry-Basis								
background mean ± std. dev. [1]			72.7±0.5	18.5±0.1	6.7±0.1	0.3±0.3	0.0±0.0	0.8±0.0
15 s mean ± std. dev. [2]			82.2±1.0	10.0±0.3	3.8±0.3	2.1±0.1	0.1±0.1	1.1±0.2
30 s mean ± std. dev. [2]			82.2±1.0	10.5±0.6	4.0±0.3	1.9±0.1	0.1±0.1	1.0±0.1
2 min. mean ± std. dev. [3]			81.1	11.2	4.2	1.8	0.1	0.9
30 min. mean ± std. dev. [1]			77.8±0.1	14.3±0.1	5.6±0.1	1.2±0.1	0.1±0.1	1.1±0.1
Wet-Basis								
background mean [1]			40.5	10.9	4.0	0.5		
30 min. mean [1]			37.5	6.9	2.7	1.2		

[1] Averaged over all samples (mixing fans were turned on prior to background and 30 min. samples).

[2] Average of dome and operating deck samples.

[3] Dome sample.

[4] Melt impacted internal lights and tripped an electrical circuit which prevented mixing fans from starting prior to t = 2 min. and also prevented the 2-min. ops deck samples (16-box1 and 17-box1) from pulling.

Table 13. Gas concentrations measured in the CE-3 experiment

Time	Label	Location	Species (mole %)					
			N_2	O_2	H_2	CO_2	CO	Argon
background	1-box5	dome	73.6	18.7	6.7	0.1	0.0	1.0
	2-box1	ops deck	73.4	18.7	6.7	0.1	0.0	0.9
	3-box1	ops deck	73.4	18.7	6.6	0.1	0.0	1.0
	4-box4	basement	73.4	18.7	6.6	0.1	0.0	0.9
15 s	5-box5[4]	dome	-	-	-	-	-	-
	6-box2	ops deck	89.2	6.1	0.9	2.6	0.1	1.2
	7-box2	ops deck	89.2	6.2	0.9	2.5	0.1	1.1
	8-box4	basement	77.2	16.1	5.1	0.6	0.1	1.0
	9-box2	refuel canal	77.7	13.2	7.0	1.1	0.2	1.0
30 s	10-box5[4]	dome	-	-	-	-	-	-
	11-box3	ops deck	88.3	6.4	1.3	2.6	0.1	1.1
	12-box3	ops deck	87.5	6.3	1.5	2.5	0.1	1.1
	13-box4	basement	78.2	16.4	3.7	0.6	0.0	1.0
	14-box2	refuel canal	80.5	12.1	5.0	1.3	0.1	1.0
2 min.	15-box5	dome	80.8	12.6	4.3	1.2	0.1	1.1
	16-box1[4]	ops deck	-	-	-	-	-	-
	17-box1	ops deck	80.9	12.4	4.3	1.3	0.2	1.1
	18-box4	basement	79.5	13.8	4.4	1.0	0.1	1.0
30 min.	19-box3	ops deck	80.1	13.0	4.5	1.1	0.1	1.1
	20-box3	ops deck	80.2	13.0	4.5	1.1	0.1	1.0
Dry-Basis								
background mean ± std. dev. [1]			73.5±0.1	18.7±0.0	6.7±0.1	0.1±0.0	0.0±0.0	1.0±0.0
15 s mean ± std. dev. [2]			89.2±0.0	6.2±0.1	0.9±0.0	2.6±0.0	0.1±0.0	1.2±0.1
30 s mean ± std. dev. [2]			87.9±0.6	6.4±0.1	1.4±0.1	2.6±0.1	0.1±0.0	1.1±0.0
2 min. mean ± std. dev. [3]			80.4±0.8	12.9±0.8	4.3±0.1	1.2±0.2	0.1±0.1	1.1±0.1
30 min. mean ± std. dev. [1]			80.2±0.1	13.0±0.0	4.5±0.0	1.1±0.0	0.1±0.0	1.1±0.1
Wet-Basis								
background mean [1]			41.1	11.0	3.8	0.5		
30 min. mean [1]			41.0	6.6	2.3	1.2		

[1] Averaged over all samples.

[2] Average of dome and operating deck samples.

[3] Average of all samples (mixing fans were turned on at 1 min.)

[4] Samples 5-box5 and 10-box5 did not pull, sample 16-box1 leaked.

Table 15. Results from the CES and CE DCH experiments

		CES-1	CES-2	CES-3	CE-1		CE-2		CE-3		CE-4	
Initial vessel pressure (MPa)		0.2024	0.2027	0.2021	0.2103		0.2195		0.2360		0.2353	
Initial vessel temperature (K)		298	316	305	378		376		384		380	
~6 s after thermite ignition												
ΔP (MPa)		0.015	0.014	0.014	0.059		0.121		0.137		0.125	
Dome gas temperature increase (K)		16	15	15	129		224		257		257	
Subcompartment gas temperature increase (K)		0	1	1	8		13		16		12	
Vessel average gas temperature increase (K)		9	7	8	67		109		122		120	
Mass thermite transported to dome (kg)		16.92	20.38	21.73	21.37		19.60		15.3		14.1	
Thermite transport fraction (to dome)		0.69	0.61	0.65	0.65		0.59		0.46		0.42	
Vessel pressure prior to HPME (MPa)		0.2158	0.2156	0.2157	0.2558		0.2619		0.2999		0.2968	
Vessel temperature prior to HPME (K)		307	324	314	440		456		488		479	
~1 s after HPME												
ΔP (MPa)		0.234	0.316	0.293	0.242		0.208		0.253		0.217	
Dome gas temperature increase (K)		404	503	425	152		35		228		202	
Subcompartment gas temperature increase (K)		38	68	68	94		54		126		77	
Vessel average gas temperature increase (K)		175	221	201	121		48		169		116	
Cavity ΔP (MPa)		3.08	3.28	2.78	1.74		0.41		0.72		0.69	
Initial gas composition in the Surtsey vessel (mole %)					Dry	Wet	Dry	Wet	Dry	Wet	Dry	Wet
	Steam	0.00	0.0	0.0	0.0	41.9	0.0	41.0	0.0	43.6	0.0	44.2
	N_2	99.3	99.6	99.1	78.1	45.4	73.2	43.2	72.9	41.1	72.5	40.4
	O_2	0.2	0.4	0.2	20.9	12.2	19.6	11.6	19.6	11.0	19.4	10.9
	H_2	0.3	0.1	0.4	0.0	0.0	6.2	3.7	6.7	3.8	7.2	4.0
Posttest gas composition in the Surtsey vessel (mole %)					Dry	Wet	Dry	Wet	Dry	Wet	Dry	Wet
	Steam	0.0	0.0	0.0	0.0	49.3	0.0	47.2	0.0	48.9	0.0	51.2
	N_2	96.3	96.4	95.9	77.9	39.5	76.2	40.3	80.2	41.0	77.8	37.5
	O_2	0.1	0.3	0.0	17.2	8.7	15.4	8.1	13.0	6.6	14.3	6.9
	H_2	2.3	3.7	3.7	3.1	1.6	5.9	3.1	4.5	2.3	5.6	2.7
Moles of preexisting combustible gas (g·moles)		0	0	0	0		129		139		149	
Moles of combustible gas produced (g·moles)		75	141	145	203		191		269		215	
Moles of combustible gas burned (g·moles)		0	0	0	144		202		323		256	
Net difference between production and combustion		0	0	0	60		-12		-54		-41	
Fraction of available combustible gas that burned ($N_{burn}/(N_{pre}+N_{prod})$)		0	0	0	0.71		0.63		0.79		0.70	

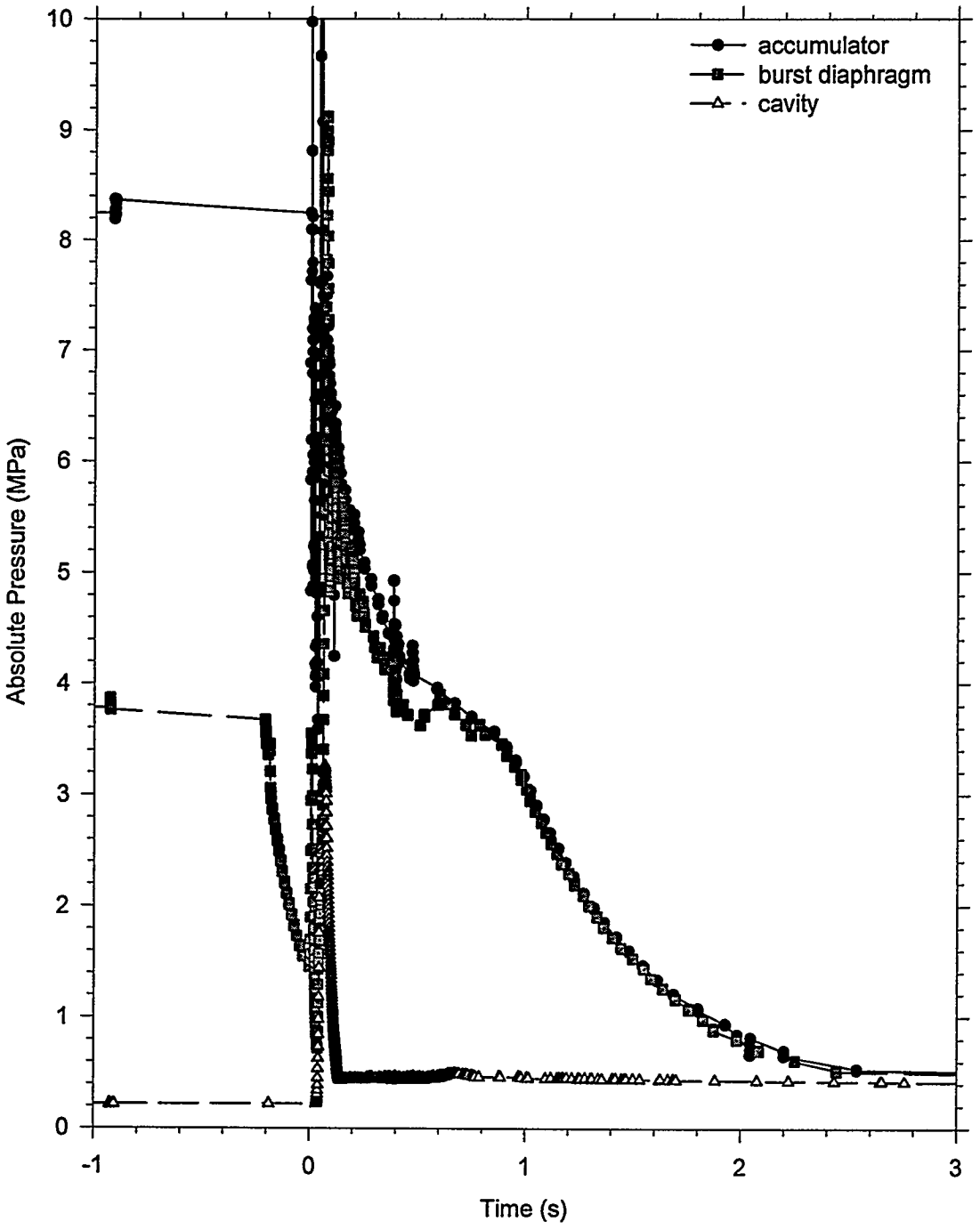

Figure 8. Blowdown history of the CES-1 experiment.

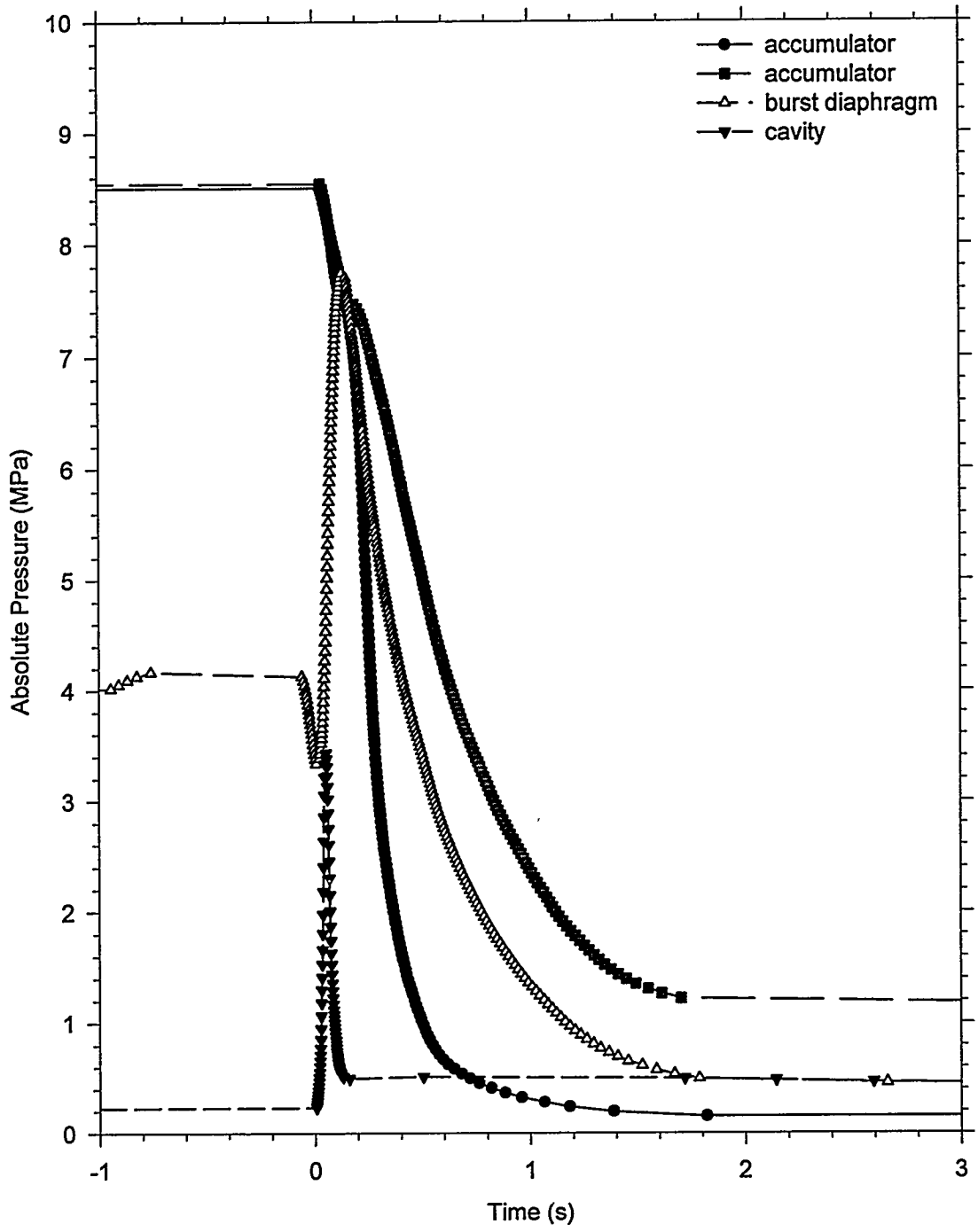

Figure 9. Blowdown history of the CES-2 experiment.

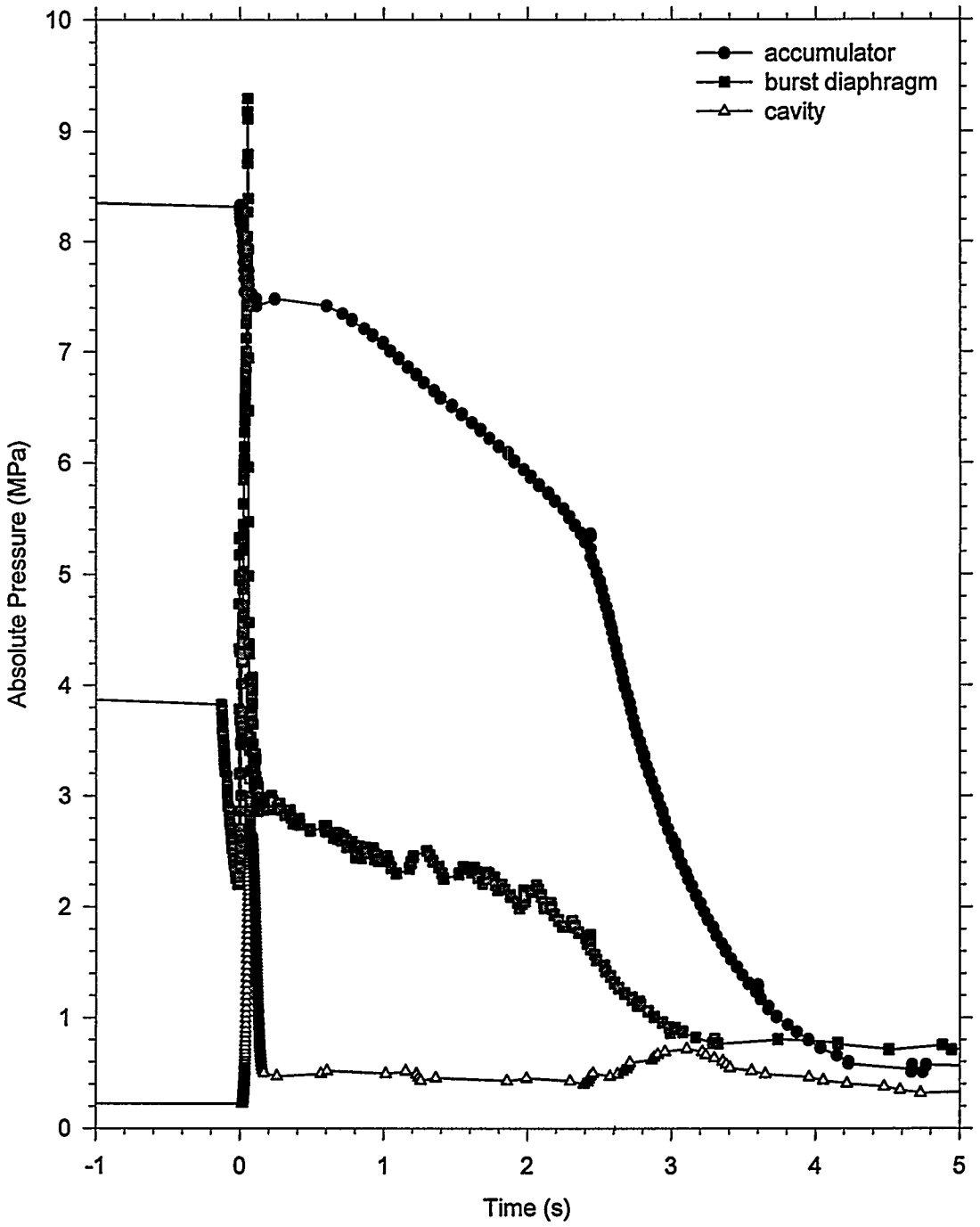

Figure 10. Blowdown history of the CES-3 experiment.

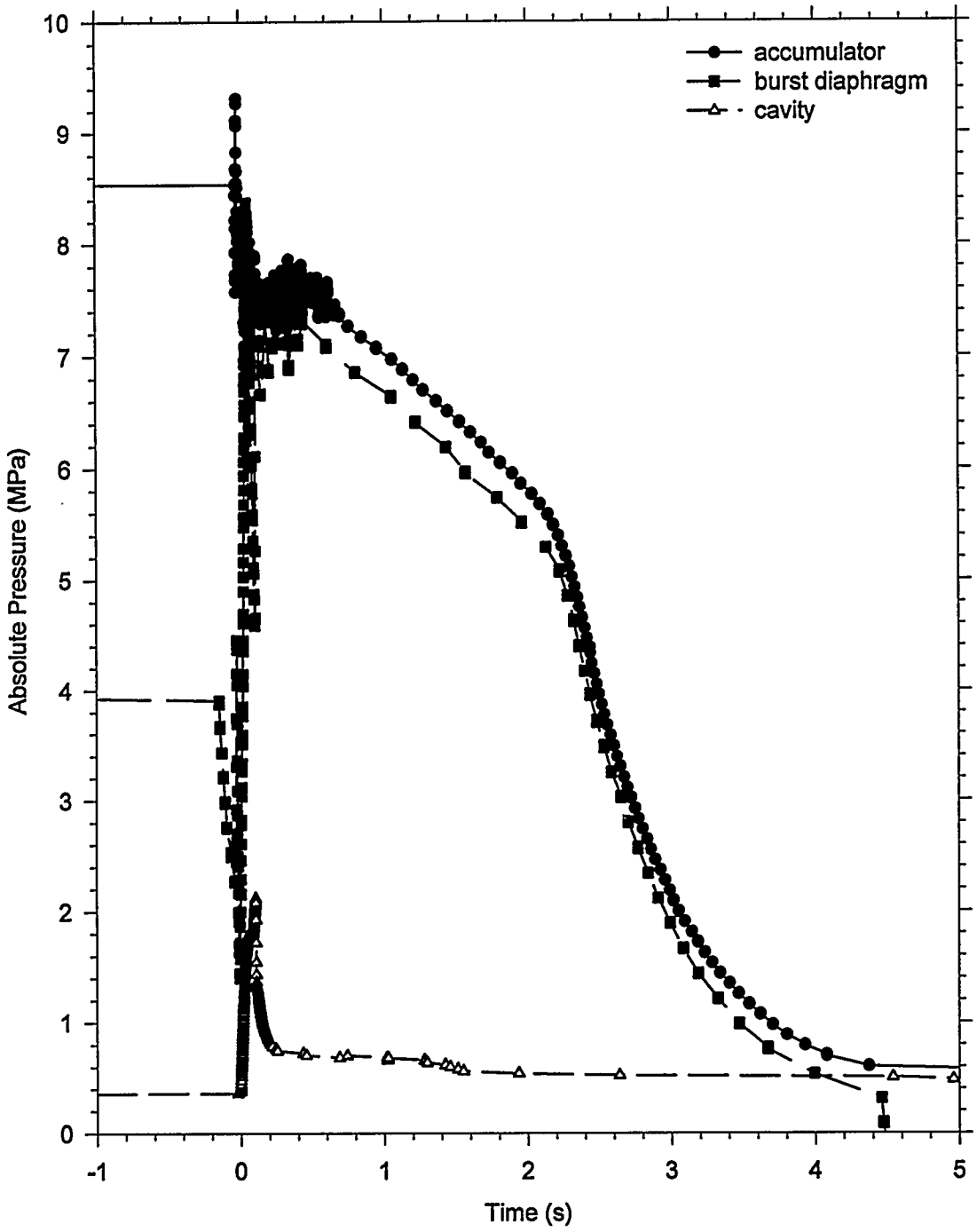

Figure 11. Blowdown history of the CE-1 experiment.

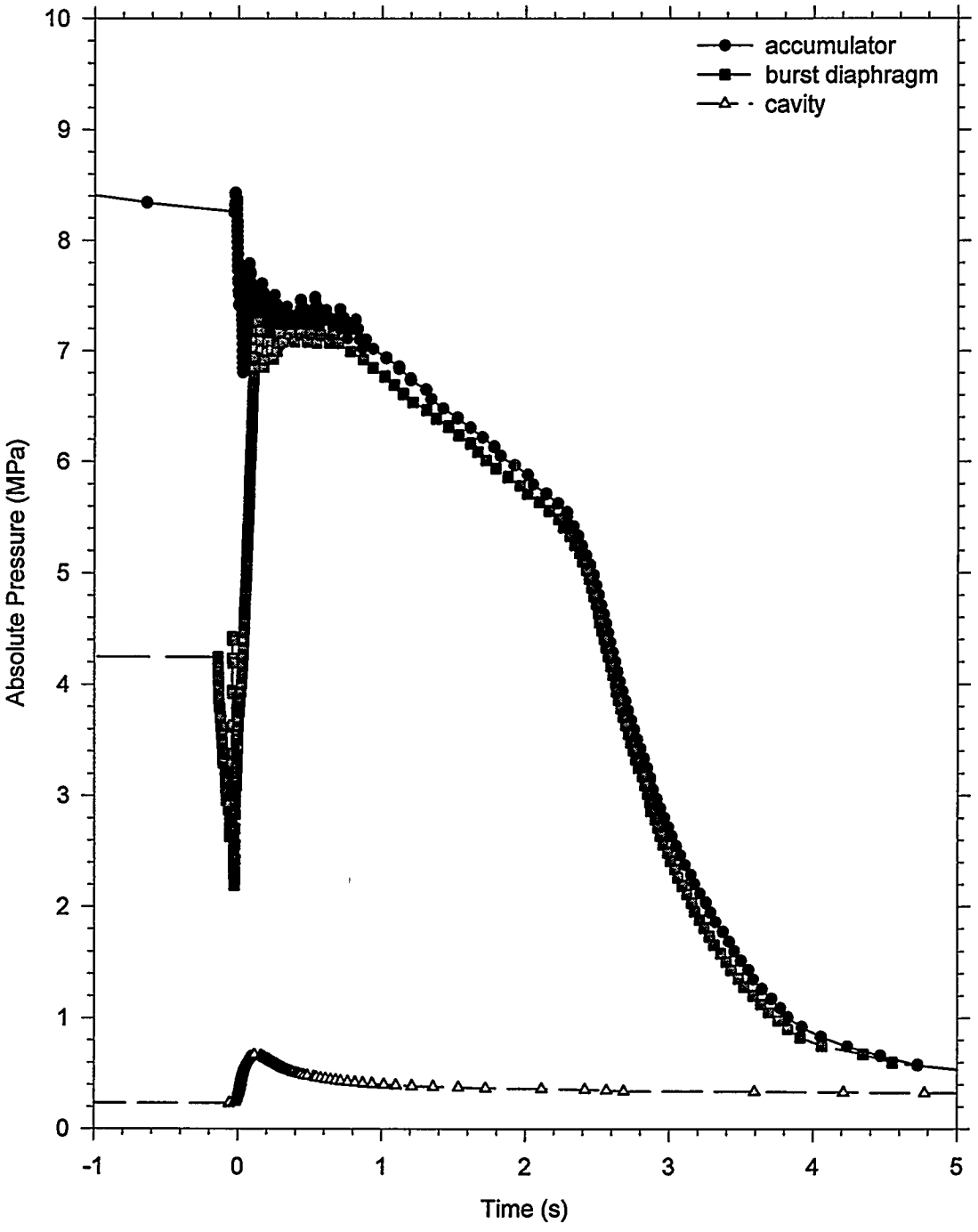

Figure 12. Blowdown history of the CE-2 experiment.

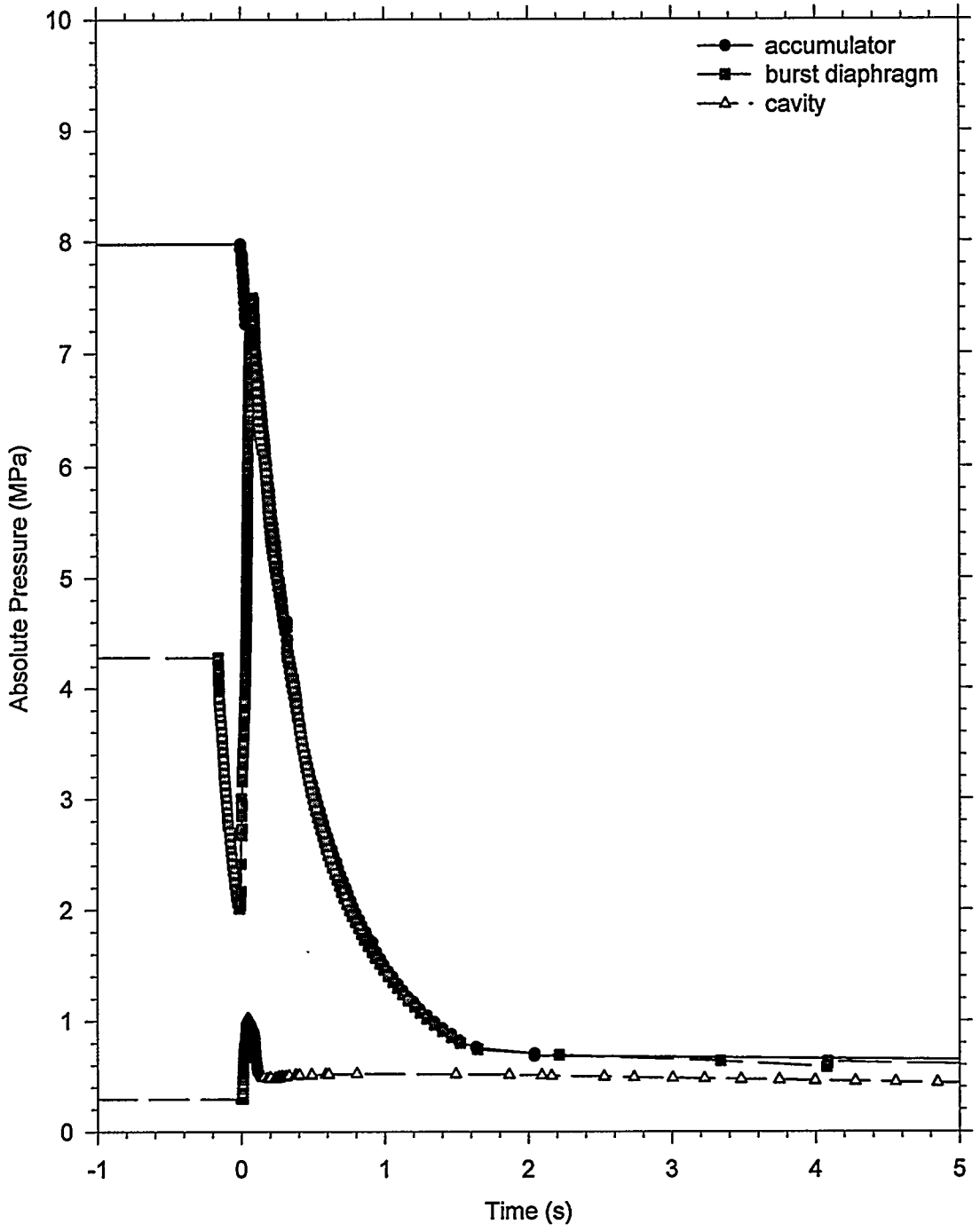

Figure 13. Blowdown history of the CE-3 experiment.

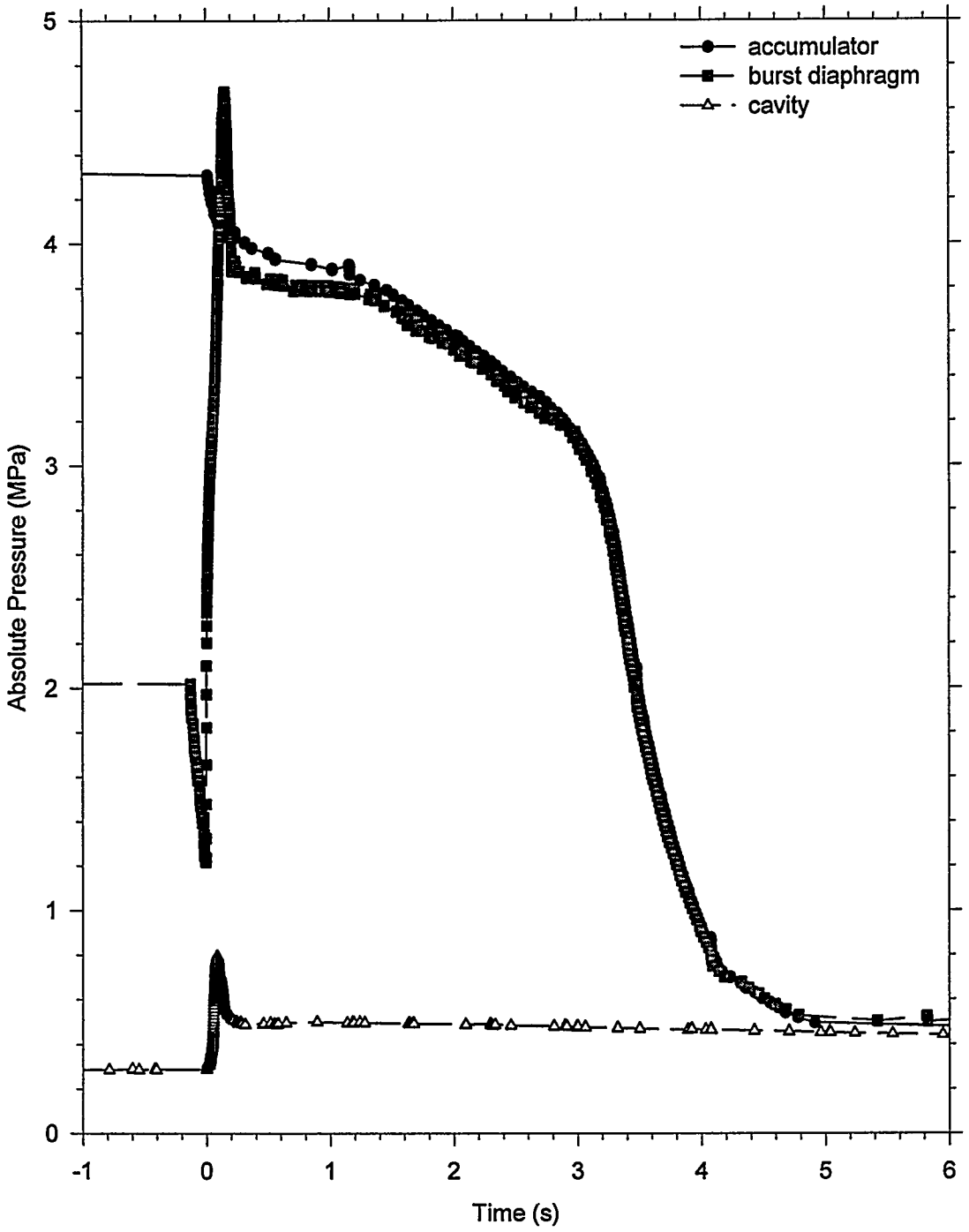

Figure 14. Blowdown history of the CE-4 experiment.

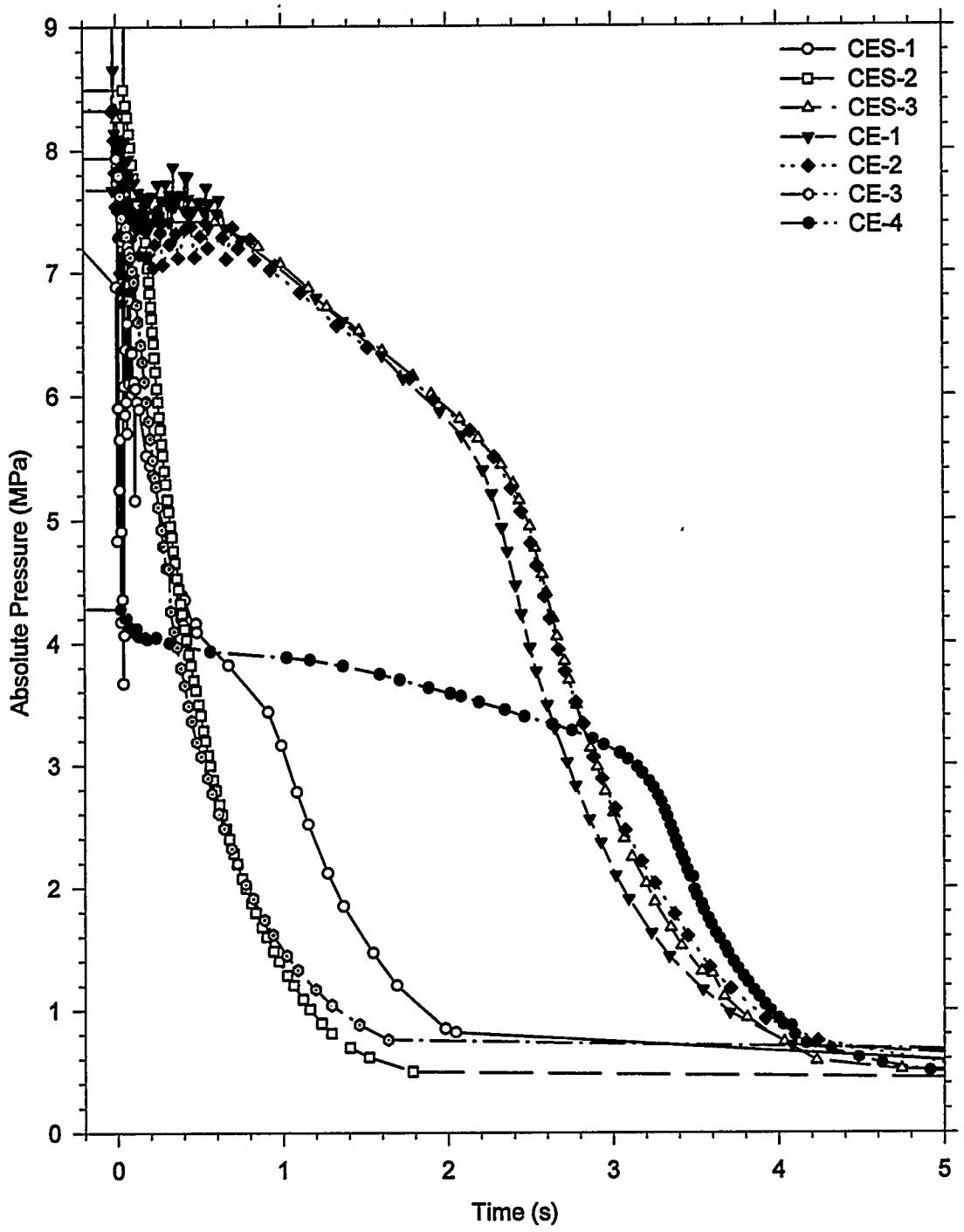

Figure 15. Accumulator pressure in the CE DCH experiments.

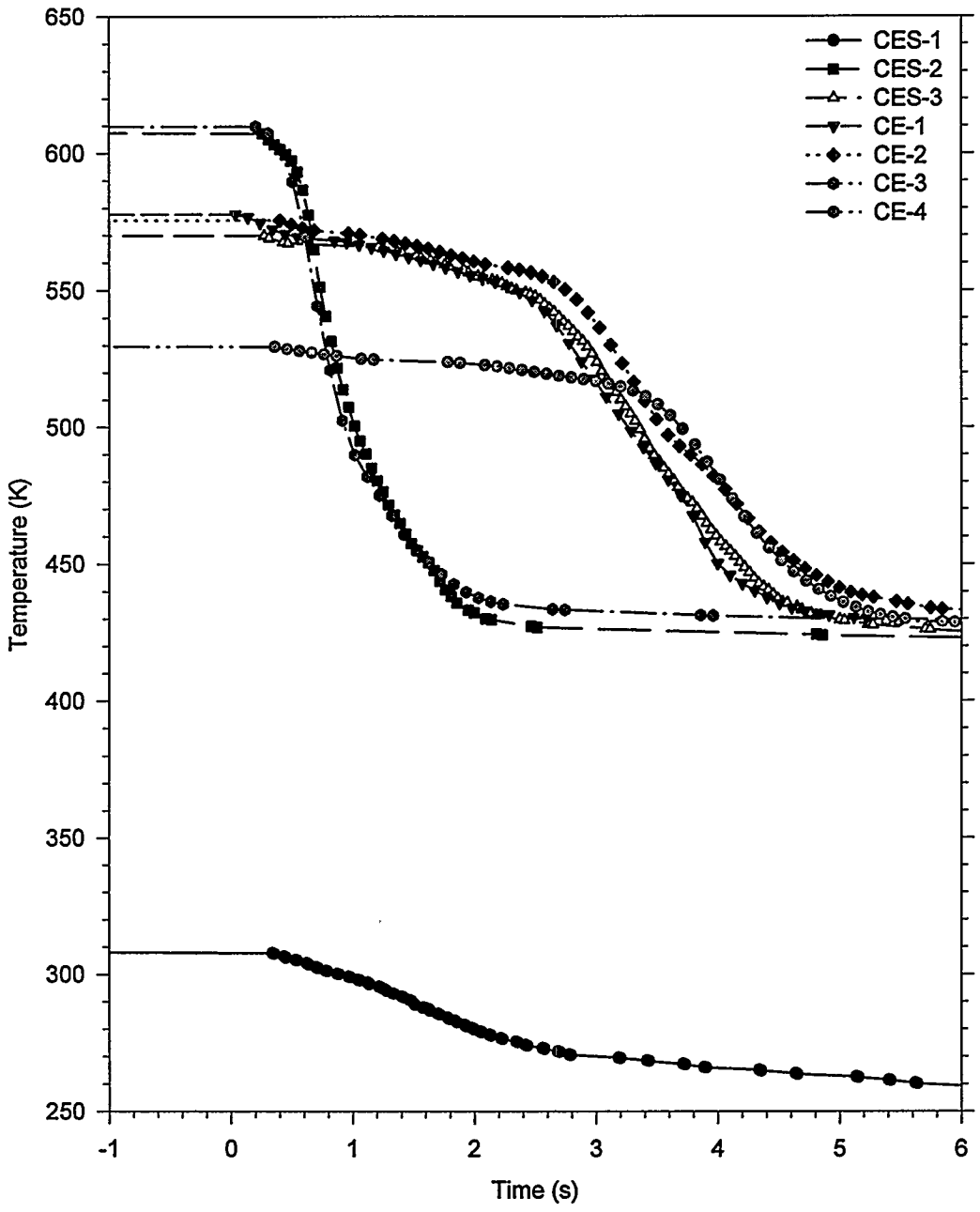

Figure 16. Accumulator gas temperatures in the CE DCH experiments.

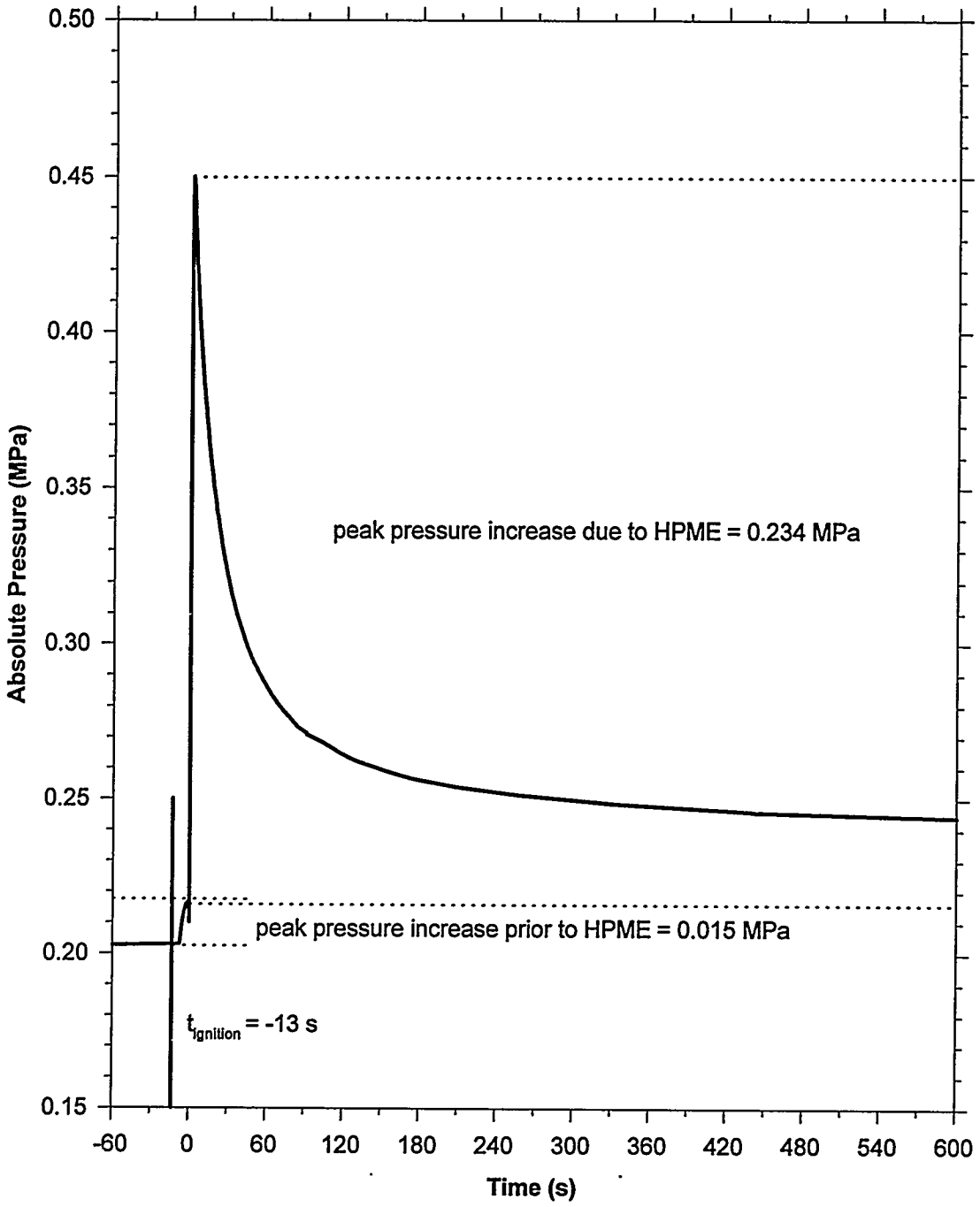

Figure 17. Vessel pressure in the CES-1 experiment from -60 to 600 s.

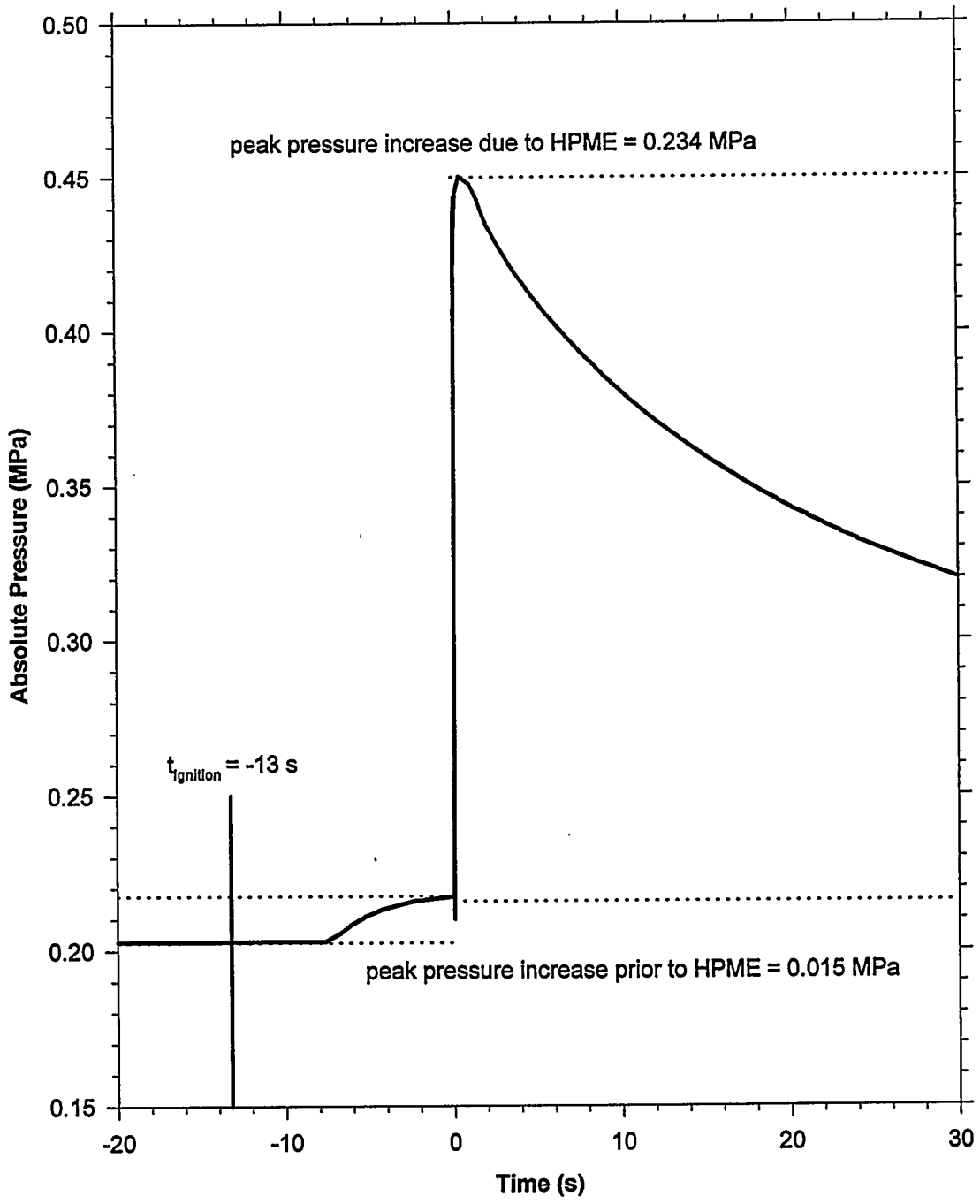

Figure 18. Vessel pressure in the CES-1 experiment from -20 to 30 s.

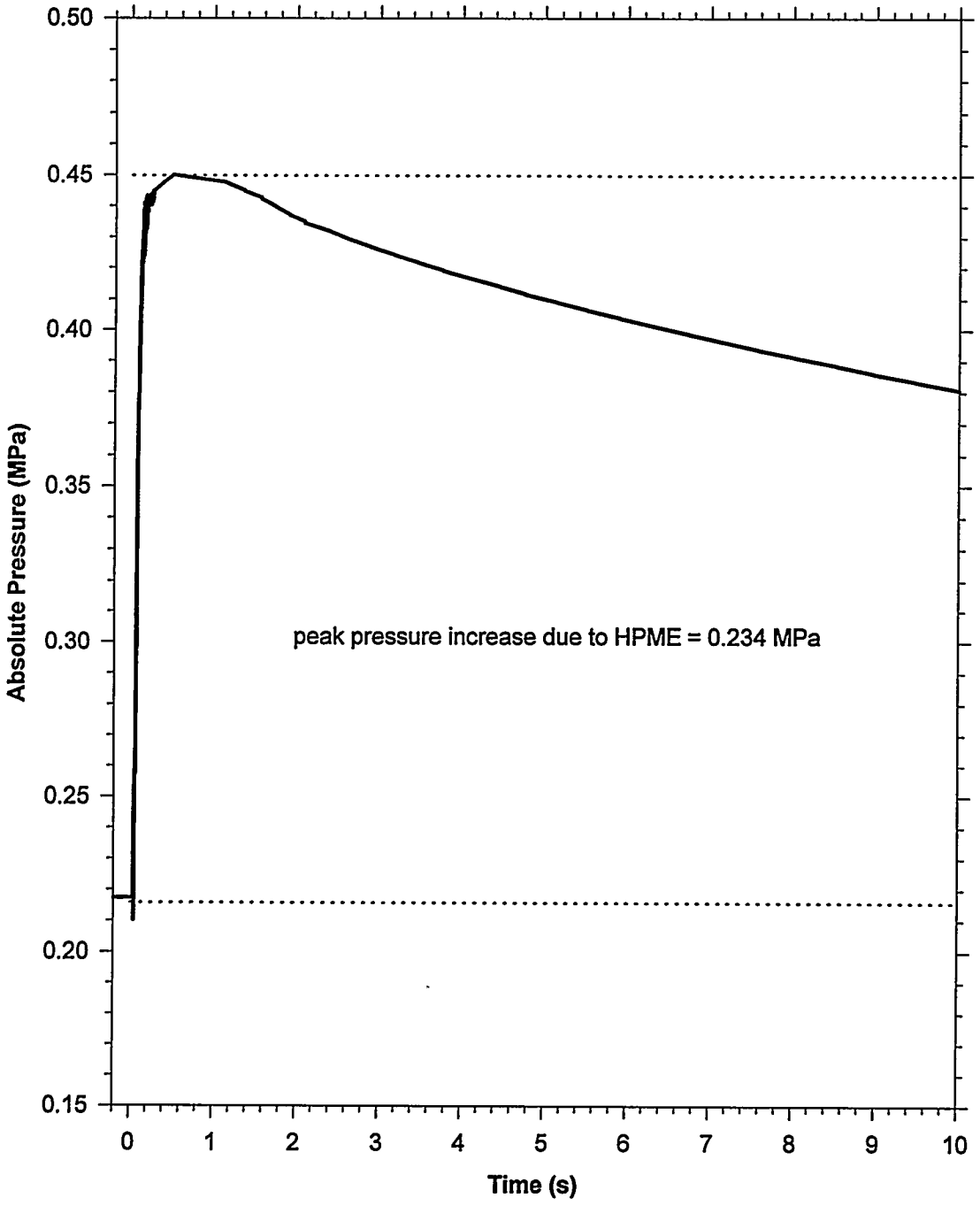

Figure 19. Vessel pressure in the CES-1 experiment from 0 to 10 s.

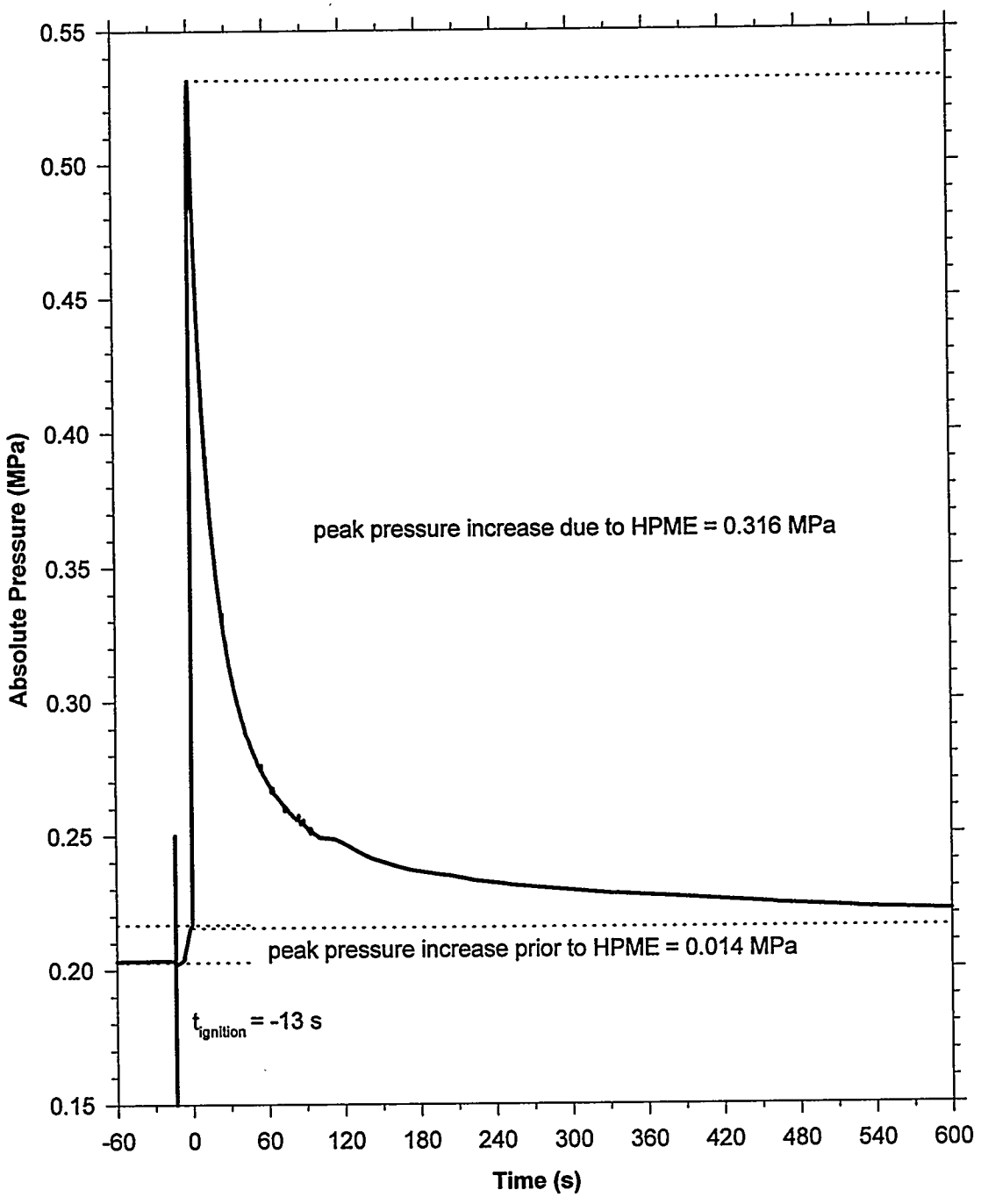

Figure 20. Vessel pressure in the CES-2 experiment from -60 to 600 s.

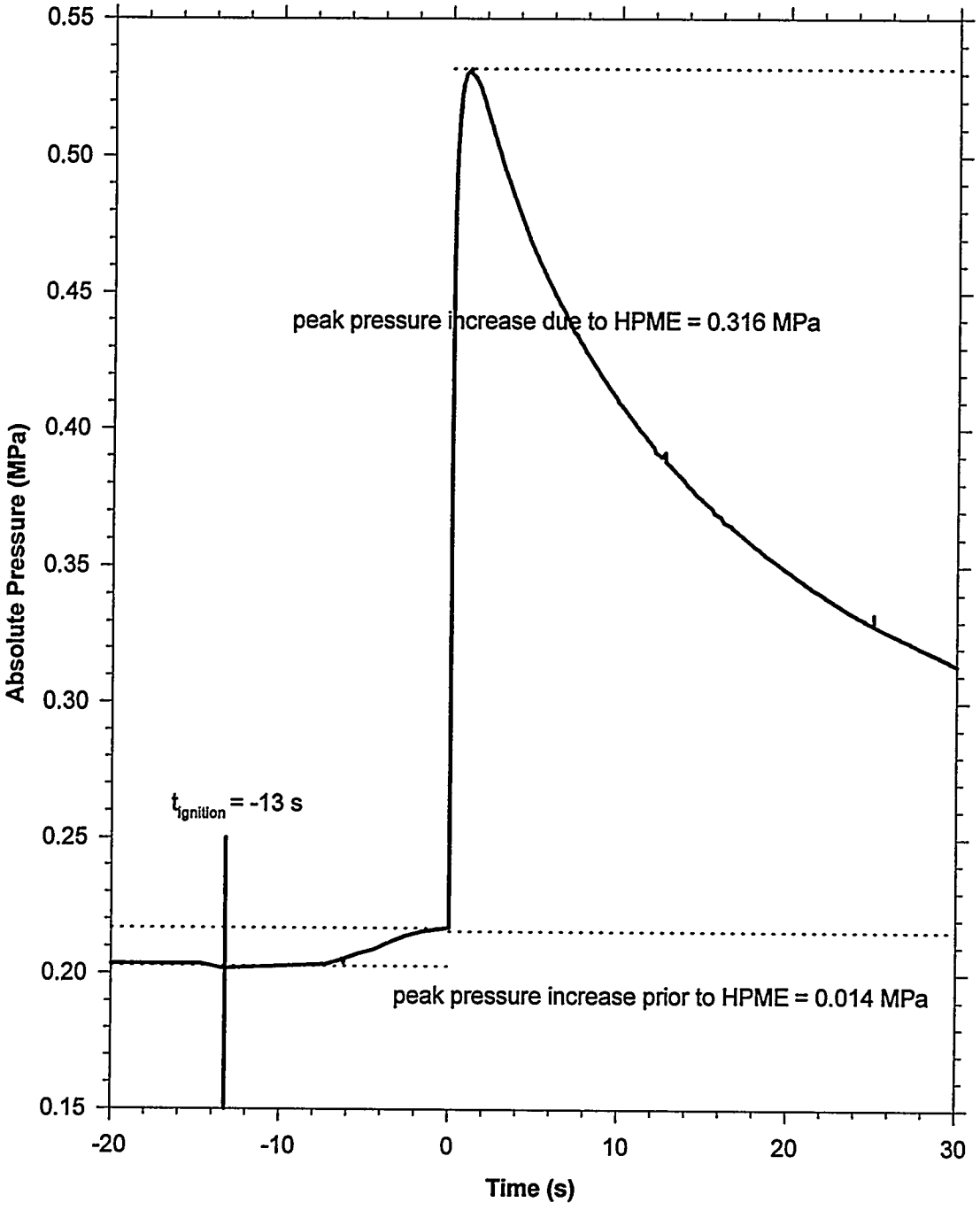

Figure 21. Vessel pressure in the CES-2 experiment from -20 to 30 s.

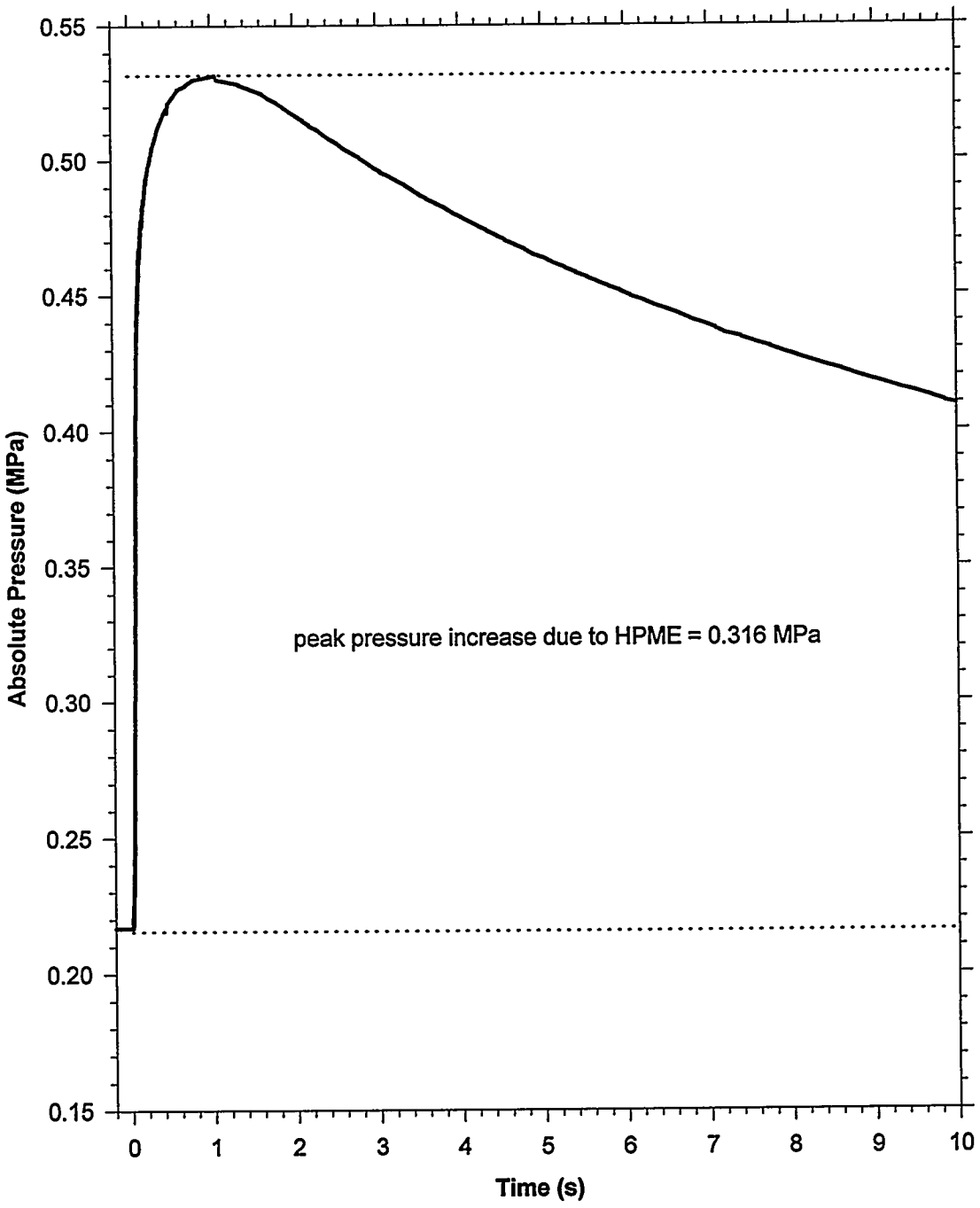

Figure 22. Vessel pressure in the CES-2 experiment from 0 to 10 s.

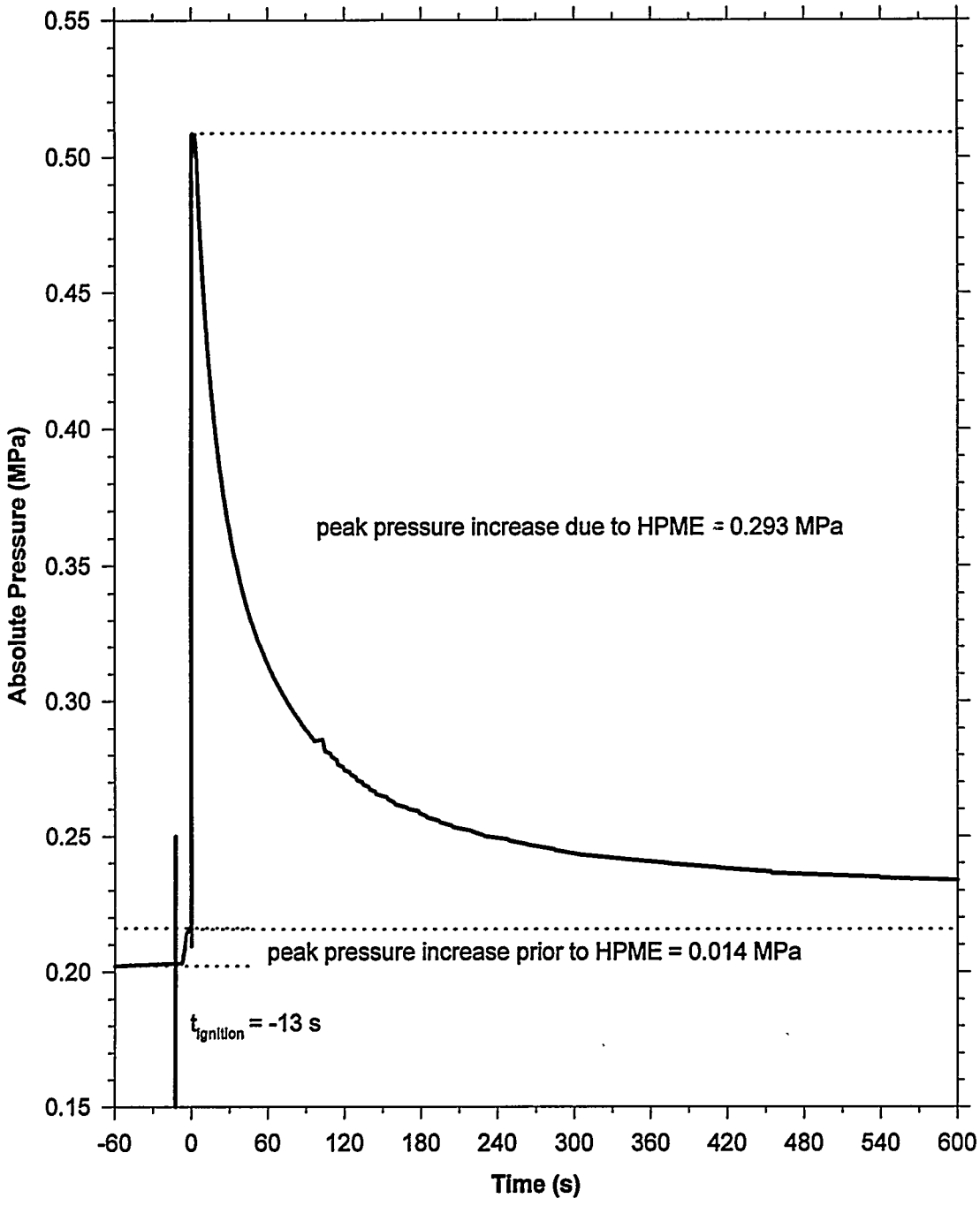

Figure 23. Vessel pressure in the CES-3 experiment from -60 to 600 s.

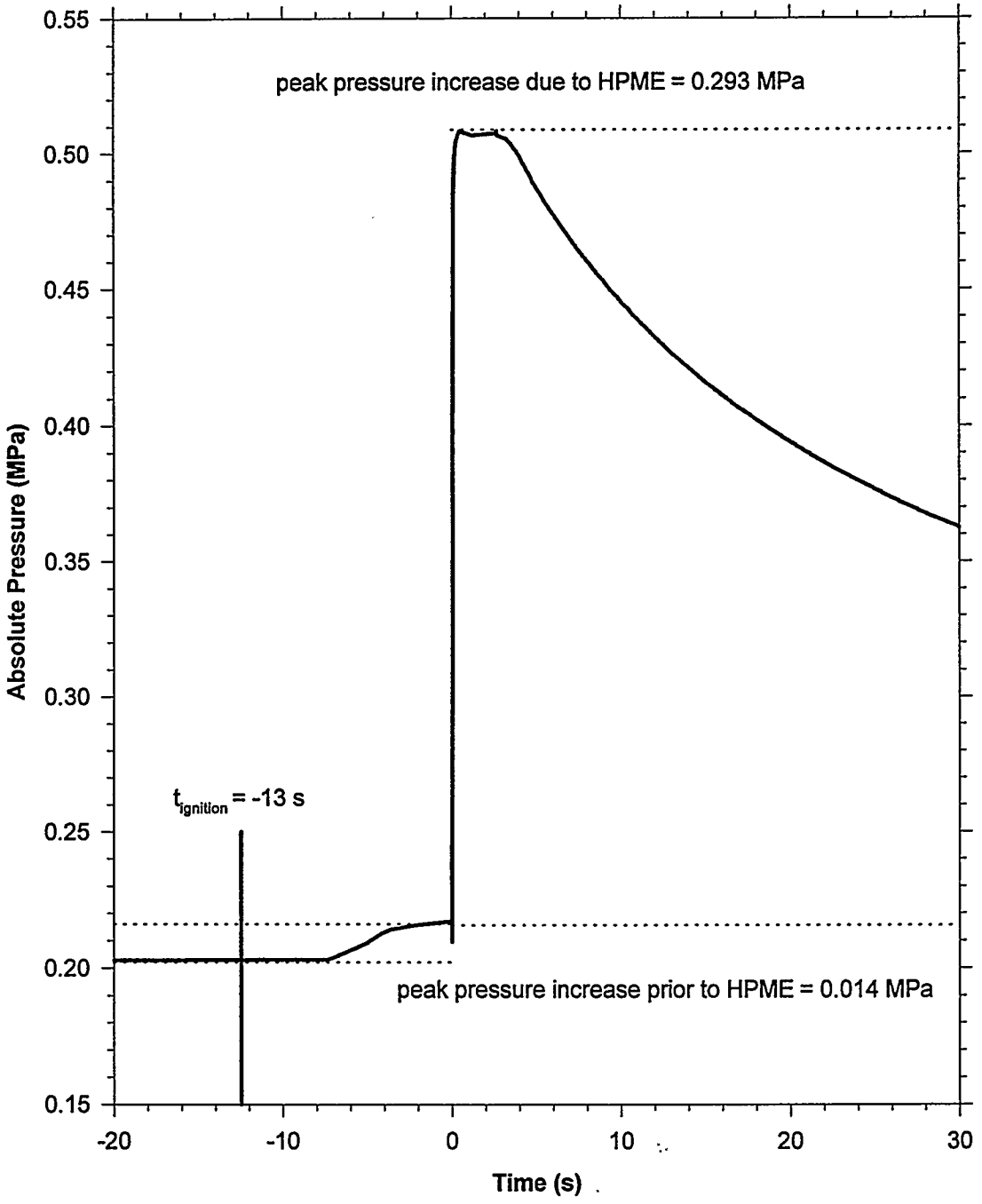

Figure 24. Vessel pressure in the CES-3 experiment from -20 to 30 s.

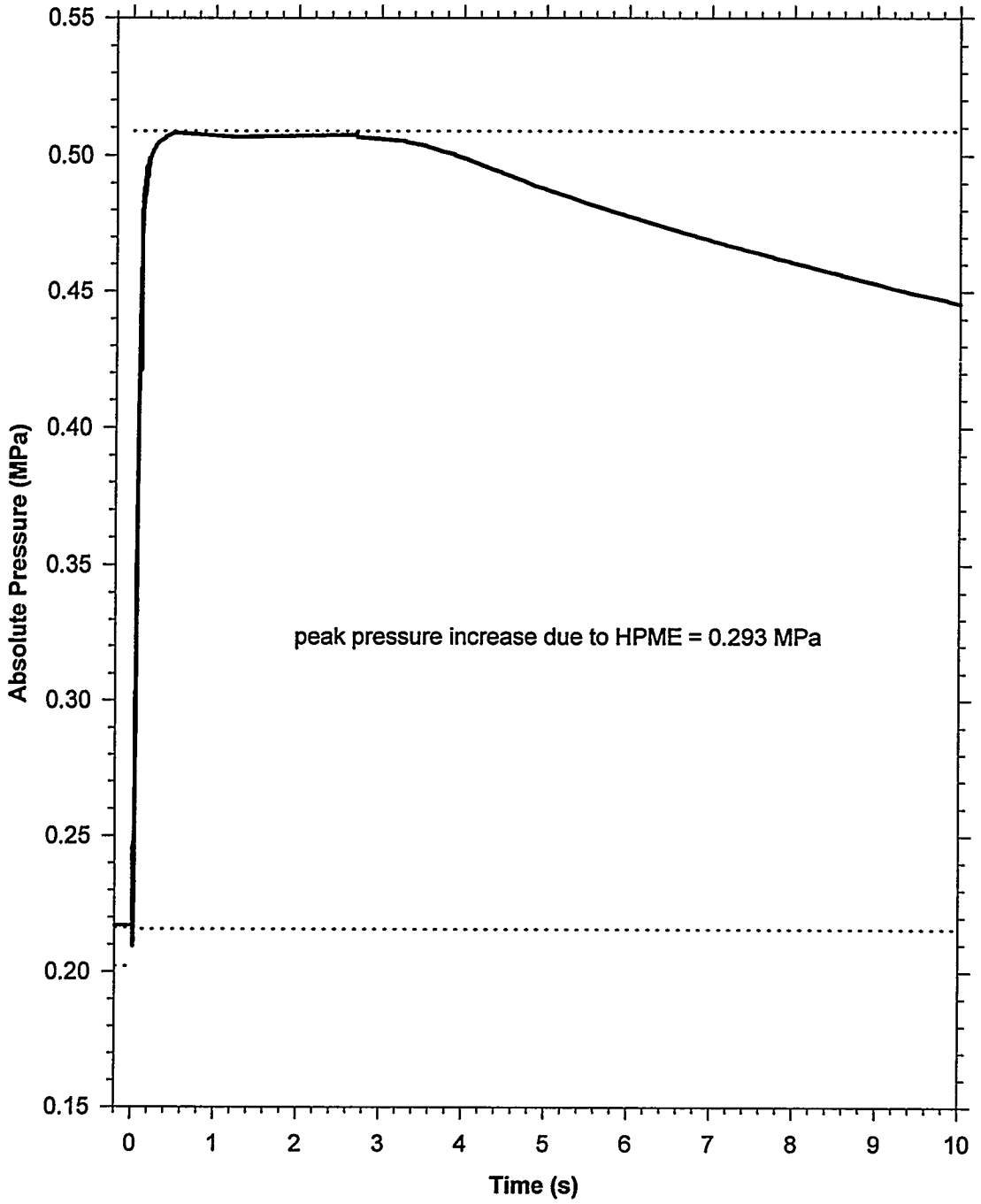

Figure 25. Vessel pressure in the CES-3 experiment from 0 to 10 s.

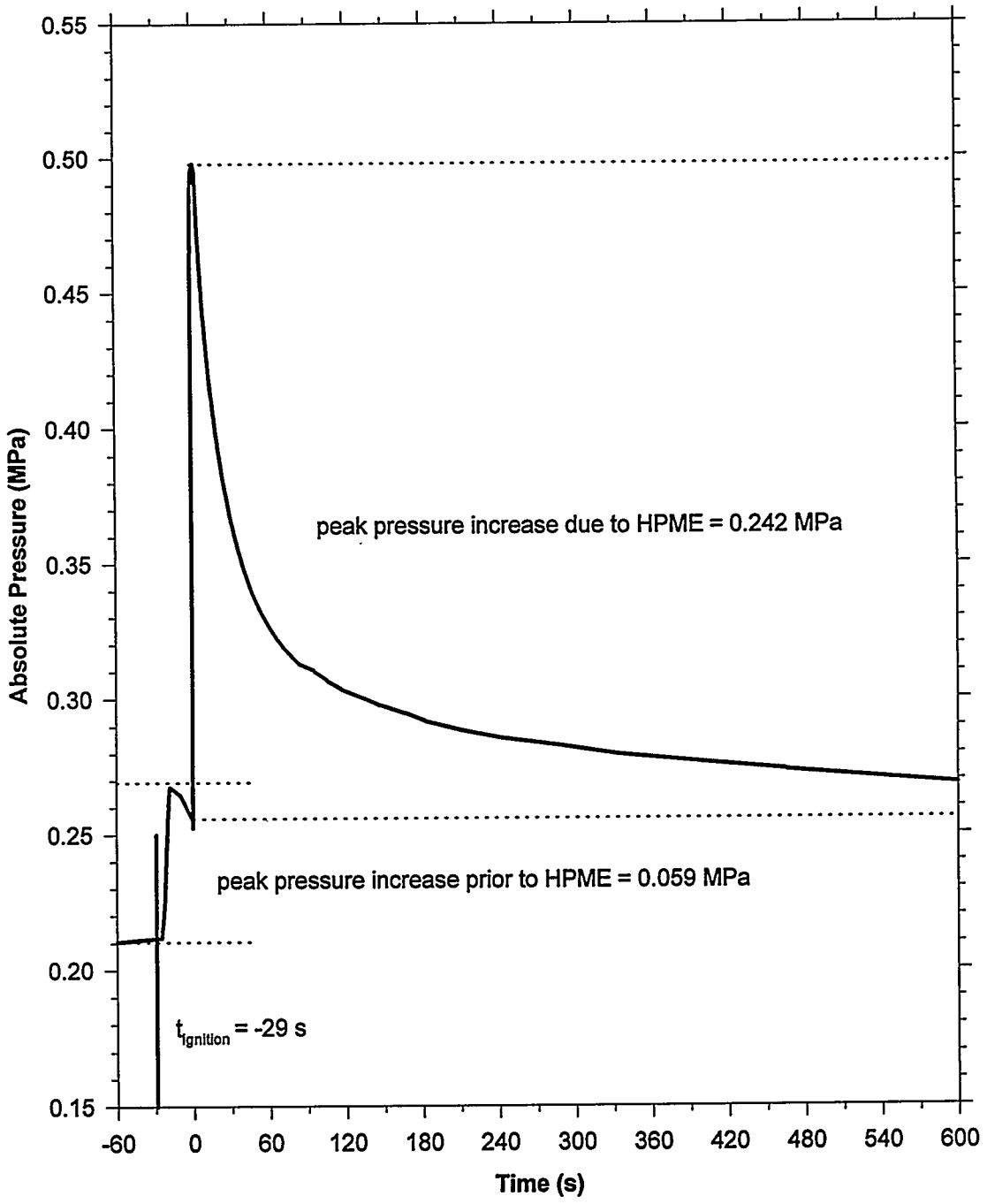

Figure 26. Vessel pressure in the CE-1 experiment from -60 to 600 s.

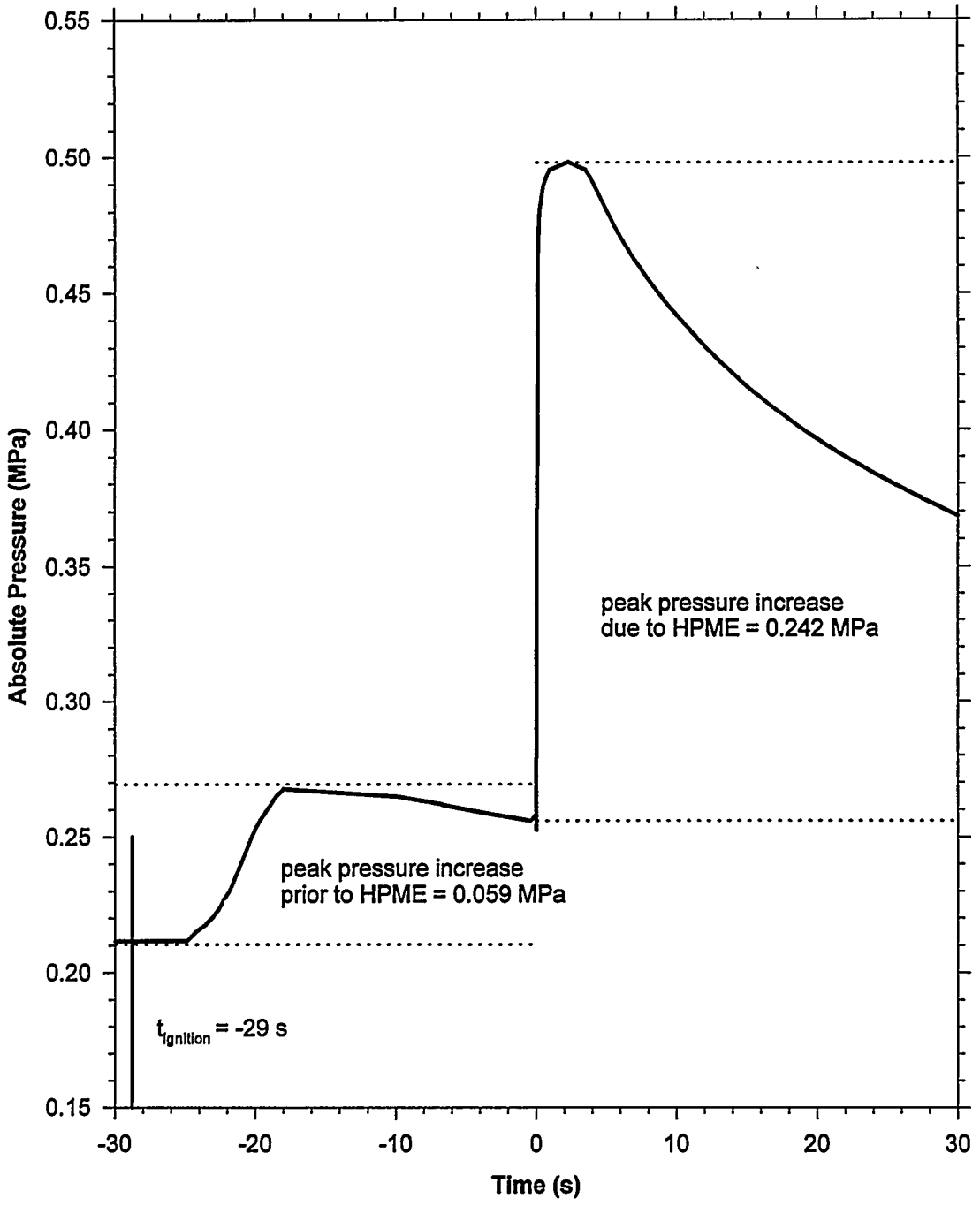

Figure 27. Vessel pressure in the CE-1 experiment from -30 to 30 s.

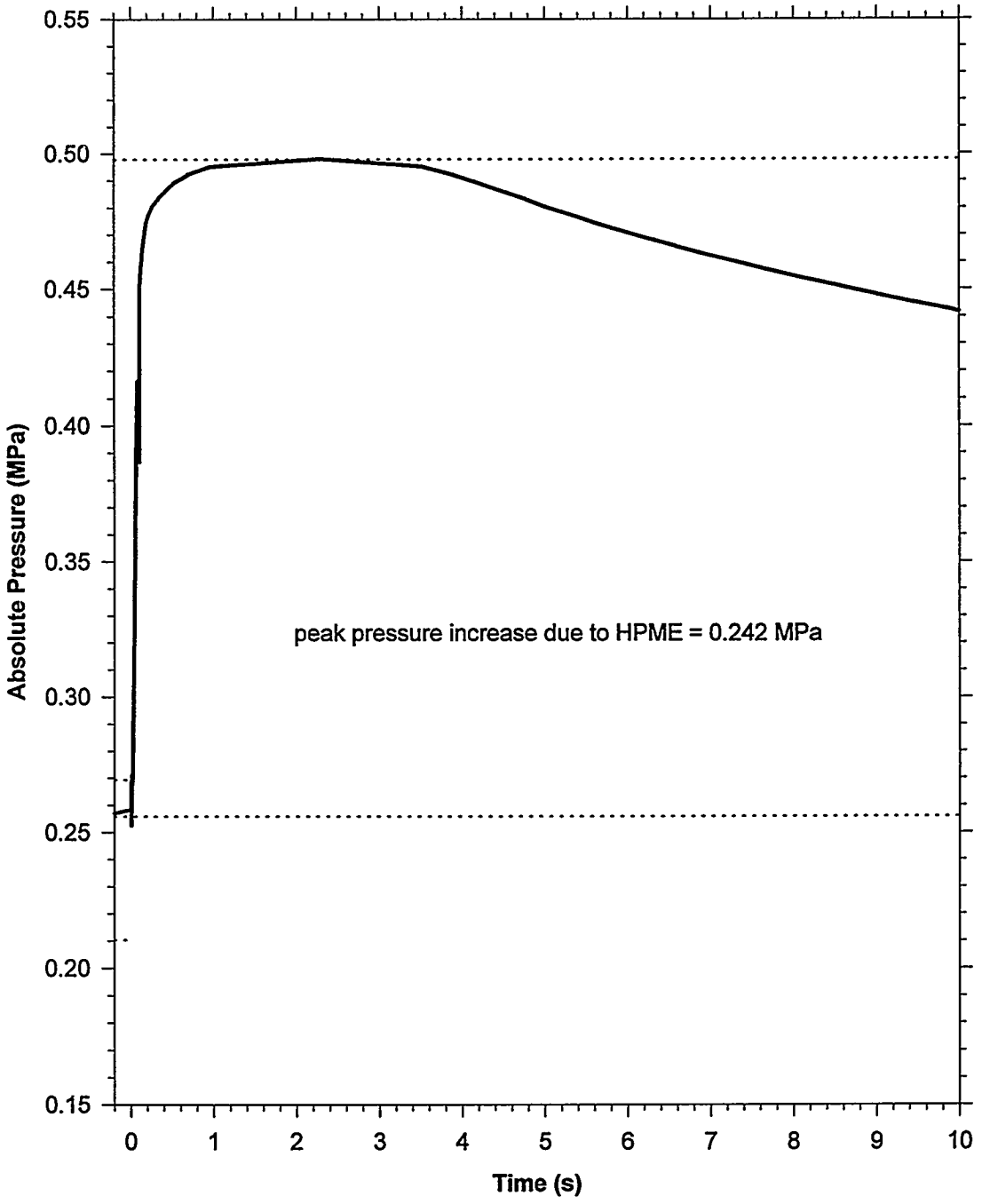

Figure 28. Vessel pressure in the CE-1 experiment from 0 to 10 s.

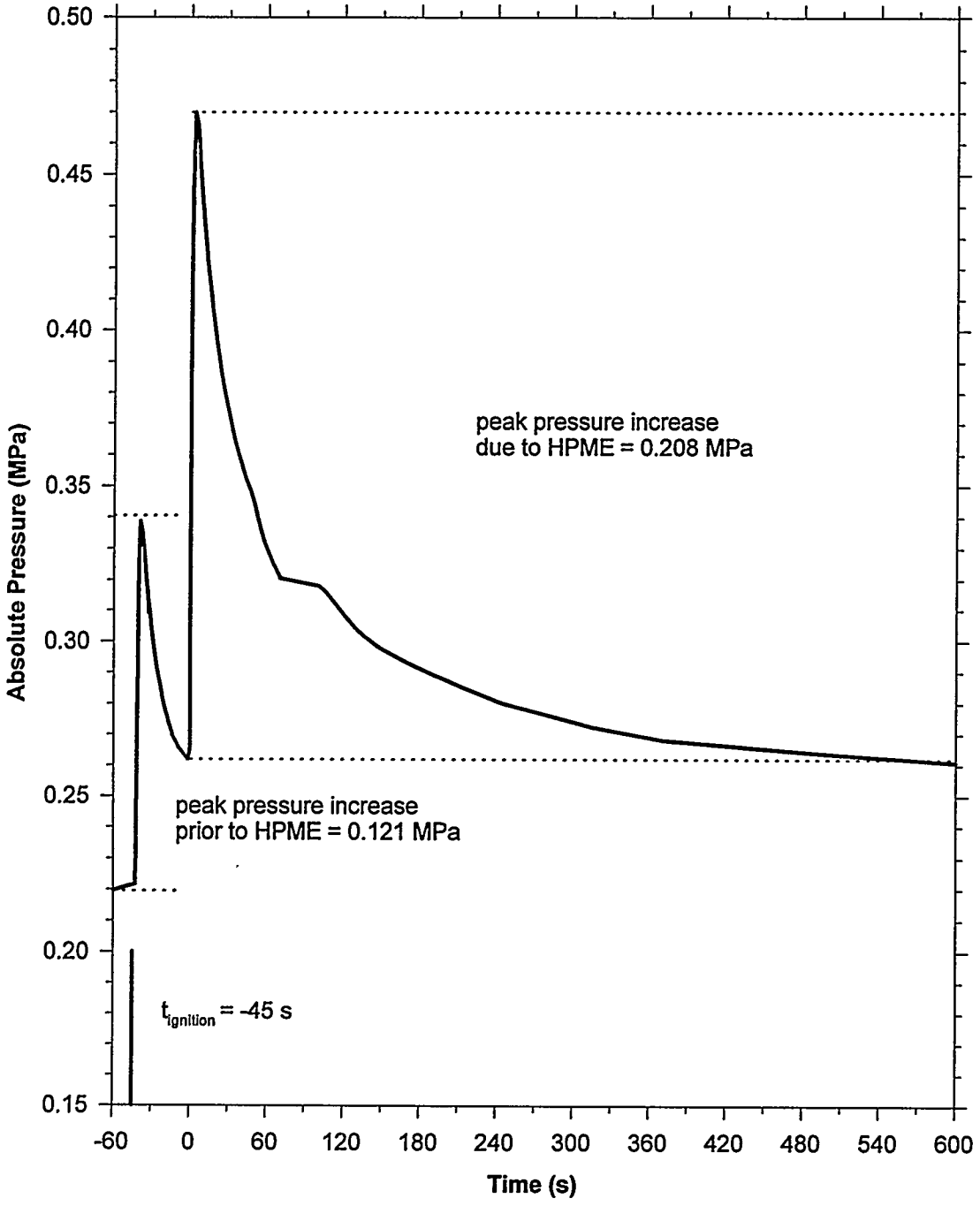

Figure 29. Vessel pressure in the CE-2 experiment from -60 to 600 s.

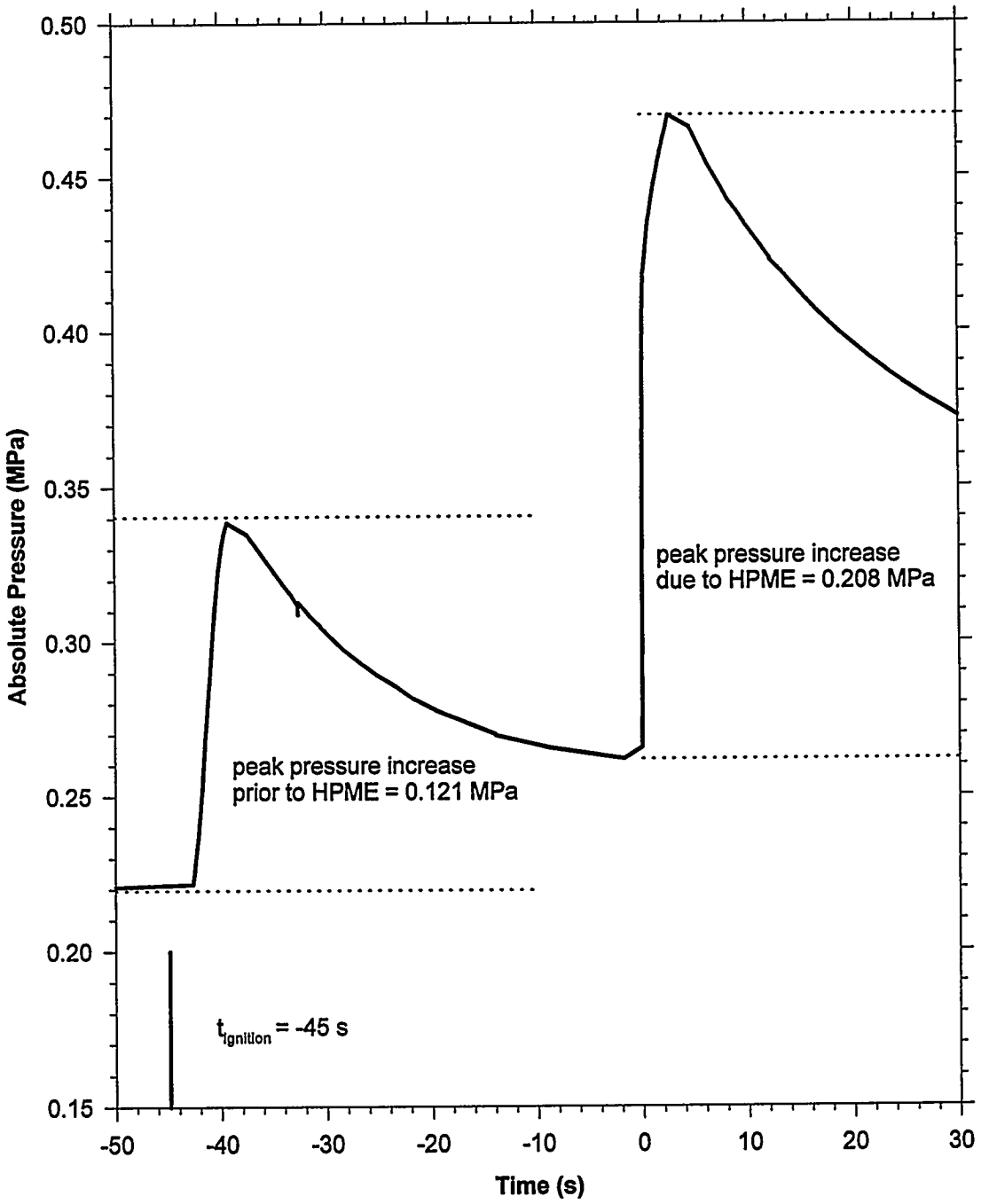

Figure 30. Vessel pressure in the CE-2 experiment from -50 to 30 s.

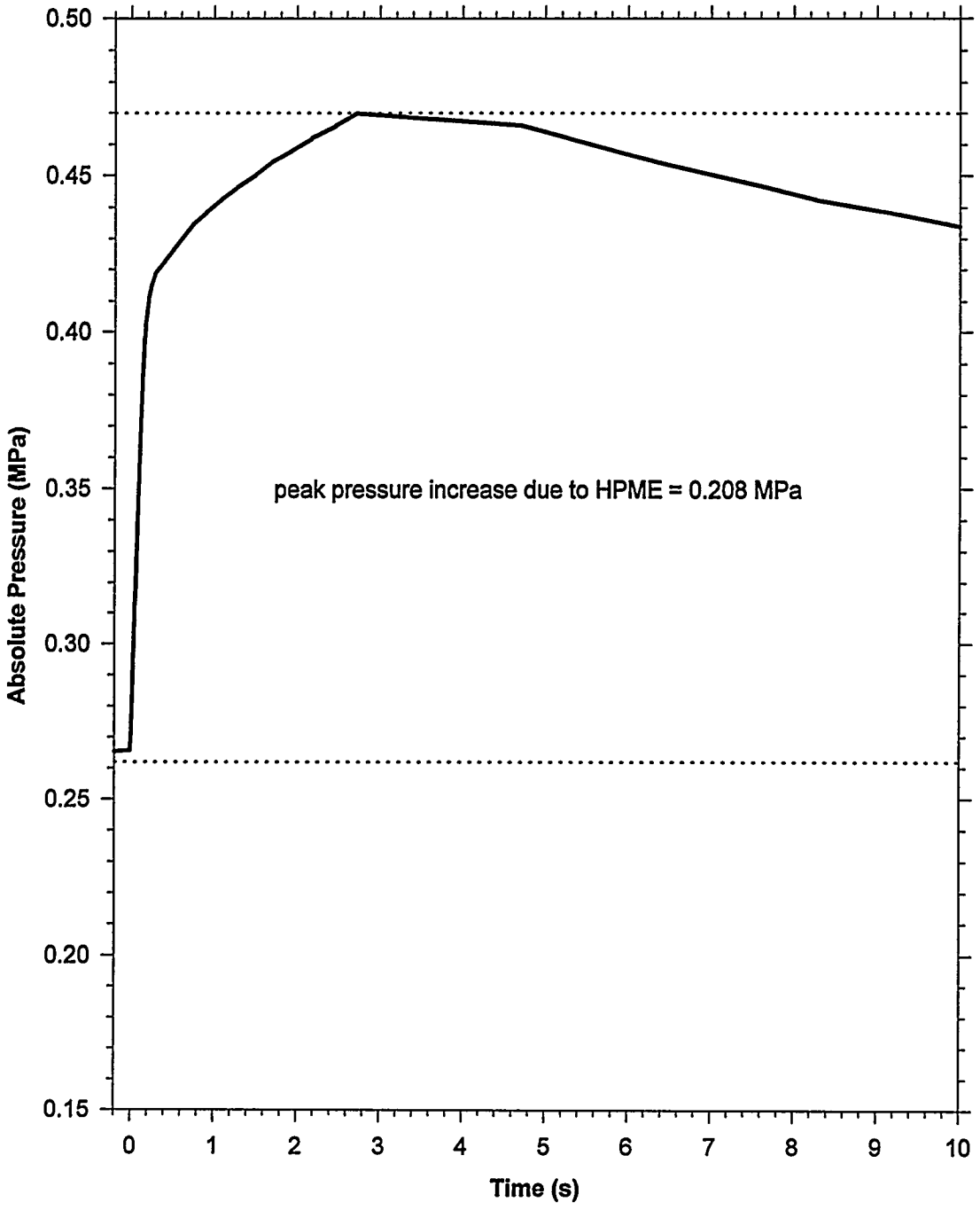

Figure 31. Vessel pressure in the CE-2 experiment from 0 to 10 s.

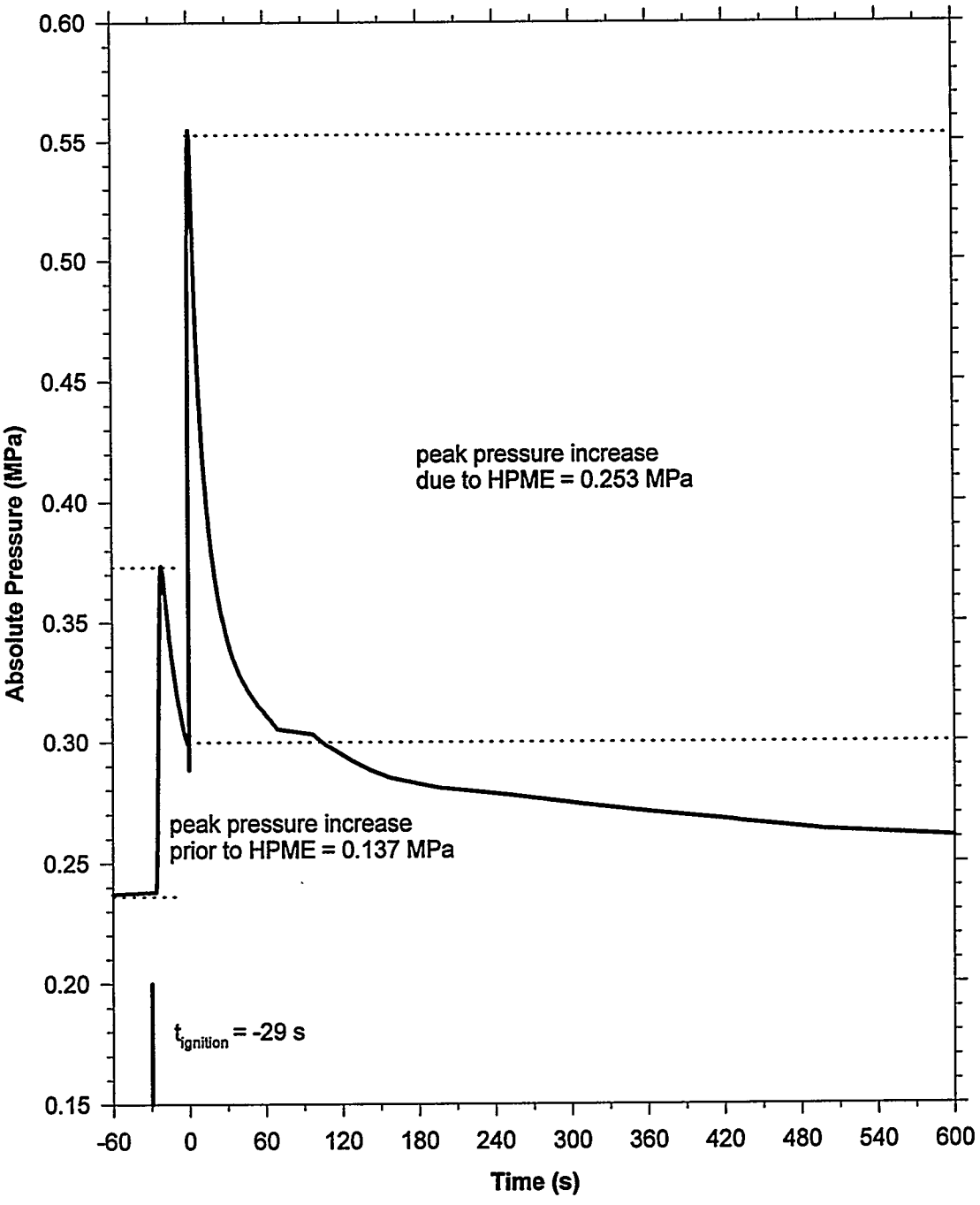

Figure 32. Vessel pressure in the CE-3 experiment from -60 to 600 s.

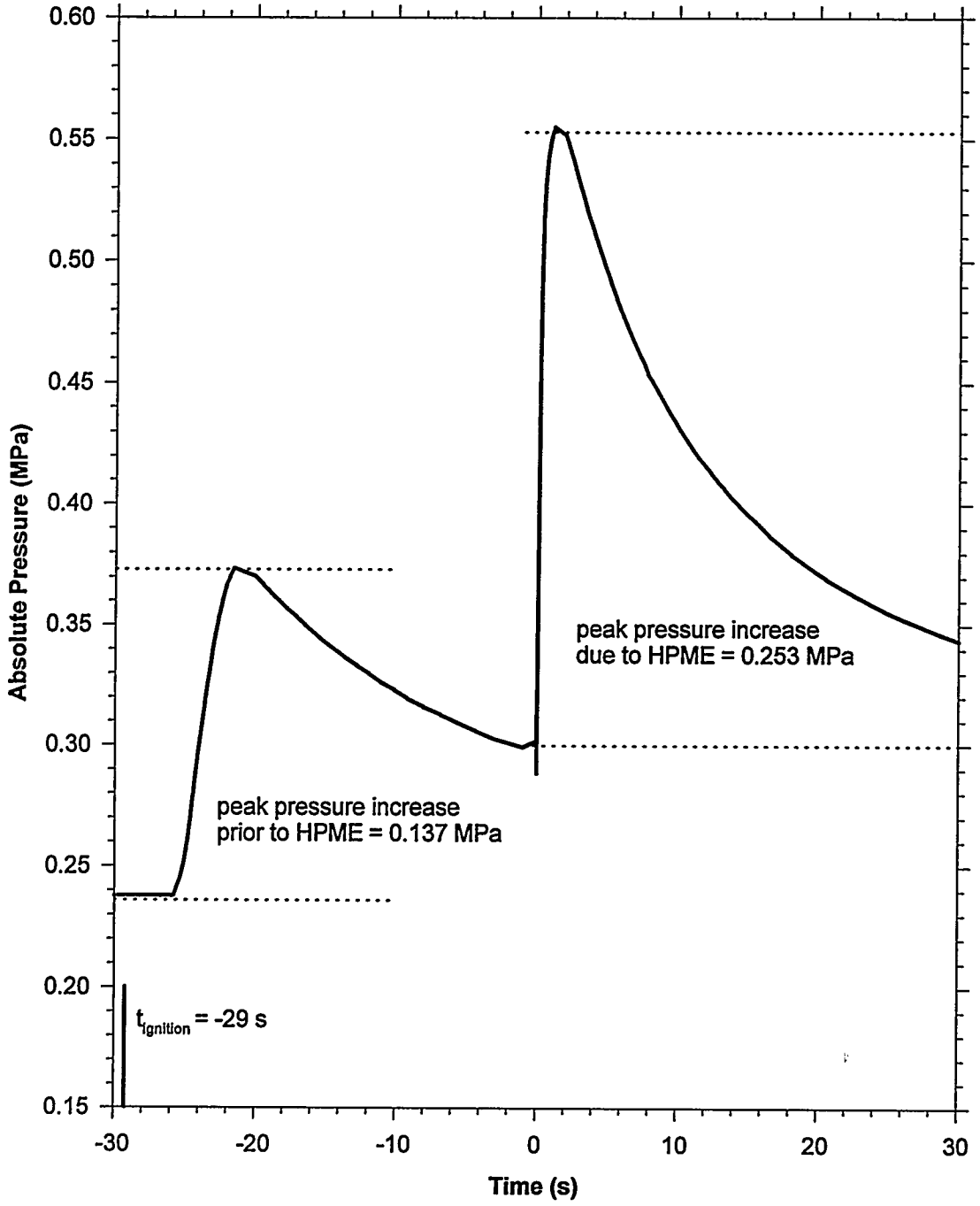

Figure 33. Vessel pressure in the CE-3 experiment from -30 to 30 s.

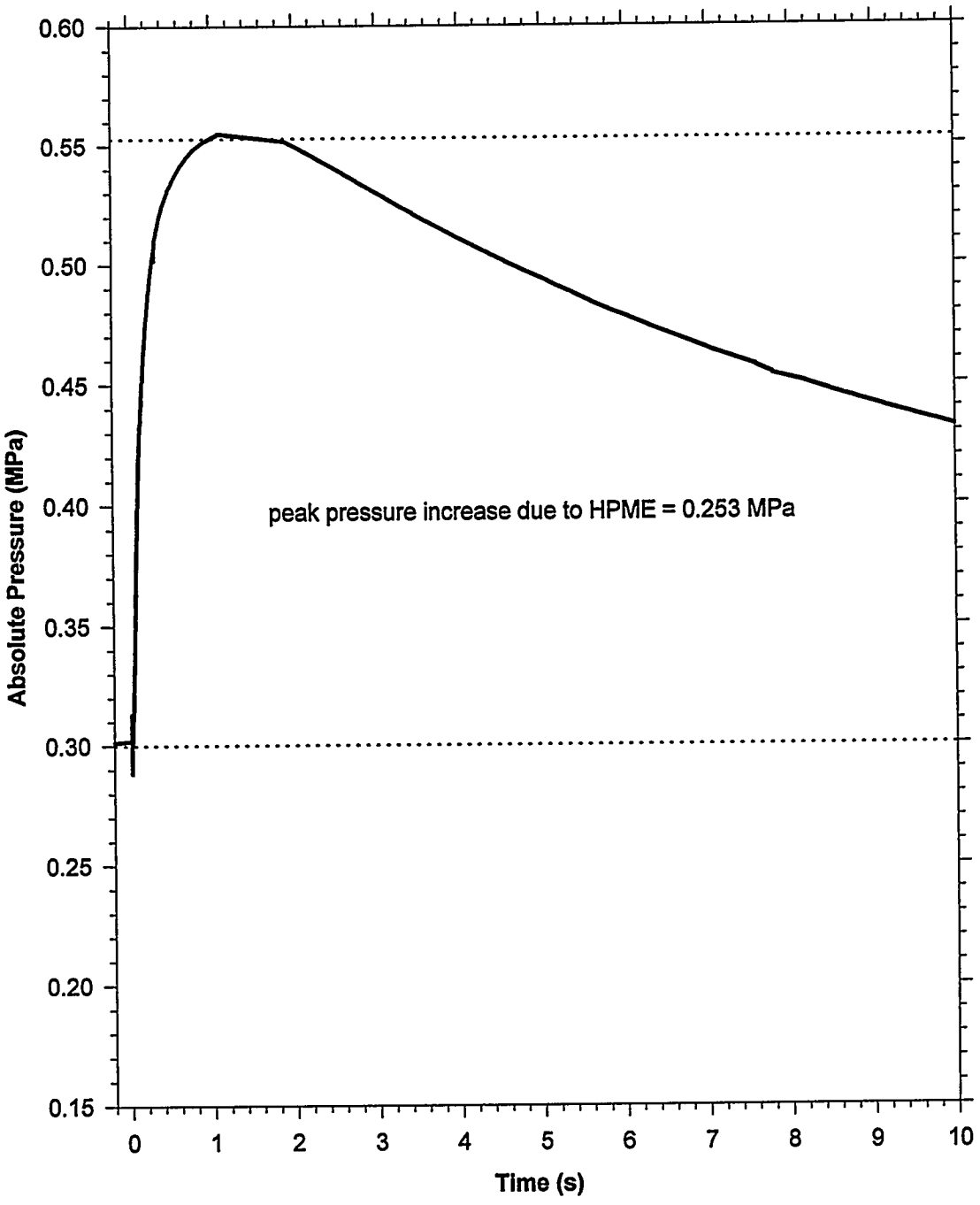

Figure 34. Vessel pressure in the CE-3 experiment from 0 to 10 s.

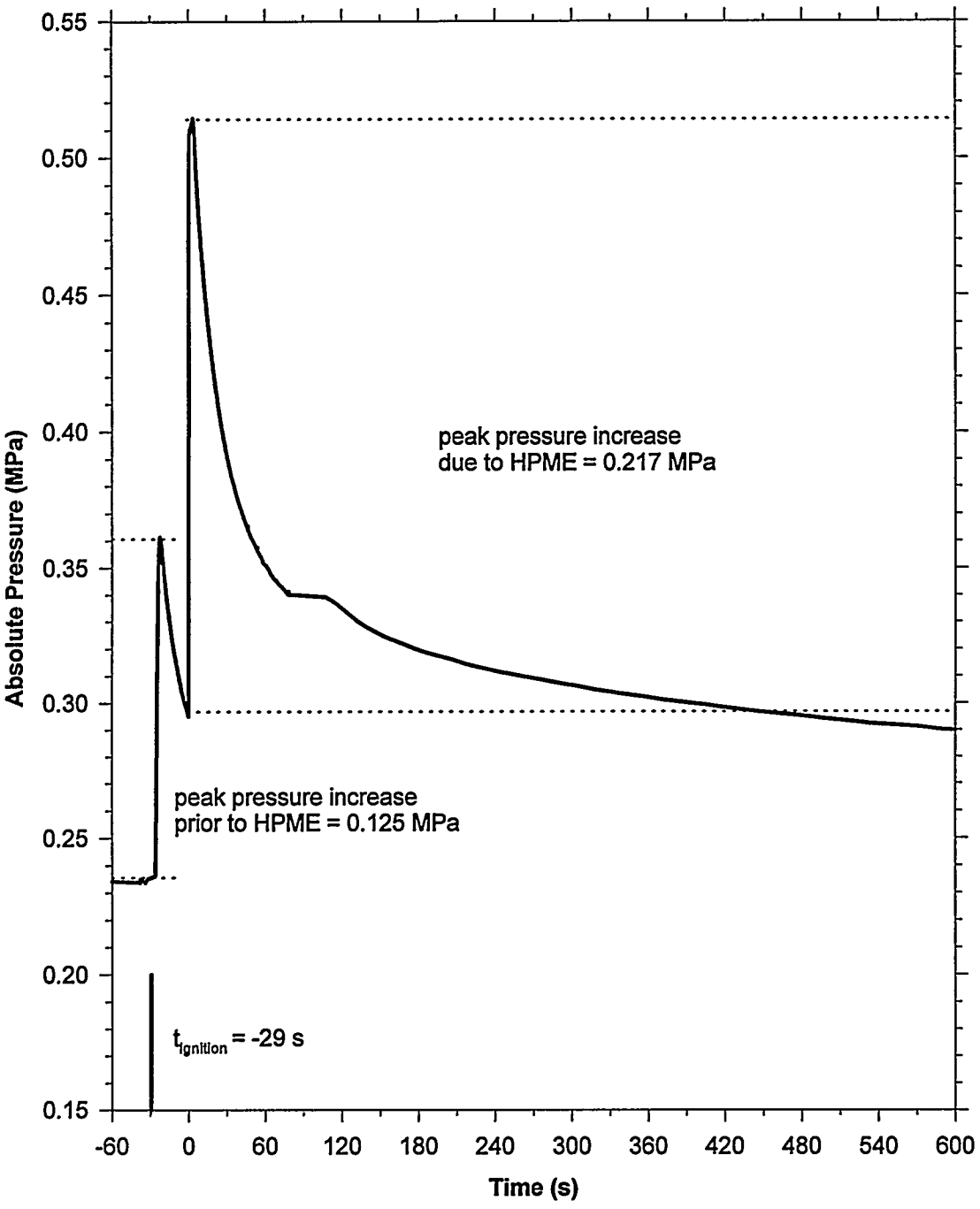

Figure 35. Vessel pressure in the CE-4 experiment from -60 to 600 s.

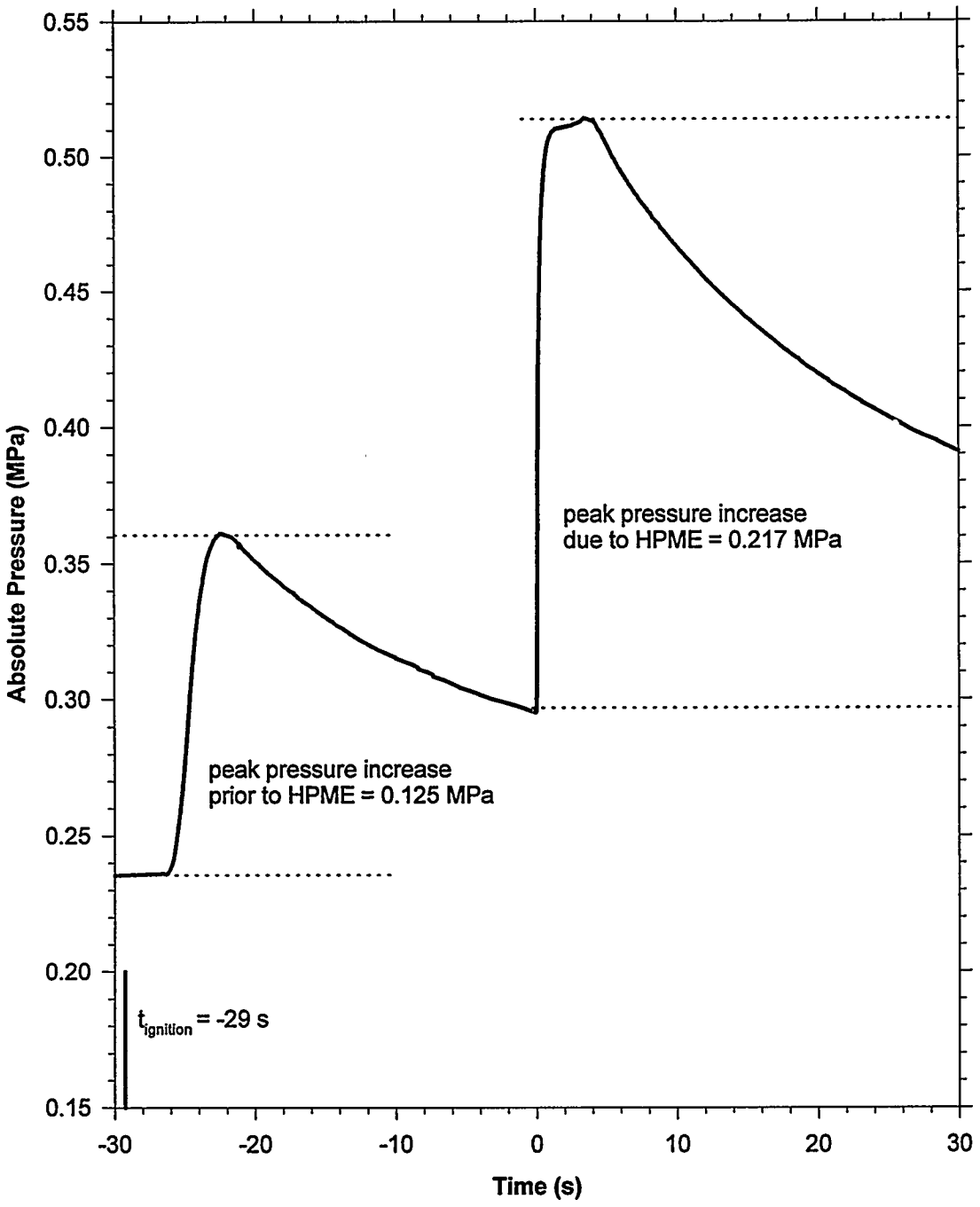

Figure 36. Vessel pressure in the CE-4 experiment from -30 to 30 s.

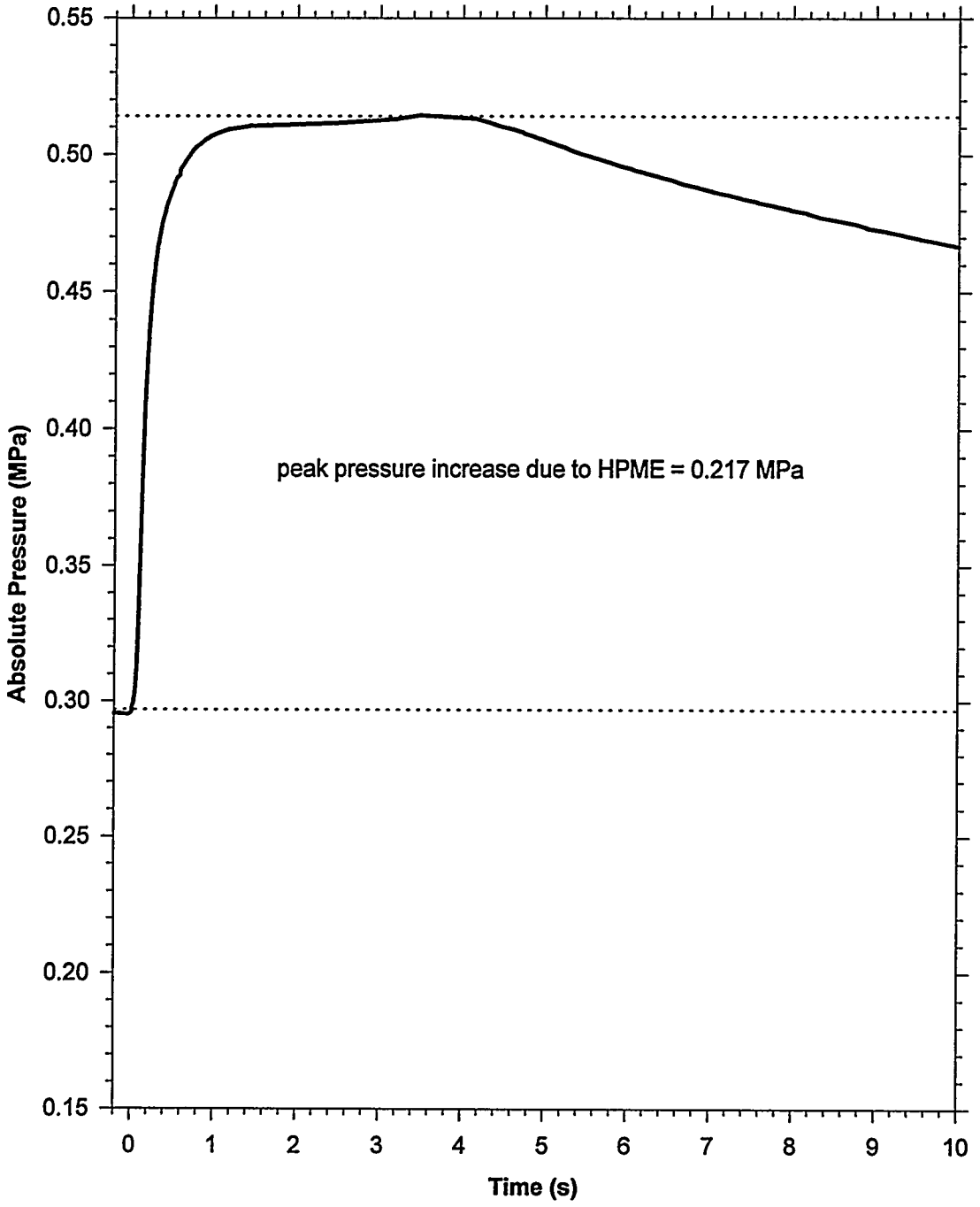

Figure 37. Vessel pressure in the CE-4 experiment from 0 to 10 s.

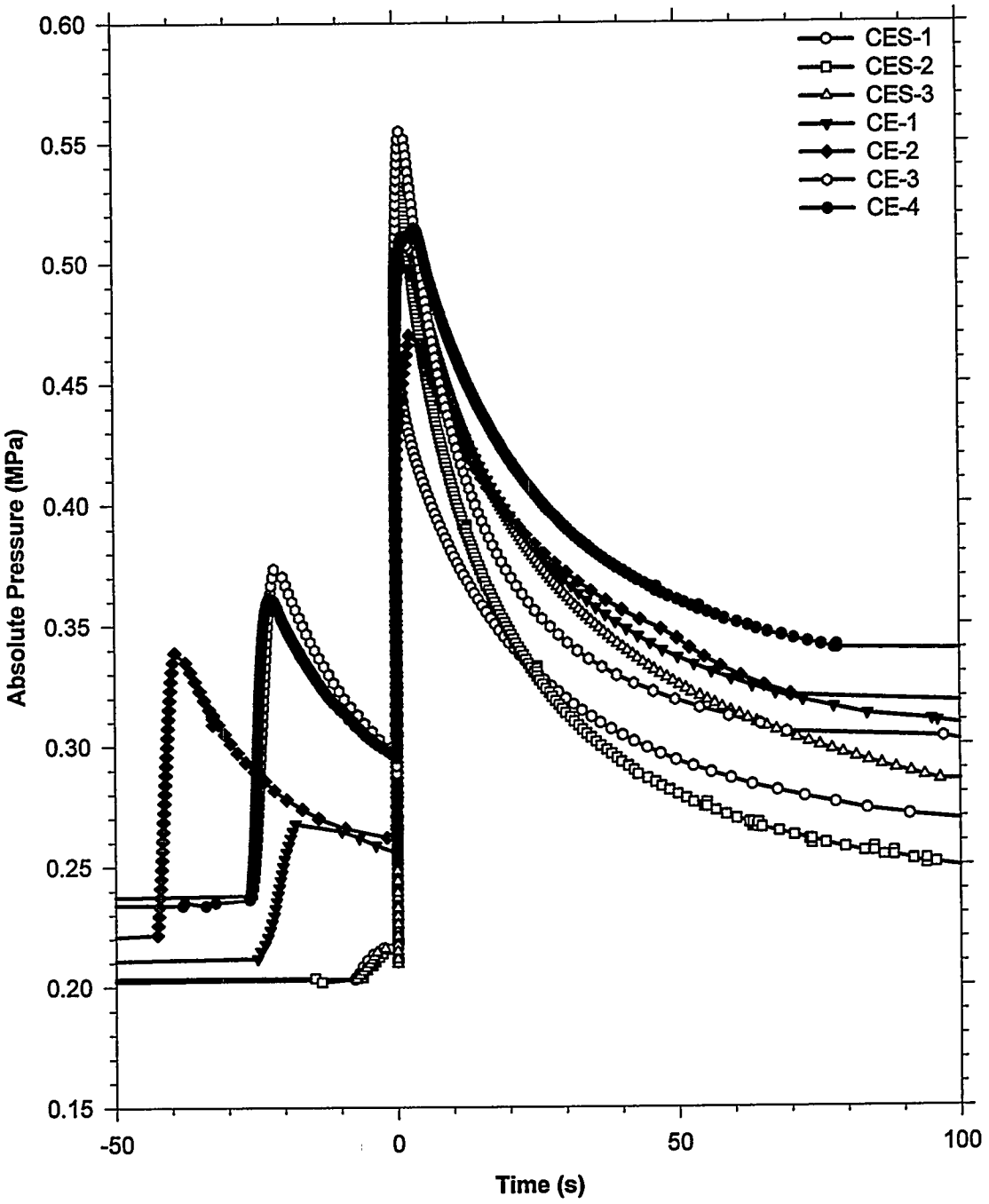

Figure 38. Vessel pressure in the CE DCH experiments.

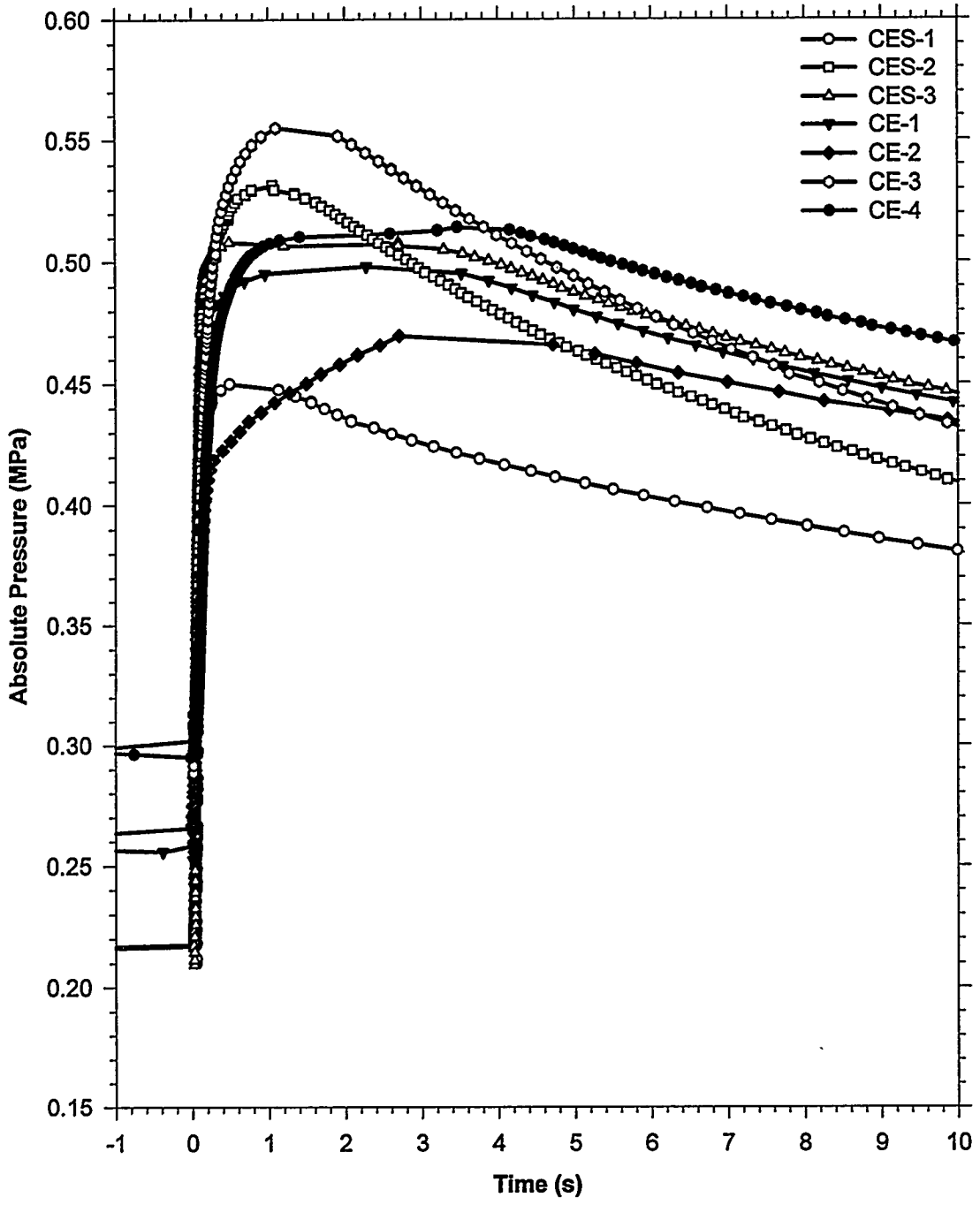

Figure 39. Vessel pressure during the HPME in the CE DCH experiments.

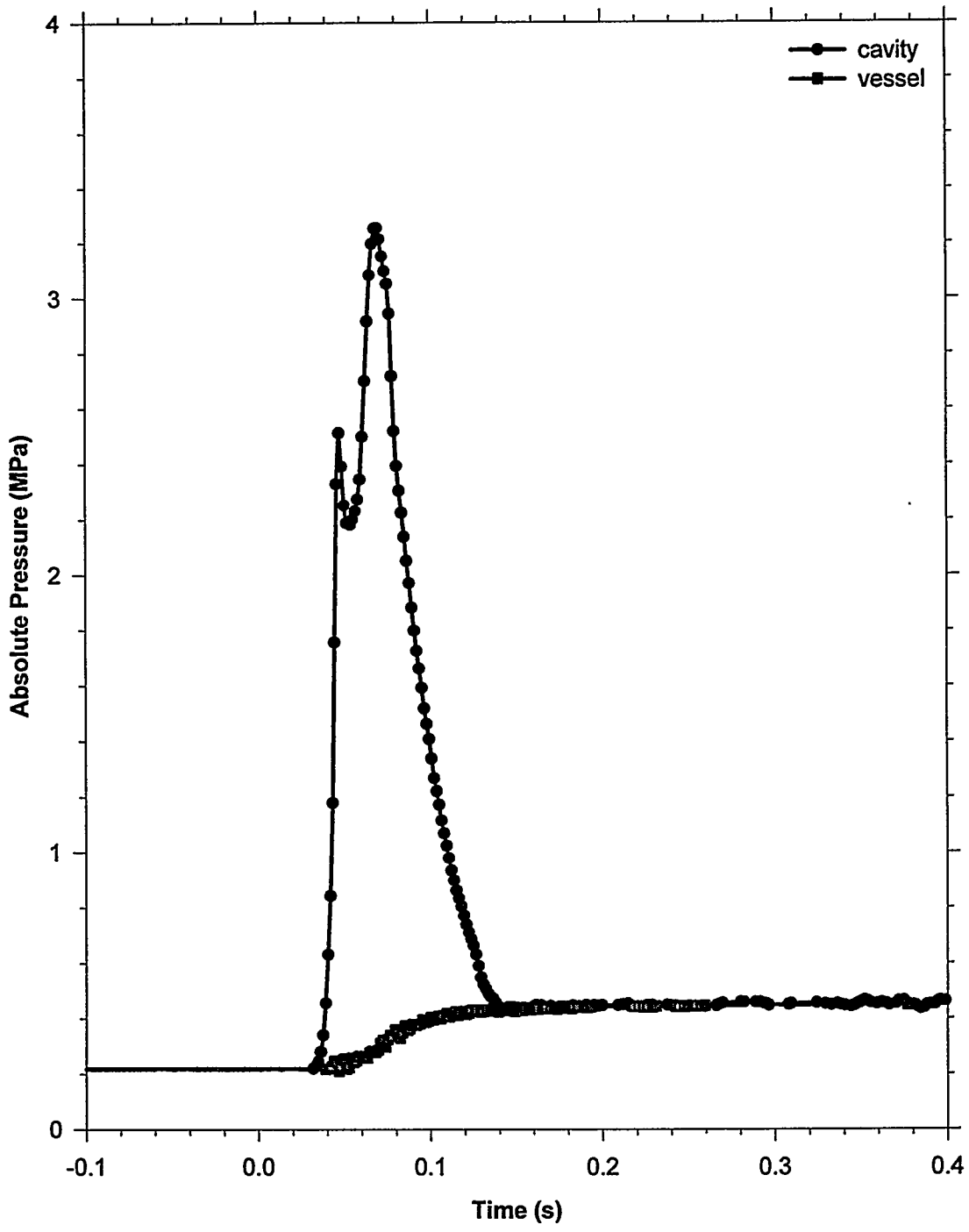

Figure 40. Cavity pressure and vessel pressure in the CES-1 experiment.

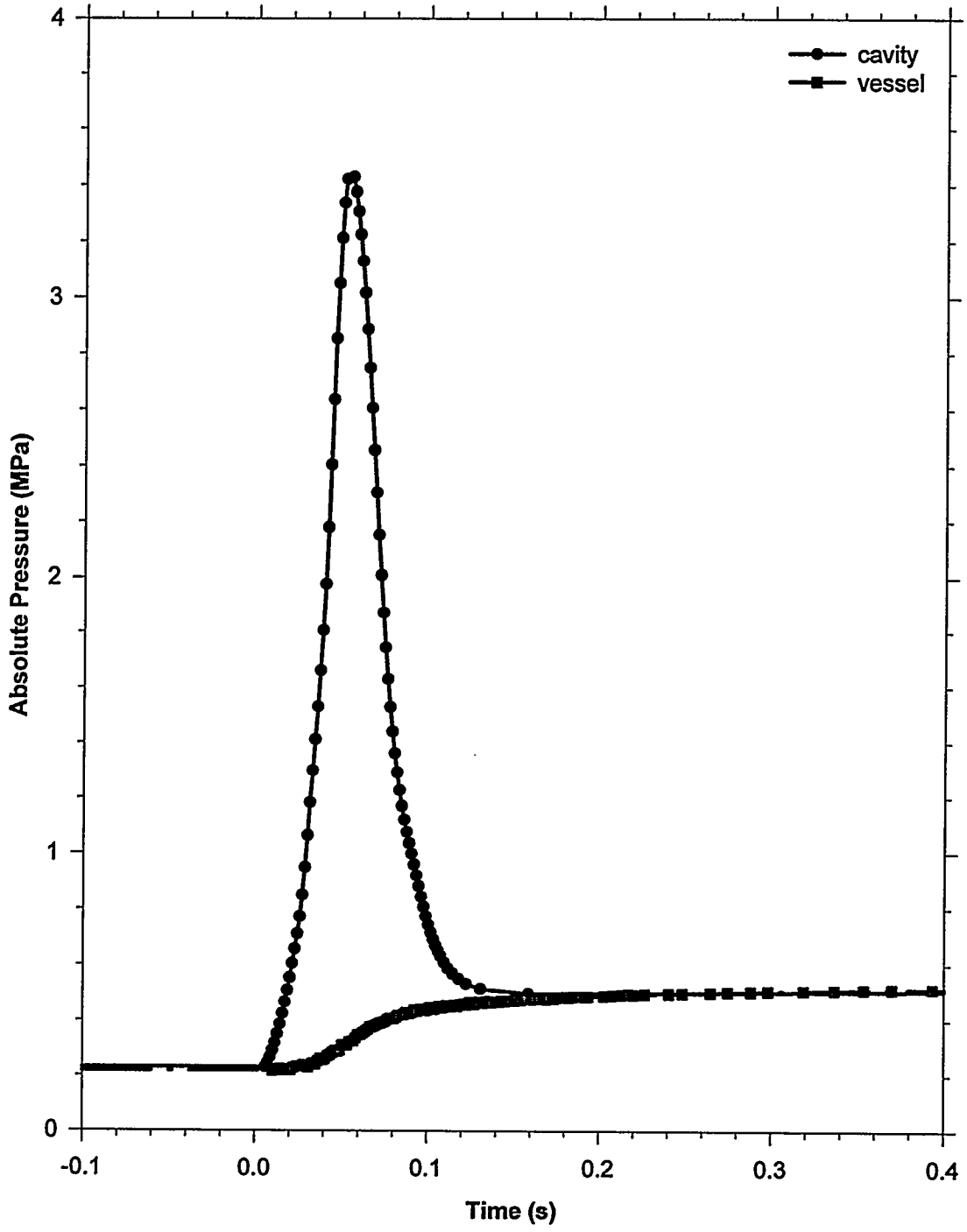

Figure 41. Cavity pressure and vessel pressure in the CES-2 experiment.

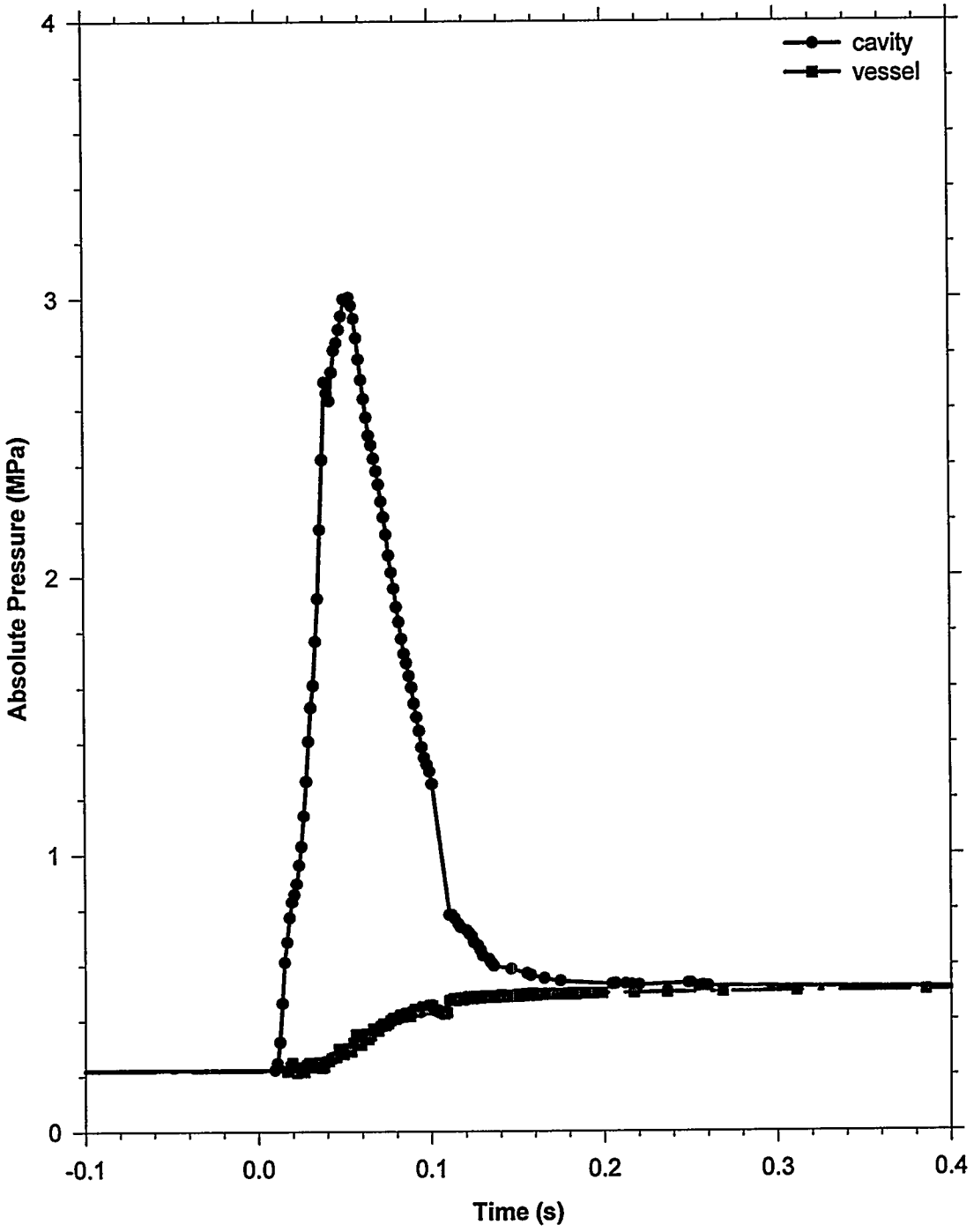

Figure 42. Cavity pressure and vessel pressure in the CES-3 experiment.

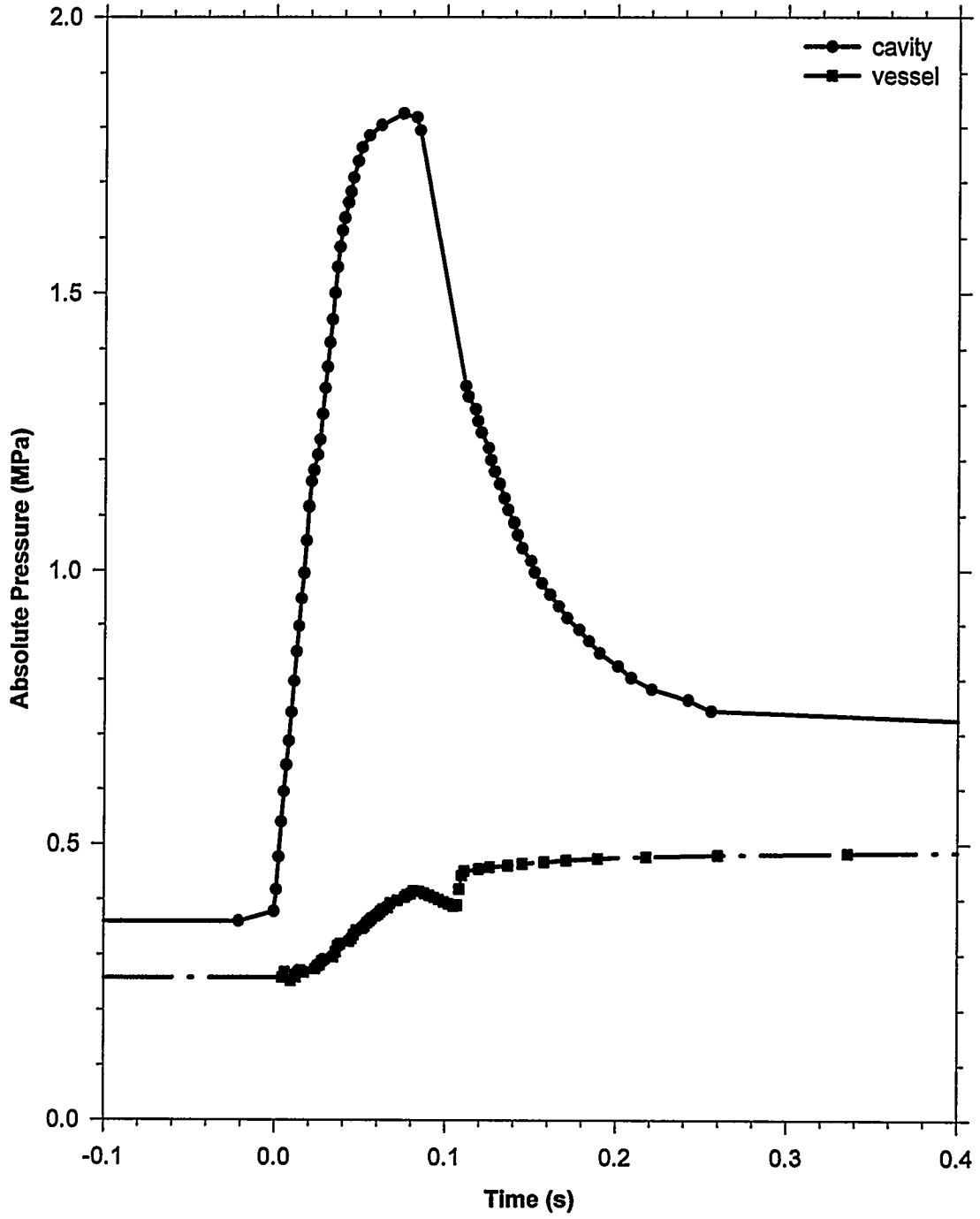

Figure 43. Cavity pressure and vessel pressure in the CE-1 experiment.

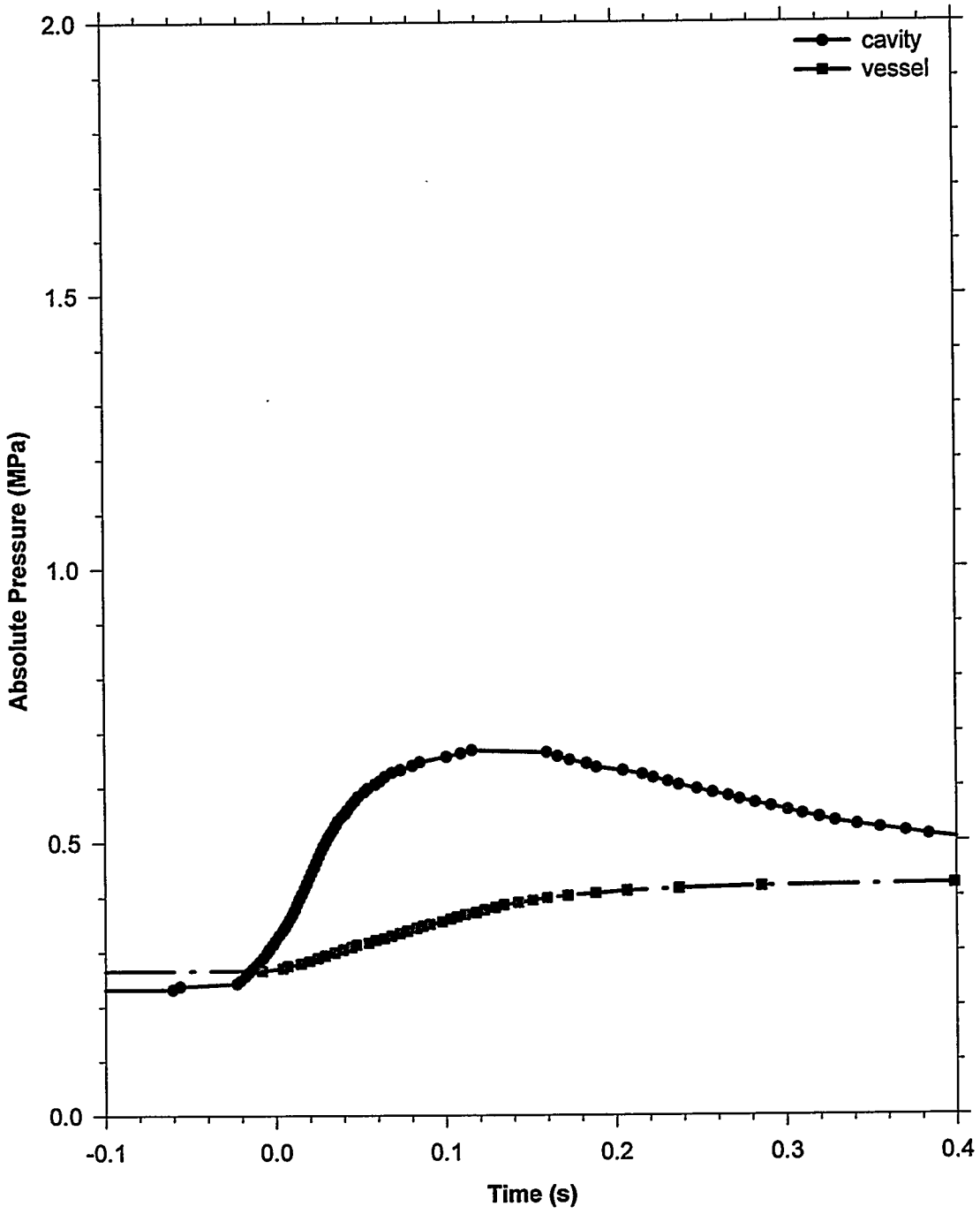

Figure 44. Cavity pressure and vessel pressure in the CE-2 experiment.

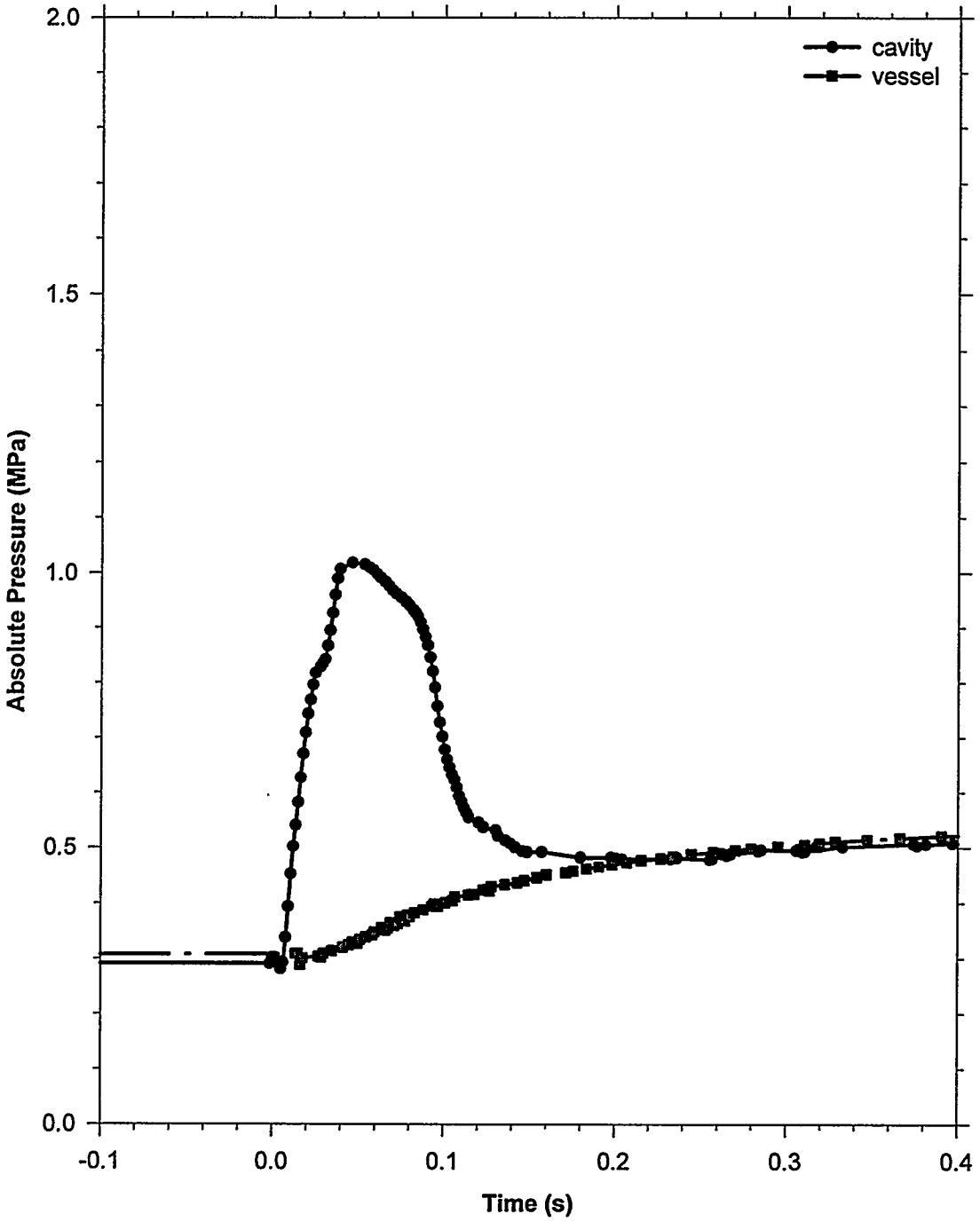

Figure 45. Cavity pressure and vessel pressure in the CE-3 experiment.

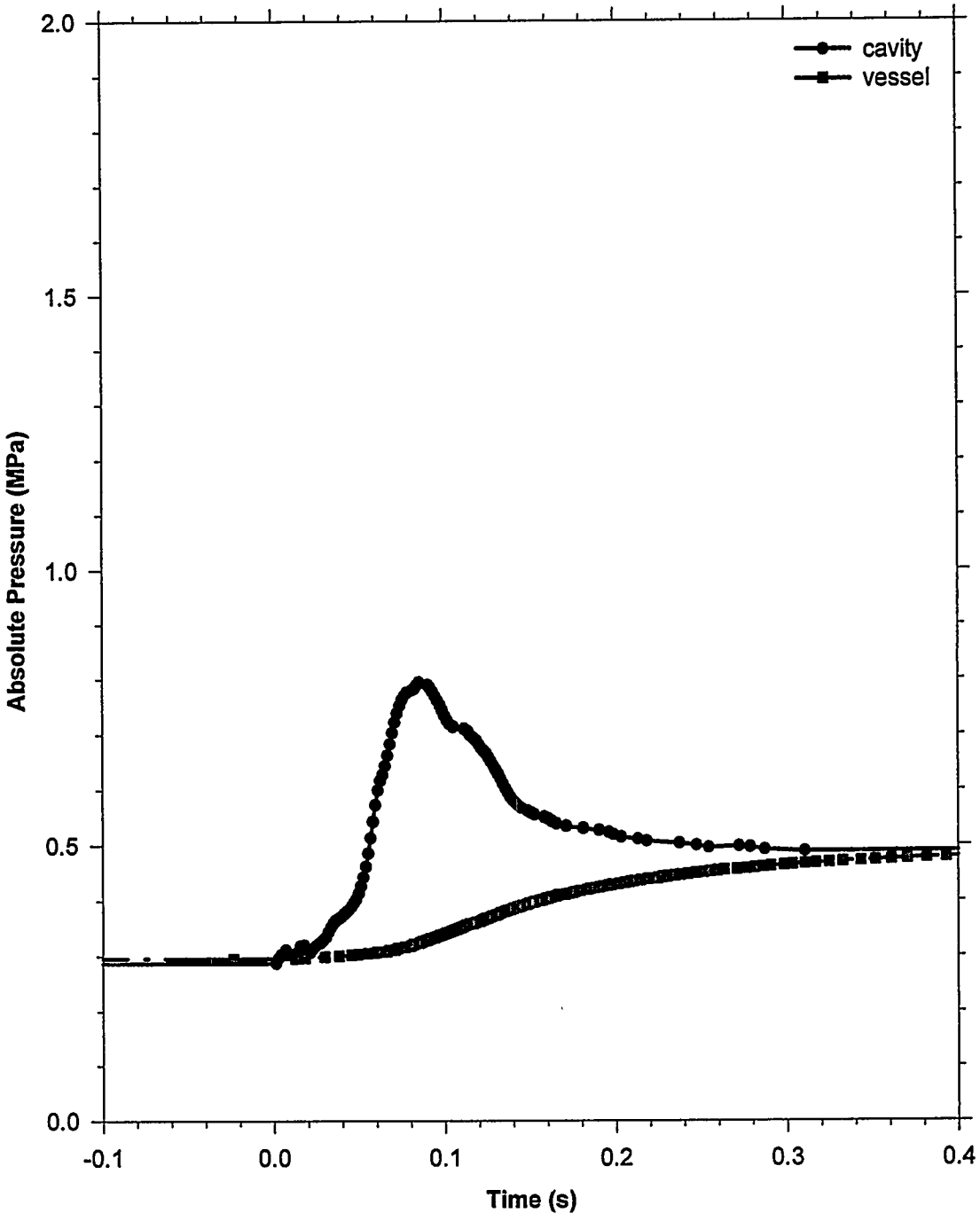

Figure 46. Cavity pressure and vessel pressure in the CE-4 experiment.

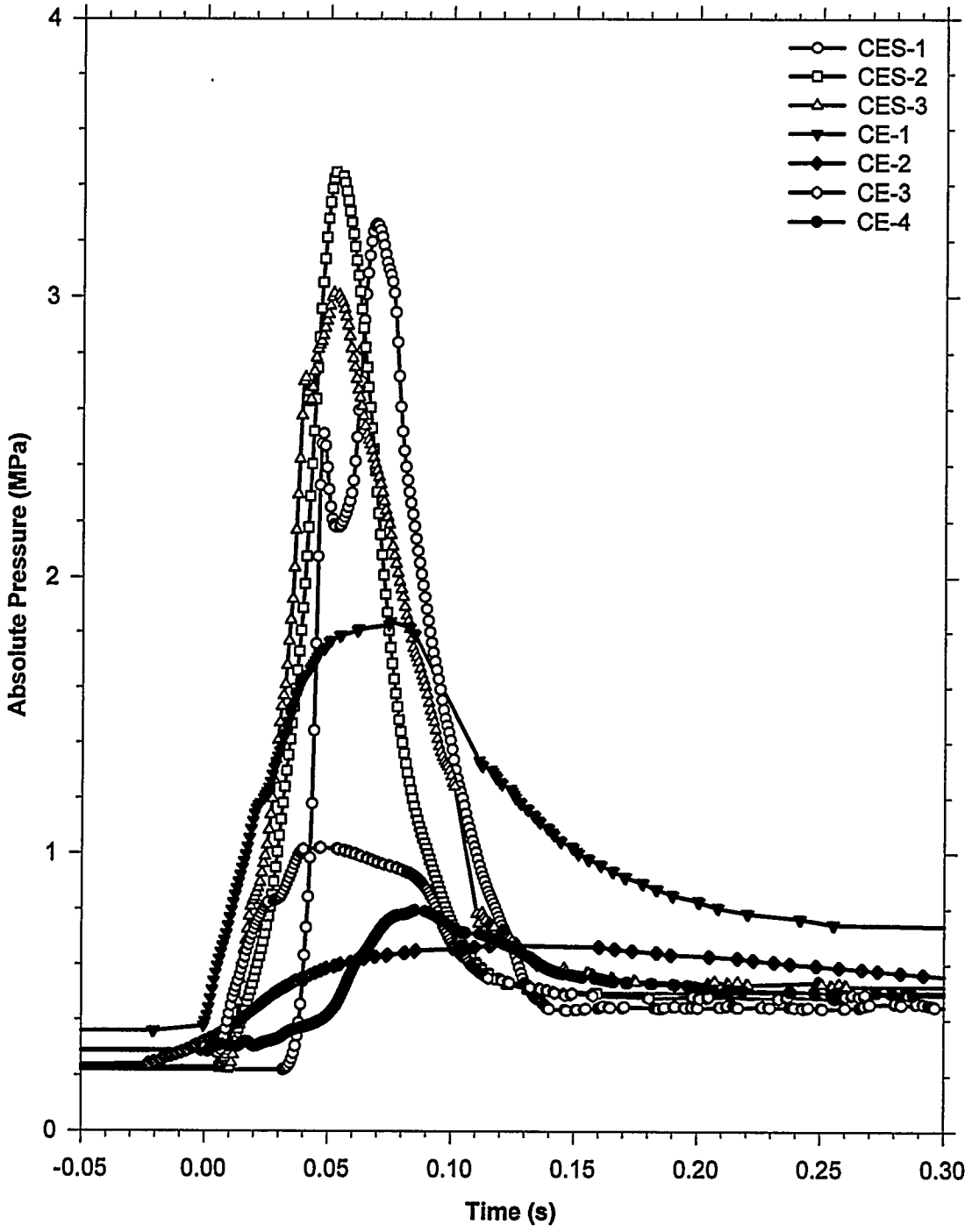

Figure 47. Cavity pressure in the CE DCH experiments.

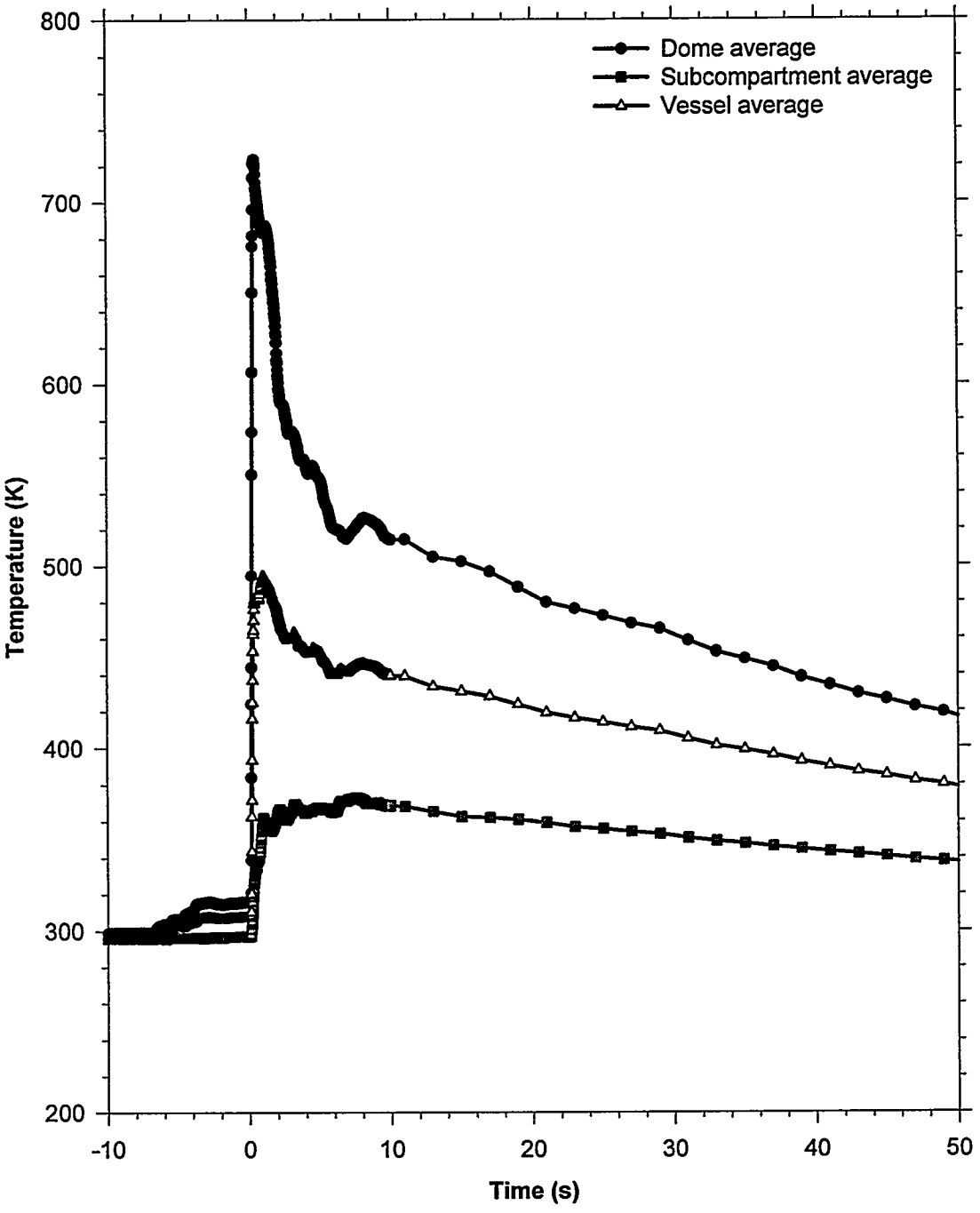

Figure 48. Average gas temperatures in the CES-1 experiment.

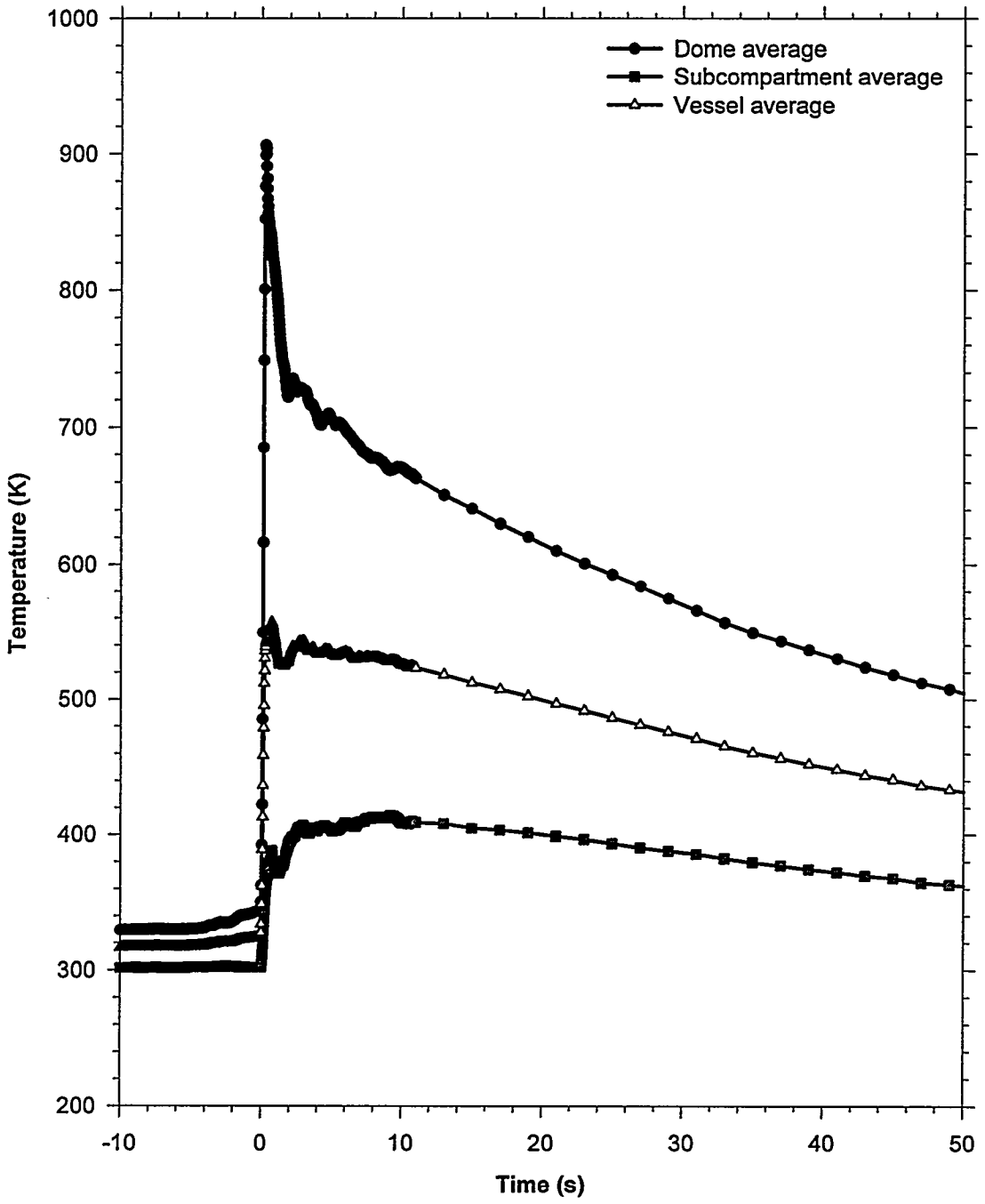

Figure 49. Average gas temperatures in the CES-2 experiment.

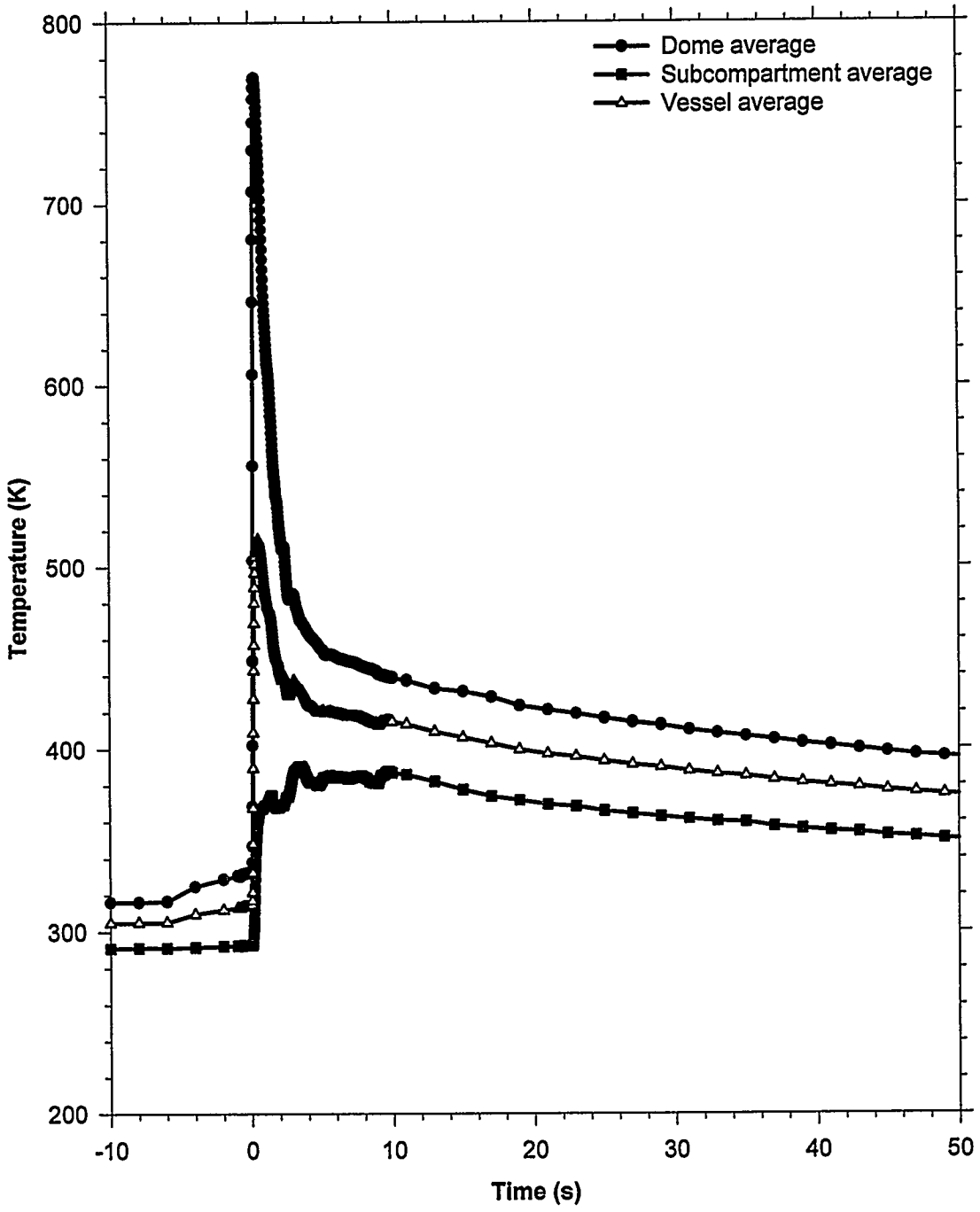

Figure 50. Average gas temperatures in the CES-3 experiment.

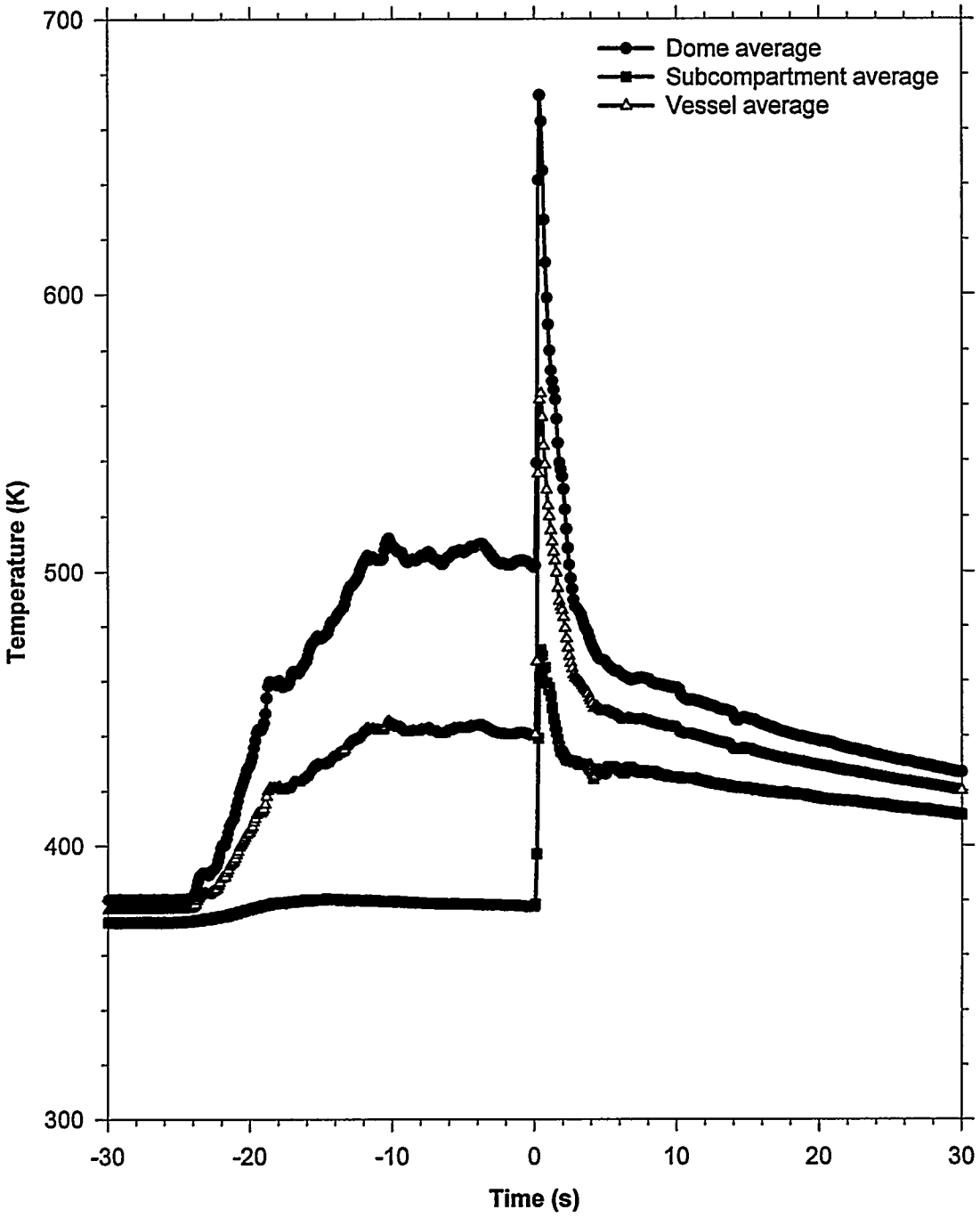

Figure 51. Average gas temperatures in the CE-1 experiment.

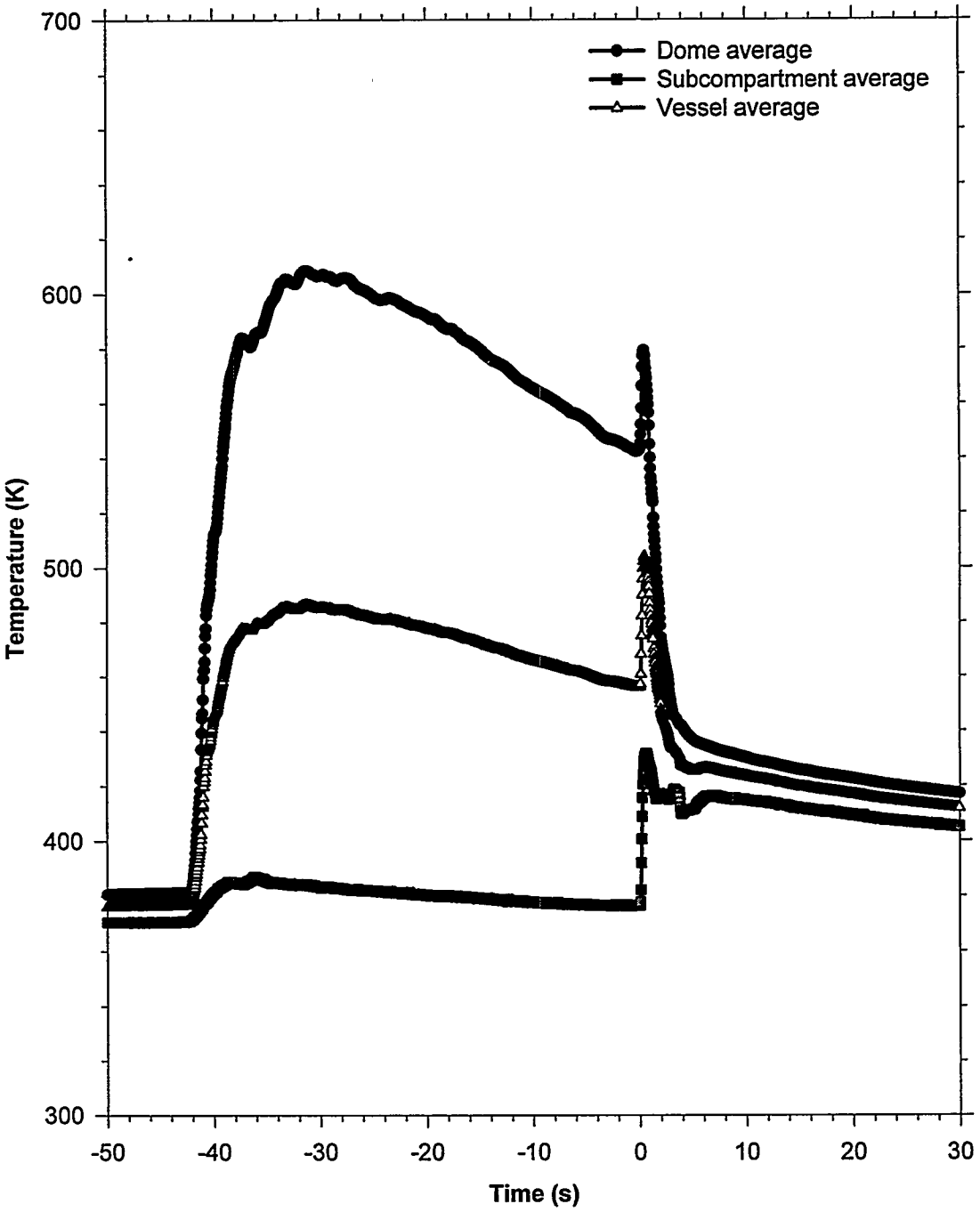

Figure 52. Average gas temperatures in the CE-2 experiment.

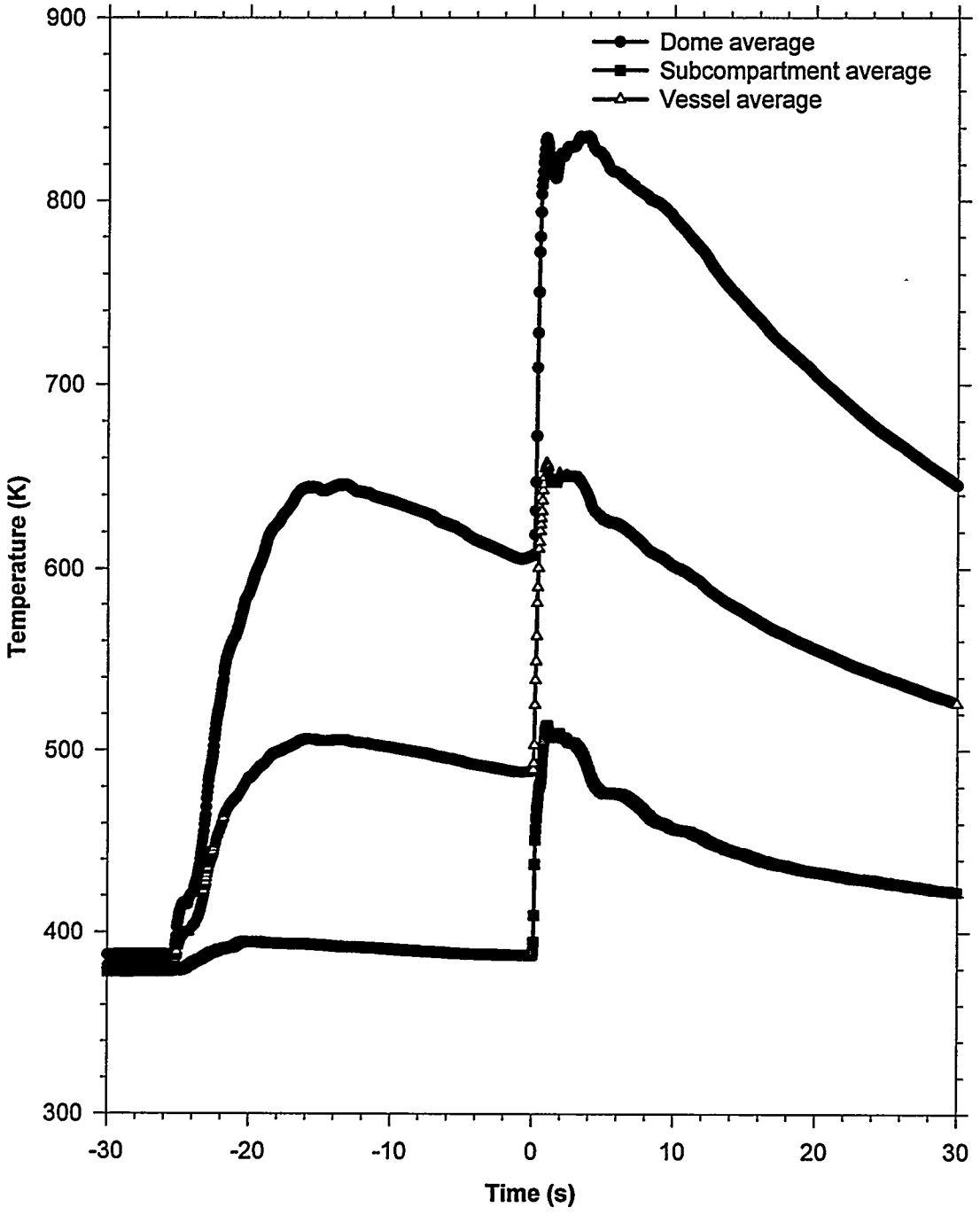

Figure 53. Average gas temperatures in the CE-3 experiment.

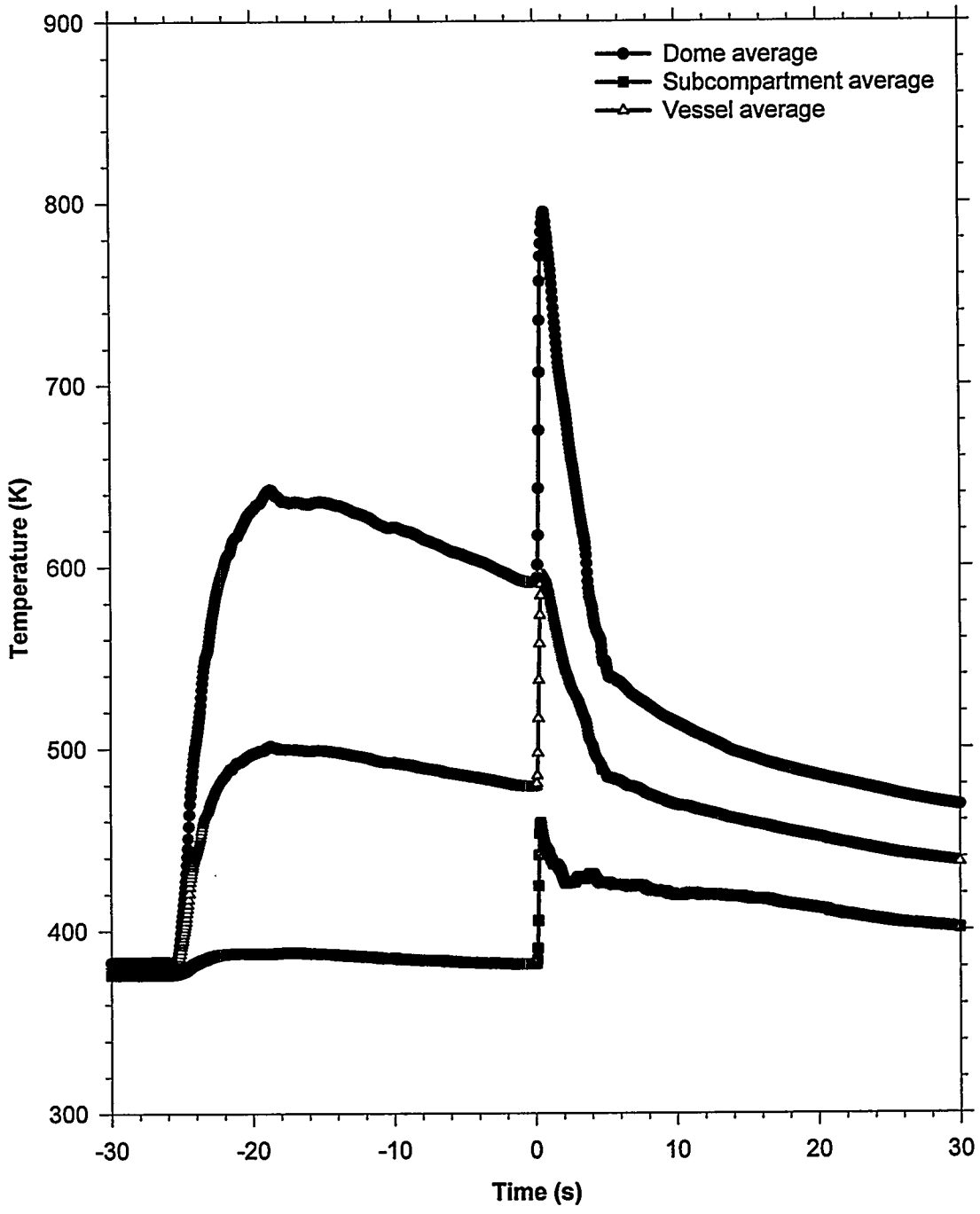

Figure 54. Average gas temperatures in the CE-4 experiment.

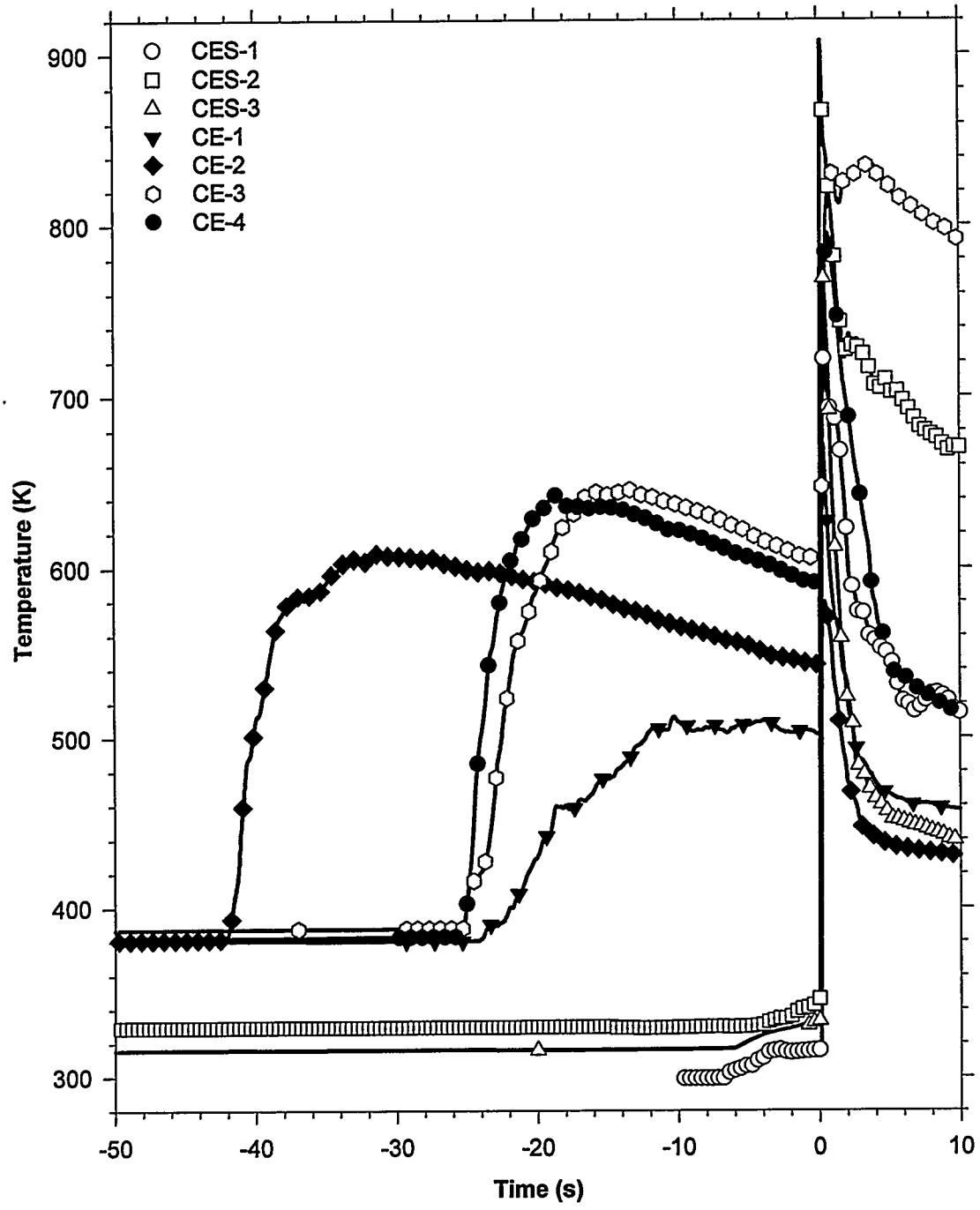

Figure 55. Comparison of the dome average gas temperatures in the CE experiments during the thermite reaction interval.

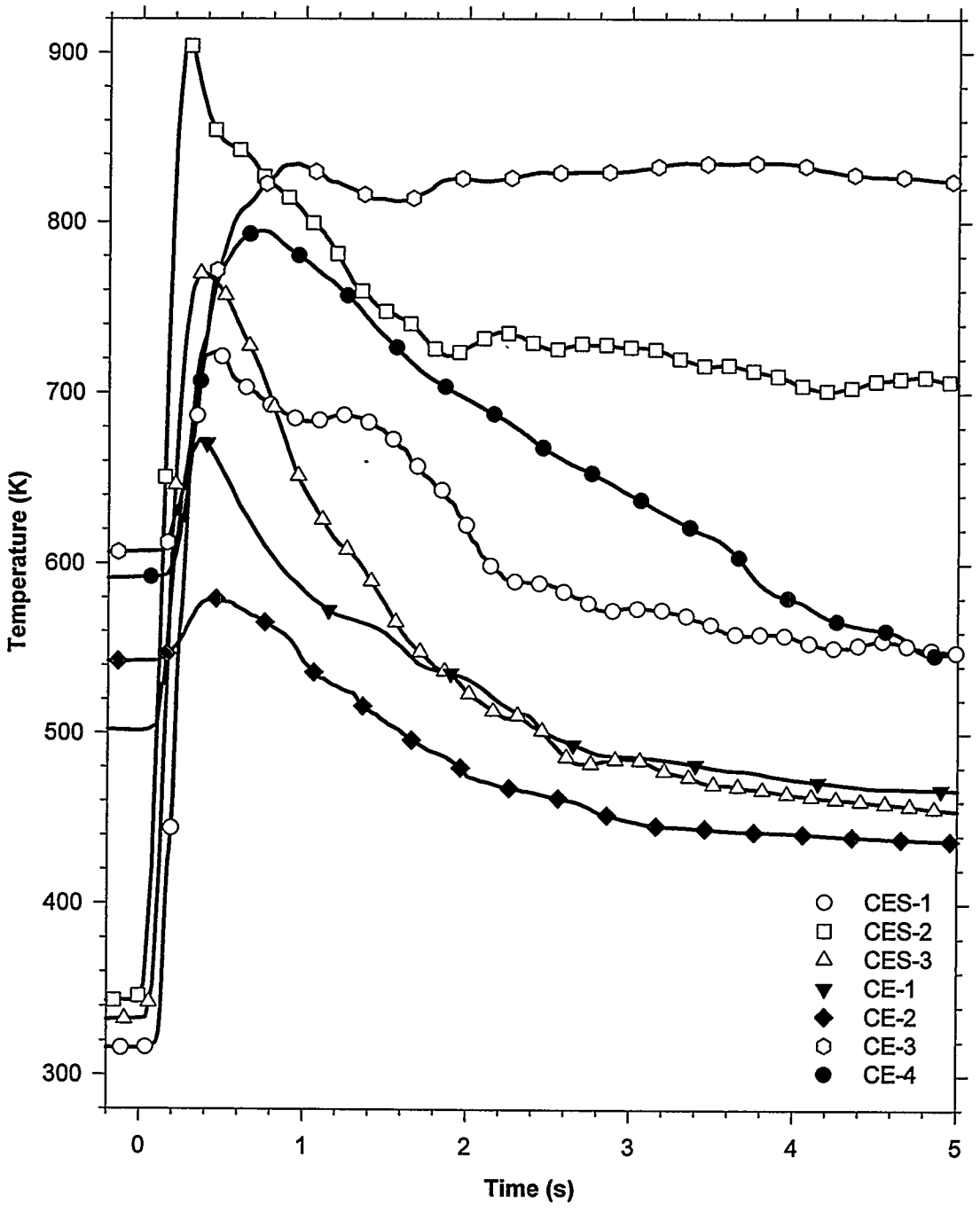

Figure 56. Comparison of the dome average gas temperatures in the CE experiments during the HPME.

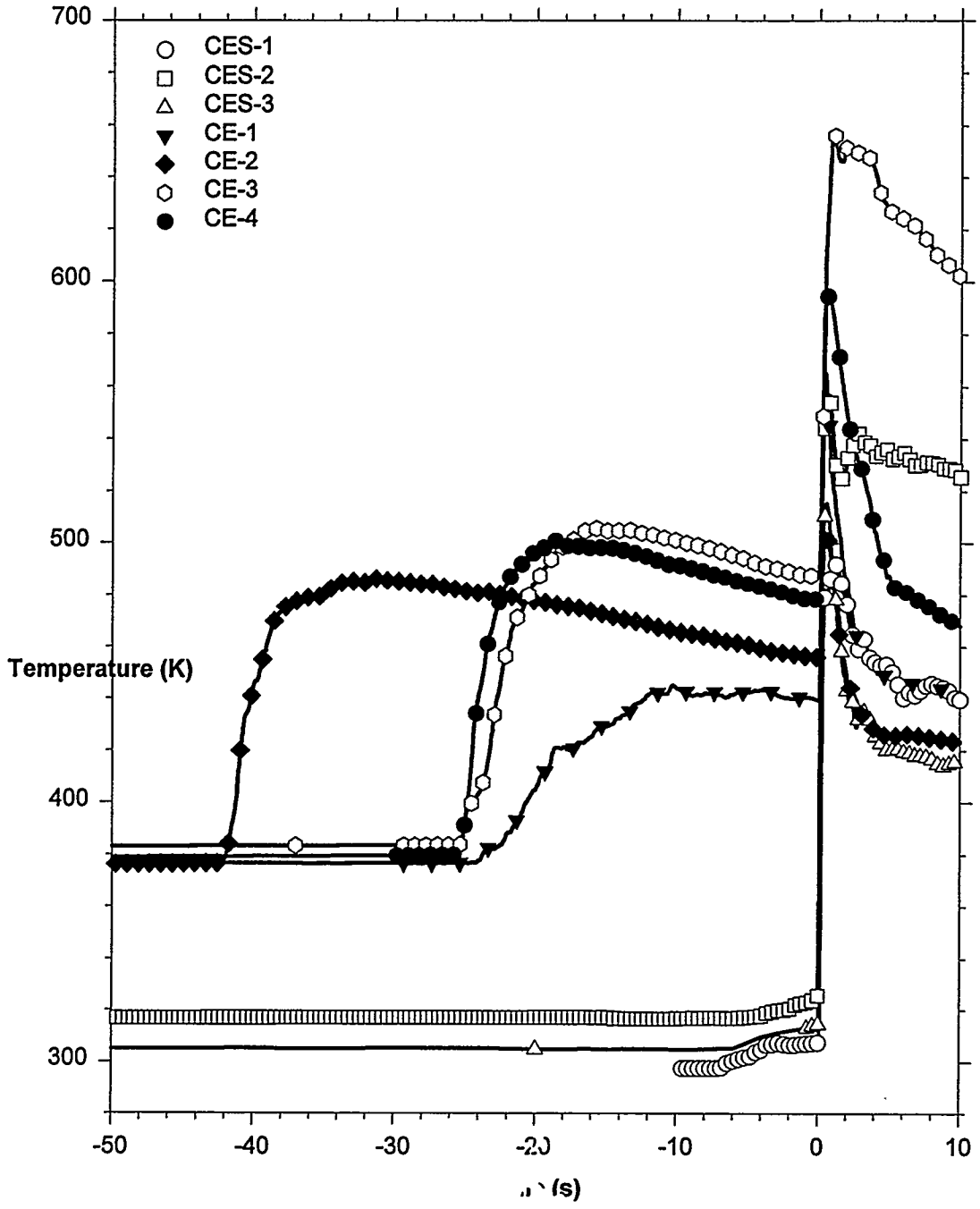

Figure 57. Comparison of the vessel mole-average gas temperatures in the CE experiments during the thermite reaction interval.

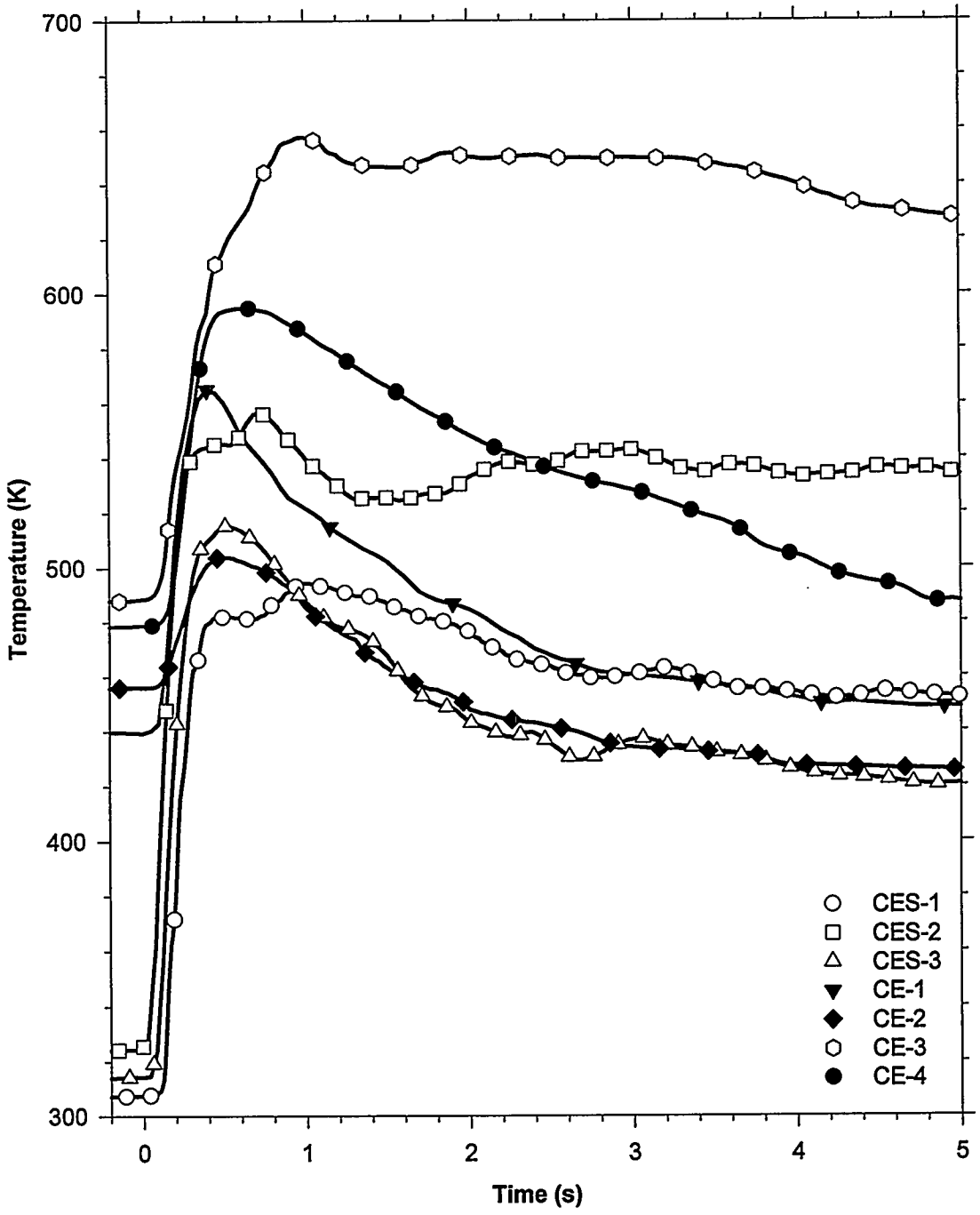

Figure 58. Comparison of the vessel mole-average gas temperatures in the CE experiments during the HPME.

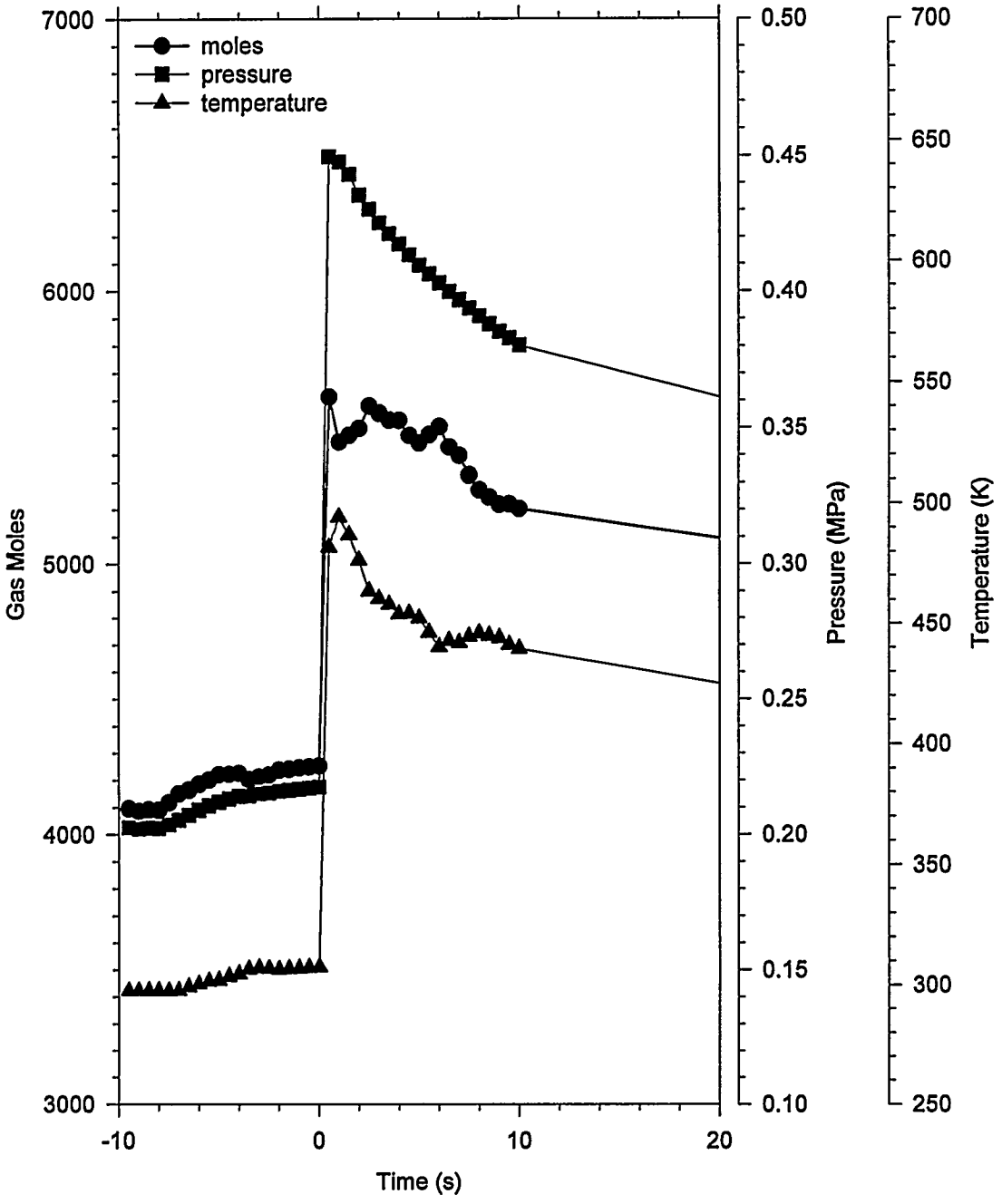

Figure 59. Vessel gas pressure, average temperature, and moles in the CES-1 experiment.

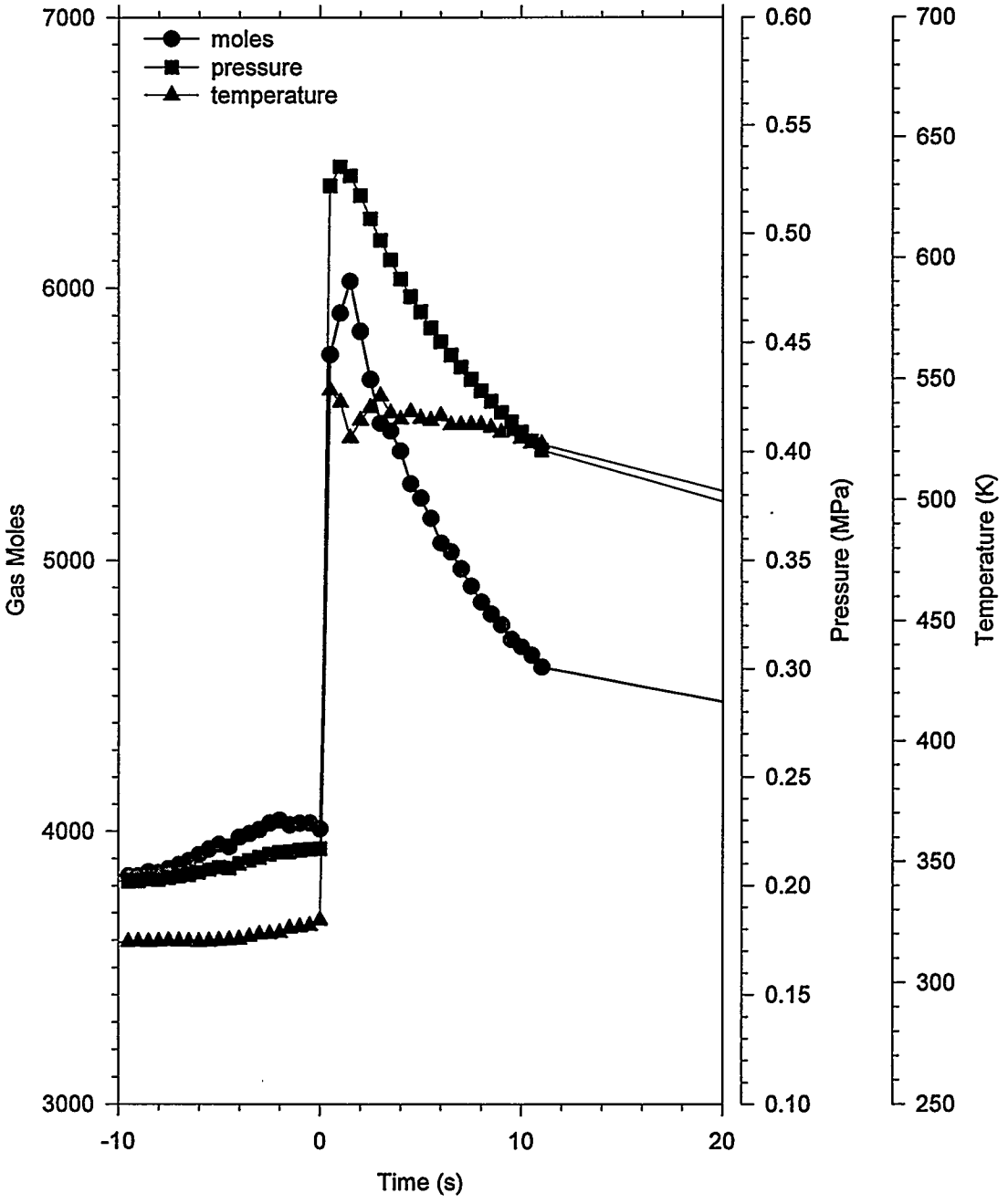

Figure 60. Vessel gas pressure, average temperature, and moles in the CES-2 experiment.

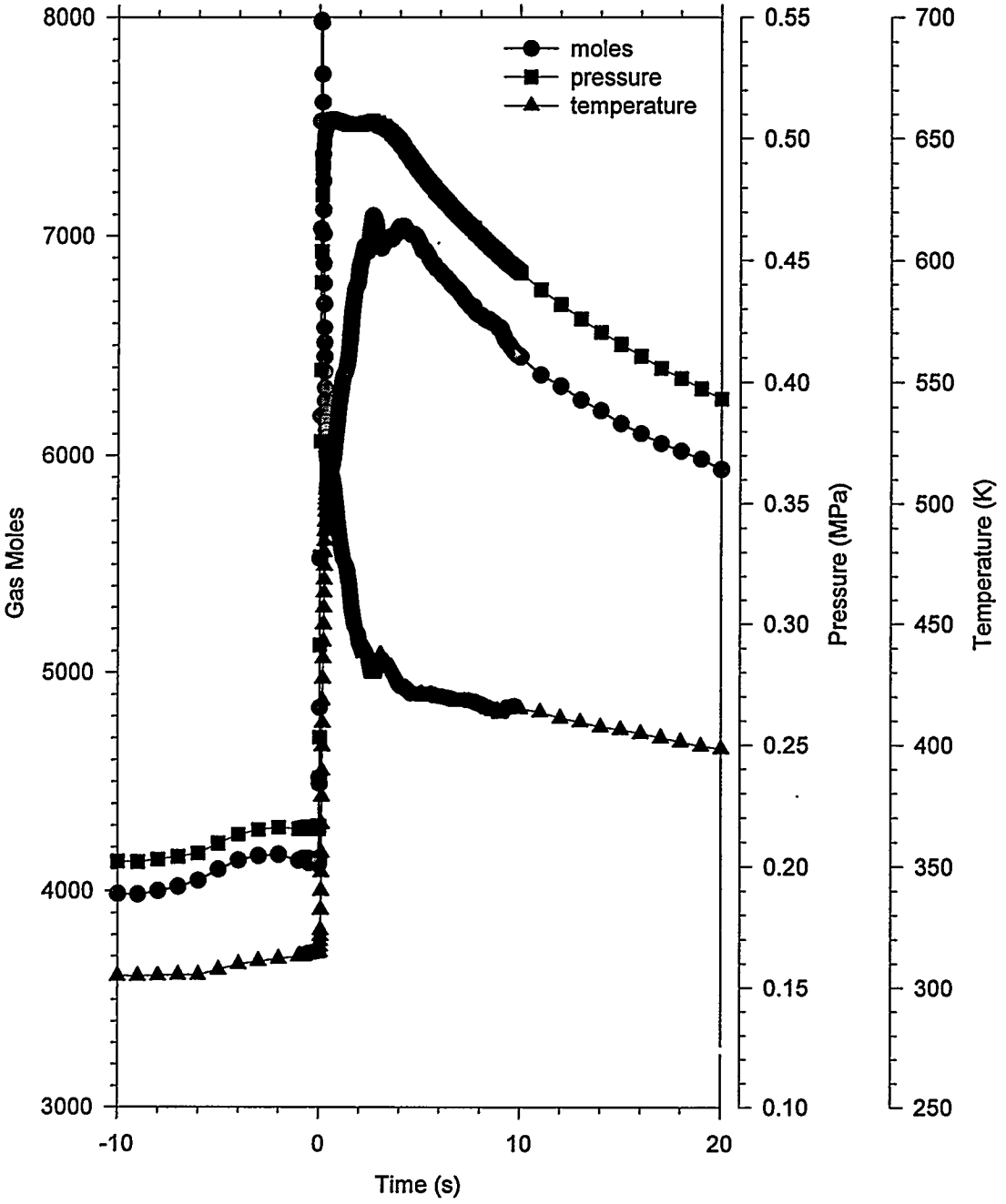

Figure 61. Vessel gas pressure, average temperature, and moles in the CES-3 experiment.

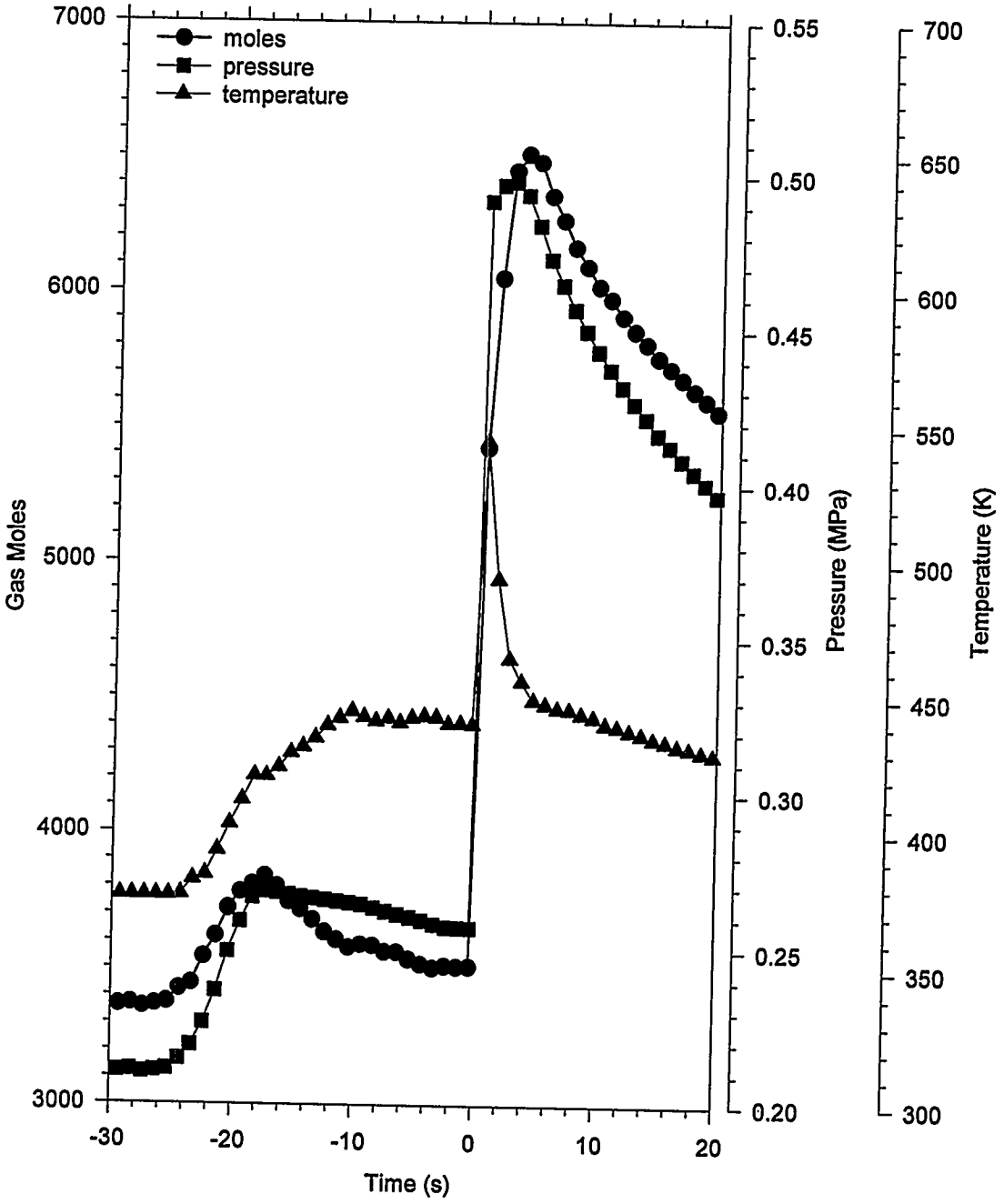

Figure 62. Vessel gas pressure, average temperature, and moles in the CE-1 experiment.

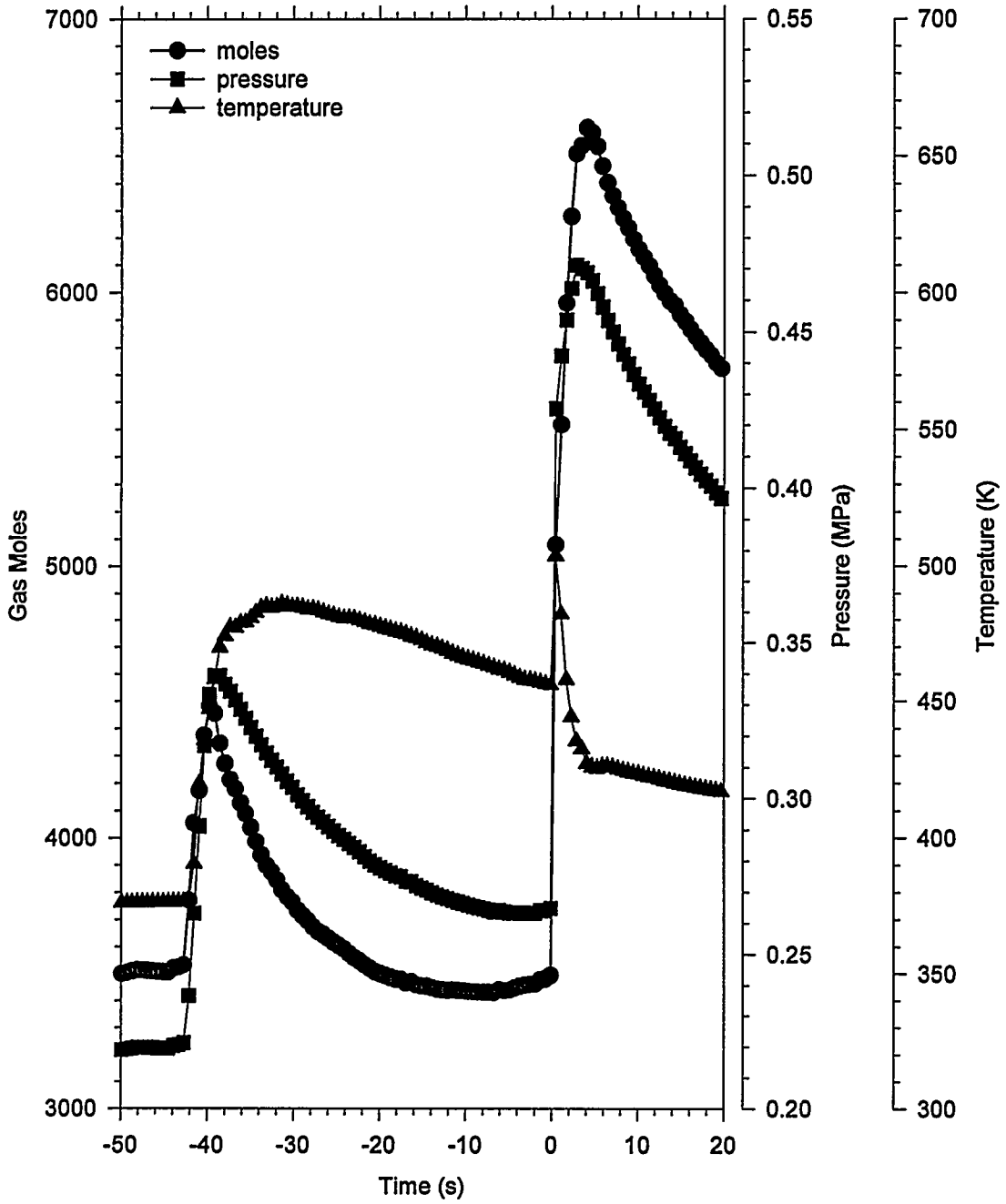

Figure 63. Vessel gas pressure, average temperature, and moles in the CE-2 experiment.

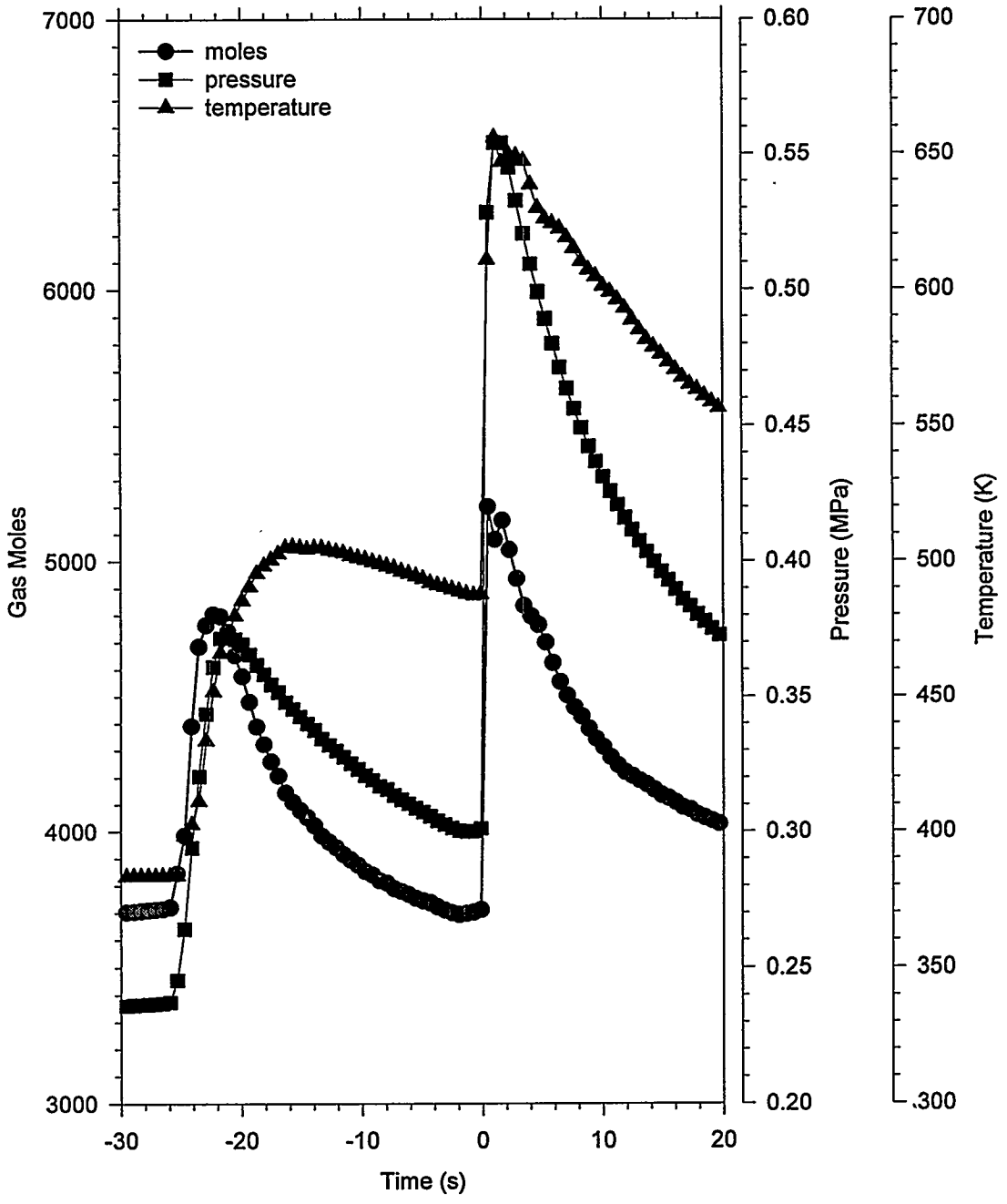

Figure 64. Vessel gas pressure, average temperature, and moles in the CE-3 experiment.

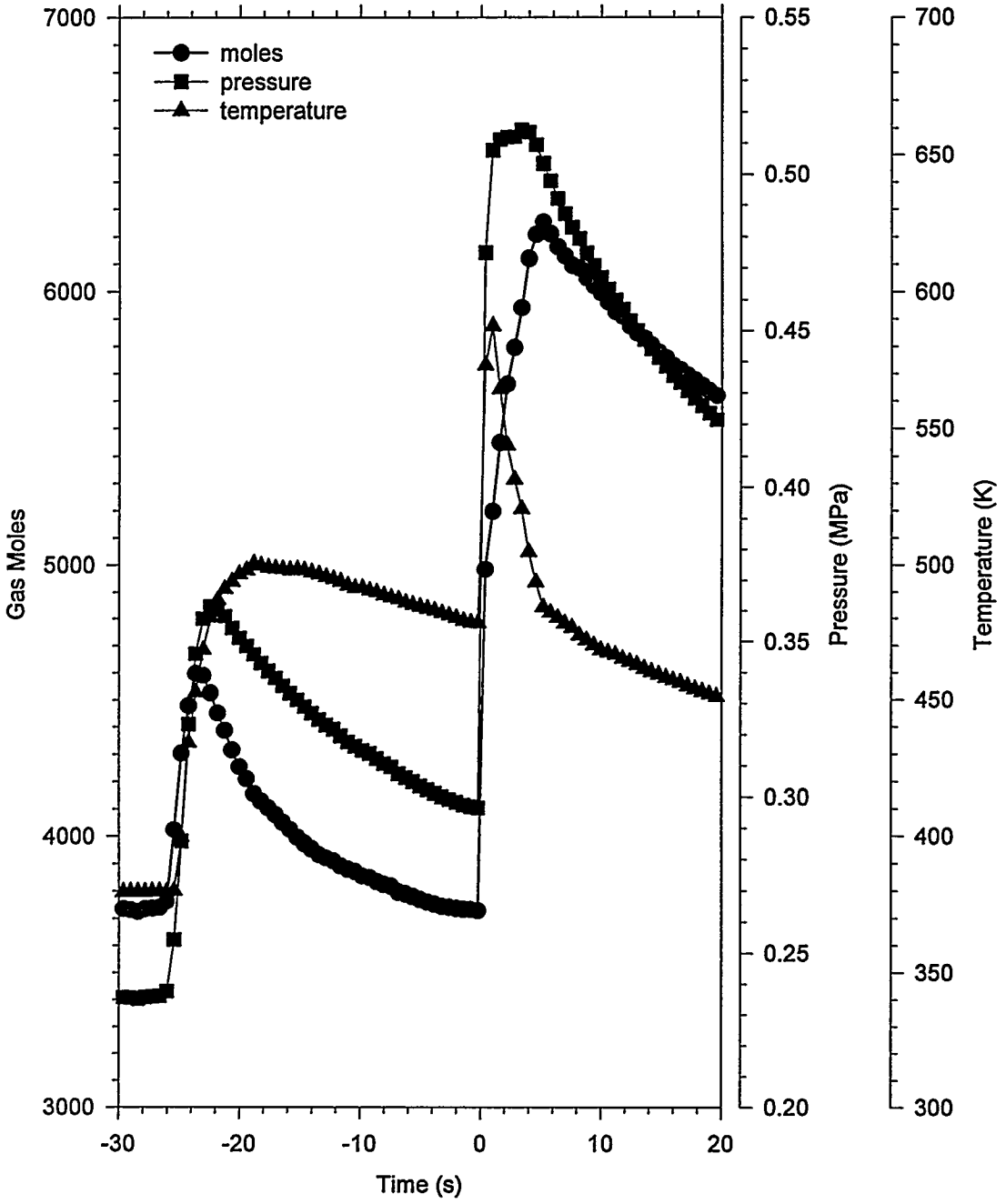

Figure 65. Vessel gas pressure, average temperature, and moles in the CE-4 experiment.

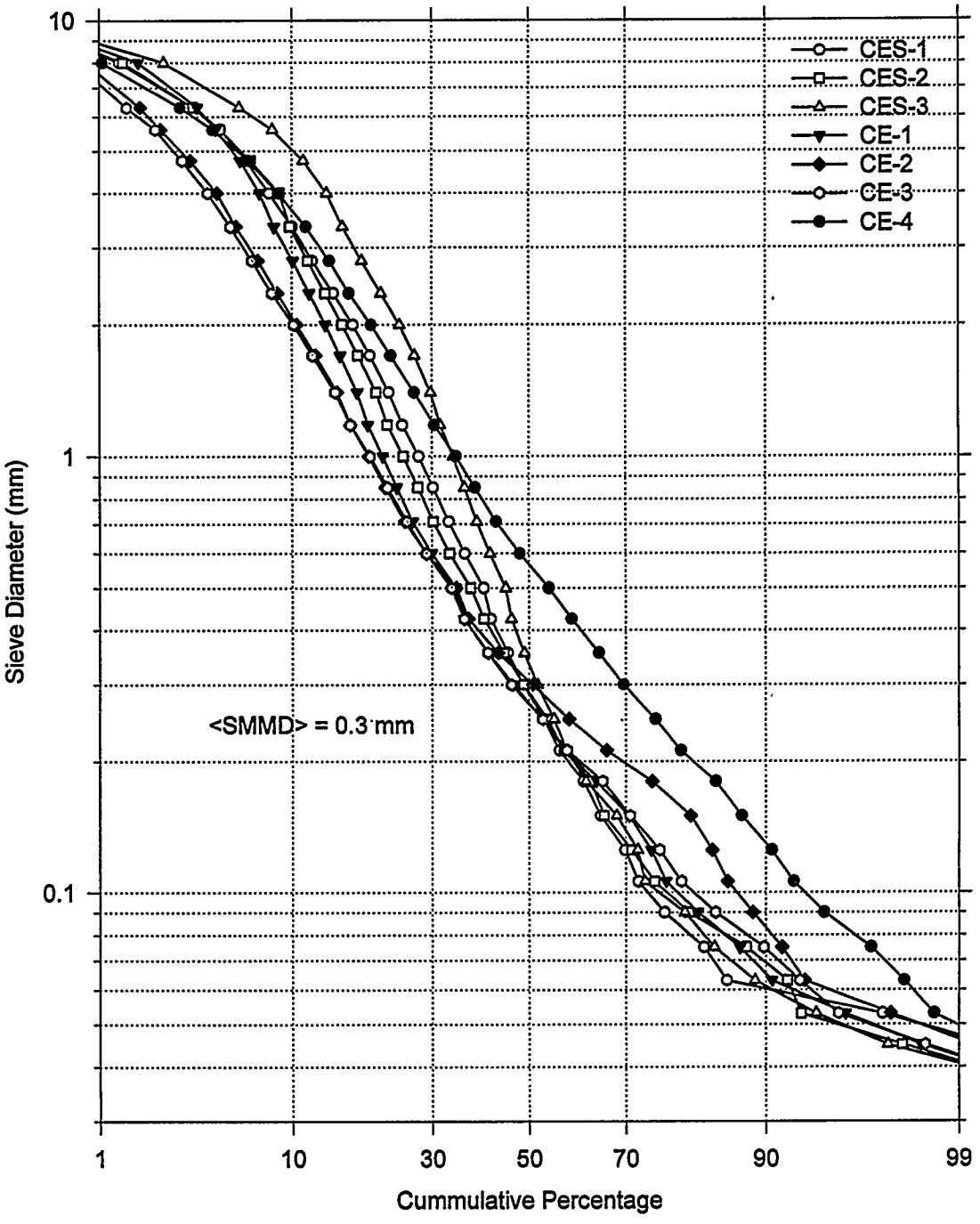

Figure 66. Sieve analysis of debris recovered from the operating deck.

4.0 ANALYSES

4.1 Debris Dispersal Prior to Water Delivery

Some scoping calculations of the dispersal phenomena that could occur prior to water delivery to the cavity were performed. Specifically, water delivery will be preceded by a "burp" of N_2 gas. The dispersal consequences of this burp are:

1. that the burp may only be partially effective at displacing melt away from the impingement region,

2. that the burp has a tendency to levitate melt up the annulus, and

3. that only trivial quantities of melt will be dispersed from the cavity prior to water injection into the cavity.

The details of these calculations follow.

Figure 67 schematically illustrates the test geometry. A large accumulator and connecting piping are partially filled with cold water. The water column is separated from the "empty" melt generator by a set of rupture disks. The empty melt generator (actually a pipe passes through the melt generator) communicates with the cavity and Surtsey atmospheric conditions prior to rupture disk failure because the orifice remains unplugged. Thermite (33 kg) is burned in the cavity.

After ignition and complete burning of thermite, the rupture disks are blown. Water accelerates into the empty crucible, compressing the small amount of gas. This gas quickly discharges (i.e., burps) into the cavity before the water slug. The purpose of these scoping calculations are: (1) to determine if the ejected water will jet into a stagnant melt pool, and (2) to determine if the gas can entrain significant quantities of melt from the cavity prior to water injection into the cavity.

4.1.1 Initial Displacement of Melt

Figure 68 illustrates the layout of the reactor cavity. The thermite powder is poured into a thin (1 mil. thick) Teflon or polyethylene bag or tube, forming a donut-like configuration in the bottom of the cavity. A pyrofuse sealed in the bag is used to ignite the thermite. When fully molten, the thermite (8.3×10^{-3} m^3) forms a layer 0.026 m deep on the cavity floor.

Table 16 summarizes some key geometry numbers used in the following calculations. Table 16 also lists the initial conditions prior to failure of the rupture disks. Neglecting flow out the orifice, we assume that the small gas volume in the melt generator compresses isentropically after failure of the rupture disks. Table 17 also summarizes these key conditions.

The burp of gas impinges on the melt surface. Depression of the liquid surface is a measure of the gas's ability to remove the melt from the impingement zone. The depression depth of a gas jet on liquid surface was correlated by Davenport et al. (1966) and later confirmed (Chatterjee and Bradshaw, 1972). Their correlation for the depression depth is given by

$$\frac{h}{h_c}\left(1+\frac{h}{h_c}\right)^2 = \frac{115}{\pi}\frac{\dot{M}}{\rho_L\, g h^3} \tag{4.1}$$

where

h	=	distance between orifice and liquid surface
h_c	=	depth of depression
$\dot{M}$	=	jet momentum flow
ρ_L	=	liquid density
g	=	acceleration due to gravity.

The correlation has received validation in the metals industries over the range

$$10^{-4} < \frac{\dot{M}}{\rho_L\, g h^3} < 10^{-1}\,. \tag{4.2}$$

The jet momentum flow is given by

$$\dot{M} = \rho_g^* V_g^{*2} A_n = \frac{\dot{m}_g}{\rho_g^* A_h}, \tag{4.3}$$

where

$$\dot{m}_g = C_d \rho_g A_h \left(\frac{MW_g}{R_u T_g}\gamma\left(\frac{2}{\gamma+1}\right)^{\frac{\gamma+1}{\gamma-1}}\right)^{1/2} \tag{4.4}$$

is the characteristic flow rate from the compressed gas volume in the melt generator to the cavity, and where

$$\rho_g^* = \rho_g\left(\frac{2}{\gamma+1}\right)^{\frac{1}{\gamma-1}} \tag{4.5}$$

is the gas density in the orifice. For nitrogen (MW_g = 0.028 kg/g-mole, γ = 1.33), the orifice density is $\rho^* g$ = 23.3 kg/m^3, the mass flow rate is $\dot{m}_g$ ~9 kg/s, and the jet momentum flow is $\dot{M} = 2.76 \times 10^3$ N.

The jet momentum flow is well outside the valid range of the correlation, but applying the correlation anyway predicts a depression of $h_c \sim 1.4$ m. This depth may not be realized in a deep pool, but the melt layer in the experiment is only 0.026 m deep. Clearly, the gas burp will punch through to the cavity floor and displace liquid radially so that the water jet will not impinge directly on a melt surface. This does not preclude, however, that melt and water can mix violently in the corners of the cavity after the water jet is redirected by the floor.

The previous argument ignores the dynamics of the process, i.e., ignoring the time to move the molten thermite in comparison to the short lived burp. The burp time constant is

$$\tau_{burp} \sim \frac{m_g}{\dot{m}_g} = 6.61x10^{-3} s. \tag{4.6}$$

The time required to move a liquid plug (orifice diameter x pool depth) at least one orifice diameter is,

$$\tau_{motion} \sim \left(\frac{2D_h \, \rho_L \, A_h \, \delta}{F} \right)^{1/2} \tag{4.7}$$

where the force is given by

$$F = \frac{1}{2} \rho_g \, V_g^2 \, A_h = \frac{1}{2} \, \frac{\dot{M}_g^2}{\rho_g^* \, A_h} = \frac{1}{2} \dot{M}. \tag{4.8}$$

The motion time constant is about 2.76 x 10^{-3}s, which is only about half the burp time constant. Consequently, the burp is only partially effective at moving liquid away from the impingement region before water delivery to the cavity.

4.1.2. Entrainment Prior to Water Delivery

The threshold for particle levitation up the annulus is based on the Kutateladze number,

$$Ku = \frac{\left(\rho_g \, V_g^2 \right)_{annulus}}{\left(\rho_L \, g\sigma \right)^{1/2}} \; \frac{\dot{m}_g^2}{\rho_{g,cav} \, A_{annul}^2} > 14. \tag{4.9}$$

The gas density in the cavity is a function of the gas temperature (which we assume equilibrates with the debris, $T_{g,cav} \sim 2500$ K) and the cavity pressure. The orifice flow area, cavity flow area, and driving pressure do not differ too greatly from the Zion IET tests where representative cavity

pressures were $P_{cav} \sim 0.8$ MPa. Under such conditions, the gas density is $\rho_{g,cav} \sim 1.08$ kg/m^3 and the Kutateladze number is ~ 400, which exceeds the threshold for dispersal.

The potential exists to levitate melt up the annulus, so we must examine the dynamics of the dispersal process by computing the coherence ratio,

$$R_\tau = \frac{\tau_{disp}}{\tau_{burp}} \approx 1.7 \left(\frac{T}{T_d^o} \right)^{1/4} \left(C_d \frac{M_d}{M_g} \frac{A_h V_{cav}^{1/3}}{V} \right)^{1/2}, \qquad (4.10)$$

where the lead constant (1.7, Section 4.5) is indicative of CE geometry. Substituting values, we compute $R_\tau \sim 14$. Consequently, the time required to disperse all the melt from the cavity is an order of magnitude longer than the burp time. As a result, we expect that only negligible quantities of melt will be dispersed from the cavity prior to water injection.

4.2 Pre-HPME Vessel Behavior

Combustion of DCH-produced hydrogen played an important role in the Zion IET tests. This is illustrated in Figure 69, where the pressure rise in tests with a reactive atmosphere are a factor of ~2.5 times greater than pressure rises in tests with inert atmospheres. Reactive atmosphere tests were performed with and without hydrogen preexisting in the containment atmosphere. We concluded, therefore, that the observed differences were due to combustion of DCH-produced hydrogen (produced during cavity dispersal) and that hydrogen (~3%) preexisting in the atmosphere had no observable impact on DCH loads.

We anticipated that hydrogen combustion could also be a significant contributor to DCH loads in some of the CE tests, but the experiment data clearly shows that this was not the case. Figure 70 compares two steam-driven tests. The CES-2 experiment was conducted with a fully inert atmosphere (N_2) while the CE-3 test had a reactive air/steam atmosphere with ~4% hydrogen preexisting in the atmosphere prior to the thermite ignition event. Because of the different atmosphere compositions in the CES-2 and CE-3 tests, the pressure rise is normalized by γ-1 for comparison. This normalization is suggested by the single cell equilibrium model

$$\Delta P = \frac{\gamma - 1}{V} \frac{\sum \Delta E_i}{1 + \psi}. \qquad (4.11)$$

Figure 70 shows that hydrogen combustion, whether DCH-produced hydrogen or preexisting hydrogen had a negligible impact on the HPME pressure rise in the vessel. Some small amount of hydrogen combustion may have occurred in CE-3 to offset a somewhat lower dispersal, but the effect is not large. Figure 71 shows that similar conclusions are derived from the saturated water tests. Dispersal was nearly identical in all the tests driven with saturated water.

Table 17 shows key information regarding hydrogen production and combustion in the CES/CE tests. Row 13 shows that substantial hydrogen burned some time during the test. It is

significant that the number of moles burned (130-323 mole) far exceeds the amount of hydrogen (~80 moles) preexisting in the dome (subcompartment temperatures are never high enough to burn hydrogen at test conditions). Consequently, the production and combustion must be associated with either cavity phenomena or some long term production and combustion. There is no evidence of the latter in the gas samples, so production and combustion must be associated with cavity phenomena. In fact, the combustion numbers are more closely correlated with the production number than they are with available hydrogen in the dome.

Assume for the moment that all the hydrogen was produced and burned on the HPME time scale (~0.1 - 1 s). The potential pressurization,

$$\Delta P = \frac{\gamma - 1}{V} N_{H2} \Delta e_{H2} , \tag{4.12}$$

resulting from adiabatic combustion on the HPME time scale is comparable to or substantially greater than the total HPME pressure rise measured in the tests. This is inconsistent with Figures 70 and 71, which clearly show that potential hydrogen combustion has no impact on observed DCH loads. We, therefore, conclude that the bulk of the hydrogen production and combustion occurred during the thermite burn prior to the HPME event. Such phenomena are not prototypic of a NPP accident where melt is forcibly ejected into the cavity.

Figure 72 shows the pressure in the Surtsey vessel prior to the HPME event. The atmosphere is inert and the cavity is dry in the CES tests. Negligible pressurization of the vessel occurs when the thermite is ignited at ~-10s.

Figure 72 shows that substantial vessel pressurization occurs prior to the HPME event in the four CE tests. These tests all had reactive atmospheres; consequently, significant quantities of hydrogen were produced and burned prior to the HPME event. Videos all show large flames jetting from the RPV annulus into the refueling canal; however, the videos show that this process is noticeably less vigorous in the CE-1 experiment, which had no hydrogen preexisting in the atmosphere. This video observation is consistent with the reported number of moles of hydrogen burned in CE-1 relative to the latter tests.

A lower bound to the number of hydrogen moles produced in the cavity and burned prior to the HPME event can be estimated from the observed pre-HPME pressurization,

$$N_{H2} = \frac{V(\Delta P - 0.014x10^6)}{(\gamma - 1)\Delta e_{H2}} , \tag{4.13}$$

by assuming a complete and adiabatic burn of any hydrogen produced during the thermite burn. Here we subtract out a small contribution to pressurization due to debris/gas heat transfer as inferred from the CES tests. Table 17 (row 17) shows that a minimum of ~30 - 80 moles of hydrogen could have been produced and burned prior to the HPME event in the CE tests. This amount of hydrogen is substantially less than the quantities of hydrogen reported as produced and

burned in the tests. The combustion of preexisting hydrogen, either before or after the HPME event, cannot explain the shortfall in the amount of hydrogen produced. It is likely then, that there are additional processes occurring during the thermite burn that produce additional hydrogen and combustion processes that do not contribute to loads.

Complete oxidation to FeO of all the Fe in the thermite could produce ~330 moles of hydrogen; consequently, the potential source of hydrogen is limited by other processes. The CE tests had air/steam atmospheres such that condensed steam accumulated in the cavity. However, a drain was intended to limit the depth to ~3 - 6 mm. This translates into ~53 - 106 moles of water (and potential hydrogen) in the iron oxidation reaction noted above.

Thermite powders can be hydroscopic to the extent of ~0.3 moles-H_2O/kg-thermite (Gronager et al. (1986). Experiment procedures require baking the thermite to reduce this value by about half; consequently, the water vapor driven from the thermite could produce ~5 moles of hydrogen. Thermal decomposition of the cavity concrete could also release both bound and unbound water as an additional source of steam for iron oxidation. Unbound water, however, is the more likely source since the concrete has been dehydrated from multiple uses while unbound water can be reabsorbed from standing water following each CE test. The decomposition velocity is ~0.35 mm/s for thermite on concrete; consequently, ~10 - 15 moles of unbound water can be driven from the concrete. These numbers are roughly consistent with the inferred amount of hydrogen combustion based on pre-HPME pressurization as noted above. We conclude, therefore, that there is adequate metal and an adequate steam supply in the CE tests to produce sufficient hydrogen to explain the pre-HPME pressurization.

Figure 72 shows that the three tests (CE-2, 3, 4) with preexisting hydrogen in the atmosphere all have higher pre-HPME pressurizations than CE-1, which did not have preexisting hydrogen in the atmosphere. This strongly suggests that preexisting hydrogen burned prior to the HPME event. There are two mechanisms by which preexisting hydrogen can burn prior to the HPME event: entrainment into the burning hydrogen jet venting from the cavity, and by inducing a deflagration in the dome. These mechanisms are quantified next.

Hot hydrogen jets venting from the cavity are observed to burn when they meet oxygen in the refueling canal or dome. All the oxygen for combustion must be supplied by the dome atmosphere. Entrainment, which supplies oxygen to the jet, also carries preexisting hydrogen into the burning jet. This additional hydrogen can also burn. Pilch et al. (1994c), has shown that the moles of preexisting hydrogen that can be entrained and burned is given by

$$N_{H2,e} \sim N^{o}_{H2,dm} \quad \frac{N_{H2,jet}}{N^{o}_{tot,dm}} \quad \frac{1}{2X_{O2} - X_{H2}} \; . \tag{4.14}$$

From CE-1, we estimate $N_{H2,jet}$ ~29.3 moles because all hydrogen must have been supplied by the jet since there was no preexisting H_2. Using test specific input, Table 17 (Row 22) shows that only ~6 moles of preexisting hydrogen need be entrained into the jet. This is an insignificant depletion

of the ~80 moles of hydrogen preexisting in the dome atmosphere. It could be that more hydrogen was produced in the cavity in the CE-2, 3, and 4 tests relative to CE-1, but a factor of two increase would imply that ~12 moles of preexisting hydrogen would be entrained into the jet. This is an upper bound to possible depletion of dome hydrogen because some of the oxygen required to burn the jet hydrogen could have been sucked in through the nozzle cutouts from the subcompartment. Consequently, jet combustion alone is not likely to significantly deplete the hydrogen concentration in the dome.

Hydrogen concentrations (~4%) in the vessel prior to ignition of the thermite are below the flammability limits for the atmosphere composition. However, the production of hydrogen during the burn interval and its subsequent combustion as it vents to the dome could heat the dome possibly to the point where the mixture is no longer inert. It is also possible that not all the H_2 produced in the cavity burned in the jet; consequently, it is possible that the preexisting hydrogen concentrations were increased from their initial value.

Figure 73 shows the pre-HPME dome temperatures in the CE-1 experiment. Huge variations, with temperatures ranging from ~440K to ~630K, are observed throughout the dome region. Subcompartment temperatures show almost no response suggesting that all potential pre-HPME combustion is confined to the dome. We note, however, that there is ~30% reduction in subcompartment hydrogen based on posttest gas analyses, so there must have been some combustion in the subcompartment. However, it cannot be determined if this occurred pre- or post-HPME. The large temperature variations in the dome may be indicative of large composition variations also. For instance, the hottest regions may be composed predominately of combustion products of the burning jet while the cooler regions are more representative of the preexisting atmosphere. The potential for deflagrations is impossible to quantify in such situations because deflagrations are both composition and temperature dependent. We can scope the problem, however, by assessing the potential for deflagrations using the test-specific average dome temperature in conjunction with the test-specific atmosphere composition prior to the thermite burn.

This analysis uses the constitutive relations recommended by Pilch et al. (1994b, Appendix E). The upward and downward flammability limits are given by

$$X_{H2}(up) = 0.037 + 0.0238\ X_{stm} - 5x10^{-5}(T-373)$$

$$X_{H2}(dwn) = 0.075 + 0.02381\ X_{stm} - 1.0135x10^{-4}(T-373) \qquad \textbf{(4.15)}$$

in terms of composition and temperature. Deflagrations will not propagate if the hydrogen concentration is below the upward flammability limit. Complete combustion of all hydrogen is expected when the hydrogen concentration exceeds the downward flammability limit. Between these extremes, the combustion completeness can be approximated by

$$\eta = \frac{X_{H2} - X_{H2}(up)}{X_{H2}(dwn) - X_{H2}(up)} \ . \qquad \textbf{(4.16)}$$

Table 17 suggests that there is some potential for deflagrations (rows 24 and 25) in CE-2, 3, and 4, but maybe not in CE-1. The video records show a brief pulsating orange glow at the end of the thermite burn in CE-2, 3, and 4, suggesting that some deflagration may have occurred. CE-1 did not exhibit this behavior. Table 17 (row 27) shows that ~0 - 15 moles of hydrogen may have burned as a deflagration in the dome. Considering ~6 moles from entrainment plus ~15 moles from deflagration would represent ~25% of the hydrogen preexisting in the dome. As an upper bound, the deflagration potential was recomputed using the maximum dome temperature. In this case, nearly complete combustion of all dome hydrogen is predicted.

DCH produced hydrogen burned and contributed significantly to DCH loads in the Zion IET tests (Figure 69). Figures 70 and 71 show that this is not the case in the CES/CE tests regardless of whether the melt was steam-driven or water-driven. It is plausible that coejected water could quench the melt or inert the combustion. For instance, there is ~2.8 kg of water coherent with debris dispersal in the water-driven CE tests. Vaporization of all this water would quench the melt by ~160K. The Al_2O_3 phase may become partially solidified but the Fe phase would still have a superheat of ~600K; consequently, Fe steam reactions should still be efficient. Fine melt fragmentation (~0.3 mm mass mean) suggests that both phases remained molten, so quenching is not likely the major mitigator.

Inerting of DCH-produced hydrogen is also a distinct possibility in the water-driven tests, but the steam-driven tests also exhibited no signs of significant combustion of DCH-produced hydrogen. In the steam-driven tests, ~50 moles of steam is coherent with dispersing melt; and if all 50 moles of steam is converted to hydrogen which burns, then an additional ~0.077 MPa of pressure should be realized. In reality, the Fe reaction will not go to completion because of thermodynamic limitations, consequently, the potential for pressurization is even less.

The dispersal interval is quite short (~0.1 s) in all the tests, so we ask if there is sufficient time to consume the ~50 mole of steam by metal oxidation during dispersal.

The characteristic time constant,

$$\tau_{rxn} \sim \frac{N_{H2O}}{\dot{R}_{RXN}} = \frac{N_{H2O}}{6k_r \dfrac{M_d}{\rho_d D_d} \dfrac{P_{H2O}}{R_u T}} , \qquad (4.17)$$

$$k_r \sim Sh \frac{\mathcal{D}}{D_d} ,$$

can be computed for cavity conditions (P_{H2O} ~0.8 MPa, $\mathcal{D}$ ~10^{-5} m^2/s) and the posttest measured particle size of 0.3mm. For these conditions and Sh ~2, the reaction time, τ_{RXN} ~0.07, is comparable to the ~0.1s time required to disperse the melt, so it is possible that processes are too rapid to convert coherent steam to hydrogen. The interaction times will be ten times longer at plant

scale so it is reasonable that dispersal will be accompanied by more complete hydrogen production and combustion.

The potential for deflagrations in the dome is small following the HPME event in water-driven CE tests. Although peak dome temperatures range from 650-900K in the tests, these temperatures rapidly drop below ~500K during the ~3 - 4 seconds of blowdown. In addition, blowdown adds a minimum of ~2000 moles of steam from the flashing water, which raises the steam concentration in the dome to ~69 percent while reducing the hydrogen concentration (assuming no pre-HPME depletion) to ~2 percent. It would be impossible to induce a deflagration in the dome under these conditions.

The steam-driven test, CE-3, is not subject to these quenching and inerting processes to nearly the same extent as the water-driven tests. For the limiting conditions T_{max} ~800K, X_{H2} ~0.04, and X_{stm} ~0.42, we find that combustion could be nearly complete, η ~0.88, in the dome. However, the energy release rate is less than half of what is required to overcome heat losses to structures. Consequently, any possible deflagration in the dome would not contribute to containment loads. This conclusion is also true for all pre-HPME deflagrations.

This simple analysis is consistent with the observation (Figure 70) that any possible hydrogen combustion in the dome does not contribute significantly to loads. It is interesting to note that posttest gas analyses show only ~1 percent hydrogen (on a dry basis, no mixing fans) in the dome for CE-3 while CE-4 showed ~3.4 percent hydrogen under similar conditions. Both tests had similar pre-HPME behavior, so the difference likely is due to differences in post-HPME combustion. Thus, post-HPME deflagrations are possible, but they may not contribute to containment loads for the test conditions.

In summary, experiment results show that significant quantities of hydrogen were produced and burned in the CE tests. Significant pressurization of the vessel during the thermite burn, but prior to the HPME event, can be attributed to some of this hydrogen combustion. The video records, in conjunction with scoping analyses, suggest that significant quantities, and possibly all, of the preexisting hydrogen in the dome burned prior to the HPME event. These processes, which are not prototypic, altered the temperature and composition of the atmosphere prior to the HPME event. Experiment results also suggest that DCH-produced hydrogen and any post-HPME deflagrations did not contribute significantly to loads in the HPME; however, this is probably due to the fact that most of the hydrogen burned prior to the HPME, which is an artifact of the experimental method used. Bounding analyses for post-HPME deflagrations suggest that, if they did occur, they would not be expected to contribute to loads. Uncertainties in the timing of hydrogen production and combustion preclude definitive conclusions concerning mitigative processes in NPP analyses.

4.3 Thermite Reaction and HPME Interval

The thermite burn was executed in the cavity rather than the crucible in all CES/CE tests. Rupture disks were then intentionally failed in order to initiate blowdown of water or steam into the

cavity. It is imperative that the thermite reaction be complete prior to blowdown and melt dispersal from the cavity. To ensure this, two scoping tests were performed outside Surtsey using a 33 kg tube of thermite laying on the concrete floor of a test cavity (dimensions similar to the scaled Calvert Cliffs cavity). The purpose of the tests was to determine the minimum delay time after ignition of the thermite prior to commencing the HPME (to ensure reaction completeness). The concrete floor was dry in the first experiment. The thermite appeared to be fully reacted after 12 s. A dark slag appeared to form on the surface of the melt pool by 30 s. A 0.6 cm deep pool of water was placed on the floor in the second test. Again, the thermite appeared to be fully reacted by 12 seconds. However, the burn seemed more intense and slag was not seen until about 50 s after ignition.

Thermite was ignited ~15 - 45 s prior to failure of the rupture disks in the CES/CE tests. This time interval, by design, was sufficiently long to ensure complete reaction of the thermite prior to blowdown. In some cases, however, the delay was sufficiently long to raise questions about energy loss from the thermite and partial freezing of the melt prior to blowdown. Figure 74 shows no decisive correlations of melt retention with the correlation delay time prior to blowdown. Scoping calculations were performed to estimate the magnitude of such energy losses.

Figure 75 depicts the relevant geometry. The bulk averaged temperature can be calculated from a simple energy balance,

$$mc_p \frac{dT}{dt} = -h_{up} A_f (T - T_{w,o}) - h_{dwn} (A_f + A_w)(T - T_{w,o}), \qquad \textbf{(4.18)}$$

where energy is lost upwards by radiation and downwards by conduction into the concrete. Thermal resistances in the melt pool are also represented so that the upward and downward effective heat transfer coefficients are given by

$$\frac{1}{h_{up}} = \frac{1}{h_r} + \frac{1}{h_{Al2O3}} = \frac{1}{\sigma \varepsilon T^3} + \frac{0.67\delta}{K_{Al2O3}}$$

$$\frac{1}{h_{dwn}} = \frac{1}{h_c} + \frac{1}{h_{Fe}} = \frac{2(\alpha_c t)^{1/2}}{K_c} + \frac{0.33\delta}{K_{Fe}}, \qquad \textbf{(4.19)}$$

respectively. Note that the thermal boundary layer in the concrete is time dependent.

These equations apply provided the alumina or iron phases are not freezing. Alumina is the only real concern here because it freezes at 2300K. Once alumina freezing is initiated, the temperature is assumed to remain constant at 2300K until the alumina's heat of fusion has been completely extracted,

$$\int \left\{ h_{up} A_f (T - T_{w,o}) + h_{dwn} (A_f + A_w)(T - T_{w,o}) \right\} dt = 0.45 M \; h_{f,Al2O3} \, . \qquad \textbf{(4.20)}$$

Note that thermite is composed of 45% alumina by weight.

Table 18 lists the material properties used in the analysis. The equations have been solved numerically and the results plotted in Figure 76 for two bounding cases. The first case considers both radiation from the top surface and conduction into concrete. As a bound, the top surface is assumed to radiate to a cold environment at 300K. This situation more closely represents the two scoping tests that were performed outside Surtsey.

Radiation from the top surface is expected to be greatly reduced in the actual experiments carried out inside Surtsey. This is because the top surface no longer radiates to a cold open environment. Instead, the top surface radiates to concrete walls and the melt generator, both of which are splattered by thermite during the early phases of the burn. As a second bound, the heat losses from the top surface are set to zero and conduction into concrete dominates heat losses from the thermite.

Figure 76 shows that the thermite cools to approximately 2300K during the interval (~15-45 s) between thermite ignition and the start of blowdown. Depending on how effective radiation was from the top surface, some freezing of the alumina might have been initiated. At most, ~25% of the alumina or 11% of the total thermite mass may have solidified for those tests with the longest cooling period prior to blowdown (29-45 s). The iron phase will still have ~600 K of superheat at 2300 K, so we expect that it is fully molten and easily oxidized.

4.4 Accumulator Depressurization

4.4.1 Introduction

Accumulator depressurization histories for representative CE tests have been examined. Analyses were performed to quantify the extent to which experiment observations are understood. Blowdown in the SNL/CES/ICE tests can be logically grouped into one of three categories as noted in Table 19. The following sections analyze blowdown records for each category.

4.4.2 Accumulator Depressurization During and After Ejection of a Nonflashing Liquid

Figure 77 depicts the situation to be analyzed. Such a situation exists only in the CES-1 experiment. A pressurized accumulator is partially filled with water, and water ejection is initiated at t = 0. Depressurization occurs in two phases: liquid ejection followed by gas discharge. During the liquid ejection phase, the gas mass in the accumulator remains constant but its volume increases. Single phase gas discharge begins when all the water is discharged from the accumulator. Gas expansion during both phases is assumed to be isentropic and that gas flow through the hole is also assumed to be isentropic during the gas discharge phase. Simple analytic expressions for the depressurization history are developed below for each phase.

Liquid Discharge Phase

A three-step procedure is used:

1. The governing equation for the depressurization transient is developed from (a) water continuity, (b) a state equation for isentropic gas expansion, and (c) constancy of total accumulator volume,

2. The governing equation is normalized to develop an expression for the characteristic depressurization time constant during water ejection, and

3. Simple analytic solutions are derived for the water ejection time and the depressurization transient during water ejection.

The water continuity equation is given by

$$\frac{dV_w}{dt} = - C_d A_h \left(\frac{2\,(P - P_a)}{\rho_w} \right)^{1/2} . \qquad \textbf{(4.21)}$$

There are two time dependent unknowns here: the water volume (V_w) and the accumulator pressure (P). An equation for P alone is sought, so the instantaneous water volume must be related to the instantaneous accumulator pressure. Constancy of accumulator volume requires that

$$V_w = V_g^o + V_w^o - V_g \qquad \textbf{(4.22)}$$

where the instantaneous gas volume (V_g) can be related to instantaneous pressure through a state equation for isentropic expansion,

$$\frac{V_g}{V_g^o} = \left(\frac{P^o}{P} \right)^{\frac{1}{\gamma}} . \qquad \textbf{(4.23)}$$

Combining equations 4.21-4.23 yields the governing equation for depressurization during the water discharge phase,

$$\frac{dP}{dt} = - \frac{\gamma\, C_d A_h}{V_g^o} \left(\frac{P}{P^o} \right)^{\frac{1}{\gamma}} P \left(\frac{2(P - P_a)}{\rho_w} \right)^{1/2} , \qquad \textbf{(4.24)}$$

subject to the initial condition $P\,(t = 0) = P^o$.

This equation is now normalized such that P and its derivative are of order unity. This is achieved by defining normalized variables:

$$t^* = \frac{t}{t_{ref}}, \tag{4.25}$$

$$P^* = \frac{P - P_{\min}}{P^o - P_{\min}} = \frac{P - P_{\min}}{\Delta P}. \tag{4.26}$$

The pressure normalization can be written in a number of useful alternative forms. First,

$$P = P_{\min} + \Delta P\, P^* \tag{4.27}$$

from the basic definition (Eq. 4.26). Divide and multiply the right hand side (RHS) by $P^o = P_{min} + \Delta P$, so that

$$P = P^o \frac{1 + \pi_1 P^*}{1 + \pi_1} = P^o P^+ \tag{4.28}$$

where

$$\pi_1 = \frac{\Delta P}{P_{\min}} \tag{4.29}$$

is a "coupling factor" and

$$P^+ = \frac{1 + \pi_1 P^*}{1 + \pi_1} \tag{4.30}$$

is a transient term that varies from one to $(1+\pi_1)^{-1}$ as P* varies from one to zero. In this way, the physical pressure (Eq. 4.28) is written as a product of a constant term, P^o, that carries the magnitude of the transient and a second term of order unity, P^+, that defines the transient. Physically, when $\pi_1 << 1$, then the accumulator pressure is essentially constant ($P \sim P_{min} \sim P^o$), and the accumulator pressure is decoupled from the water ejection transient. This is the origin of the name "coupling factor."

The utility of these manipulations becomes obvious when the governing equation is normalized,

$$\frac{\Delta P}{t_{ref}} \frac{dP^*}{dt^*} = -\frac{\gamma C_d A_h}{V_g^o} P^o \left(\frac{2(P^o - P_a)}{\rho_w} \right)^{1/2} (P^+)^{\frac{\gamma+1}{\gamma}} \left(\frac{P^+ - \pi_2}{1 - \pi_2} \right)^{1/2}. \tag{4.31}$$

where $\pi_2 = \frac{P_a}{P^o}$.

The intent of normalization is that dP*/dt* and P^+ be transient terms of order unity; consequently,

$$\frac{\Delta P}{t_{ref}} \sim \frac{\gamma C_d A_h}{V_g^o} P^o \left(\frac{2(P^o - P_a)}{\rho_w} \right)^{1/2} \tag{4.32}$$

if both the left hand side (LHS) and the RHS are the same order of magnitude, as they must be. With this recognition, the normalized equation for the pressure transient reduces to

$$\frac{dP^*}{dt^*} = -(P^+)^{\frac{\gamma+1}{\gamma}} \left(\frac{P^+ - \pi_2}{1-\pi_2} \right)^{1/2}, \tag{4.33}$$

which is subject to the initial condition

$$P^*(t^* = 0) = 1 \quad or \quad P^+(t^* = 0) = 1 \quad . \tag{4.34}$$

The characteristic depressurization time during water ejection is then given by

$$t_{ref} = \frac{1}{\gamma} \frac{\Delta P}{P^o} \frac{V_g^o}{C_d A_h \left(\frac{2(P^o - P_a)}{\rho_w} \right)^{1/2}} \tag{4.35}$$

which can also be written as

$$t_{ref} = \frac{1}{\gamma} \frac{\Delta P}{P^o} \frac{V_g^o}{V_w^o} \frac{m_w^o}{\dot{m}_w^o} \tag{4.36}$$

where

$$\dot{m}_w^o = \rho_w C_d A_h \left(\frac{2(P^o - P_a)}{\rho_w} \right)^{1/2}. \tag{4.37}$$

is the characteristic water discharge rate.

An analytic solution to Eq. 4.33 is easily obtained when $\pi_2 = P_a/P^o << 1$, which is the common case of practical interest. Note also that

$$\frac{dP*}{dt*} = \frac{1+\pi_1}{\pi_1}\frac{dP^+}{dt*} \tag{4.38}$$

from Eq. 4.28. With the former approximation and the latter substitution, the governing equation becomes

$$\frac{dP^+}{dt*} = -\frac{\pi_1}{1+\pi_1}(P^+)^{\frac{3\gamma+2}{2\gamma}}, \tag{4.39}$$

which is easily integrated yielding

$$P^+ = \frac{P}{P^o} = \left(\frac{1}{1+\frac{\gamma+2}{2\gamma}\frac{\pi_1}{1+\pi_1}t*}\right)^{\frac{2\gamma}{\gamma+2}}, \tag{4.40}$$

or alternatively,

$$P^+ = \frac{P}{P^o} = \left(\frac{1}{1+\frac{\gamma+2}{2}\frac{\pi_1}{1+\pi_1}\frac{P^o}{\Delta P}\frac{V_w^o}{V_g^o}\frac{\dot{m}_w^o}{m_w^o}t}\right)^{\frac{2\gamma}{\gamma+2}}, \tag{4.41}$$

when written in real time.

Note that P^+ goes to $(1+\pi_1)^{-1}$ as P approaches P_{min}. This observation in conjunction with Eq. 4.36 can be used to find the precise time that marks the end of depressurization during water ejection,

$$t* = \frac{2\gamma}{\gamma+2}\frac{1+\pi_1}{\pi_1}\left((1+\pi_1)^{\frac{\gamma+2}{2\gamma}}-1\right) \tag{4.42}$$

or alternatively

$$t = \frac{2}{\gamma+2}\frac{1+\pi_1}{\pi_1}\frac{\Delta P}{P^o}\frac{V_g^o}{V_w^o}\frac{m_w^o}{\dot{m}_w^o}\left((1+\pi_1)^{\frac{\gamma+2}{2\gamma}}-1\right) \tag{4.43}$$

when expressed as real time.

All parameter evaluations should be written in terms of initial and boundary conditions. This is explicitly obvious, except in the case of

$$\pi_1 = \frac{\Delta P}{P_{\min}} = \frac{P^o - P_{\min}}{P_{\min}} = \frac{P^o}{P_{\min}} - 1, \tag{4.44}$$

where we require an estimate of P^o/P_{min}. Evaluation of P^o/P_{min} falls naturally into one of two phenomenological regimes: inadequate gas volume resulting in incomplete water ejection or adequate gas volume with complete water ejection.

Consider the first regime. The gas volume is small so that the accumulator pressure drops to ambient terminating water ejection before its completion. Under these conditions,

$$\pi_1 = \frac{\Delta P}{P_{\min}} = \frac{P^o}{P_a} - 1. \tag{4.45}$$

The water remaining in the crucible is given by

$$V_{w,f} = V_g^o + V_w^o - V_{g,f} \tag{4.46}$$

where the final gas volume can be expressed in terms of the pressures with the isentropic state equation (Eq. 4.23),

$$V_{w,f} = V_w^o - V_g^o \left\{ \left(\frac{P^o}{P_a} \right)^{\frac{1}{\gamma}} - 1 \right\}. \tag{4.47}$$

The second phenomenological regime has adequate gas to completely eject all the water from the accumulator before the pressure is reduced to ambient. The final pressure is given by the isentropic state equation,

$$\frac{P_m}{P^o} = \left(\frac{V_g^o}{V_g^o + V_w^o} \right)^{\gamma}, \tag{4.48}$$

so that

$$\pi_1 = \frac{\Delta P}{P_{\min}} = \left(\frac{V_g^o + V_w^o}{V_g^o} \right)^{\gamma} - 1 \quad and \quad \frac{\Delta P}{P^o} = 1 - \left(\frac{V_g^o}{V_g^o + V_w^o} \right)^{\gamma}. \tag{4.49}$$

The accumulator temperature at the end of water ejection is also obtained from an isentropic state equation

$$\frac{T_f}{T^o} = \left(\frac{P}{P^o}\right)^{\frac{\gamma-1}{\gamma}} = \left(\frac{V_g^o}{V_g^o + V_w^o}\right)^{\gamma-1} . \tag{4.50}$$

The second regime, which is more relevant to our applications, is assured provided

$$\left(\frac{V_g^o}{V_g^o + V_w^o}\right)^{\gamma} \geq \frac{P_a}{P^o} . \tag{4.51}$$

Gas Discharge Phase

Isentropic depressurization and flow after the water ejection phase are assumed. The depressurization transient is given in gas dynamics text as

$$\frac{P}{P^o} = \left(\frac{1}{1 + \frac{\gamma-1}{2}\frac{\dot{m}_g^o}{m_g^o}\, t}\right)^{\frac{2\gamma}{\gamma-1}} \tag{4.52}$$

where

$$\dot{m}_g^o = C_d A_h P^o \left(\frac{mw_g}{R_u T_g^o}\, \gamma \left(\frac{2}{\gamma+1}\right)^{\frac{\gamma+1}{\gamma-1}}\right)^{1/2} \tag{4.53}$$

is the characteristic gas flow rate. Care must be taken when evaluating these expressions because $P^o = P_f$ and $T^o = T_f$ are the accumulator conditions at the end of the water ejection phase. Likewise, time here is also referenced to the end of the water ejection phase.

Application to the CES-1 Test

Table 20 summarizes input parameters for the depressurization models. The volume of the flow nozzle region below the rupture disks is 0.009 m^3, which is 3.54% of the total volume above the rupture disk. Following failure of the rupture disk, the gas volume above the rupture disk expands as water pushes gas from the flow nozzle. Assuming isentropic expansion of the cover gas, modified initial conditions for the calculation are given by

$$\frac{P}{P^o}=\left(\frac{V_g^o}{V_g^o+V_{gn}^o}\right)^{\gamma}=\left(\frac{T}{T^o}\right)^{\frac{\gamma}{\gamma-1}}. \tag{4.54}$$

The modified initial conditions are in parenthesis in Table 20.

Figure 78 compares experiment data with model predictions. Using a standard orifice discharge coefficient 0.6, the model predicts transition from water to gas discharge reasonably well but tends to overpredict the pressure during any given instant during water discharge. The actual nozzle is better characterized as a reducer from a 10 cm pipe to 30 cm of 5 cm pipe. For such situations, one might expect the discharge coefficient to exceed the orifice value but be less than ideal. Figure 78 shows model predictions for $C_d = 0.8$. Predictions better track the pressure during water discharge, but transition to gas discharge occurs too soon.

Simple hand calculations can be performed to gain insight into the better value. If the pressure were constant, the water discharge time would be given by

$$t=\frac{m_w^o}{\dot{m}_w}=\frac{m_w^o}{C_d A_h\left(2\rho_w(P-P_a)\right)^{1/2}}. \tag{4.55}$$

Using the smaller of the candidate discharge coefficients ($C_d \sim 0.6$), the discharge time would be ~0.62s for a constant pressure of 8 MPa and ~0.88s for a constant pressure of 4 MPa. The actual discharge time should be somewhere in between, ~0.75s. Figure 78 shows that the actual transition time is ~0.9s, which is outside the plausible range and noticeably larger than a reasonable estimate. This apparent inconsistency would be even worse for a discharge coefficient of 0.8.

The explanation probably lies in the ambiguous transient phenomena that occurs in the first 0.1s. These phenomena are largely associated with pressurization and voiding of the nozzle region, and Figure 78 shows that wild pressure oscillations occur during this period before a quasi-steady behavior is observed. Quantitative resolution of this early behavior is outside the scope of this effort. Analysis of the other tests indicates that a discharge coefficient of ~ 0.6 does a good job predicting the data, so it is recommended that $C_d \sim 0.6$ be used in the analysis of CES-1 also. For our purposes, the model developed here provides confidence that our basic interpretation of water discharge followed by gas discharge is adequate.

4.4.3 Steam Only Blowdown

The CES-2 experiment had no water in the accumulator and was pressurized with steam. The blowdown history for such a situation is given by Eq. (4.52). Table 21 summarizes the relevant initial conditions. Figure 79 shows that model predictions are in good agreement with experiment data for a discharge coefficient of 0.6. These predictions provide confidence that steam only blowdowns are adequately understood.

4.4.4 Ejection of a Flashing Liquid Followed by Steam Blowdown

Four tests (CES-3, CE-1, CE-2, and CE-4) were performed with 100 kg of saturated water in the accumulator. The test procedure was to pour 100 kg of cold water into the accumulator. The sealed accumulator was then heated until the partial pressure of steam reached the target conditions of the test. The procedure was reliable and repeatable; consequently, only CES-3 and CE-3 need be analyzed as they are representative of the others. The CE-4 experiment was conducted with about half the driving pressure as the other tests. Table 22 lists the key initial conditions for CES-3.

Water/Steam Inventory

The accumulator pressurization realized in these tests comes as a consequence of vaporizing some of the initial water inventory. Here, we quantify the relative portions. The volume fraction of gas at saturation is given by

$$f_g = \frac{\rho_{l,s} - \rho^o}{\rho_{l,s} - \rho_{g,s}} \tag{4.56}$$

where $\rho^o \sim 100/.254 = 393.7$ kg/m^3 is the initial water inventory averaged over the entire accumulator volume (i.e., the small air mass at one atmosphere is ignored), and where the liquid and gas densities are taken as saturated at the target pressure of 8.33 MPa. The steam volume fraction is 0.473 from which the gas and liquid volumes are computed to be 0.120 m^3 and 0.134 m^3, respectively. Using the appropriate densities, the steam and liquid masses are computed to be 4.37 kg and 95.63 kg, respectively. Consequently, very little of the water inventory is vaporized to achieve the target pressure in the accumulator. Table 22 summarizes these results for later use.

Water Discharge Rate and Flux

Figure 80 shows the depressurization history for CES-3, CE-1, and CE-2. It is obvious that flashing water is being discharged for ~ 2.4s. The mass discharge rate (39.8 kg/s) and the mass flux (3.17 x 10^4 kg/(m^{2}s)) are then quantified and listed in Table 22 as experiment values. We now compare these values with predictions for flashing two phase flow from a nozzle.

The mass flux for critical flashing flows is bounded by

$$G_{HEM} < G < G_{Bernouli}\,. \tag{4.57}$$

The Bernouli mass flux is given by

$$G_{Bernouli} = .61 \left(2\rho_{l,s}(P^o - P_{crit})\right)^{1/2}, \tag{4.58}$$

where the pressure difference driving the flow is controlled by critical pressure (Todreas and Kazimi, 1990; pp. 513). Figure 11-25 (page 511 in Todreas and Kazimi) gives the critical pressure ratio (P_{crit}/P^o) as a function of the nozzle L/D ratio. For the experiment nozzle, L/D ~ 5.7 and $P_{crit}/P^o \sim 0.45$. The Bernouli mass flux is then 3.49×10^4 kg/(m^{2}s).

For sufficiently long nozzles, Lahey and Moody (1993) state that the critical mass flux can be reasonably predicted with the homogenous equilibrium model (HEM). This is illustrated by Lahey and Moody in Fig. 9-20, on page 457 in their text. Figure 9-10a in Lahey and Moody shows that G_{HEM} can be read from a plot with the stagnation enthalpy ($h_{l,s}^o$) of the outflow and system pressure (P^o) as parameters. The stagnation enthalpy of the saturated liquid is 1.35 MJ/kg so that $G_{HEM} \sim 2.93 \times 10^4$ kg/(m^{2}s).

In summary, the experimentally determined mass flux of flashing water is tightly bounded by predictions using the Bernouli discharge model and the homogeneous equilibrium model.

Depressurization Rates

Figure 80 shows that the depressurization rate is nearly constant at 1.16 MPa/s during the period of flashing discharge. Lahey and Moody (1993, pp. 475) express the depressurization rate as

$$\frac{dP}{dt} = - \frac{A_h \, G(P^o, h_{l,s}^o)}{M \, F(P^o, V/M)} \left[h_{l,s}^o - f(P^o) \right] \qquad \textbf{(4.59)}$$

where $F(P^o, V/M)$ and $f(P^o)$ can be read from Figures 9-27 and 9-28 in Lahey and Moody (1993). Using the measured mass flux, the depressurization rate is estimated to be ~ 0.84 MPa/s. This is lower than the experimentally determined rate of ~ 1.16 MPa/s, and the reason is not readily apparent.

Eq. (4.52) can be used to predict the gas blowdown phase provided the time of transition is properly taken into account. The initial pressure and temperature are 6.31 MPa and 552 K as estimated from a predicted depressurization rate of 0.84 MPa/s up to 2.4s. A discharge coefficient of 0.6 is used.

Figure 80 compares model predictions with the experiment data. The models generally overpredict the pressure during discharge of flashing liquid; however, these predictions are adequate to demonstrate a basic understanding of the key processes. The gas discharge phase is well predicted if the somewhat higher initial conditions are acknowledged. Figure 80 also shows a prediction assuming the water is discharged as a nonflashing liquid. These predictions are in gross disagreement with the data.

4.5 Coherence of Debris Dispersal and Blowdown

The TCE model assumes that debris/gas interactions in the cavity are limited to that portion of the blowdown gas that is coherent with the dispersal process. The ratio of the characteristic dispersal time to the characteristic time constant of blowdown is termed the coherence ratio. Smaller values of the coherence ratio means that the primary heat sink for debris/gas thermal interactions is smaller and that metal/steam reactions are more likely to be steam limited.

The notion that noncoherence (between debris dispersal and RCS blowdown) can limit DCH interactions is not unique to the TCE model. Ginsberg and Tutu (1987) were the first to suggest this limitation. Early CONTAIN calculations (Williams and Louie, 1988) also exhibited some sensitivity to coherence, though the effect found was not large. The CLCH model (Yan and Theofanous, 1993) also considers noncoherence as a basic modeling process. These analytic reflections all have a solid basis in experiment observations. Unpublished real-time flash x-rays taken at SNL show that dispersal is complete well before blowdown. In addition, many experiments have been conducted (e.g., Allen et al., 1991; Allen et al., 1992a,b) with pyrometers focused on the cavity exit. Pyrometer signals also confirm the notion of noncoherence, and they suggest that cavity pressurization records can also be used to define the coherent interval. Despite this physical evidence, no systematic experiments have ever been performed for the purpose of directly validating the impact of noncoherence on DCH loads.

Pilch (Appendix E in Pilch et al., 1994b) developed a correlation for the coherence ratio based on momentum considerations. The Pilch correlation can be expressed as

$$R_\tau = \frac{\tau_e}{\tau_b} = C_{R\tau} f_{disp} \left(\frac{T^o_{RCS}}{T^o_d} \right)^{1/4} \left(C_{d,h} \frac{M^o_d}{M^o_g} \frac{A_h V_c^{1/3}}{V_{RCS}} \right)^{1/2}, \tag{4.60}$$

where $C_{R\tau}$ is determined from experiment data. For an isentropic blowdown of the RCS, the fraction of blowdown gas that is coherent with debris dispersal is given by

$$f_{coh} = 1 - \frac{M^o_g}{M_{g,e}} = 1 - \left(\frac{P_{e,RCS}}{P^o_{RCS}} \right)^{\frac{1}{\gamma}} = 1 - \left(1 + \frac{\gamma - 1}{2} R_\tau \right)^{\frac{-2}{\gamma - 1}}. \tag{4.61}$$

for $R_\tau \le 0.5$, $f_{coh} \sim R_\tau$, so that R_τ is directly proportional to the amount of blowdown gas that can react with the debris.

The coherence ratio determines how much blowdown gas has been vented from the RCS (or accumulator) on the same time scale as debris dispersal. Figure 81 shows a conceptual cavity pressurization record and a conceptual accumulator blowdown curve. The entrainment interval is determined primarily from the cavity pressurization record and is defined as the interval of time when cavity pressure exceeds vessel pressure. Pyrometers and video cameras placed at the cavity exit show that the cavity pressure joins the containment pressure at the end of debris dispersal.

Despite these independent measures, cavity pressure and pyrometers, the interpretation of the entrainment interval is still inherently subjective. The end of the entrainment interval is marked by τ_e' and corresponds to a final pressure P_e in the RCS. The decline in RCS pressure over the entrainment interval is a direct measure of the amount of gas vented into the cavity, and for an isentropic expansion within the RCS,

$$f_{coh} = \frac{\Delta M_g}{M_g^o} = 1 - \frac{M_g^o}{M_{g,e}} = 1 - \left(\frac{P_e}{P^o}\right)^{1/\gamma} . \tag{4.62}$$

For computational convenience, it is useful to idealize the blowdown process as a single-phase gas discharge from a fixed size orifice (after any possible ablation). For isentropic expansion in the RCS and isentropic nozzle flow, the ideal blowdown history can be approximated by

$$\frac{P}{P^o} = \left(1 + \frac{\gamma - 1}{2}\,\frac{t}{\tau_b}\right)^{\frac{-2\gamma}{\gamma-1}} , \tag{4.63}$$

where the characteristic blowdown time is given by

$$\tau_b = \frac{M_g^o}{\dot{M}_g^o} . \tag{4.64}$$

Physically, the pressure will be reduced to 29 percent of its initial value (for $\gamma = 1.33$) after one time constant, and 61 percent of the initial gas mass will have been vented from the RCS.

The "measured" coherence ratio, assuming the idealized blowdown and consistent with the measured depressurization over the entrainment interval, is obtained from Equation 4.65,

$$R_\tau = \frac{\tau_e}{\tau_b} = \frac{2}{\gamma - 1}\left[\left(\frac{P^o}{P_e}\right)^{\frac{\gamma-1}{2\gamma}} - 1\right]. \tag{4.65}$$

The real utility of this formulation is that the idealized flow will predict the same quantity of vented gas (using this value of the coherence ratio) as the actual flow will vent by the end of the *measured* entrainment interval. Measured values of the coherence ratio are presented in the last column of Table 23. The supporting experiment information is listed in the prior two columns.

Figure 82 shows a correlation of the measured coherence ratio with Equation 4.60 for those cases where steam alone is the dispersing medium. The more extensive database for the Zion and Surry cavities is also shown for comparison. The solid lines represent least squares regressions through the data. The cavity-specific constant, $C_{R\tau}$, is also determined from the least squares

analysis, with the $C_{R\tau}$ values being listed in Table 24. Table 24 also shows two statistical measures for the correlation: the relative bias and the relative RMS error (standard deviation) referenced to the bias line. The statistical measures are defined by

$$e_{bias} = \frac{\Sigma\left(\frac{\Delta P_{pred,i} - \Delta P_{meas,i}}{\Delta P_{pred,i}}\right)}{N} \qquad \sigma^2_{rms} = \frac{\Sigma\left(\frac{\Delta P_{pred,i} - \Delta P_{meas,i}}{\Delta P_{pred,i}} - e_{bias}\right)^2}{N-1} \; . \tag{4.66}$$

The statistics for the Calvert Cliffs cavity are not very good because of the limited database and because the "measured" values of R_τ are sensitive to the selected values of P°/Pe when they are close to unity . The key observation, however, is that the Calvert Cliffs cavity is approximately six times more dispersive than Zion-like or Surry-like cavities even with the acknowledged uncertainties.

Columns 2-8 of Table 23 provide all the information necessary to evaluate the RHS of Equation 4.60. Consistent with the blowdown transients, the discharge coefficient is taken at 0.6. Table 25 examines the applicability of the existing database to Calvert Cliffs applications. It is clear that the database largely overlaps typical reactor applications. We note that ignition of thermite in the cavity (rather than pressure driven ejection into the cavity) probably maximizes coherence. In the more prototypic case some melt may have already exited the cavity under its own momentum prior to gas blowdown. Furthermore, we note that complete oxidation of the zirconium in-core debris is predicted in NPP applications, even with this much reduced coherence.

It is useful to examine the Zion and Surry databases for validation insights on parameters other than cavity design. This is because the database for Calvert Cliffs is too limited. Zion and Surry experiments have been conducted at 1/40th, 1/30th, 1/20th, 1/10th, and 1/5.75th scale. The data confirm model predictions that there is no effect of physical scale. Experiments have been conducted at driving pressures ranging from 4 to 13 MPa, with hole sizes ranging from 0.4 m to 1.0 m (full scale equivalent), and melt densities ranging from 4000 - 8000 kg/m^3. These dependencies are adequately accounted for by the model. Cavity design is the sole systematic deviation of the data from the correlation. Variations with cavity design, which are not fully accounted for by the model, are not surprising given that such variations are well documented in experiments that define the low pressure dispersal curve. This implies that different values of $C_{R\tau}$ are required in Equation 4.60 for each cavity design.

Table 26 shows how many moles of steam are coherent with the dispersal process,

$$N_{coh} \sim N^o_{acc} \; R_\tau \; , \tag{4.67}$$

for the two steam driven tests. It is instructive to compute the amount of coherent steam (flashing) and water in the water-driven tests. We can ignore the accumulator steam (or nitrogen) in the water-driven tests because the dispersal interval is only ~0.1 s while the water ejection interval is ~2.5 s.

The moles of coherent steam and water in the water-driven tests can be computed from

$$N_g \sim \frac{X_g \dot{M}_w t_e}{MW_{H20}} \tag{4.68}$$

$$N_w \sim \frac{(1-X_g) \dot{M}_w t_e}{MW_{H20}} . \tag{4.69}$$

The water ejection rate $(\dot{M}_w)$ is estimated by dividing the initial 100 kg of water by the ejection interval as observed in accumulator blowdown plots. If the water is superheated relative to the containment pressure, then some of the water will flash to steam when it discharges into the cavity. The thermodynamic quality (X_g) can be estimated by assuming isenthalpic blowdown to containment pressure. The dispersal interval is estimated from the cavity pressurization interval. With this input, the moles of coherent steam and water can be computed with Equations 4.68 and 4.69. The results are presented in Table 26.

The amount of coherent steam in tests with saturated water is approximately double that in the steam-driven tests with the same driving pressure. Coherent steam in the steam-driven tests is only a small fraction (~15%) of 330 moles required to oxidize all the Fe in the thermite. In the water-driven tests, there is sufficient coherent steam from flashing and coherent saturated water to oxidize 50-90% of the iron.

4.6 Flow of Dispersed Material Into the Subcompartments

The Calvert Cliffs geometry favors debris dispersal into the dome. In the CES/CE experiments, approximately 75% of the dispersed melt passed into the dome. This is obtained directly from the posttest mass balance. This can be contrasted to the 10 - 20% dome transport observed in the Zion and Surry test. Figure 83 depicts the Calvert Cliffs geometry. There are two paths by which ~25% of the dispersed melt can enter the subcompartments: through the small manway on the cavity floor and through the six nozzle cutouts in the biological shield wall. Our intent here is to estimate how much material enters the subcompartment through the nozzle cutouts.

Below the RPV, melt may enter the annular gap around the RPV or may disperse out the manway opening. Pilch (1994b, Appendix I) has shown for Zion and Surry cavities that the fraction of dispersed melt entering the gap,

$$f_g \sim \frac{A_g}{A_g + A_{mw}}, \tag{4.70}$$

is just the area fraction for that particular flow direction. Table 27 shows that ~95% of the dispersed material is expected to enter the gap. This is because the manway area is small compared to the gap

area, and because a plug (in the experiment) in the manway fully opened as intended in only the CES tests. The manway area was partially plugged in the CE tests. To first order, almost all the material collected in the subcompartments must pass through the nozzle cutouts. This is quantified more carefully as follows.

The fraction of material entering the dome

$$f_{dm} = f_g(1 - f_{nz}) \tag{4.71}$$

is determined largely by how much material passes up the gap, subject only to some attenuation as material is diverted through the nozzle cutouts. The dome transport fraction, f_{dm}, is determined experimentally, and f_g has been estimated previously; consequently, the inferred nozzle split fraction can be computed as

$$f_{nz} = 1 - \frac{f_{dm}}{f_g}. \tag{4.72}$$

Table 27 shows that approximately 22% of the melt passing through the gap is diverted by the nozzles into the subcompartment. Comparing the steam-driven tests (CES-2, CE-3) with the others suggests that f_{nz} is not sensitive to the dispersing medium. Comparing CE-4 (4 MPa) with the other tests (8 MPa) suggests that f_{nz} is not a strong function of driving pressure. This lack of pressure sensitivity contradicts observations by Bertodano (1993) using a similar geometry.

Bertodano performed 1/20th scale experiments with Woods metal as the melt simulant and N_2 or He as the dispersing medium. Bertodano found that ~21% of the dispersed material passed through the nozzle cutouts. This fraction is similar to our results, except that Bertodano reports some sensitivity to flow parameters. Bertodano found that increasing the pressure from 4.1 MPa to 6.8 MPa decreased the amount of material dispersed through the nozzles from 31% to 13%. Bertodano cautions that the experiments were not scaled for this phenomena. In particular, the amount of finely fragmented entrained material was far less than expected at plant scale. The measured sieve mass mean size is ~0.3 mm in the CES/CE tests suggests that more prototypic conditions were achieved, perhaps because of the increase in physical scale, the higher driving pressure, and the feedback of gas heating in the cavity.

There are two physical mechanisms by which dispersing melt can be diverted into the nozzle cutouts. The first involves splashing off the underside of the nozzles. As an upper bound, we assume that everything striking the bottom of the nozzles is diverted into the cutouts

$$f_{nz,splash} \sim \frac{A_{nz,bottom}}{A_g}, \tag{4.73}$$

where $A_{nz,top}$ is the projected area of the nozzles on the gap looking up from the bottom. Table 27 shows that this approach overpredicts f_{nz} by more than a factor of two; however, it is reasonable that

not all the projected area of the nozzles in the gap is effective at diverting the dispersing melt. Since our experiments are geometrically scaled, we expect that this contribution to flow into the cutouts will be preserved.

The second mechanism for diverting melt into the nozzle cutouts is for small particles to follow the gas flow into the cutouts. As an upper bound, we can assume that all the particles are efficient at following the gas flow. In this bound,

$$f_{nz,flow} \sim \frac{A_{nz}}{A_{nz} + A_g}. \tag{4.74}$$

Table 27 shows that this simple expression also overpredicts f_{nz} by more than a factor of two.

This is not surprising since it is well known that dispersing melt does not follow gas streamlines very well. For a geometrically scaled experiment such as ours, the relevant scaling parameter is

$$\pi = \frac{\rho_g}{\rho_d} \frac{L}{d}. \tag{4.75}$$

Particles follow gas streamlines for larger values of this scaling group. Thermite has half the density of corium, but this distortion is overcompensated for by a factor of ten increase in length scale when extrapolating to plant scale. Since we expect similar particle sizes at plant scale, there is the potential for enhanced diversion through the cutouts at plant scale.

In summary, the experiments suggest that ~20% of the melt passing up the gap will be diverted into the nozzle cutouts and that number is not sensitive to driving pressure or driving medium. Scaling arguments imply that comparable or greater diversion into the cutouts can be expected at plant scale. Simplistic arguments based on splashing areas or perfect coupling of debris and gas are inadequate for predicting debris diversion into the cutouts.

4.7 Validation of the TCE Model in Open Geometry Experiments

The Calvert Cliffs cavity geometry is such that most melt will be dispersed directly to the upper dome of the containment. Thus, the Calvert Cliffs geometry does not favor the mitigating processes resulting from debris trapping in subcompartment structures as observed in Zion and Surry geometries. The TCE model was successful in predicting experiment results in Zion and Surry geometries, and it is our desire here to validate TCE for application to the Calvert Cliffs geometry.

Experiment results clearly show that DCH loads are lower in the water-driven CES/CE tests compared to the steam-driven tests. Since TCE has no model for water interactions, we validate the TCE model against the more bounding steam-driven tests: CES-2 and CE-3. We note that thermite was burned in the cavity rather than forcibly ejected from the melt generator. This

nonprototypicality is not expected to influence significantly the experimental pressure rises because debris/gas interactions in the dome dominate debris/gas interactions in the cavity. The experiment is conservative in this regard (i.e., more time for cavity interactions) because in the more prototypic pressure driven case, some melt may exit the cavity under its own momentum prior to gas blowdown.

Figure 84 compares TCE loads predictions with experiment observations. The model conservatively overpredicts loads by 21% and 24% for the CES-2 and CE-3 tests, respectively. The Calvert Cliffs experiment geometry faithfully modeled subcompartment structures (~40% of the total volume), although most debris is dispersed to the dome. Experimentally observed dispersal fractions and the experimentally determined distribution of mass between the dome and subcompartment were used in the input. Experimentally observed coherence ratios were also used in the input. The thermite burn altered containment conditions prior to the HPME event. The bulk average vessel temperature just prior to the HPME event was used in the TCE input. Atmosphere composition was also altered during the thermite burn in some unquantifiable manner. The calculations were performed with the initial atmosphere composition prior to the thermite burn; however, TCE predicted that deflagrations would not contribute to the observed experiment loads. The specification of these quantities for plant calculations is addressed in other sections.

Figure 84 also shows TCE validation against other experiments in the database where all debris was dispersed directly to the dome. These experiments differ from the CES/CE experiments in that no subcompartment structures whatsoever existed in the test chamber. Figure 84 shows that TCE (taken in a limiting case of only one cell) often overpredicts these older experiments by ~100%. This is somewhat surprising since it might be expected that TCE's equilibrium assumptions might be more closely approached in these open geometry tests. This apparent discrepancy is addressed below to gain better confidence in model predictions.

Two potential mitigating processes have been identified: freezing of dispersed melt on the dome, and time-of-flight (TOF) limitations to debris/gas interactions in the dome. Table 28 summarizes the assessment of these processes for the various test series. The "measured" efficiency,

$$\eta_{meas} = \frac{\Delta P_{meas}}{\Delta P_{pred}}, \tag{4.76}$$

is taken as the ratio of measured to predicted loads. It is seen that the CES/CE tests are more efficient than the earlier tests.

Freezing of dispersed melt on the dome was important in the SNL/DCH/TDS tests. The settling time for debris to fall from the roof to the floor is about six times longer than the time for debris to rise from the cavity and freeze on the dome. In addition, the rising debris travels in a tight plume and does not significantly interact with the atmosphere as a whole. Consequently, we expect that DCH loads in the SNL/DCH/TDS tests will be greatly mitigated due to excessive freezing on

the dome. The TCE predictions for these tests used the entire dispersed mass and not just what settled to the floor.

A measure of this effect is given by

$$\eta_{mass} = 1 - \frac{M_{roof}}{M_{disp}}. \tag{4.77}$$

Table 28 summarizes the appropriate numbers. Almost half the dispersed mass froze on the bare steel dome in the SNL/DCH/TDS tests. This was not the case in the latter tests. A painted concrete slab intercepted debris just prior to impact with the dome in the SNL/WC/LFP8 tests. Melt did not adhere to this surface. In the SNL/CE-3 test, melt did not adhere to structures because they were wet from condensing steam. Debris did not adhere to structures in the SNL/CES-2 test, but for reasons that are not readily identifiable.

Time-of-flight limitations to debris/gas interactions is the second possible mitigating mechanism. Debris may settle to the floor before debris/gas interactions can achieve equilibrium. Debris that has settled on the floor is not very efficient at heating the bulk atmosphere because heat is lost to the floor, because debris velocities are reduced to zero, and because the settled debris can interact with only a thin layer of the atmosphere near the floor.

An analytical expression,

$$\eta_{KE} = 1 - exp\left(-\tau_{trap} / \tau_{HT}\right), \tag{4.78}$$

is easily derived for the kinetic efficiency, which describes how much debris/gas heat transfer actually occurs prior to debris settling relative to how much must occur in order to achieve equilibrium. The time for debris to fall at terminal velocity from the roof to the floor is given by

$$\tau_{trap} = \frac{H}{v_d}, \tag{4.79}$$

where the terminal velocity is

$$v_d = \left(\frac{4}{3}\,\frac{1}{c_d}\,\frac{\rho_d}{\rho_g}\,g\,D\right)^{1/2}. \tag{4.80}$$

The time constant for all airborne debris to reach thermal equilibrium with the atmosphere is given by

$$\tau_{HT} = \frac{m_d \Delta e_d}{1+\psi}\,\frac{1}{\dot{R}_{HT}} \tag{4.81}$$

where the heat capacity ratio,

$$\psi = \frac{m_d c_{p,d}}{m_a c_{v,a}}, \tag{4.82}$$

appears because the debris/gas equilibrium temperature may be high and not all the latent and sensible heat in the debris will be transferred to the gas in order to achieve equilibrium. The characteristic energy exchange rate,

$$\dot{R}_{HT} = 6\ h_{dg}\ \frac{M_d}{\rho_d D}\left(T_d^o - T_a^o\right), \tag{4.83}$$

is the sum of the energy exchange rates for all airborne particles. Lastly, radiation and convection contribute as parallel processes to the effective debris/gas heat transfer coefficient

$$h_{dg} = h_r + h_c = \sigma_d \varepsilon_d T_d^3 + \frac{k_a}{D}(2 + 0.6\,Re\,0.5\,Pr\,0.33). \tag{4.84}$$

It should be noted that the kinetic efficiency (η_{KE}) is a function of particle size, and a broad spectrum of particle sizes are observed in the tests. Bigger particles fall faster (small τ_{trap}) and have less efficient debris/gas heat transfer (longer τ_{HT}). The kinetic efficiency is computed for each test series using the atmosphere conditions appropriate to the tests and using the sieve mass mean particle size appropriate to the individual test. In general, the sieve mass mean particle size was ~1 mm for all the tests except the SNL/CES/CE tests where the sieve mass mean particle size was ~0.3 mm.

The computed kinetic efficiency for each test series is listed in Table 28 where the mass mean particle size (50%) is used as the basis. For the lower half of the observed particle size distribution, complete or nearly complete energy exchange can be expected. The process was completed again for particle sizes representative of the midpoint of the upper half (75%) of the particle size distributions. At the upper end of the particle size distribution, Table 28 shows that debris/gas interactions can be inefficient.

The overall efficiency of debris/gas interactions in the tests can be estimated by taking a weighted average of the kinetic efficiency and considering only the debris mass that does not freeze quickly on the roof of the test chamber,

$$\eta_{pred} = \eta_{mass}\left[0.5\,\eta_{KE}(50\%) + 0.5\,\eta_{KE}(75\%)\right]. \tag{4.85}$$

Table 28 shows that a combination of freezing on the dome or TOF limitations for some dispersed particles can explain the relatively low measured efficiencies observed in some of the open geometry tests.

All structure surfaces in a NPP are painted and are expected to wet from condensed steam; consequently, freezing of dispersed melt on the dome is not expected to be a significant mitigator of DCH loads. Dome heights are a factor of 5 - 10 bigger in a NPP relative to the experiments, while particle sizes are expected to be comparable. Thus, TOF limitations are not expected to be a significant mitigator of DCH loads at plant scale.

In summary, it is expected that near equilibrium conditions were achieved in the SNL/CES-2 and SNL/CE-3 tests. Significant mitigation in earlier open geometry tests can be explained in terms of a combination of freezing on the dome and TOF limitations. The TCE model is not expected to be overly conservative in NPP applications.

4.8 Impact of Coejected Water on DCH Loads in Calvert Cliffs Geometry

Water is expected to be in the lower plenum of the reactor pressure vessel in DCH-relevant accident sequences. The quantity of water present is a function of the accident sequence and potential operator interventions. Should the lower head fail while the RCS is still pressurized, melt and water would be coejected from the RPV into the reactor cavity. The TMI-II accident came close to this situation.

Water coejected from the RPV, unlike water that might be present in the cavity, has the potential to pressurize the containment even in the absence of DCH contributions. This is because coejected water (at high pressure) will be superheated relative to containment pressure, so some of the water will flash to steam during the blowdown.

With an RCS full of saturated water at system setpoint pressure (16 MPa), blowdown into the containment (the large LOCA design basis accident) could pressurize the containment by ~0.3 MPa. The question then arises as to whether DCH loads are additive to this pressurization. The flashing water could be an additional source of hydrogen, but hydrogen combustion may be less likely because of additional steam inerting.

The possible interactions are complex and beyond current modeling capabilities; consequently, we rely on experiments for a more direct answer. Table 29 summarizes the observed effects of coejected water on DCH loads in Calvert Cliffs geometry. Driving with saturated water reduces loads by 10 - 20% relative to the steam-driven tests, and driving with room temperature water reduces loads by ~25%. Consequently, we conclude that large amounts of coejected water reduces DCH loads (when hydrogen combustion is not significant) in Calvert Cliffs geometry.

These observations are from experiments where any potential hydrogen combustion had an insignificant impact on DCH loads. Situations in the NPP can exist where preexisting hydrogen concentrations can be well above the flammability limits. In these cases, coejected water can partially quench the atmosphere (i.e., keep it cooler) and the flashing component can significantly increase the steam concentration in the dome. Taken together, it is likely that coejected water could mitigate hydrogen combustion; however, this mitigation has not been demonstrated decisively in

the tests; consequently, a more conservative approach to hydrogen combustion is recommended that takes no credit for coejected water's potential to mitigate hydrogen combustion.

Figure 71 compares the post-HPME pressure rise for tests driven with saturated water. It can be seen that the bulk of the pressurization occurs on the debris dispersal time scale (~0.1 - 0.2s). Following this rapid pressure rise (which is associated with rapid heating of the dome atmosphere) the containment pressure holds constant for the ~3s of flashing discharge from the RPV.

Gas temperatures in the dome are observed to drop significantly during the blowdown period when the containment pressure remains constant. Thus, containment pressure is being maintained by additional moles from the flashing fraction of the blowdown and possibly from the vaporization of the liquid fraction of the blowdown by the hot atmosphere. The processes that contribute to the maintenance of containment pressure can be expressed as

$$\frac{V}{\gamma - 1}\frac{dP}{dt} = X_g \dot{m}_w h_g + f_w(1 - X_g)\dot{m}_w(h_g - h_{fg}) = 0 \qquad \textbf{(4.86)}$$

where the first term is the enthalpy addition to the atmosphere resulting from the flashing fraction (X_g ~0.37 in the test driven with 8 MPa) of the blowdown. The second term represents additional enthalpy addition to the atmosphere resulting from vaporization of some fraction (f_w) of the liquid portion of the blowdown. Note that X_g is a weak function of RCS and containment pressures and that h_g (0.744 MJ/kg-w) and h_{fg} (2.26 MJ/kg-w) are only weak functions of the containment pressure. In this formulation, we note that the reference temperature for h_g is zero degrees Kelvin so that $h_g \sim c_p T$.

If all the blowdown water (f_w = 1) was tightly coupled with the atmosphere temperature, then dP/dt would be strongly negative and the containment pressure should decline rapidly following the initial pressure rise during the dispersal interval. For the pressure to remain constant, only ~29% of the liquid water (f_w ~0.29) must be vaporizing as the hot atmosphere is quenched. Thus, there is not much potential for coejected water to enhance loads unless substantially larger quantities of hydrogen are produced by metal/steam reactions during dispersal, and this HPME-produced hydrogen burns. Figures 70 and 71 show that this is not the case. At reactor scale, the time available for water interactions with the hot atmosphere are increased significantly, so that a greater fraction of the water may couple with the atmosphere and participate in its quenching. Thus, the potential for blowdown of flashing water to mitigate loads is increased at plant scales.

In conclusion, the SNL/CES/CE tests demonstrate that DCH loads with coejected water are comparable to or less than DCH loads for steam-driven tests. The potential for mitigation is expected to increase at plant scale.

4.9 Consistency in Pressure, Temperature, and Moles

The ideal gas law,

$$Z = \frac{PV}{NRT} = 1, \tag{4.87}$$

requires consistency in pressure, temperature, and moles in the containment atmosphere. We test this consistency for each test at three different times. The first time is at the end of the pre-HPME thermite burn interval. This is just prior to failure of the rupture disks and after the thermite burn. The time of peak pressure is examined next. It is difficult to get a representative average temperature during this period, so we make the last assessment at 20 s after failure of the rupture disk.

The pressure measurements are reliable and consistent everywhere in the vessel. Temperature is more problematic because strong temperature gradients exist in the vessel, especially during the blowdown period. This requires that we use a mole average temperature in the vessel. We have only point measurements (thermocouple arrays) of temperature in the dome and subcompartment, so we approximate the mole average by taking the arithmetic average within the dome and within the subcompartment and then performing a mole average of the dome and subcompartment. This is only an approximation because strong temperature gradients exist within the dome and subcompartment separately.

The number of moles in the vessel prior to the thermite burn is well characterized; however, processes occurring during the thermite burn can alter the molar content of the atmosphere prior to the HPME event. These processes include: vaporization of the bag containing the thermite, offgasing of the thermite, concrete decomposition, vaporization of condensate water in the cavity, hydrogen combustion, and oxygen uptake by the metals. All these processes occur in the CE tests. The CES tests are simpler in that only the first three processes can occur because the cavity is dry and because the atmosphere is inert. In Table 30, consistency is tested based on the initial number of moles in the vessel so any significant deviation of Eq. 4.87 from unity is a measure of the importance of these other processes.

Table 30 shows that Z ~1 for the pre-HPME period. It is interesting to note that Z is slightly greater than unity for the CES tests. The number of additional "produced" moles necessary to force Z=1 is also listed. For the CES tests, these numbers follow closely the reported number of H_2 moles produced. This suggests that a large portion of the H_2 may have been produced prior to the HPME event; however, uncertainties in the vessel average temperature preclude a definitive interpretation.

The CE tests have many more processes that can alter the number of moles in the vessel. In spite of this, Z more closely approaches unity in the CE tests. This may be because we have a limited ability to estimate an average temperature or it may be because there are processes in the CE tests that both add or consume moles in the vessel, so there may be some tradeoff.

Peak pressure in the CES/CE tests usually occurs at the end of the blowdown period. We tested consistency based on the initial moles in the vessel plus any moles added during blowdown. This includes that fraction of any coejected water that flashes to steam during blowdown. It does not include water that does not flash but subsequently vaporizes through heat transfer from the melt or the hot atmosphere. We did not consider the impact of hydrogen combustion or metal oxidation on the mole basis. Table 30 shows that there is not good consistency during the blowdown period, but we suspect that this may be due to particularly poor estimates of the average atmosphere temperature.

We examined consistency at a later time (~20 s) when things are perhaps more settled in the vessel. The basis for vessel moles is the same as the analysis at peak pressure.

Consider first the two steam-driven tests (CES-2, CE-3) at 20 s. The Z value is near unity as expected. The Z value is also near unity for the four tests driven with flashing water (CES-3, CE-1, CE-2, and CE-4) at 20 s. The large amount of flashing blowdown is comparable to about half the number of moles initially in the vessel. Second order effects like additional water vaporization or molar changes due to combustion would be difficult to resolve with so many moles in the vessel.

Consider now CES-1 at 20 s. The Z value exceeds unity by a potentially significant amount, suggesting that excess moles (~509) were created by water vaporization. This 509 moles of additional vaporization (in addition to flashing during blowdown) represents about 15 percent of the water that did not originally flash upon blowdown. The 33 kg of thermite has sufficient thermal energy to vaporize ~2000 moles of saturated water.

Table 16. Debris dispersal prior to water delivery

Parameters	Accumulator	Melt Generator	Orifice	Cavity
Geometry				
V^o (m^3)	0.17	$2.5x10^{-2}$		0.113
D_h (m)				0.04
A_h (m^2)			$1.26x10^{-3}$	
A_{ANNUL} (m^2)				$8.96x10^{-2}$
A_{FLOOR} (m^2)				0.317
Initial State				
P^o (MPa)	8.17	0.2		0.2
T^o (K)	283	283		283
ρ^o_g (kg/m^3)				
M_g (kg)		$5.95x10^{-2}$		
M_d (kg)				33
T_d (K)				2500
After Rupture Disk Failure and Gas Compression				
P (MPa)		8.17		
T (K)		710		
V (m^3)		$1.54x10^{-3}$		
ρ_g (kg/m^3)		38.8		
M_g (kg)		$5.95x10^{-2}$		
ρ^*_g (kg/m^3)		23.3		
Gas Flow Through Cavity				
P				0.8
T				2500
ρ_g				1.08

Table 17. Hydrogen combustion and analyses in CES/CE tests

ROW NUM.	PARAMETER	TEST						
		CES-1	CES-2	CES-3	CE-1	CE-2	CE-3	CE-4
	INITIAL CONDITIONS							
1	Driving Pres. (MPa)	8	8	8	8	8	8	4
2	Driving Media	Cold Water	Steam	Sat. Water	Sat. Water	Sat. Water	Steam	Sat. Water
3	Atmosphere	Inert	Inert	Inert	Reactive	Reactive	Reactive	Reactive
4	Cavity Water?	N	N	N	Y	Y	Y	Y
5	Mixing Fans?	N	30 min	30 min	N	0 min	2 min	30 min
6	Total Moles in Vessel	4091	3851	3986	3346	3506	3700	3730
7	% Steam in Atmosphere	0	0	0	49.2	47.3	48.9	51.2
8	% O_2 in the Vessel	0	0	0	12	11.6	11	10.9
9	% H_2 in Atmosphere	0	0	0	0	3.7	3.8	4
10	Moles H_2 Preexisting in Vessel	0	0	0	0	129	139	149
11	Moles H_2 Preexisting in Dome	0	0	0	0	77.4	83.4	89.4
	EXPERIMENT RESULTS							
12	Moles H_2 Produced	75	141	145	191	191	269	215
13	Moles H_2 Burned	0	0	0	130	203	323	256
14	ΔP Pre HPME (MPa)	0.015	0.014	0.014	0.059	0.121	0.137	0.125
15	ΔP HPME (MPa)	0.234	0.316	0.293	0.242	0.208	0.253	0.217
	INSIGHTS							
16	Pred ΔP (MPa) based on Row 13	0	0	0	0.200	0.312	0.496	0.393
17	Pred moles based on preHPME ΔP	0	0	0	29.3	69.7	80.1	72.3
18	Max Moles H_2 form Complete Fe Oxidation	330	330	330	330	330	330	330
19	Moles of H_2 from Cavity Water	0	0	0	53-106	53-106	53-106	53-106
20	Moles H_2 from Thermite Burn	5	5	5	5	5	5	5
21	Moles H_2 form Concrete Decomposition	8.9	8.9	8.9	8.9	15.4	11.4	11.4

Table 17. Hydrogen combustion and analyses in CES/CE tests

ROW NUM.	PARAMETER	TEST						
		CES-1	CES-2	CES-3	CE-1	CE-2	CE-3	CE-4
	PREHPME H_2 COMBUSTION							
22	Moles H_2 Entrained into Jet	0	0	0	0	5.5	6.0	6.6
23	Average (Meas) Dome Temperature	0	0	0	500	600	640	640
24	Upward Flammability Limit	0	0	0	0.0424	0.0369	0.0353	0.0358
25	Downward Flammability Limit	0	0	0	0.0738	0.0633	0.0596	0.0601
26	Reaction Completeness	0	0	0	0	0.003	0.111	0.171
27	Moles of Dome H_2 Burned in Deflagration	0	0	0	0	0.3	9.3	15.3
28	Maximum (Meas) Dome Temperature	0	0	0	630	850	780	800
29	Upward Flammability Limit	0	0	0	0.0359	0.0244	0.0283	0.0278
30	Downward Flammability Limit	0	0	0	0.0607	0.0379	0.0454	0.0439
31	Reaction Completeness	0	0	0	0	0.932	0.568	0.756
32	Moles of Dome H_2 Burned in Deflagration	0	0	0	0	72.1	47.3	67.6

Table 18. Material properties for thermite cooling

Property	Al_2O_3	Fe	Thermite
ε	0.8	---	---
h_f (MJ/kg)	1.16	---	---
k (w/m/k)	5	20	---
C_p(J/kg/K)	---	---	1178

Table 19. Categories for accumulator blowdown histories

Tests	Distinguishing Features
CES-1	100 kg of room temperature water expelled with pressurized nitrogen, i.e., nonflashing water discharge
CES-2 CE-3	No water, steam blowdown only
CES-3 CE-1 CE-2 CE-4	100 kg of saturated water expelled by pressurized steam, i.e., flashing water discharge

Table 20. Input parameters for the CES-1 experiment

Parameter	Value
ρ_w (kg/m^3)	960
V_g° (m^3)	0.150 (0.159)
V_w° (m^3)	0.104
MW_g (kg/g·mole)	0.028
γ	1.40
D_h (m)	0.0525
P° (MPa)	8.27 (7.62)
T° (K)	311 (304)
P_a (MPa)	0.2024
C_d	0.70

Values in ( ) represent modified initial conditions as noted in text.

Table 21. Input parameters for the CES-2 experiment

Parameter	Value
V_g° (m^3)	0.254
V_w° (m^3)	0.0
MW_g (kg/g·mole)	0.018
γ	1.10
D_h (m)	0.0525
P° (MPa)	8.52
T° (K)	607
P_a (MPa)	0.2027
C_d	0.6

Table 22. Initial conditions and computations for CES-3

Parameter	Value
Initial Conditions	
P° (MPa)	8.33
T° (K)	571
$M_{w/cold}^\circ$ (kg)	100
M_g° (kg)	4.37
M_w° (kg)	95.63
V_g° (m^3)	0.120
V_w° (m^3)	0.134
D_h° (m)	0.04
Properties	
ρ° (kg/m^3)	393.7
$\rho_{g,s}$ (kg/m^3)	36.4
$\rho_{l,s}$ (kg/m^3)	714.5
$h_{l,s}^\circ$ (MJ/kg)	1.35
Water Discharge	
G_{exp} ($kg/m^2/s$)	3.17×10^4
$G_{Bernouli}$ ($kg/m^2/s$)	3.49×10^4
G_{hem} ($kg/m^2/s$)	2.93×10^4
Depressurization Rate	
$\dot{P}_{exp}$ (MPa/s)	1.16
$F(P^\circ, VIM)$ (J/kg/Pa)	0.05
$f(P^\circ)$ (MJ/kg)	1.25

Table 23. Experiment data on coherence ratio for Calvert Cliffs cavity geometry

Test	f_{disp}	$C_{d,c}$	T^{o}_{d} (K)	T_{rcs} (K)	M^{o}_{d} (kg)	D_h (m)	V_c (m^3)	V_{rcs} (m^3)	t'_e (s)	$\frac{P_{rcs}}{P_o}$	R_τ
SNL/CES-2	.852	.6	607	33.2	9.76	.05	.22	.254	.1	1.11	.081
SNL/CES-3	.644	.6	622	33.2	8.59	.04	.22	.254	.1	1.14	.104

Table 24. Key parameters characterizing the coherence correlation

	Zion	Surry	Calvert Cliffs
N_{data}	21	13	2
$C_{R\tau}$	9.618	12.2	1.717
e_{bias}	0.014	-0.014	-0.184
σ_{rms}	0.240	0.154	0.585

Table 25. Applicability of the Calvert Cliffs database to reactor applications

	f_{disp}	T^{o}_{d}/T^{o}_{rcs}	M^{o}_{d}/M^{o}_{g}	$\frac{A_h V_c^{1/3}}{V_{rcs}}$
Database CES-2, CE-3	.64 - .85	0.26	3.7	3×10^{-3} - 4.7×10^{-3}
NPP - Scenario VI P^o = 8 MPa D_h = 0.4m T^o = 1000K M^o_d = 40 - 85 mt	~.9	0.25	7.7 - 16.3	2.2×10^{-3}
NPP - Scenario V P^o = 16 MPa D_h = 0.4m T^o = 700K M^o_d = 25 -65 mt	~.9	0.36	1.3 - 3.5	2.2×10^{-3}

Table 26. Coherent steam and water during dispersal in the SNL/CES and SNL/CE tests

Parameter	CES-1	CES-2	CES-3	CE-1	CE-2	CE-3	CE-4
Steam Driven Tests							
N^{o}_{acc} (moles		538				477	
R_{τ}		0.081				0.104	
Coh. stm. (moles)		44				50	
Coh. water (moles)		0				0	
Water Driven Tests							
$\dot{M}_{w}$ (kg/s)	166		41.7	37.0	41.7		31.3
X_{g}	0		0.37	0.37	0.37		0.26
t_{e}	0.15		0.10	0.15	0.10		0.15
Coh. stm. (moles)	0		86	114	86		45
Coh. water (moles)	1383		146	194	146		129

Table 27. Assessment of debris flow through nozzle cutouts

Parameter	Test							Avg.
	CES-1	CES-2	CES-3	CE-1	CE-2	CE-3	CE-4	
A_g (m^2)	0.0825	0.0825	0.0825	0.0825	0.0825	0.0825	0.0825	
A_{mw} (m^2)	0.0058	0.0058	0.0058	0.0029	0.0029	0.0029	0.0029	
A_{nz} (m^2)	0.0878	0.0878	0.0878	0.0878	0.0878	0.0878	0.0878	
A_{nz} bottom (m^2)	0.091	0.091	0.091	0.091	0.091	0.091	0.091	
f_g pred	0.934	0.934	0.934	0.966	0.966	0.966	0.966	
f_{dm} meas	0.792	0.720	0.760	0.763	0.740	0.713	0.742	
f_{nz} inferred	0.152	0.229	0.187	0.210	0.234	0.262	0.232	0.22
f_{nz} splash	0.524	0.524	0.524	0.524	0.524	0.524	0.524	0.52
f_{noz} flow	0.516	0.516	0.516	0.516	0.516	0.516	0.516	0.52

Table 28. Loads mitigation in open geometry experiments

Test Series	η_{meas}	η_{mass}	η_{KE}(50%)	η_{KE}(75%)	η_{pred}
SNL/DCH	0.40	0.52	0.95	0.62	0.41
SNL/TDS	0.50	0.60	0.97	0.52	0.45
SNL/WC/LFP8	0.51	0.93	0.73	0.28	0.47
SNL/CES/CE	0.78	≤0.97	1.00	0.79	0.87

Table 29. Experiment insights on coejected water

Test	Driving Medium	Atmosphere	ΔP_{HPME}
CES-2	steam	inert	0.316
CES-3	sat. water	inert	0.293
CES-1	cold water	inert	0.234
CE-3	steam	reactive	0.253
CE-2	sat. water	reactive	0.208

Table 30. Test of P, T, N consistency

	Pre-HPME	Post-HPME	
	t=-0s	t @ Pmax	t=20s
CES-1			
P (MPa)	0.215	0.450	0.360
T (K)	309	495	425
N (g-moles)	4091	4585	4585
PV/(NRT)	1.02	1.19	1.11
Nprod(g-moles)	93	882	509
CES-2			
P (MPa)	0.217	0.530	0.380
T (K)	325	540	500
N (g-moles)	3851	4389	4389
PV/(NRT)	1.04	1.34	1.04
Nprod(g-moles)	164	1514	182
CES-3			
P (MPa)	0.215	0.510	0.395
T (K)	310	430	400
N (g-moles)	3986	6231	6231
PV/(NRT)	1.05	1.14	0.95
Nprod(g-moles)	185	902	-292
CE-1			
P (MPa)	0.257	0.495	0.395
T (K)	440	445	430
N (g-moles)	3346	5597	5597
PV/(NRT)	1.05	1.20	0.99
Nprod(g-moles)	167	1093	-73
CE-2			
P (MPa)	0.265	0.47	0.395
T (K)	455	425	415
N (g-moles)	3506	5751	5751
PV/(NRT)	1.00	1.16	1.00
Nprod(g-moles)	-3	900	-27
CE-3			
P (MPa)	0.3	0.545	0.37
T (K)	485	650	555
N (g-moles)	3700	4177	4177
PV/(NRT)	1.01	1.21	0.96
Nprod(g-moles)	20	865	-168
CE-4			
P (MPa)	0.295	0.512	0.42
T (K)	475	500	450
N (g-moles)	3730	5299	5299
PV/(NRT)	1.00	1.16	1.06
Nprod(g-moles)	5	859	314

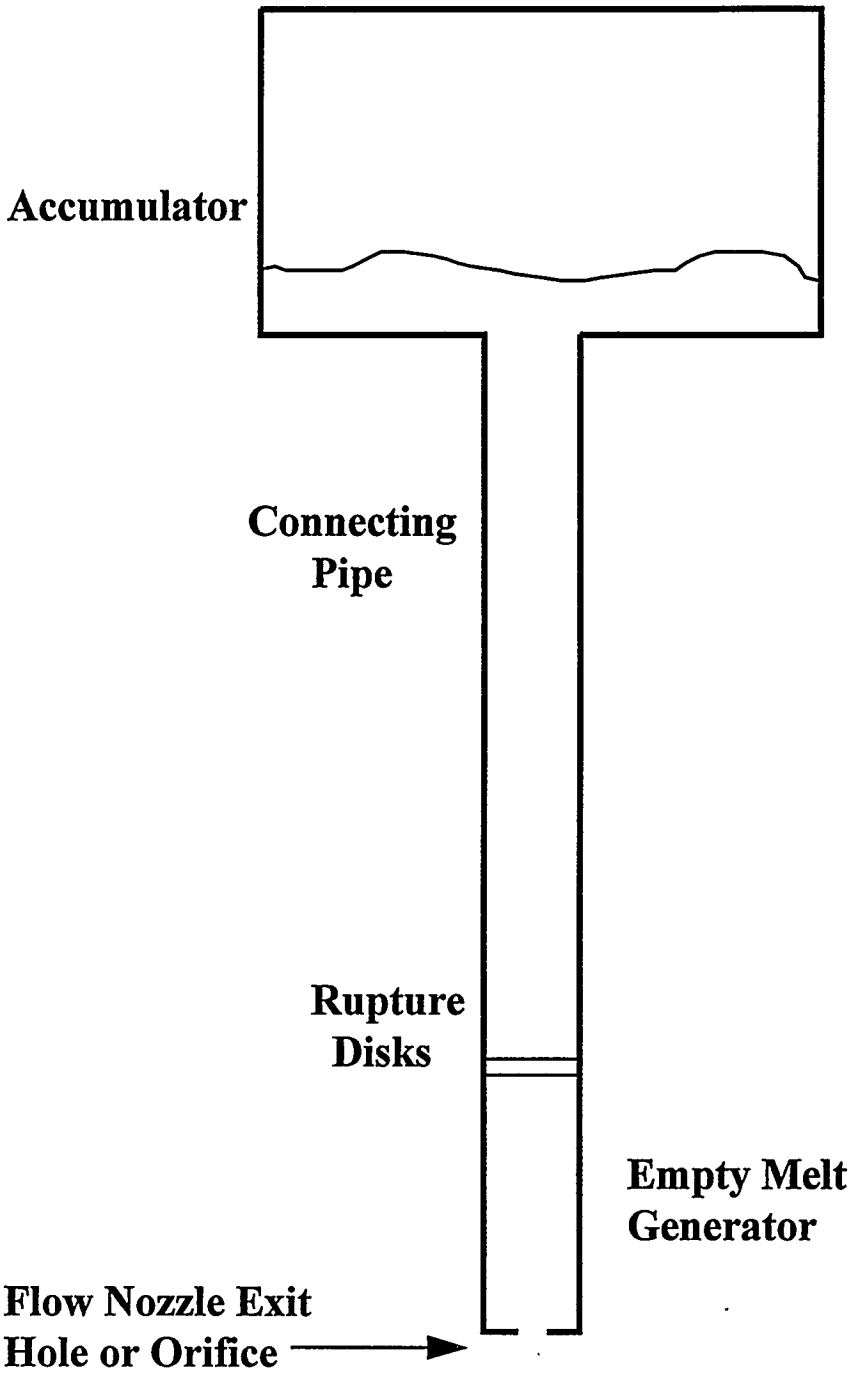

Figure 67. Conceptual layout of the system.

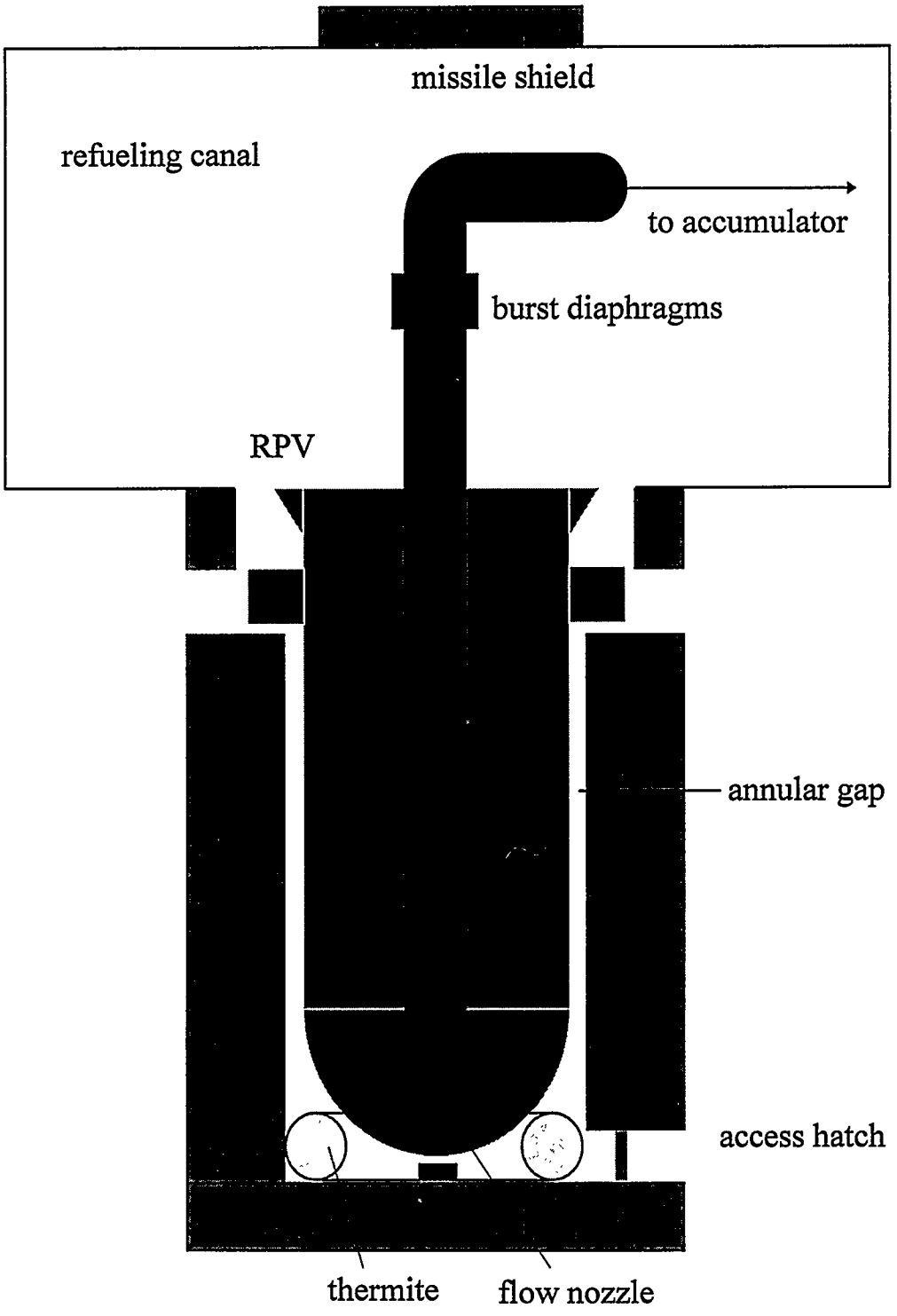

Figure 68. Details of the melt generator/cavity layout.

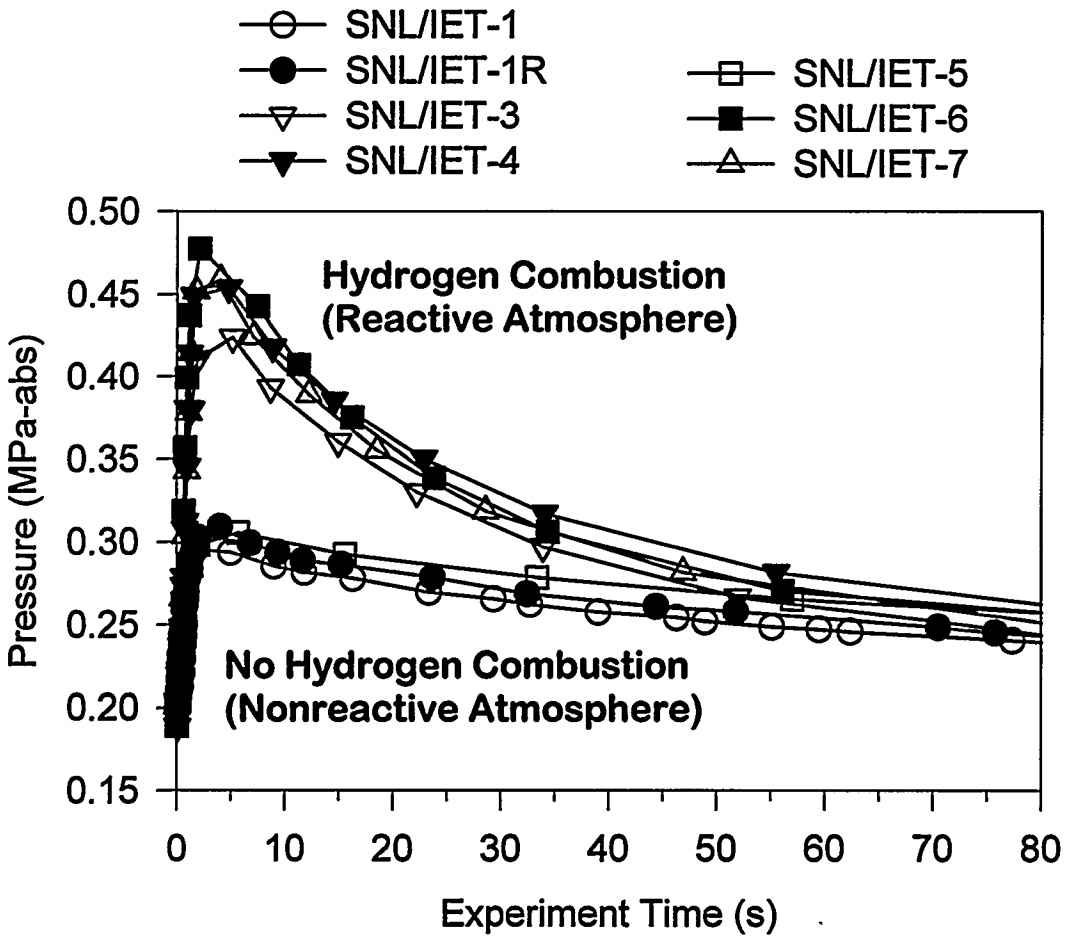

Figure 69. Hydrogen combustion in Zion geometry SNL/IET tests.

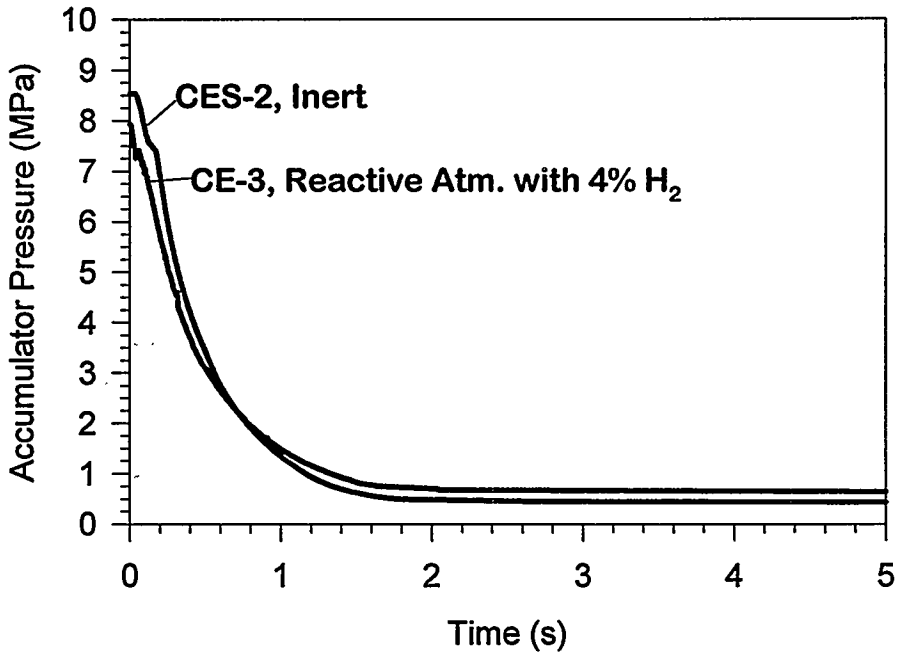

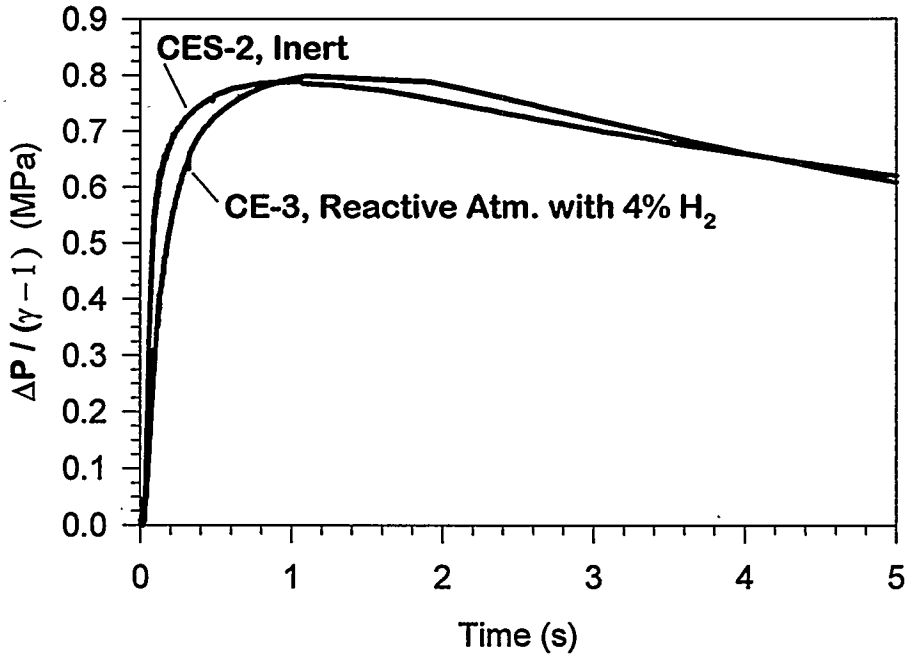

Figure 70. Hydrogen combustion in steam-driven tests.

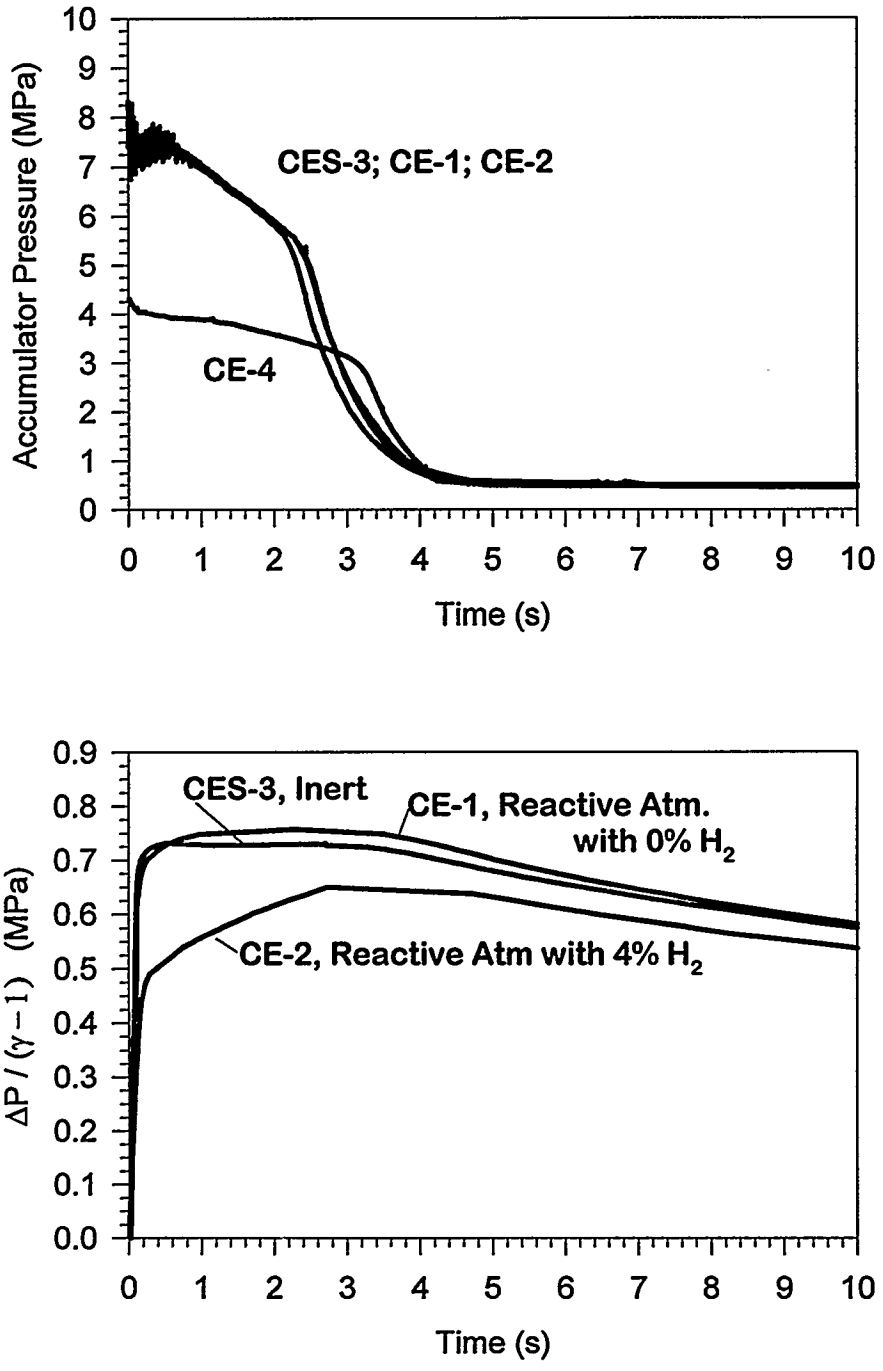

Figure 71. Hydrogen combustion in saturated water-driven tests.

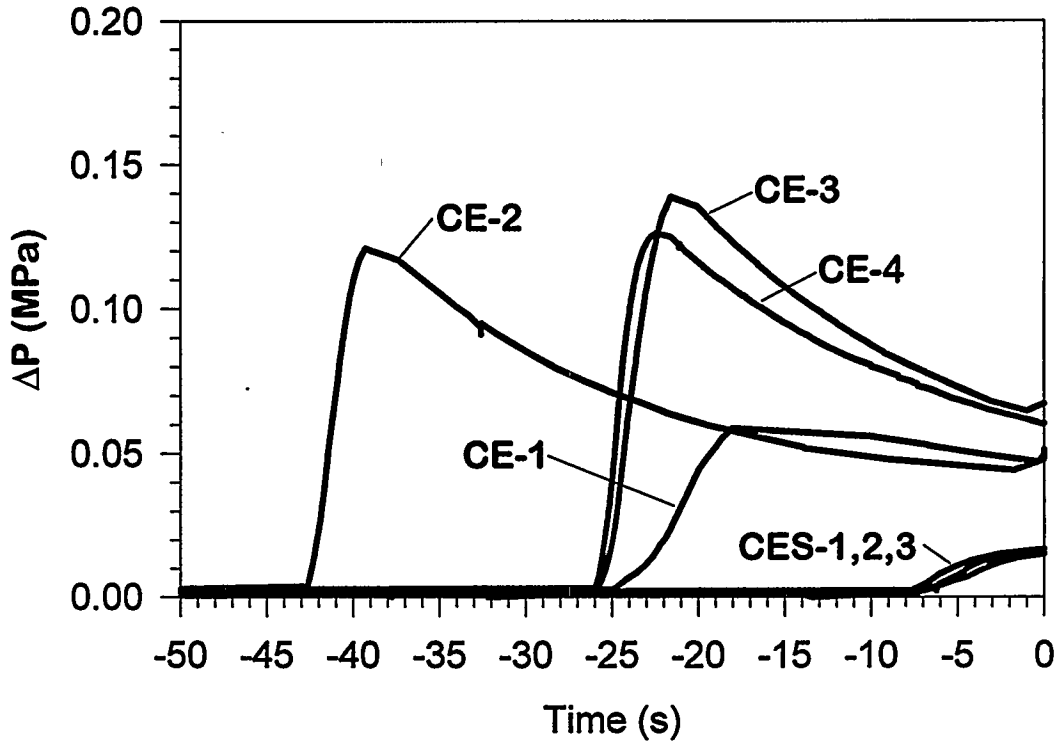

Figure 72. Vessel pressurization during thermite burn in cavity and prior to HPME event.

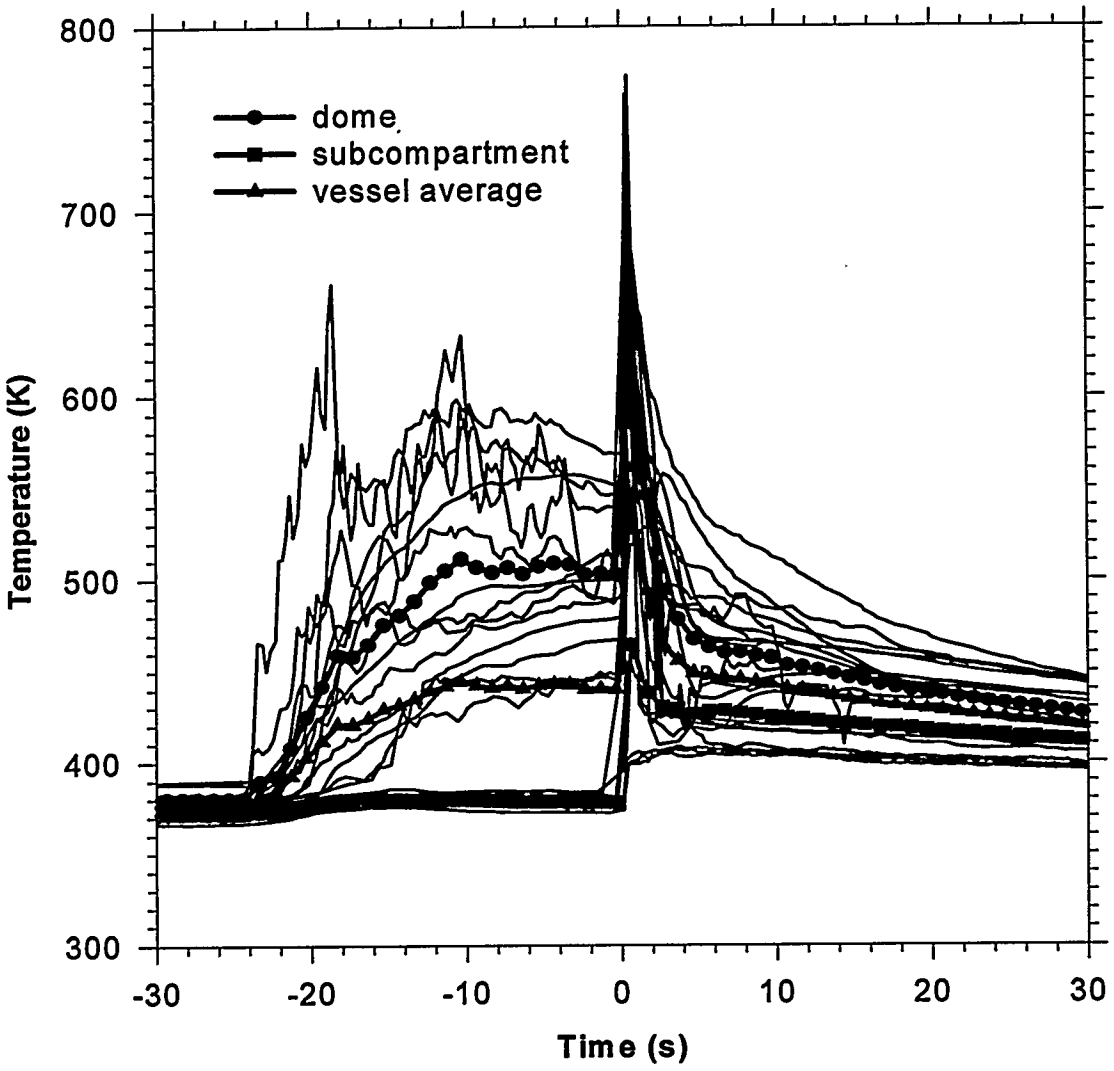

Figure 73. Pre-HPME dome temperatures in the CE-1 experiment.

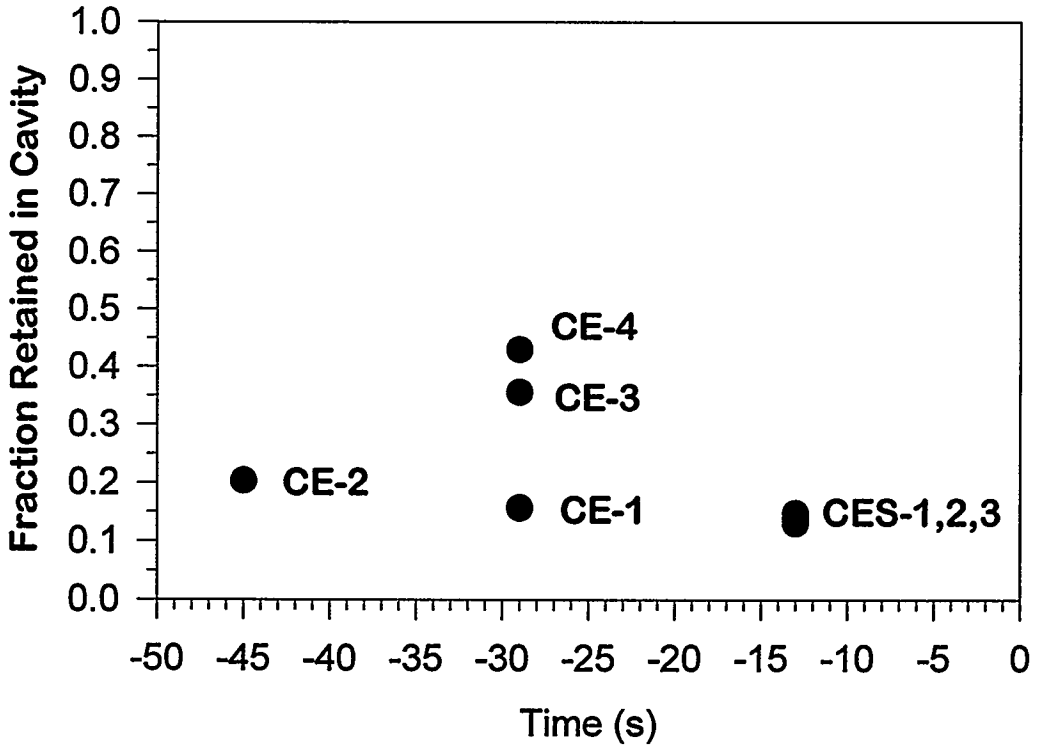

Figure 74. Dependence of melt retention on the delay between thermite ignition and blowdown.

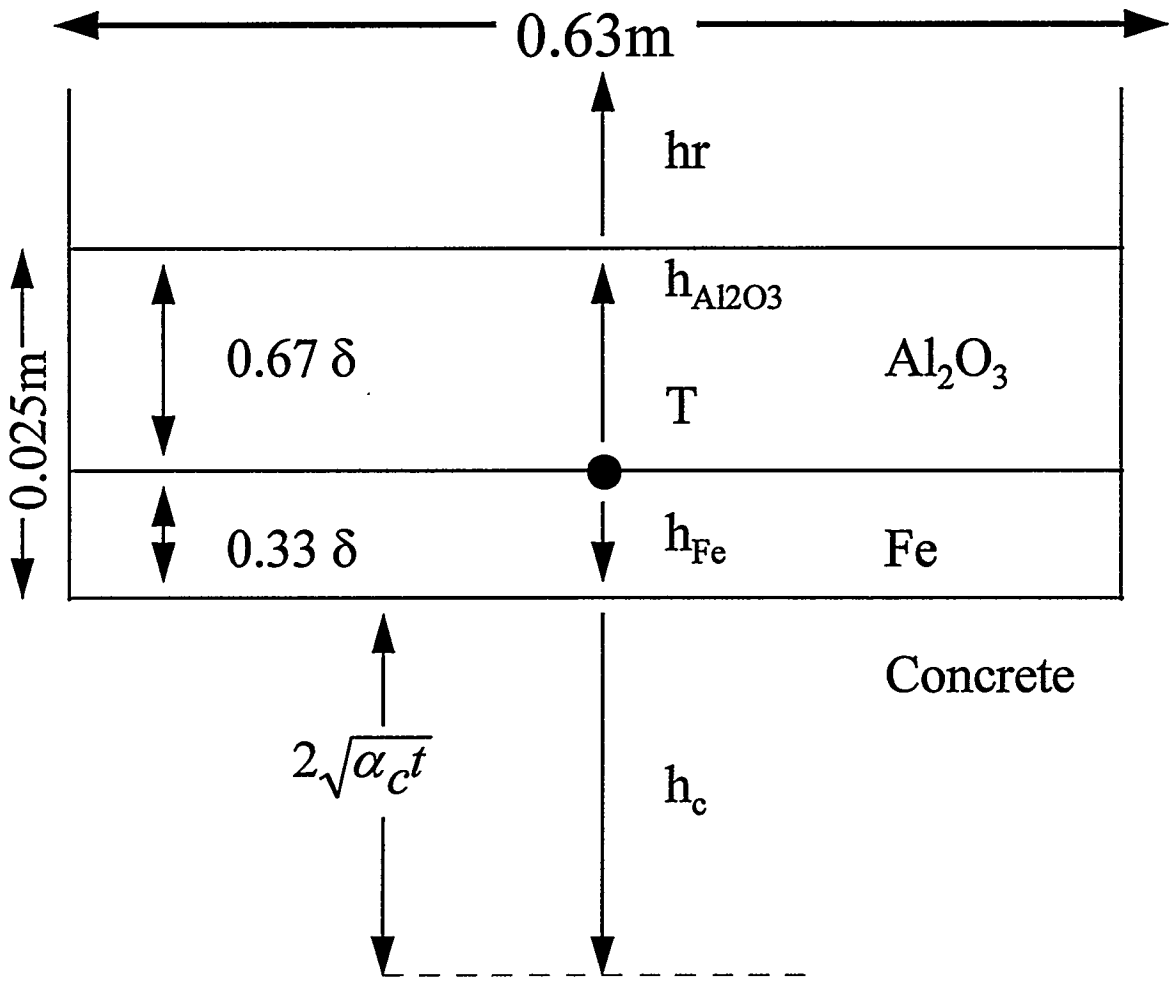

Figure 75. Heat losses from thermite on the cavity floor prior to blowdown.

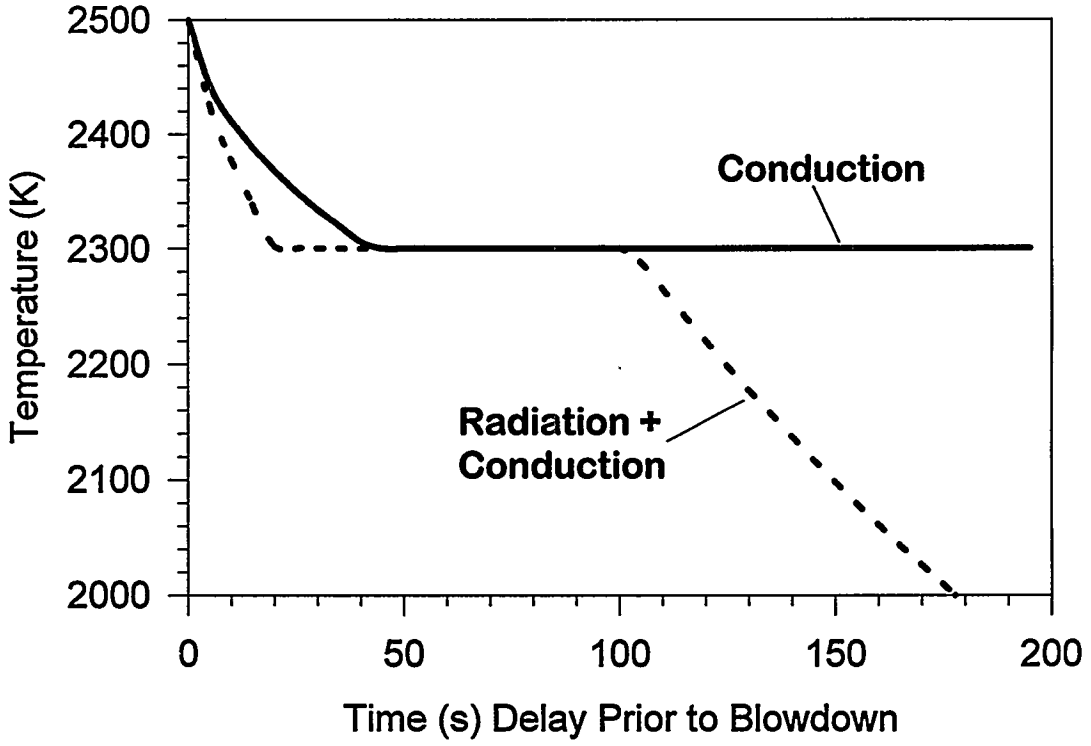

Figure 76. Predicted temperature history of thermite in the cavity prior to blowdown.

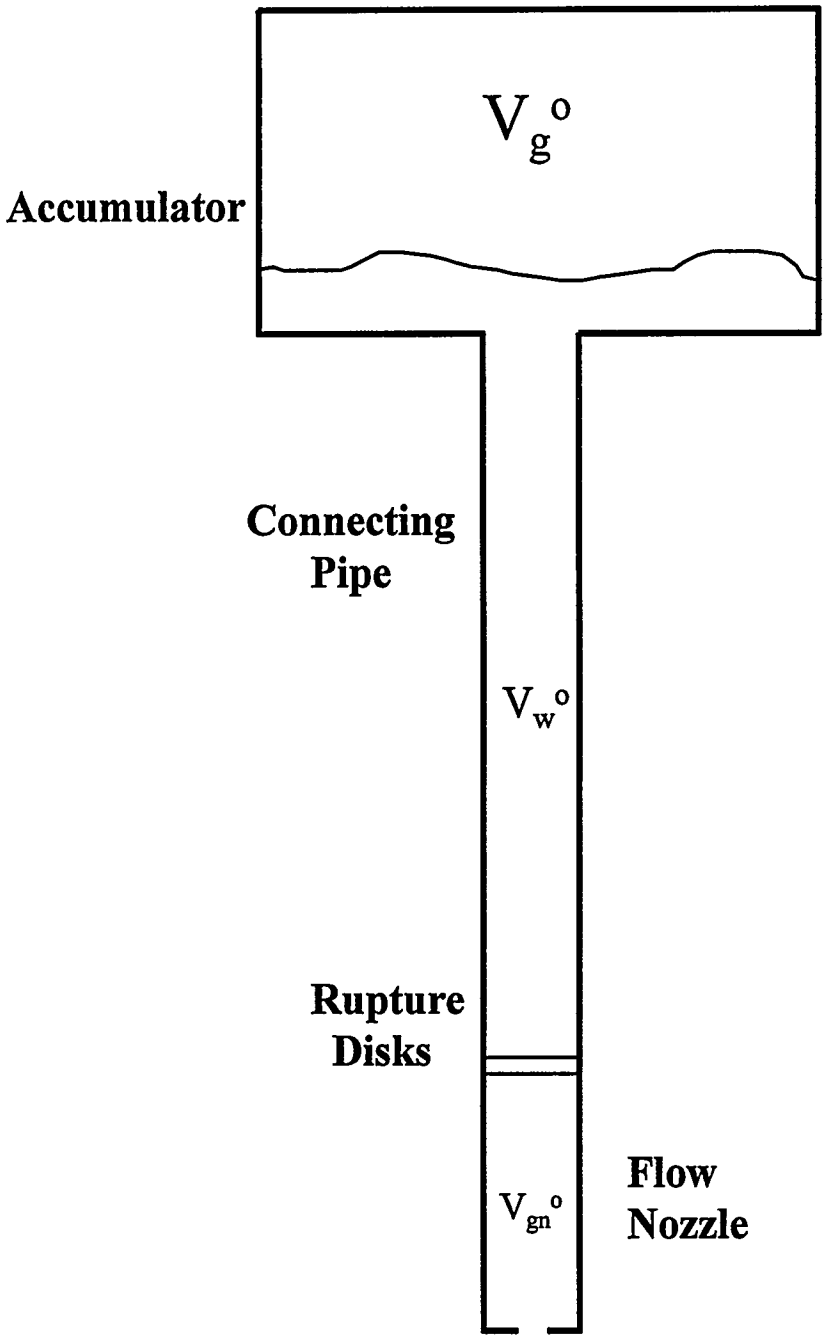

Figure 77. Conceptual layout of the system.

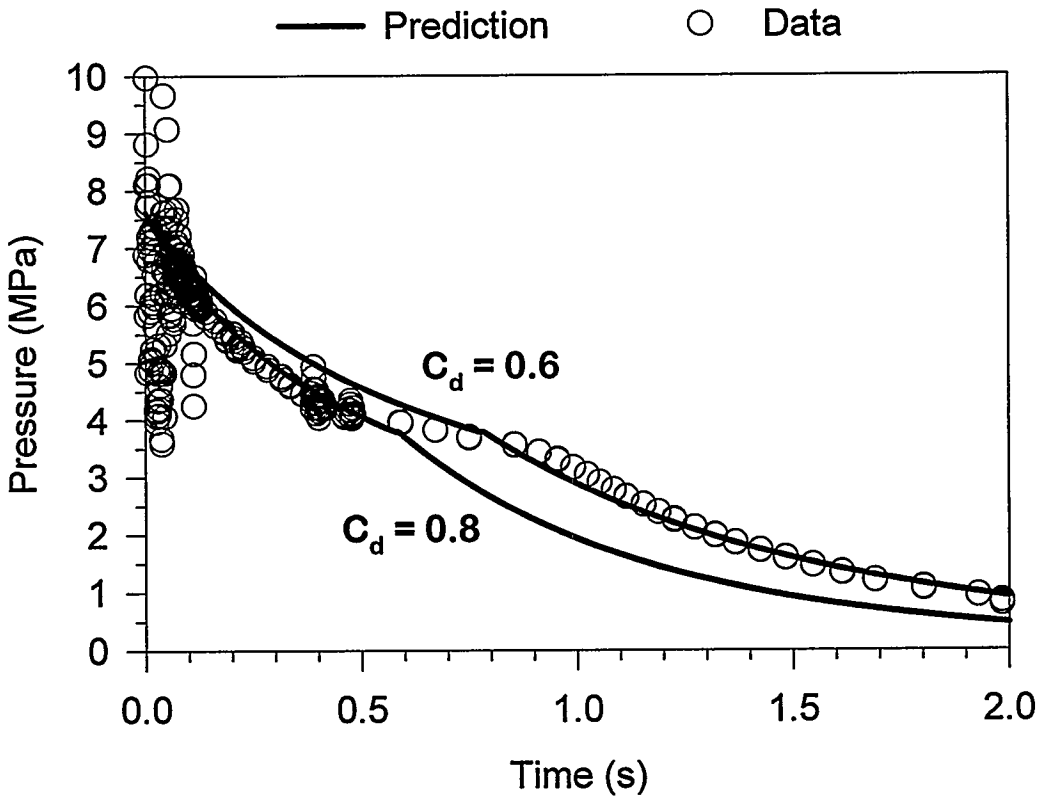

Figure 78. Comparison of the predicted depressurization history for CES-1 with experiment data.

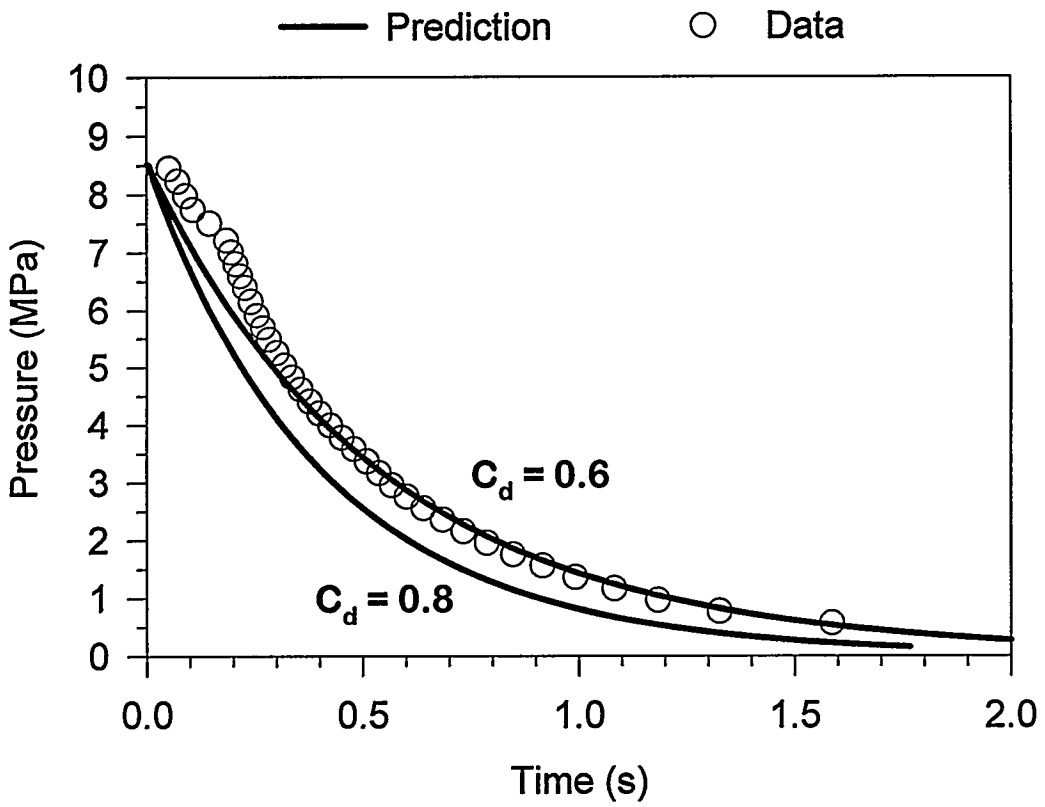

Figure 79. Comparison of the predicted depressurization history for CES-2 with experiment data.

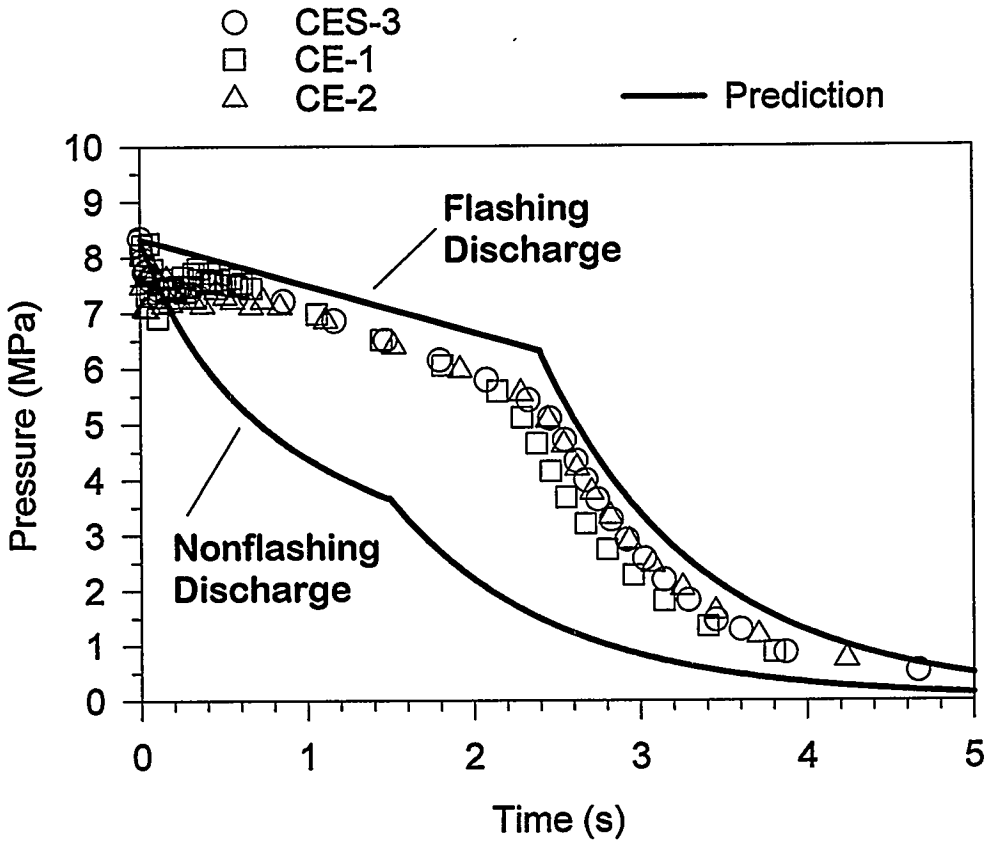

Figure 80. Accumulator depressurization in the CES-3, CE-1, and CE-2 experiments.

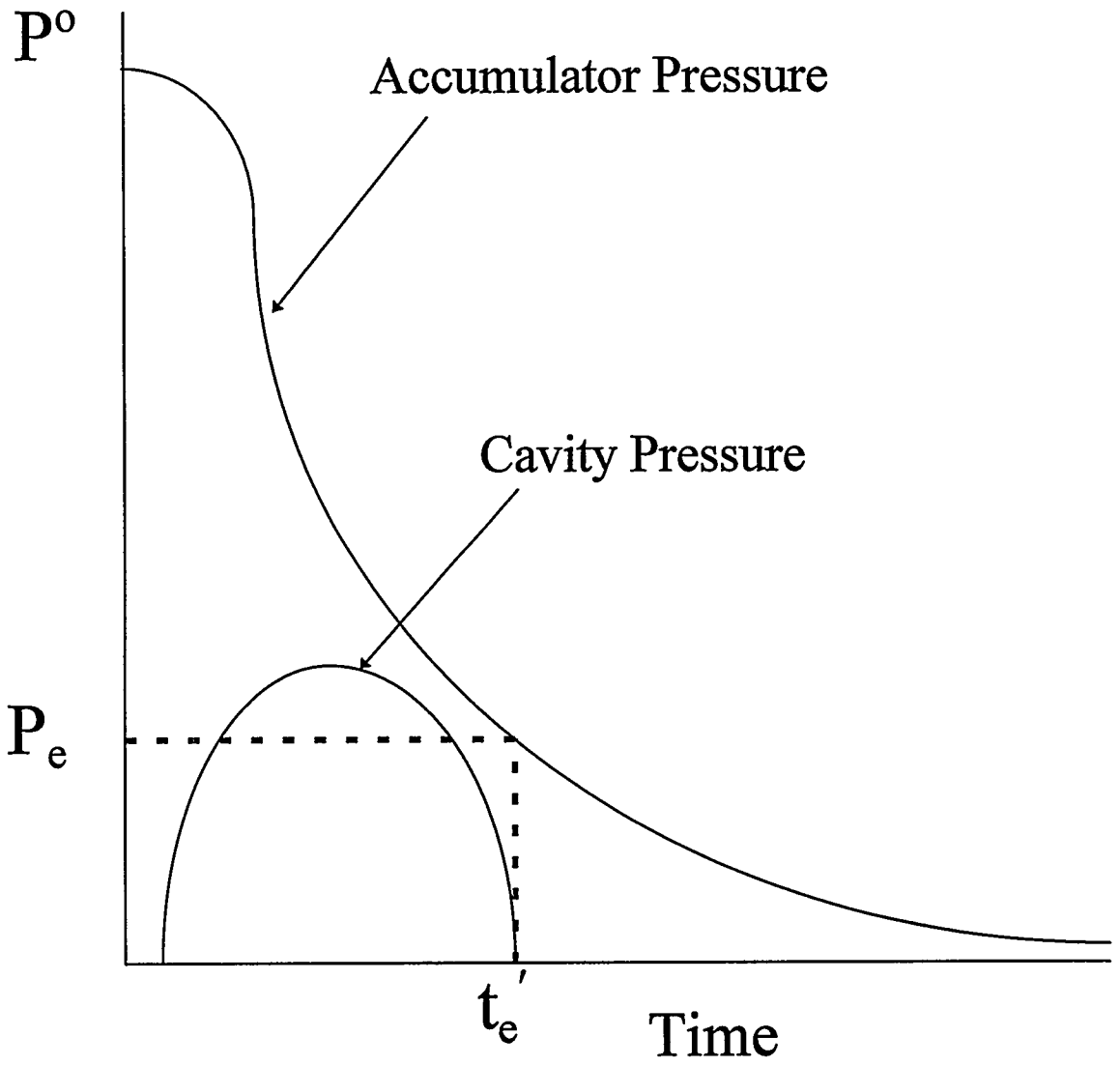

Figure 81. Procedure for estimating the coherence interval.

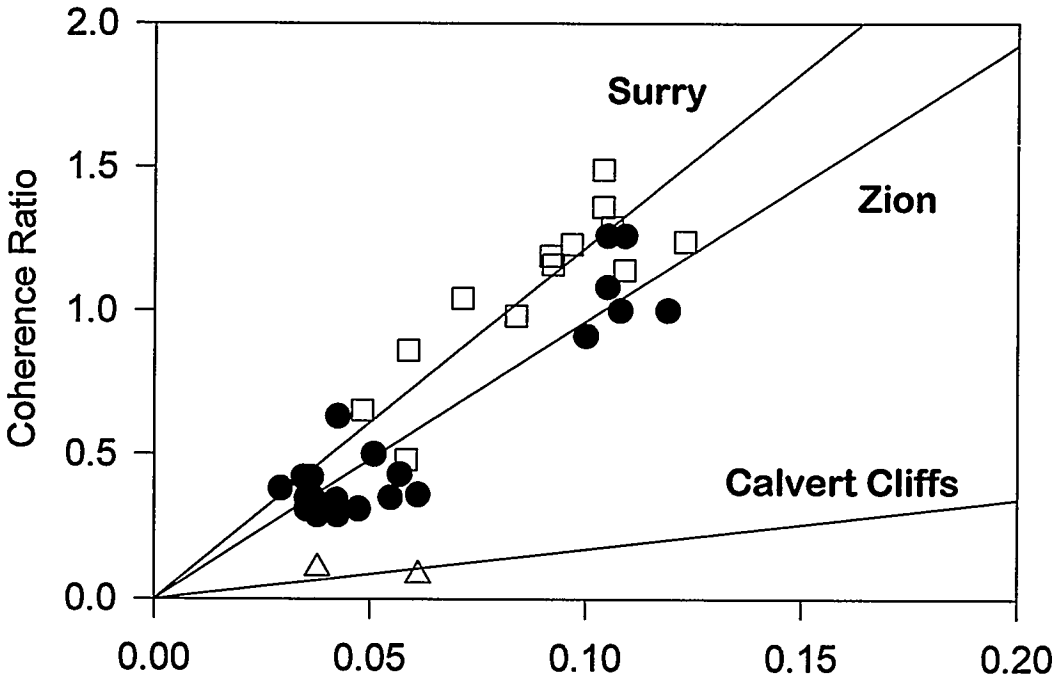

$$f_{disp}\left(\frac{T^o_{RCS}}{T^o_d}\right)^{1/4}\left(C_{d,h}\frac{M^o_d}{M^o_g}\frac{A_h V_c^{1/3}}{V_{RCS}}\right)^{1/2}$$

Figure 82. Coherence of dispersed debris and blowdown during cavity dispersal.

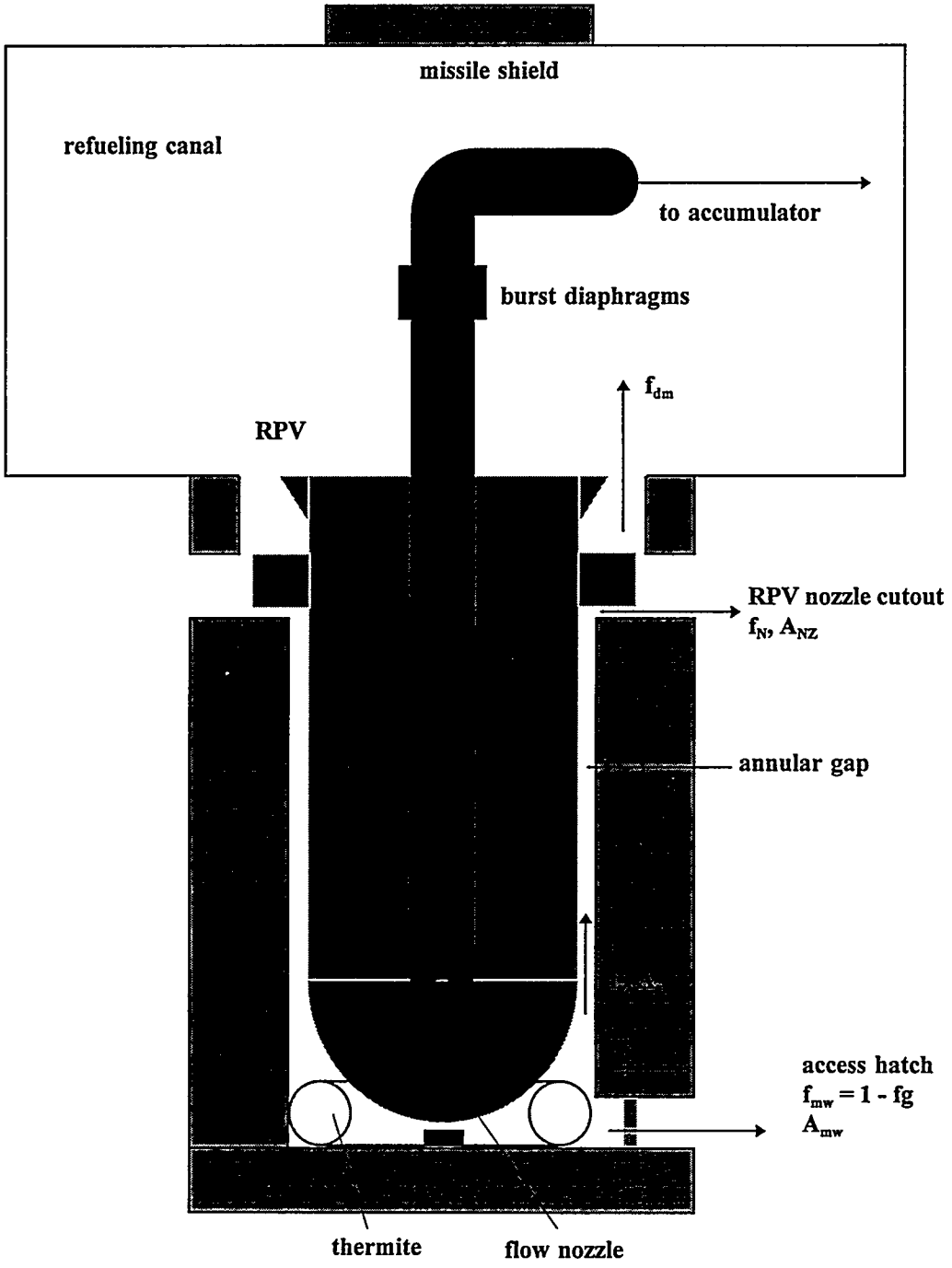

Figure 83. Validation of the TCE model for Calvert Cliffs geometry and other open geometry tests.

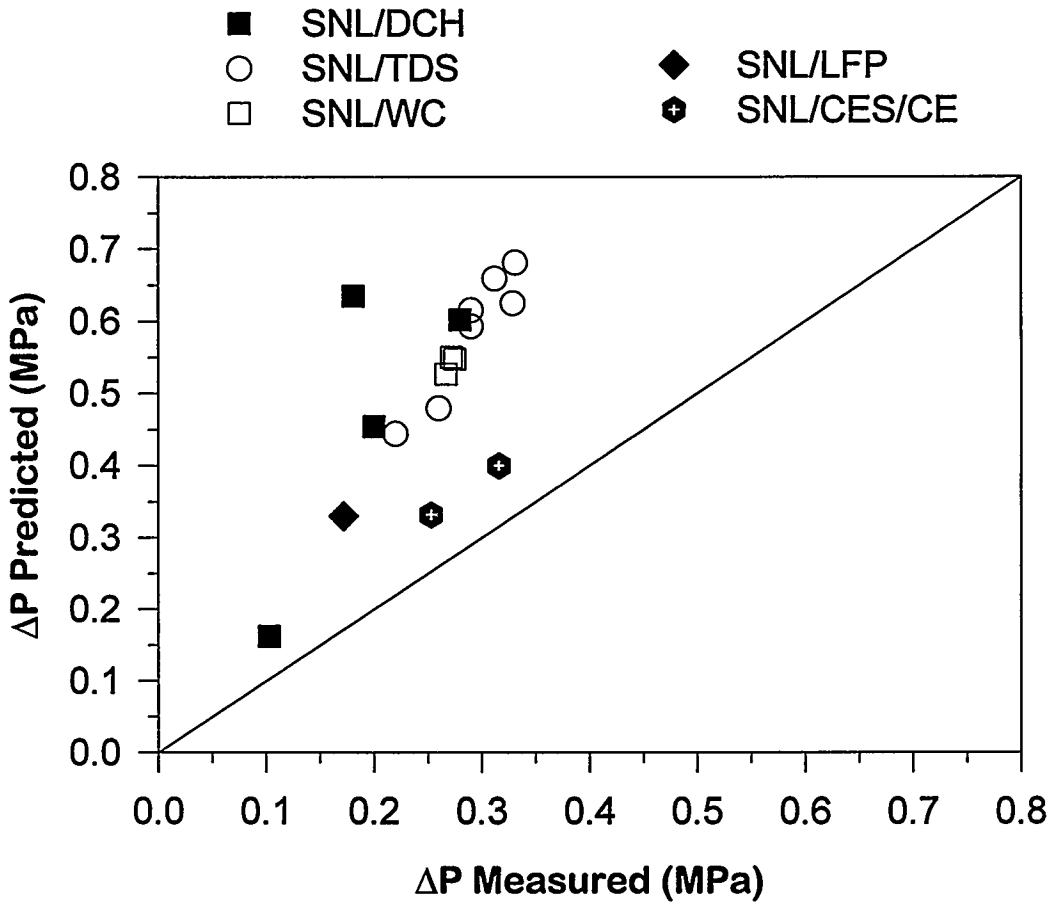

Figure 84. Validation of the TCE model in "open geometry" experiments.

5.0 CONCLUSIONS

The Surtsey Test Facility at Sandia National Laboratories (SNL) was used to perform DCH tests with scaled models of the Calvert Cliffs NPP structures. These structures were intended to be representative of Combustion Engineering plants with a Bechtel annular cavity design (Calvert Cliffs 1 and 2, Millstone 2, Arkansas Nuclear One Unit 2, and Palisades). The model included the reactor pressure vessel (RPV), cavity, refueling canal, operating deck, control rod drive missile shield, and crane wall. A corium simulant (thermite) was reacted on the floor of a 1/10th scale Calvert Cliffs cavity. The melt was entrained out of the cavity into the Surtsey vessel by a high-velocity steam or water/steam blowdown of an accumulator modeling the RCS. Seven tests were conducted: three tests with inert atmospheres (CES-1, 2, 3) and four tests with reactive atmospheres (CE-1 with air/steam and CE-2, 3, 4 with air/steam/hydrogen). The major conclusions are summarized below.

1. Driving melt from the cavity with saturated water reduced DCH peak loads in the tests by 10-20% relative to steam-driven tests. Driving melt from the cavity with room temperature water reduced loads by 25%. The containment atmosphere was rapidly quenched during the period of water ejection into the atmosphere. Therefore, we conclude that large amounts of coejected water slightly mitigates loads in the Calvert Cliffs geometry.

2. Significant amounts of hydrogen, preexisting in the Surtsey atmosphere and also produced by the thermite reaction with condensate water, burned in the reactive atmosphere tests prior to the HPME event and pressurized the vessel. Experiment data suggest that any potential hydrogen combustion during the HPME event did not contribute to loads. However, the bulk of the hydrogen production and combustion probably occurred during the thermite burn prior to the HPME event. This production and combustion mechanism is an artifact of the experimental method and, therefore, is not prototypic of a NPP accident. However, the combustion of the preexisting hydrogen is considered in a NPP analysis for DCH issue resolution (NUREG/CR-6475).

3. The coherence of the melt dispersal with the steam and water/steam blowdown was small. The debris entrainment interval was about 0.1 s. This was much less than the ~0.4 to 0.8 s seen in the DCH tests that involved Westinghouse cavities with instrument tunnels. Comparable coherence ratios were seen in all CE tests, whether the melt was ejected from the cavity using steam or using water. Most of the DCH load on the vessel occurred very quickly, in the melt dispersal time frame (0.1-0.2 s) and not in the blowdown time frame (2-4 s).

4. Approximately 78% ± 12% of the melt in the 1/10th scale Calvert Cliffs reactor cavity was dispersed into the Surtsey vessel. This was comparable to the previous Surry and Zion DCH tests. In the 1/6th scale Surry tests there was 81% dispersal into the Containment Technology Test Facility vessel and in the 1/10th scale Zion tests there was 77%* dispersal into the Surtsey vessel.

5. Results of all seven Calvert Cliffs experiments indicated that 58% of the total debris recovered posttest was transported to the upper dome. In the Zion and Surry tests without the annular gap modeled, only 7%* to 10% of the total debris recovered was found in the upper dome.

6. Substantial cavity pressures were measured in some of the tests. However, the experimental pressure may have resulted from the nonprototypic contact of blowdown and melt in the cavity.

* Data from IET-4, IET-8A, and IET-8B were excluded when calculating these averages due to nonprototypic damage to structures.

6.0 REFERENCES

Allen, M.D., M. Pilch, R.T. Nichols and R.O. Griffith, Oct. 1991, *Experiments to Investigate the Effect of Flight Path on Direct Containment Heating (DCH) in the Surtsey Test Facility - The Limited Flight Path (LFP) Experiments*, NUREG/CR-5728, SAND91-1105, Sandia National Laboratories, Albuquerque, NM.

Allen, M.D. et al. (1992a). *Experiments to Investigate the Effect of Water in the Cavity on Direct Containment Heating (DCH) in the Surtsey Test Facility - The WC-1 and WC-2 Tests*, SAND91-1173, Sandia National Laboratories, Albuquerque, NM.

Allen, M.D. et al. (1992b). *Experimental Results of Tests to Investigate the Effects of Hole Diameter Resulting from Bottom Head Failure on Direct Containment Heating (DCH) in the Surtsey Test Facility - The WC-1 and WC-3 Tests*, SAND91-2153, Sandia National Laboratories, Albuquerque, NM.

Allen, M.D., M. Pilch, T.K. Blanchat, R.O. Griffith, and R.T. Nichols, May 1994, *Experiments to Investigate Direct Containment Heating Phenomena with Scaled Models of the Zion Nuclear Power Plant in the Surtsey Test Facility*, NUREG/CR-6044, SAND93-1049, Sandia National Laboratories, Albuquerque, NM.

Bertodano, M. Lopez de (1993). *Direct Containment Heating DCH Source Term Experiment for Annular Reactor Cavity Geometry*, Ninth Proceedings of Nuclear Thermal Hydraulics, 1993 ANS Winter Mtg., Nov. 14-18, 1993, San Francisco, CA, p. 111-120.

Blanchat, T.K., M.D. Allen, M. Pilch, and R.T. Nichols, June 1994, *Experiments to Investigate Direct Containment Heating Phenomena with Scaled Models of the Surry Nuclear Power Plant*, NUREG/CR-6152, SAND93-2519, Sandia National Laboratories, Albuquerque, NM.

Blanchat, T.K., January 1995, "Results of the Oxide Thermite Scoping Tests," letter report to R. Lee (USNRC), Sandia National Laboratories, Albuquerque, NM.

Chatterjee, A. and A.V. Bradshaw, March 1972, "Break-up of a Liquid Surface by an Impinging Gas Jet," *J. of the Iron and Steel Institute,* pp. 179-187.

Davenport, W.G., D.H. Wakelin, and A.V. Bradshaw, 1966, "Interaction of Both Bubbles and Gas Jets With Liquids," *J. of Heat and Mass Transfer in Process Metallurgy*, pp. 207-244.

Ginsberg, T. and N.K. Tutu (1987). *Safety Research Programs Sponsored by Office of Nuclear Regulatory Commission*, Quarterly Progress Report, NUREG/CR-2331, Vol. 7, No. 2.

Gronager, J.E. et al. (1986). *TURC1: Large Scale Metallic Melt-Concrete Interaction Experiments and Analysis*, SAND85-0707, NUREG/CR-4420, Sandia National Laboratories, Albuquerque, NM.

Lahey, Jr., R.T. and F.J. Moody (1993). The Thermal Hydraulics of Boiling Water Reactors, 2nd Edition, American Nuclear Society, La Grange Park, IL.

Pilch, M.M., Oct. 1991, "Adiabatic Equilibrium Models for Direct Containment Heating," SAND91-2407C, presented at the 19th Water Reactor Safety Information Meeting, Washington, DC.

Pilch, M.M., (1994a), "Plant Selection for Confirmatory Testing for CE Plants," Letter report to R. Lee (USNRC), Sandia National Laboratories, Albuquerque, NM.

Pilch, M.M. et al. (1994b). *The Probability of Containment Failure by Direct Containment Heating in Zion*, NUREG/CR-6075, Supplement 1, Sandia National Laboratories, Albuquerque, NM.

Pilch, M.M. et al. (1994c). *The Probability of Containment Failure by Direct Containment Heating in Zion*, SAND93-1535, NUREG/CR-6075, Sandia National Laboratories, Albuquerque, NM.

Pilch, M.M., M.D. Allen, and E.W. Klamerus, October 1995, *Resolution of the Direct Containment Heating Issue for All Westinghouse Plants with Large Dry Containments or Subatmospheric Containments*, NUREG/CR-6338, SAND95-2381, Sandia National Laboratories, Albuquerque, NM.

Pilch, M.M. et al. (1996). *Resolution of the Direct Containment Heating Issue for all Combustion Engineering Plants and Babcock & Wilcox Plants*, NUREG/CR-6475, Sandia National Laboratories, Albuquerque, NM.

Todreas, N.E. and M.S. Kazimi (1990). NUCLEAR SYSTEMS I Thermal Hydraulic Fundamentals, Hemisphere Publishing Corporation.

Williams, D.C. and D.L.Y. Louie (1988). "CONTAIN Analyses of Direct Containment Heating Events in the Surry Plant," ANS/ENS International Meeting, ANS Thermal Hydraulics Division, Washington, DC.

Yan, H. and T.G. Theofanous (1993). "The Prediction of Direct Containment Heating," *ANS Proceedings*, 1993 National Heat Transfer Conference, Atlanta, GA, p. 294-309.

Zuber, N. et al., 1991, *An Integrated Structure and Scaling Methodology for Severe Accident Technical Issue Resolution*, NUREG/CR-5809, EGG-2659.

NRC FORM 335 (2-89) NRCM 1102, 3201, 3202

U.S. NUCLEAR REGULATORY COMMISSION

BIBLIOGRAPHIC DATA SHEET

(See instructions on the reverse)

1. REPORT NUMBER (Assigned by NRC, Add Vol., Supp., Rev., and Addendum Numbers, if any.)

NUREG/CR-6469
SAND96-2289

2. TITLE AND SUBTITLE

Experiments to Investigate Direct Containment Heating Phenomena With Scaled Models of the Calvert Cliffs Nuclear Power Plant

3. DATE REPORT PUBLISHED

MONTH	YEAR
February	1997

4. FIN OR GRANT NUMBER

W6162

5. AUTHOR(S)

T.K. Blanchat (SNL)
M.M. Pilch (SNL)
M.D. Allen (SNL)

6. TYPE OF REPORT

Technical

7. PERIOD COVERED *(Inclusive Dates)*

8. PERFORMING ORGANIZATION – NAME AND ADDRESS *(If NRC, provide Division, Office or Region, U.S. Nuclear Regulatory Commission, and mailing address; if contractor, provide name and mailing address.)*

Sandia National Laboratories
Dept. 6402/MS1137
P.O. Box 5800
Albuquerque, NM 87185-1137

9. SPONSORING ORGANIZATION – NAME AND ADDRESS *(If NRC, type "Same as above"; if contractor, provide NRC Division, Office or Region, U.S. Nuclear Regulatory Commission, and mailing address.)*

Division of Systems Technology
Office of Nuclear Regulatory Research
U.S. Nuclear Regulatory Commission
Washington, DC 20555-0001

10. SUPPLEMENTARY NOTES

R. Lee, NRC Project Manager

11. ABSTRACT *(200 words or less)*

The Surtsey Test Facility at Sandia National Laboratories (SNL) is used to perform scaled experiments for the Nuclear Regulatory Commission (NRC) that simulate High Pressure Melt Ejection (HPME) accidents in a nuclear power plant (NPP). These experiments are designed to investigate the effects of direct containment heating (DCH) phenomena on the containment load. In previous experiments, high-temperature, chemically reactive (thermitic) melt was ejected by high-pressure steam into a scale model of either the Zion or Surry NPP. The results from the Zion and Surry experiments were extrapolated to other Westinghouse plants. This report describes tests performed with Combustion Engineering plant geometries (in particular, Calvert Cliffs-like) and the impact of codispersed water as part of the overall DCH issue resolution. Integral effects tests were performed with a 1/10th scale model of the Calvert Cliffs NPP inside the Surtsey test vessel. The experiments investigated the effects of codispersal of water, steam, and molten core simulant materials on DCH loads under prototypic accident conditions and plant configurations. The results indicated that large amounts of coejected water reduced the DCH load by a small amount. Large amounts of debris were dispersed from the cavity to the upper dome (via the annular gap).

12. KEY WORDS/DESCRIPTORS *(List words or phrases that will assist researchers in locating the report.)*

coejected water
Combustion Engineering (CE)
Direct Containment Heating (DCH)
high pressure melt ejection
severe accident
pressurized water reactor
Calvert Cliffs

13. AVAILABILITY STATEMENT

Unlimited

14. SECURITY CLASSIFICATION

(This Page) Unclassified

(This Report) Unclassified

15. NUMBER OF PAGES

16. PRICE